Johannes Görthofer

Microstructure generation and micromechanical modeling of sheet molding compound composites

Johannes Görthofer

Microstructure generation and micromechanical modeling of sheet molding compound composites

Eine Übersicht aller bisher in dieser Schriftenreihe erschienenen Bände
finden Sie am Ende des Buchs.

Microstructure generation and micromechanical modeling of sheet molding compound composites

by
Johannes Görthofer

KIT Scientific Publishing

Karlsruher Institut für Technologie
Institut für Technische Mechanik
Bereich Kontinuumsmechanik

Microstructure generation and micromechanical modeling
of sheet molding compound composites

Zur Erlangung des akademischen Grades eines Doktors der Ingenieur-
wissenschaften von der KIT-Fakultät für Maschinenbau des
Karlsruher Instituts für Technologie (KIT) genehmigte Dissertation

von Johannes Görthofer, M.Sc.

Tag der mündlichen Prüfung: 28. April 2022
Hauptreferent: Prof. Dr.-Ing. Thomas Böhlke
Korreferent: Jun.-Prof. Dr. rer. nat. Matti Schneider
Korreferent: Prof. Dr. Andrew N. Hrymak

Zusammenfassung

Aufgrund ihrer hohen spezifischen Festigkeit und Steifigkeit bieten faserverstärkte Polymere (FRP) ein hohes Leichtbaupotenzial. Die gute Formbarkeit diskontinuierlicher (DiCo) FRP erlaubt eine hohe Designfreiheit bei vergleichsweise geringen Kosten. Kontinuierliche (Co) FRP zeigen außergewöhnliche richtungsabhängige mechanische Eigenschaften. Die hier vorgestellte Forschung wurde im Rahmen des internationalen Graduiertenkollegs "Integrated engineering of continuous-discontinuous long fiber reinforced polymer structures" (IRTG 2078) durchgeführt. Hierbei soll DiCoFRP lokal mit CoFRP verstärkt werden, so dass der neue Hybridwerkstoff (CoDiCoFRP) die individuellen Vorteile optimal kombiniert.

Betrachtet wird ein Sheet Molding Compound (SMC) Komposit auf Basis eines ungesättigten Polyester-Polyurethan-Hybrid (UPPH) Harzes. Diese Duromerklasse ermöglicht eine stabile Zwischenkonfiguration des Komposits und erlaubt einen integrierten Herstellungsprozess von CoDiCoFRP Bauteilen. Der Prozess führt zu einer inhomogenen Mikrostruktur mit anisotroper Orientierungsverteilung. Die nachfolgende Arbeit beschäftigt sich mit der mikromechanischen Modellierung der Schädigungsentwicklung im Komposit unter Berücksichtigung der charakteristischen Faserbündelmikrostruktur.

Ein auf einer zufälligen sequentiellen Addition basierender Algorithmus ermöglicht die schnelle Generierung von SMC Mikrostrukturen. Die Verwendung einer exakten Schließung in zwei Dimensionen in Kombination mit einer quasi-zufälligen Orientierungsrasterung, führt zu einer bemerkenswerten Genauigkeit und ermöglicht die Erzeugung von äußerst

realitätsnahen Mikrostrukturen. Dies erlaubt eine Sensitivitätsanalyse der effektiven elastischen Eigenschaften des Komposites mit Hinblick auf mikrostrukturelle Parameter. Zudem werden die Ergebnisse mit direkten numerischen Simulationen auf digitalen Volumenbildern und mit "Mean-Field" Methoden verglichen.

Im Weiteren wird ein Modell zur Berechnung anisotroper Schädigungsentwicklung im Kontext verallgemeinerter Standardmaterialien eingeführt. Unter Ausnutzung der Konvexität der elastischen Energiedichte in Bezug auf Dehnung und Nachgiebigkeit ist eine thermodynamisch konsistente Formulierung möglich, die zudem das Schädigungskriterium nach Wulfinghoff erfüllt. Ein modularer Aufbau unter Verwendung von Extraktionstensoren und Schädigungsfunktionen, in Analogie zur Elastoplastizität, erlaubt ein breites Anwendungsspektrum und die Beschreibung komplexer Schädigungsentwicklungen. Eine effiziente Integration der Biot-Gleichung wird diskutiert und die Vielseitigkeit des Modells wird an verschiedenen Beispielen auf der Mikro- und Makroskala demonstriert.

Untersuchungen zur Verteilung der Bruchfestigkeit und Steifigkeitsreduzierung von SMC Proben werden ausgewertet. Um die entsprechende Schädigungsentwicklung zu erfassen, werden Extraktionstensoren eingeführt, die durch die Laminattheorie von Puck motiviert sind. Diese bilden verschiedene Schädigungsmechanismen ab und berücksichten sowohl gemittelte als auch maximale Spannungszustände. Um die Schädigungsparameter zu identifizieren, wird eine Bayes'sche Optimierung mit Gauß'schen Prozessen verwendet. Abschließend wird ein ganzheitlicher Multiskalen-Ansatz zur Identifikation anisotroper Versagenskriterien basierend auf Vollfeldsimulationen der mikroskaligen Schädigungsentwicklung präsentiert. Darauf basierend werden Versagensflächen im Spannungsraum und durch Steifigkeitsreduktion induzierte Versagensflächen vorgestellt, um sowohl die Perspektive einer Strukturanalyse als auch die eines Designprozesses abzudecken.

Summary

Fiber reinforced polymers (FRP) offer lightweight potential due to their high specific strength and stiffness. The good formability of discountinuous (DiCo) FRP enables a high freedom in design at comparatively low costs in mass production. Continuous (Co) FRP show extraordinary directional-dependent mechanical properties. The here presented research was conducted within the International Research Training Group "Integrated engineering of continuous-discontinuous long fiber reinforced polymer structures" (IRTG 2078). The development and characterization of a new hybrid material combining DiCoFRP with local reinforcing CoFRP (CoDiCoFRP) to make the most of their individual advantages is the main goal of the IRTG 2078.

In this thesis, we are concerned with an E-glass fiber reinforced sheet molding compound (SMC) composite based on an unsaturated polyester polyurethane hybrid (UPPH) resin. This thermoset class enables a stable bi-stage condition of the composite and hence allows for a co-molding manufacturing process of CoDiCoFRP components. The manufacturing process leads to an inhomogeneous microstructure of the SMC composite with an anisotropic orientation distribution. Our work aims at micromechanical modeling of the damage evolution in the composite while accounting for the characteristic fiber bundle microstructure.

We introduce an algorithm based on random sequential addition that allows for a fast generation of SMC composite microstructures. Using an exact closure approximation in two dimensions in combination with a quasi-random orientation sampling derived from a Sobol' sequence leads to a remarkable accuracy and enables the generation of high fidelity

microstructures. We comprehensively investigate the sensitivity of the effective elastic properties of our SMC composite w. r. t. microstructural parameters such as phase properties or volume fraction. We compare the results using generated microstructures to direct numerical simulations on large scale digital volume images and mean-field estimates.

We introduce a framework for anisotropic damage evolution in the context of generalized standard materials. Exploiting the joint convexity of the elastic energy density in terms of strain and compliance, we attain the model to be thermodynamically consistent and to fulfill Wulfinghoff's damage growth criterion, yielding mesh-independent results. A modular formulation of our model using our concept of stress-extraction tensors and damage-hardening functions, in analogy to elastoplasticity, allows for a wide range of applications and the description of complex damage-degradation behavior. We discuss how to efficiently integrate Biot's equation implicitly and demonstrate the versatility of our model for a variety of examples on the micro- and macroscale.

We evaluate experimental investigations regarding distributions of ultimate strength and stiffness reduction of SMC composite specimens. To capture the corresponding damage evolution, we introduce stress-extraction tensors motivated by Puck's laminate theory accouting for different damage mechanisms in both an averaged and a maximum stress setting. To identify all damage parameters associated to our SMC composite, we utilize Bayesian optimization with Gaussian processes. With these tool at hand, we present a holistic multiscale approach for constructing anisotropic failure criteria based on full-field simulations of microscale damage evolution. We propose failure surfaces in stress space and stiffness-reduction triggered failure surfaces to cover both a structural analysis and a design process perspective.

Acknowledgments

First and foremost, I would like to thank my supervisors Thomas Böhlke and Matti Schneider for their support, guidance and patience. Their exceptional combination of immense mechanical and mathematical knowledge, our countless discussions and helpful advice made my research possible in the first place and shaped my scientific work.

I also would like to thank my co-supervisor Andrew Hrymak for his unhesitating support and advice. Our fruitful discussions deepened my understanding of composites and their specific behavior.

I thank Malte Schemmann for his support and guidance, especially during the initial phase of my research period. He was not only an incredible predecessor, who prepared me perfectly for my time in the IRTG 2078, but also a genuinely good colleague and friend.

I thank Michael J. Hoffmann for chairing the doctoral committee and the related organizational aspects regarding my doctoral thesis.

I especially would like to thank Ute Schlumberger-Maas and Helga Betsarkis for all their administrative and personal support. Furthermore, I thank Tom Langhoff for taking care of all organizational matters and technical issues, both at ITM-CM and within the IRTG 2078. Helga, Ute and Tom always had my back so that I could focus on my research. I do not even want to begin counting the hours they saved me.

I am truly thankful for all my colleagues and friends in the IRTG 2078. I absolutely enjoyed working and spending time with you. Special thanks go to Loredana Kehrer (ITM-CM), Pascal Pinter (IAM-WK) and Anna Trauth (IAM-WK) who supported me on my transition to the IRTG 2078

and beyond. Furthermore, I want to thank Ludwig Schöttl (IAM-WK) for his μCT scan analyses, Nils Meyer (FAST) for his compression molding simulations and Miriam Bartkowiak (IAM-WK) for her expertise on the characterization of our material. Our countless discussions, technical and personal, played a key part in the progress of my research. I thank Julian Bauer (IFM), Sven Revfi (IPEK), Lucas Bretz (WBK) and Thilo Richter (IPEK) for their catching motivation and fruitful discussions.

I thank all of my colleagues and friends at the ITM-CM for their support, stimulating coffee breaks and discussions, and just a great time overall. Special thanks go to Sebastian, Mr. President himself Andreas, Hannes, Jürgen, Daniel, Eric, Johannes, Felix, Jannick, Tarkes and Julian who were never short of helpful advice.

I thank my family, Rosi, Reinhold, Manuel, Andreas and Maria for their unconditional support. I especially want to thank my wife Anne for always having my back. Without her encouragement and understanding, my time wouldn't have been so easy. I am happy to enjoy your presence every day.

I also want to thank all my premium friends on and off the Ultimate pitch. You provided awesome diversion, an open ear and you kept me motivated. I thank Dewey, J.D. and Dendemann for much-needed distraction during stressful times.

Karlsruhe, July 2022   Johannes Görthofer

Contents

Chapter 1

Introduction[1]

1.1 Motivation

Weight savings. One key element to combat climate change and its impacts is a drastic lowering of carbon dioxide emissions and a long-term systemic shift (United Nations Environment Programme, 2015; 2019). Regarding the automotive sector, the fuel consumptions of cars and trucks can be reduced by about 0.40 l to 0.49 l per 100 km for each 100 kg of weight savings. Consequently, 1.20 US\$ to 13.70 US\$ are being paid per kilogram of weight savings in that industry (Bandivadekar et al., 2008).

Fiber reinforced polymers. Lightweight design plays a significant role in the reduction of fuel consumption and eventually the carbon dioxide emissions. One approach is the substitution of (non-structural) metallic parts with lighter fiber reinforced polymer (FRP) components. Generally, these composites consist of a matrix resin system, reinforced by fibers and conceivably some additives and fillers. Current fiber materials include glass, wood, carbon and cotton, see Fig. 1.1b. Typically, matrix resins are categorized in thermosets (TS) and thermoplastics (TP). Im-

---

[1] This chapter is based on excerpts of the publications "Computational homogenization of SMC composites based on high fidelity representative unit cells" (Görthofer et al., 2020), "A convex anisotropic damage model based on the compliance tensor" (Görthofer et al., 2022b) and "A computational multiscale model for anisotropic failure of SMC composites" (Görthofer et al., 2022a)

proved manufacturing technologies allow for cost-effective productions and consequently applications that are not restricted to the automotive or aerospace sector, but also include construction, sports or leisure, see Fig. 1.1a.

(a) Market segments for glass fiber reinforced composites (Witten et al., 2017)

- Transportation 35 %
- Construction and infrastructure 34 %
- Sports and leisure 15 %
- Electrical and electronic equipment 15 %
- Others 1 %

(b) Different fiber types (Reddy, 2015)

- Glass 85 %
- Wood 7 %
- Cotton 4 %
- Carbon 2 %
- Others 2 %
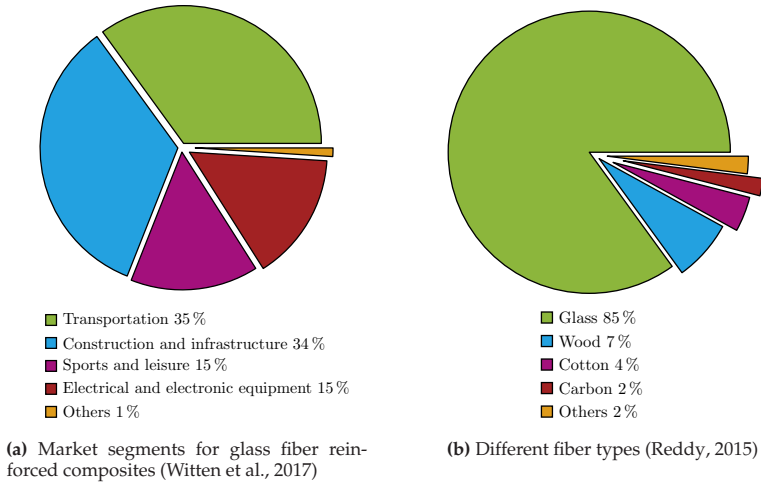
Figure 1.1: Distributions of composites and fiber types in Europe (Kehrer, 2019)

Types of FRP. Depending on the composition, FRP exhibit a high mass specific strength and stiffness. Generally, FRP are sub-divided into different classes, i. e., discontinuous FRP (DiCoFRP) where (short or long) fibers are dispersed more or less randomly and continuous FRP (CoFRP) with unidirectionally aligned fibers, see Fig. 1.2. The latter enable a loading case specific manufacturing of high performance components due to designated arrangements of the continuous fibers. A fiber volume fraction of up to 60 % further supports high strength and stiffness properties. The known fiber directions facilitate the modeling and dimensioning process of CoFRP components. Drawbacks of this

material class include long cycle times, high scrap rates and a limited formability. Complementary, DiCoFRP generally show lower stiffness and strength properties compared to CoFRP, but offer a high freedom in design at short cycle times. The manufacturing processes, including compression molding and injection molding, allow for an economic high-volume production of complex components, counting, e. g., beads or ribs. DiCoFRP are currently applied as non-structural components (Ernst et al., 2006), and thus make a first contribution towards lightweight applications as replacements for certain metallic parts. As the complex mold-filling process leads to a process-dependent and heterogeneous fiber orientation distribution, the development of efficient modeling approaches and dimensioning tools is a challenging task.
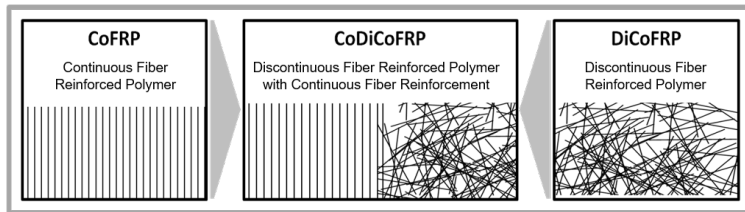
Figure 1.2: Classification of different fiber reinforced polymers

Hybridization. A combination of CoFRP and DiCoFRP to a new hybrid class of continuous-discontinuous FRP (CoDiCoFRP), see Fig. 1.2, aims at merging the individual advantages. Specific reinforcements of CoFRP within the DiCoFRP part are used to sustain application-based loadings where necessary. Hence, CoDiCoFRP offer a high potential for the production of composite parts to be used as structural components with a high specific strength and stiffness at comparably low cycle times and reduced costs. A CoDiCoFRP demonstrator part is shown in Fig. 1.3,

where the black areas are carbon fiber CoFRP reinforcements within the lighter glass fiber DiCoFRP.
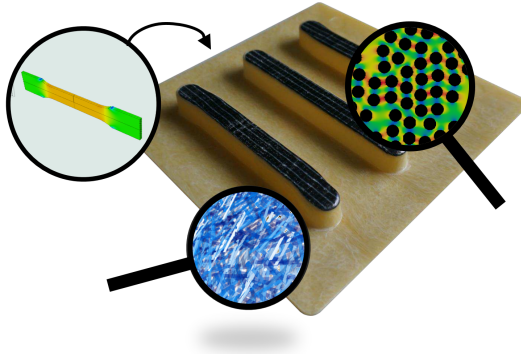
Figure 1.3: IRTG 2078 demonstrator part made of glass fiber DiCoFRP with local carbon fiber CoFRP reinforcements (manufactured at Fraunhofer Institute of Chemical Technology (ICT) Pfinztal)

IRTG 2078. In order to unlock the full potential of these hybrid materials, a profound understanding, covering technological manufacturing and experimental characterization aspects, as well as component design and simulation prospects, is of importance. Therefore, the complex multiscale material is analyzed in an integrated engineering approach within the International Research Training Group "Integrated engineering of continuous-discontinuous long fiber reinforced polymer structures" (IRTG 2078). The international and interdisciplinary collaboration links necessary expertise to propel research on CoDiCoFRP aiming at a full understanding of the material's behavior and development of associated simulation methods. To fully cover both the physical

Figure 1.4: Logo of IRTG 2078

and virtual process chain for CoDiCoFRP components, IRTG 2078 is
sub-divided into four research areas, i. e., technology, characterization,
design and simulation, see Fig. 1.5.
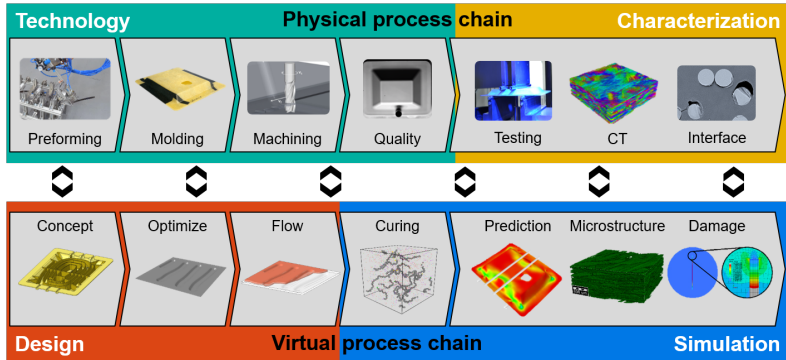
Figure 1.5: Schematic of physical and virtual process for CoDiCoFRP (Görthofer et al.,
2019a) including an interface μCT scan performed at Fraunhofer Institute for Mechanics of
Materials (IWM) Freiburg (Schober et al., 2017)

Physical process chain. The physical process chain is established within
the research areas technology and characterization. Key aspects are
the application-based preforming of CoFRP tapes (Kupzik et al., 2020),
the simultaneous co-molding of DiCoFRP and CoFRP while ensuring
proper interface bonding (Bücheler, 2018) and the subsequent machin-
ing processes (Langer et al., 2020). A continuous surveillance of the
individual production steps is important to ensure a consistent high
quality of the manufactured parts (Bretz et al., 2021). Accompanying
the manufacturing process, experimental investigations are conducted
ranging from microscale analysis to macroscopic structural component
testing. Interface characterization provides information about fiber
and matrix bonding (Rohrmüller et al., 2020). Local variations of fiber
orientations are identified via micro-computed tomography analysis

(Schöttl et al., 2021b). Component scale testings are used to identify effective properties of DiCoFRP and CoFRP and the reinforcing effects of the hybrid material regarding, inter alia, quasi-static (Trauth et al., 2017a) and fatigue loading scenarios (Bartkowiak et al., 2020).

Virtual process chain. The associated virtual process chain mimics the physical process chain providing a constant data and knowledge exchange to improve the manufacturing of CoDiCoFRP components. Within research area design a consistent system of objectives is established to gather all achieved progress and provide structured concept criteria for the working engineer (Richter et al., 2020). CoDiCoFRP components are optimized w. r. t. their shape, usage of beads and ribs, as well as positioning of CoFRP tapes to maximize application-based criteria such as strength or stiffness (Fengler et al., 2019; Revfi et al., 2021). Process simulation techniques are developed to correctly predict the flow of the DiCoFRP during molding and hence allow for the prediction of inhomogeneous orientation states within the manufactured parts (Meyer et al., 2020). In order to describe the structural behavior of CoDiCoFRP components, different key aspects are analyzed in the research area simulation. Curing simulations on the microscale help quantifying residual stresses (Pallicity and Böhlke, 2021; Schwab, 2019). Mean-field (Schemmann et al., 2018b) and full-field models (Görthofer et al., 2022b) taking into account the FRP microstructure, phase properties and different damage mechanisms allow for an micromechanics-based evaluation of the effective stiffness reduction. The junction of these simulative approaches enables a component scale computation of the structural behavior (Görthofer et al., 2019b).

1.2 Objectives and originality of this thesis

Categorization. In this thesis we present investigations and results conducted within the scope of project "S3: micro-mechanical modeling"

in research area simulation of the second generation in the IRTG 2078. The material system under consideration is sheet molding compound (SMC), which is a thermoset (TS) matrix reinforced with glass and carbon fibers within the DiCo and Co phases, respectively. To ensure a proper co-molding of this CoDiCoFRTS hybrid, an unsaturated polyester polyurethane hybrid (UPPH) resin is used (Bücheler et al., 2017).

Objectives. The main objective of our presented research is the development of a micromechanical model, incorporating damage, that helps to propel scale transition and provide micromechanics-based input for the macroscopic component scale simulations. Therefore, we mainly address three topics in this thesis.

(I) In a first step, we establish a microstructure generator that accounts for the characteristic fiber bundle structure of SMC composites, see Fig. 1.6, and enables the generation of high fidelity representative unit cells. The means to individually adjust any volume fraction and orientation state within the unit cells serves as basis for a sensitivity analysis of effective elastic properties, as well as a utilization of the generated microstructures in the further process of material modeling (Görthofer et al., 2020).

(II) In a second step, we propose a general damage model framework that allows for a description of *any* anisotropic damage evolution and associated stiffness reduction. The model is formulated in the setting of generalized standard materials (GSM) of dissipative solids, ensuring thermodynamical consistency. A convex modeling of the free energy density and the force potential enables a unique solution for any material that exhibits a damage hardening regime prior to total failure. The compliance tensor serves as natural and observable internal damage variable (Görthofer et al., 2022b).

(III) In the third step, we apply our presented model to SMC composites in order to predict damage evolution on the microscale.

Therefore, we identify corresponding damage cases, inspired by Puck's criteria for laminates. We design specific extraction tensors that describe matrix and fiber bundle damage in SMC composites, taking into account either an averaged stress state or maximum stresses. We use a Bayesian optimization approach to identify all associated SMC composite damage parameters. Using our generated unit cells, we compute a variety of loading scenarios on different microstructures to analyze the damage evolution. A comparison to μCT scans and experimental results yields micromechanics-based anisotropic failure criteria to be used on a component scale level (Görthofer et al., 2022a).

Originality of this thesis. Our presented research on SMC composites and damage modeling exhibits the following novelties:

- **SMC composite characteristics:** We explicitly consider the inherent three-scale structure of SMC composites taking into account the characteristic fiber bundles. Furthermore, we account for the macroscopic strain hardening behavior due to accumulation of damage on the microscale that eventually leads to abrupt failure.

- **Microstructure generation:** Using a quasi-random orientation sampling based on a Sobol' sequence in combination with the exact closure approximation allows for an accurate microstructure reconstruction yielding high fidelity representative SMC composite unit cells. We present an algorithm that enables a fast and robust generation of SMC composite microstructures based on random sequential addition.

- **Sensitivity analysis:** Utilizing a large variety of generated unit cells, we provide a comprehensive sensitivity analysis of effective stiffness properties w. r. t. changing phase properties, volume fraction and orientation.

- **Anisotropic and convex damage framework:** Our anisotropic damage model is not only derived in the GSM framework, thermodynamically consistent and features a convex free energy and a convex

dissipation potential, but also fulfills Wulfhinghoff's damage growth criterion. Our presented framework is local, but nonetheless well-posed and hence leads to a unique, mesh-independent solution. We show and make use of the fact that the elastic energy density of linear elasticity is jointly convex in the strain and the compliance tensor. The compliance tensor as a primary damage variable serves as an experimentally measurable internal state variable.

- **Modularity:** A modular framework in combination with extraction tensors enables the application of our model to a broad set of materials on the micro- and the macroscale. We introduce specific extraction tensors motivated by Puck's laminate theory. Based on an averaging process, as well as a pencil glide approach, we define both extraction tensors accounting for average stress states and maximum stresses, respectively. Furthermore, we introduce loading case specific extraction tensors accounting, inter alia, for distortion and dilatation.

- **Micromechanis-based failure criteria:** We present a holistic multi-scale approach for constructing anisotropic criteria describing the macroscopic failure based on microscale full-field damage evolution. Failure surfaces in stress space and stiffness-reduction triggered failure cover both a structural analysis and a design process perspective.

1.3 State of the art

1.3.1 Research on SMC composites

Characteristics. For lightweight applications, DiCoFRP combine low material and manufacturing costs with a high degree of freedom in design (Wilkinson and Ryan, 1998). In particular, sheet molding compound (SMC) composites are frequently used in applications due to their high strength-to-weight ratio (Huang and Zhao, 2012; Asadi et al., 2017). Standard SMC composite products consist of discontinuous fiber

bundles, a mixture of thermosetting resin (typically, polyester, vinylester or epoxy), fillers (calcium carbonate, alumina, etc.) and additives (such as initiators, inhibitors, thickeners), see Dumont et al. (2007) or Kim et al. (2011a). The compression molding manufacturing process allows for producing components at comparatively low costs while offering a high freedom in design (Wilkinson and Ryan, 1998). Furthermore, the manufacturing process of SMC leads to a characteristic microstructure where fibers are almost aligned in bundles (Le et al., 2008; Meyer et al., 2020; Schöttl et al., 2021b), see Fig. 1.6.
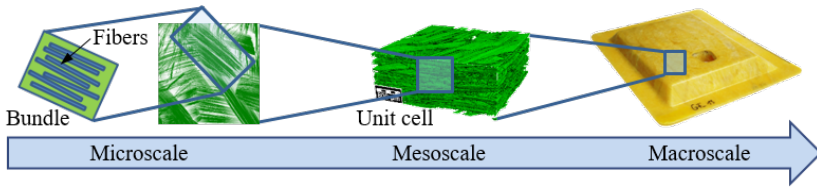
Figure 1.6: Three-scale structure of SMC composites, see Görthofer et al. (2019b)

Hybridization. Combining glass and carbon fiber bundles (Brinson and Brinson, 2008; Anagnostou et al., 2018; Trauth, 2020) permits applying SMC composites as load-bearing structural components. A modern unsaturated poylester polyurethane hybrid (UPPH) resin without fillers allows to manufacture SMC composites with discontinuous glass fiber bundles and local continuous carbon fiber patch reinforcements within a simultaneous co-molding process (Bücheler et al., 2017; Böhlke et al., 2019).

Experimental investigations. The increased use of SMC composites fosters the development of accurate mechanical models (Görthofer et al., 2019b; Böhlke et al., 2019). Experimental investigations of the microstructure (Motaghi and Hrymak, 2017; Schöttl et al., 2020; 2021b), the effective elastic behavior in a quasi-static (Trauth et al., 2017a; Chen et al., 2018b)

and dynamical setting (Fitoussi et al., 2005; Jendli et al., 2005; Kehrer et al., 2018) were performed. In-situ testing using micro-computed tomography (µCT) sheds light on the underlying damage mechanisms (Dumont et al., 2007; Arif et al., 2014; Rohrmüller et al., 2020) and microcrack distributions (Schöttl et al., 2020; Schöttl et al., 2021a).

The influence of temperature, especially with an eye towards the glass transistion of the polymer resin, was analyzed by Kehrer et al. (2018) for the elastic regime. Meyer, Hohberg and co-workers studied the flow and curing behavior during the manufacturing process (Hohberg et al., 2017; Meyer et al., 2020). The behavior of SMC composites under fatigue loading was studied by Ben Cheikh Larbi et al. (2006) and Bartkowiak et al. (2019; 2020). Investigations on the structural behavior of SMC composites under combined stress states were performed via dedicated cruciform specimens (Ogihara and Koyanagi, 2010; Schemmann et al., 2018a;c). Non-destructive measurement techniques were developed for quantifying manufacturing uncertainties and hence the quality of SMC composite parts (Schäferling et al., 2018; Bretz et al., 2020; 2021).

Damage and failure. Further focus of recent research on SMC composites is devoted to damage and failure. Fitoussi et al. (1996; 1998) presented approaches for predicting anisotropic damage evolution based on multilocal criteria, also at high strain rate (Fitoussi et al., 2013). Matrix degradation and interface decohesion, two major damage mechanisms in SMC composites, were analyzed and modeled by Meraghni and co-workers (Meraghni and Benzeggagh, 1995; Meraghni et al., 1996) and implemented in a micromechanical framework (Meraghni et al., 2002). A similar approach for predicting the non-linear behavior of SMC composites was proposed by Baptiste (2003). Dedicated models were developed that account for the multiscale and anisotropic nature of SMC composites (Drugan and Willis, 1996a; Guo et al., 1997), taking into account reliability (Desrumaux et al., 2000), inclusion distributions

(Zheng and Du, 2001; Lee and Simunovic, 2001), humidity (Arif et al., 2014) or dynamical behavior (Jendli et al., 2009).

SMC composites typically show an elasto-damageable behavior that is driven by anisotropic damage evolution (Fitoussi et al., 2005; Ogihara and Koyanagi, 2010) and eventually ends in abrupt failure. Damage evolution on the microscale induces an effective stress-strain relationship characterized by a hardening, rather than a softening, regime (Trauth et al., 2017a; Trauth, 2020). Hence, no localization occurs prior to a specific loading point right before total failure of the SMC composite (Meraghni and Benzeggagh, 1995; Görthofer et al., 2019b).

1.3.2 Microstructure generation

Motivation. To reduce safety factors in dimensioning SMC parts, accurate material models need to be provided, accounting both for the intrinsic complexity of the composite behavior – temperature- and strain-rate dependent mechanical behavior involving damage (Schemmann et al., 2018b; Shirinbayan et al., 2017) – and the manufacturing process induced variation of microstructural parameters (such as fiber volume content and fiber orientation).

To account for the inherent anisotropy of the effective material behavior of fiber reinforced composites, both analytical (Mori and Tanaka, 1973; Ponte Castañeda and Suquet, 1998; Duschlbauer et al., 2003; Doghri and Tinel, 2005; Anagnostou et al., 2018) and computational homogenization techniques (Matouš et al., 2017) are frequently used to obtain accurate effective material models and to identify the physical mechanisms responsible for the effective mechanical behavior.

SMC composite unit cells. Using representative unit cells as the basis for computational homogenization has become a standard technology for short fiber reinforced composites, cf. the overview articles of Matouš et al. (2017) and Bargmann et al. (2018). Of key importance here

is generating high fidelity volume elements, accounting both for the high fiber volume content and the fiber orientation to high precision (Schneider, 2017). For long fiber reinforced composites, the fibers can no longer be described by straight cylinders, and more elaborate methods for generating unit cells need to be employed, see for instance Altendorf and Jeulin (2011) or Fliegener et al. (2014).

Due to differences in the production process, the microstructures of long fiber reinforced thermoplastics (LFT) and SMC composites exhibit different characteristics. In contrast to the former, distinct fiber bundles are apparent for SMC composites. In particular, unit cell generation techniques for LFT cannot be applied to SMC in a straightforward fashion. For illustration, Fig. 1.7 shows a microstructure generated by the SAM algorithm (Schneider, 2017) for a fiber orientation that is almost planar isotropic and fibers with an aspect ratio of 100. The edge length of the cubical unit cell is roughly twice the fibers' length.
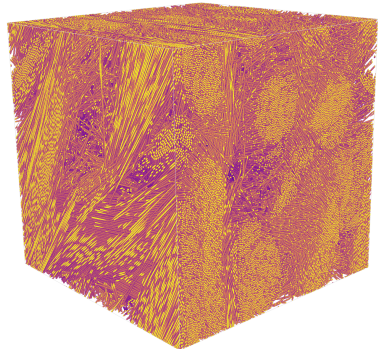
Figure 1.7: LFT microstructure generated by the SAM algorithm (Schneider, 2017) for 22.5 % fibers with an aspect ratio of 100 and a second-order fiber orientation tensor of $\mathrm{diag}(0.475, 0.475, 0.05)$, see Görthofer et al. (2020)

For a fiber volume fraction of 22.5 %, the cell contains 24682 fibers. For this kind of microstructure, computational homogenization is difficult. Furthermore it should be noted that the aspect ratio for the fibers used in SMC composites is even one order of magnitude higher. Furthermore, the induced bundle structure of the LFT microstructure in Fig. 1.7 is different from the bundle structure observed in SMC, cf. Fig. 1.6.

Physical approaches. For this reason, unit cell modeling of SMC composites is focused on the apparent three-scale structure, as shown in

Fig. 1.6, modeling fiber bundles (sometimes also called tows) directly. Extending the work of Fliegener et al. (2014) on LFT, Fette et al. (2017) used a commercial finite element code to compress previously placed fiber bundles accounting for developing contact between the fiber bundles. A similar approach was presented by Li et al. (2018b). Islam et al. (2016) coupled a random sequential addition algorithm to a dynamic finite element simulation. Sparse inclusion assemblies are generated in pseudo-boxes. A subsequent explicit flow simulation is used to transfer the inclusions from the pseudo-boxes into the target box. For all of these approaches, constructing these volume elements is computationally most demanding, and realizing a prescribed fiber orientation state is based on a trial-and-error procedure. Altendorf and Jeulin (2011) use a force-biased packing approach. Fibers are represented as chains of balls with a controllable level of bending. A deposition algorithm in combination with a force-directed approach based on Coulomb's law and spring forces to hinder bundle overlap was presented by Harper et al. (2017). Smooth fiber undulations are ensured via spline interpolations.

Geometric approaches. A periodic packing of general ellipsoids was presented by Ghossein and Lévesque (2013), where ellipsoids can move, rotate and collide in order to reach a desired volume fraction. Li et al. (2018a) studied a Voronoi diagram based algorithm for modeling SMC microstructures, where each Voronoi cell corresponds to a fiber bundle with a distinct orientation. These Voronoi cells recover the characteristic tesselated surfaces of carbon fiber SMC with high fiber volume content. As typical for Voronoi-based modeling, it is difficult to realize a given statistics of the cell geometry (Quey and Renversade, 2018). Motivated by the random sequential adsorption algorithm (Feder, 1980), Chen et al. (2018b) developed an algorithm for modeling SMC unit cells based on a sequential bundle deposition method. Chen et al. (2018b) model the SMC fiber bundles as cuboid cells which are placed sequentially and layer by layer, accounting for an overlap between bundles by displacing

this overlap to an adjacent layer. The advantage of this algorithm is that both the bundle dimensions and the fiber orientation can be prescribed independently. Furthermore, Chen et al. (2018b) showed a close agreement of their computational results with experimental data for carbon fiber SMC.

1.3.3 Damage modeling

Progressive degradation. Damage mechanics describes the progressive degradation of the elastic stiffness of materials upon loading, and is typically attributed to growing voids or cracks on a lower length scale (Lemaitre, 1996), see Fig. 1.8. There are two predominant approaches to continuum damage-mechanics (Krajcinovic, 1984; Lemaitre and Chaboche, 1990). The first approach accounts for the origin of damage on a lower length scale in terms to micromechanics (Fitoussi et al., 1996; Guo et al., 1997), see also Sec. 3 in Krajcinovic (1989) for an early account. With qualitative predictions in mind, the second strategy is of phenomenological nature. After selecting a suitable damage variable (or a collection thereof), suitable kinetic laws are postulated taking continuum thermodynamics into account, Sec. 4 in Krajcinovic (1989).

(a) Polycrystalline microstructure   **(b)** Microstructure composed of fiber bundles
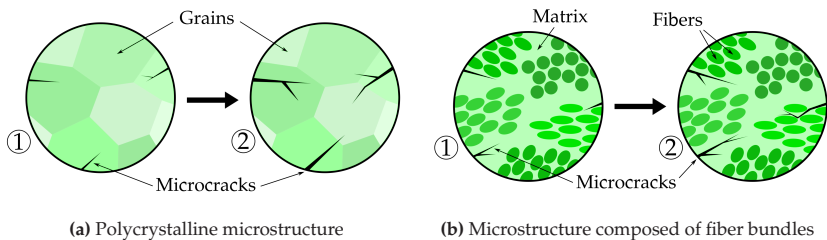
Figure 1.8: Schematics of microstructures with growing microscopic cracks, passing from state ① to state ②, similar to Fassin et al. (2019). Growing microcracks induce a reduction of the effective stiffness.

15

Micromechanics-based approaches. The micromechanics-based approach to damage mechanics takes the damage mechanisms on a lower scale into account and is still subject of current research, for instance concerning mesh-size objective modeling (Liang et al., 2018), a coupling to model-order reduction (Bhattacharyya et al., 2020) or accounting for micro-computed tomography data (Luo et al., 2020). Micromechanics-informed damage models permit taking the stochastics on the microscale into account naturally, e. g., for progressive fiber breakage in fiber reinforced composites (Ju and Wu, 2016; Wu and Ju, 2017), interfacial transition-zone effects (Chen et al., 2018a), uncertainty in the elastic moduli of fiber reinforced concrete (Liu et al., 2020), localized microcracks (Li et al., 2020) or random loading in fatigue processes (Franko et al., 2017). Another advantage concerns modeling the unilateral character of brittle damage, i. e., a different damaging behavior under tension compared to compression (Goidescu et al., 2015; Zhang et al., 2019), and accounting for interface debonding (Pupurs and Varna, 2017; Schemmann et al., 2018b; Yang et al., 2020). However, care has to be taken as homogenization and localization are incompatible (Gitman et al., 2007), in general, i. e., upon localization, the volume elements considered will not be representative for the effective mechanical behavior (Hill, 1963; Drugan and Willis, 1996b; Kanit et al., 2003).

Many micromechanics models are based on mean-field methods (Hashin and Shtrikman, 1962; Mori and Tanaka, 1973; Willis, 1981), e. g., taking into account a numerically computed Eshelby's tensor (Desrumaux et al., 2001), an evaluation of inclusion stresses (Duschlbauer et al., 2003), a Weibull probability density for the interface strength (Schemmann et al., 2018b) or a mixture of glass and carbon fibers (Anagnostou et al., 2018). Computational homogenization techniques (Schneider, 2021) were used for studying the effective elastic behavior of SMC composites (Matouš et al., 2017; Görthofer et al., 2020).

Phenomenological approaches. As an alternative to micromechanics-type strategies, phenomenological approaches to continuum-damage mechanics may be pursued. In a first step, a (scalar- or tensor-valued) damage variable is selected which describes the reduction of the effective cross-section of a typical material sample undergoing material degradation (Gurson, 1977; Voyiadjis, 2015). Then, suitable kinetic laws are postulated on the basis of continuum thermodynamics (Simo and Ju, 1987; Hansen and Schreyer, 1994).

Tensor order of damage variable. The tensor order of the damage variable naturally distinguishes different phenomenological damage models. Even today, the classical scalar isotropic damage variable serves as a reliable workhorse with numerous applications including cast steel with pores (Yan et al., 2020), concrete (Li and Wu, 2018), rocks (Liu et al., 2018; Xu et al., 2018), framed structures (Yang et al., 2017), unidirectional glass fiber reinforced plastic composite plies (Sharma and Daggumati, 2020), fibrous composite laminae (Abu-Farsakh and Asfa, 2020), notched epoxy resin specimens (Rahimi et al., 2020) and steel-fiber reinforced concrete (Moradi et al., 2020).

Second-order tensors. Damage variables with higher tensor order permit modeling an emerging anisotropy of damage. As working with second-order tensors comes naturally to disciples of continuum mechanics, it is not surprising that second-order damage-tensors (Murakami and Ohno, 1981) are used frequently in continuum damage-mechanics. Recent applications include concrete (Desmorat, 2016; Wardeh and Toutanji, 2017), metal-forming processes (Nasab and Mashayekhi, 2019), rock materials (Wang and Xu, 2020), composite fabrics and laminated panels (Wei et al., 2020) and composite laminates (Okabe et al., 2018; Onodera and Okabe, 2020). Second-order damage-tensors are always orthotropic w. r. t. their eigenbasis, limiting their degree of generality. More often than not, such a limitation is interpreted as a feature, and specific orthotropic damage models are developed, for instance for brittle materials (Kim

et al., 2016), in elastoplastic and finite-strain damage coupling (Ganjiani, 2018; Reese et al., 2021), or for ceramic-matrix composites (Alabdullah and Ghoniem, 2020).

Fourth-order tensors. As continuum damage-models primarily seek to describe a loss of stiffness due to emerging defects in solids, using a fourth-order damage-tensor (Chaboche, 1981), the same tensor order as the stiffness tensor, appears reasonable. In Sec. 4.3.4, Krajcinovic (1989) even notes that "an appropriate description of damage [...] must involve at least a fourth-rank tensor." This idea was pursued for the stiffness or compliance tensors as the primary damage variable (Dougill, 1976; Ortiz and Popov, 1982; Ortiz, 1985), also coupled to plasticity (Simo and Ju, 1987; Ju, 1989; Yazdani and Schreyer, 1990). We refer to Zhang and Cai (2010) for a modern account of anisotropic damage mechanics. However, some care has to be taken when working with tensor-valued damage variables due to possible inconsistencies arising for complex non-radial loading-unloading scenarios, see Simon et al. (2017).

Tension-compression asymmetry. The unilateral character of pores and cracks (see Fig. 1.8) often leads to a tension-compression asymmetry of the material behavior upon damage loading, see Chaboche (1993) for a discussion. To incorporate the latter effect in phenomenological models, one may introduce different damage variables for the tensile and the compressive regime (Ramtani et al., 1992; Cicekli et al., 2007). For three-dimensional stress states, spectral decompositions of either the strain or the stress tensor may form the basis of continuum damage models that differentiate between damage evolution due to tension and compression (Ladevèze and Lemaitre, 1984; Ortiz, 1985).

Softening. Whenever damage models exhibit a softening behavior, their use in a continuum formulation leads to an ill-posed problem due to localization effects (Lemaitre, 1986), which is reflected by strongly mesh-dependent results in numerical simulations (De Borst, 1996). Countermeasures in the framework of local damage models were investi-

gated (Tvergaard, 1982; Becker et al., 1988; Beremin et al., 1983). Non-local formulations (Belytschko et al., 1986; Bažant, 1991) prevent the localization responsible for the ill-posedness, and may be realized by an explicit convolution with a tapering function (Pijaudier-Cabot and Bažant, 1987), by augmenting the damage evolution equation by an elliptic differential operator (Aifantis, 1984) or by employing a gradient-enhanced formulation (Brünig and Ricci, 2005; Germain et al., 2007; Abu Al-Rub and Voyiadjis, 2009)), which may also be coupled to Hamilton's least-action principle (Junker et al., 2019; 2021). As long as the softening is not too pronounced, existence of results for non-local damage models (Thomas and Mielke, 2010) may be established. However, except for specific models (Susu, 2017; Roubíček, 2009), uniqueness (and, thus, well-posedness) cannot be ensured. For a review on ill-posedness due to localization problems and appropriate regularization methods, the reader is referred to Forest et al. (2004). Also, for a general overview on continuum damage-mechanics and further literature, the reader may consult the books of Murakami (2012) and of Voyiadjis (2015).

Hardening. Oftentimes, the ill-posedness of local damage models is taken for granted, and appropriate countermeasures are taken. A charming strategy takes a conventional local damage model with softening (but sufficient growth at infinity), and applies relaxation techniques (Balzani and Ortiz, 2012; Schmidt and Balzani, 2016; Schwarz et al., 2021), which are typically used for studying solids with emerging microstructure. When describing stable damage processes, these countermeasures should not be necessary, however. Indeed, for a moderate degree of loading, localization is excluded, and manifests only at a specific turning point in loading level. For component-scale simulations, this loading level is not readily apparent, and depends on the specimen geometry via solving the equations of continuum mechanics. To sum up and loosely speaking, we know that local damage models are perfectly reasonable up to a specific level of loading, but we do not know this level in

advance. Thus, interest arose to design damage models which give rise to a meaningful response for the entire range of loading, and which are intended to be complemented by a classical failure criterion.

1.4 Outline

Following the introduction and classification of our research in **Chapter 1**, we sub-dived this thesis into two further chapters that present some important fundamentals, three chapters based on published journal publications discussing the main research focus and a summary chapter highlighting the key achievements and possible scopes of further research.

In **Chapter 2** we briefly introduce the necessary fundamentals of continuum mechanics regarding kinematics and balance equations in the context of small deformations.

Chapter 3 is dedicated to SMC composites, i. e., we present the compression molding manufacturing process, the resulting characteristic microstructure and mathematical descriptions of such.

In **Chapter 4** we present a method that allows the generation of high fidelity microstructures of SMC composites via an adapted random sequential addition. Using a quasi-random orientation sampling and an exact closure, we are able to generate a wide range of unit cells with high accuracy. Using full-field homogenization, we conduct a sensitivity analysis of effective parameters based on microstructure variations and changes of phase properties and compare our results to mean-field calculations.

We introduce a basic framework to model anisotropic damage evolution in the context of generalized standard materials in **Chapter 5**. The modular setting allows for a straight-forward adaption of the model to different materials using extraction tensors. We discuss different such

extraction tensors and subsequently show the capacity and performance of our model via different computational examples.

In **Chapter 6** we analyze experimental investigations on SMC composites provided by M. Bartkowiak, A. Trauth and L. Schöttl. We utilize our damage model and introduce specific extraction tensors motivated by Puck's theory on laminates to capture damage in SMC composites. A Bayesian optimization approach is presented to determine all necessary damage parameters. Consequently, we present an holistic approach to identify anisotropic failure criteria for SMC composites based on the computed full-field damage evolution.

We briefly summarize our work and give concluding remarks and conceivable follow-up research in **Chapter 7**.

1.5   Notation, frequently used acronyms, symbols and operators

We follow a direct tensor notation throughout the text, representing vectors and tensors by their components or using matrix representations (in an orthonormal basis) only when necessary. Vectors and second-order tensors are denoted by lower case and upper case bold letters, respectively (e.g., $\boldsymbol{a}$ and $\boldsymbol{A}$). Fourth-order tensors are denoted by, e.g., $\mathbb{A}, \mathbb{B}$. Scalars and arrays of quantities are represented by non-bold letters (e.g., H, w or z). The transposition of a vector and second-order tensor reads $\boldsymbol{a}^{\mathsf{T}}$ and $\boldsymbol{A}^{\mathsf{T}}$, respectively. The principal transposition of a fourth-order tensor is denoted via $\mathbb{A}^{\mathsf{T_M}}$ and the left and right transpositions are $\mathbb{A}^{\mathsf{T_L}}$ and $\mathbb{A}^{\mathsf{T_R}}$. The linear mappings induced by second-order and fourth-order tensors are written as $\boldsymbol{a} = \boldsymbol{Cb}$ and $\boldsymbol{A} = \mathbb{C}[\boldsymbol{B}]$, respectively. The composition of two second-order or two fourth-order tensors is denoted by $\boldsymbol{AB}$ and $\mathbb{AB}$. The Frobenius inner product is denoted by $\boldsymbol{A} \cdot \boldsymbol{B} = \mathrm{tr}(\boldsymbol{AB}^{\mathsf{T}})$. The tensor product operator $\otimes$ is

defined as $(\boldsymbol{A} \otimes \boldsymbol{B})\,[\boldsymbol{C}] = (\boldsymbol{B} \cdot \boldsymbol{C})\,\boldsymbol{A}$. Its symmetrized version $\otimes_{\mathsf{S}}$ is defined via $\boldsymbol{a} \otimes_{\mathsf{S}} \boldsymbol{b} = (\boldsymbol{a} \otimes \boldsymbol{b} + \boldsymbol{b} \otimes \boldsymbol{a})\,/2$. We introduce the abbreviation $\boldsymbol{a}^{\otimes n} = \boldsymbol{a} \otimes \boldsymbol{a} \cdots \otimes \boldsymbol{a}$ (n repetitions). The material time derivative of a quantity w is expressed as $\dot{w} = \mathrm{D}w/\mathrm{D}t$.

We denote by $\mathrm{Sym}(d)$ the space of symmetric second-order tensors on $\mathbb{R}^d$. The unit sphere in $\mathbb{R}^3$ reads S^2. The vector space of fourth-order tensors with minor symmetries ($\mathbb{A} = \mathbb{A}^{\mathsf{T}_\mathsf{L}}$, $\mathbb{A} = \mathbb{A}^{\mathsf{T}_\mathsf{R}}$) is written as $L(\mathrm{Sym}(d))$, whereas $\mathrm{Sym}(\mathrm{Sym}(d))$ denotes those fourth-order tensors that have minor and major symmetries ($\mathbb{A} = \mathbb{A}^{\mathsf{T}_\mathsf{M}}$). Generally, we use a $\{\boldsymbol{e}_1, \boldsymbol{e}_2, \boldsymbol{e}_3\}$ Cartesian coordinate system on the (local) microscale and a $\{\boldsymbol{e}_x, \boldsymbol{e}_y, \boldsymbol{e}_z\}$ Cartesian coordinate system on the (effective) macroscale. Details on further spaces of interest, domains of definition and corresponding explicit expressions are given upon their first appearance.

Acronyms

µCT	Micro-computed tomography
CDF	Cumulative density function
CDI	Clausius-Duhem inequality
CG	Conjugate gradient
Co	Continuous
CoDiCo	Continuous-discontinuous
DiCo	Discontinuous
FE	Finite element
FFT	Fast Fourier-transform
FRP	Fiber reinforced polymer
FRTS	Fiber reinforced thermoset
GRK	Graduiertenkolleg
GSM	Generalized standard material

IRTG	International Research Training Group
KKT	Karush-Kuhn-Tucker
LFT	Long fiber reinforced thermoplastic
ODF	Orientation distribution function
OT	Orientation tensor
PDF	Probability density function
SMC	Sheet molding compound
UD	Unidirectional
UPPH	Unsaturated polyester polyurethane hybrid
YMS	Young's modulus surface

Latin letters

$a, b, A, B, \ldots$	Scalar quantities
$\boldsymbol{a}, \boldsymbol{b}, \boldsymbol{c}, \ldots$	Vectors
$\boldsymbol{A}, \boldsymbol{B}, \boldsymbol{C}, \ldots$	Second-order tensors
$\mathbb{A}, \mathbb{B}, \mathbb{C}, \ldots$	Fourth-order tensors
c	Volume fraction
d	Dimension
f	Reduced damage-activation function
h	Energy (density) accounting for degradation
m	Power-law exponent
p	Bayesian parameters
q	Damage variable
w	Free energy (density)
z	Internal variables
E	Young's modulus
G	Shear modulus
H	Hardening parameter

$\boldsymbol{e}$	Orthonormal basis vector
$\boldsymbol{k}, \boldsymbol{m}, \boldsymbol{n}, \boldsymbol{p}$	Direction vectors
$\boldsymbol{t}$	Stress traction vector
$\boldsymbol{u}$	Displacement
$\boldsymbol{x}$	Current position
$\boldsymbol{A}$	Second-order orientation tensor
$\boldsymbol{F}$	Deformation gradient
$\boldsymbol{H}$	Displacement gradient
$\boldsymbol{I}$	Second-order identity tensor
$\mathbb{A}$	Fourth-order orientation tensor
$\mathbb{B}$	Extraction tensor
$\mathbb{C}$	Stiffness tensor
$\mathbb{E}_0$	Eshelby's tensor
$\mathbb{I}$	Fourth-order identity tensor
$\mathbb{P}_0$	Polarization tensor
$\mathbb{P}_1, \mathbb{P}_2$	Isotropic projectors
$\mathbb{S}$	Compliance tensor
$\mathbb{T}$	Driving force for compliance evolution
$\mathcal{A}$	Set of active damage functions
$\mathcal{E}$	Expectation value
$\mathcal{N}$	Set of Gaussian normal distributions
$\mathcal{Q}$	Set of damage variables
S^2	Unit sphere
$\mathrm{Sym}(d)$	Set of symmetric tensors
$\mathcal{S}_d$	Set of sym. pos. definite fourth-order tensors
$\mathbb{R}$	Set of real numbers
$\mathcal{Z}$	Set of internal variables

Greek letters

β	Driving force for damage evolution
ε	Scalar strain
μ	Consistency parameter
σ	Scalar stress
σ_0	Damage-activation threshold
γ	Backtracking factor
ν	Poisson's ratio
ψ	Orientation distribution function
ϕ	Damage-activation function
Φ^*	Force potential
$\boldsymbol{\varepsilon}$	Infinitesimal strain tensor
$\boldsymbol{\sigma}$	Cauchy stress tensor

Sub- and superscripts

$(\cdot)_{\mathrm{B}}\,,(\cdot)_{\mathrm{F}}\,,(\cdot)_{\mathrm{M}}$	Bundle, Fiber, Matrix
$(\cdot)_{\mathrm{L}}\,,(\cdot)_{\mathrm{T}}$	Longitudinal, Transverse
$(\cdot)_{\mathrm{x}}\,,(\cdot)_{\mathrm{y}}\,,(\cdot)_{\mathrm{z}}$	Related to directions $\boldsymbol{e}_x,\boldsymbol{e}_y,\boldsymbol{e}_z$ (orthotropy)
$(\cdot)_{\mathrm{I}}\,,(\cdot)_{\mathrm{II}}\,,(\cdot)_{\mathrm{III}}\,,(\cdot)_{\mathrm{IV}}$	Puck-type cases
$(\cdot)_{\parallel}$	Parallel
$(\cdot)_{\perp}$	Perpendicular
$(\cdot)_{\sigma}$	Related to normal stress
$(\cdot)_{\tau}$	Related to shear stress
$(\cdot)^{\mathsf{S}}$	Symmetric
$(\cdot)^{\circ}$	Spherical
$(\cdot)'$	Deviatoric
$\dot{(\cdot)}$	Material time derivative

Operators

$\boldsymbol{AB}$	Composition of two second-order tensors
$\mathbb{A}\mathbb{B}$	Composition of tow fourth-order tensors
$\boldsymbol{Ab}$	Linear mapping by a second-order tensor
$\mathbb{A}\left[\boldsymbol{B}\right]$	Linear mapping by a fourth-order tensor
$\boldsymbol{A}\cdot\boldsymbol{B}$	Frobenius inner product of two tensors
$\boldsymbol{a}\otimes\boldsymbol{b}$	Tensor product of two vectors
$\boldsymbol{a}\otimes_{\mathsf{S}}\boldsymbol{b}$	Symmetric tensor product
$\boldsymbol{a}^{\otimes n}$	Tensor product repeated n times
$\boldsymbol{a}\times\boldsymbol{b}$	Cross product of two vectors
$(\cdot)^{\mathsf{T}}$	Transposition of a vector or second-order tensor
$(\cdot)^{\mathsf{T_M}}$	Major transposition of a fourth-order tensor
$(\cdot)^{\mathsf{T_L}}, (\cdot)^{\mathsf{T_R}}$	Left and right minor transpositions of a fourth-order tensor
$(\cdot)^{-1}$	Inverse of a symmetric tensor
$\langle\cdot\rangle_{\alpha}$	Volume or ensemble average w. r. t. phase α
$\langle\cdot\rangle$	Macaulay bracket
$\|\cdot\|$	Frobenius norm
$\mathrm{div}\,(\cdot)$	Eulerian divergence
$\mathrm{grad}\,(\cdot)$	Eulerian gradient
$\mathrm{sym}(\cdot)$	Symmetric part
$\mathrm{skw}(\cdot)$	Skew-symmetric part
$\mathrm{tr}(\cdot)$	Trace
$\mathrm{diag}\,(\cdot)$	Diagonal tensor

Chapter 2

Fundamentals of continuum mechanics

2.1 Kinematics

In this chapter, we give an overview of continuum mechanical fundamentals that provide the framework for our subsequent modeling approaches. We introduce kinematics and motivate the definition of displacement and infinitesimal strain. Furthermore, we provide an insight on the general formulation of balance equations and discuss specific, required balance equations. For further information and more detailed explanations, the reader is referred to the works of Truesdell and Toupin (1960), Holzapfel (2000), Haupt (2002) and Bertram (2011).

A three-dimensional body, in the context of Cauchy continua, is defined as a set of material points that have three translational degrees of freedom each. The current position of a material point in such a body with volume v at time t is given by the position vector

$$\boldsymbol{x} = \boldsymbol{\chi}\left(\boldsymbol{X}, t\right),\tag{2.1}$$

where $\boldsymbol{X}$ denotes the position vector of the reference placement of the body at time $t = t_0$. The deformation $\boldsymbol{\chi}$ describes the change of the body due to boundary conditions, i. e., it describes the current shape of the body w. r. t. the corresponding reference placement. The inverse

mapping $X = \chi^{-1}(x, t)$ allows for the identification of the reference placement. The displacement (field) $u(X, t)$ is the difference between the current and reference placement of all material points in a considered body

$$u(X, t) = \chi(X, t) - X. \tag{2.2}$$

A field quantity Λ can be defined in terms of the reference placement or the current placement, being called the Lagrangian $\Lambda_\mathrm{L}(X, t)$ or the Eulerian $\Lambda_\mathrm{E}(x, t)$ description, respectively. The conversion between these two descriptions is performed via the deformation χ and χ^{-1}

$$\Lambda_\mathrm{E}(x, t) = \Lambda_\mathrm{L}\left(\chi^{-1}(x, t), t\right), \tag{2.3}$$

$$\Lambda_\mathrm{L}(X, t) = \Lambda_\mathrm{E}\left(\chi(X, t), t\right). \tag{2.4}$$

The material time derivate of a field quantity (Truesdell and Toupin, 1960) can be expressed via

$$\dot{\Lambda} = \frac{\partial \Lambda_\mathrm{L}(X, t)}{\partial t} = \frac{\partial \Lambda_\mathrm{E}(x, t)}{\partial t} + \frac{\partial \Lambda_\mathrm{E}(x, t)}{\partial x} \cdot \dot{x}, \tag{2.5}$$

with the velocity $\dot{x} = v(x, t)$ of the material point. Note that definition (2.5) holds for any tensorial rank of the field quantity Λ in general.

The deformation gradient F and the displacement gradient H, being spatial derivatives of the current position x and the displacement u in a Lagrangian description, are defined as

$$F(X, t) = \mathrm{Grad}\left(x(X, t)\right) = \frac{\partial \chi(X, t)}{\partial X}, \tag{2.6}$$

$$H(X, t) = \mathrm{Grad}\left(u(X, t)\right) = \frac{\partial u(X, t)}{\partial X} = F - I. \tag{2.7}$$

Despite its designation, the deformation gradient F also accounts for rigid body motions, even though the body does not deform. There exist several deformation measures, depending on the field of application

(Bertram, 2011). One deformation measure, taking into account the change of length and angles of line elements in a body, is Green's strain tensor

$$\boldsymbol{E}^{\mathrm{G}} = \frac{1}{2}\left(\boldsymbol{F}^{\mathsf{T}}\boldsymbol{F} - \boldsymbol{I}\right) = \frac{1}{2}\left(\boldsymbol{H} + \boldsymbol{H}^{\mathsf{T}} + \boldsymbol{H}^{\mathsf{T}}\boldsymbol{H}\right). \qquad (2.8)$$

The linearized version of the deformation measure is the (infinitesimal) strain tensor

$$\boldsymbol{\varepsilon}\left(\boldsymbol{X}, t\right) = \mathrm{sym}(\boldsymbol{H}) = \frac{1}{2}\left(\boldsymbol{H} + \boldsymbol{H}^{\mathsf{T}}\right), \qquad (2.9)$$

which is valid in the context of small deformations, i. e., the condition

$$\|\boldsymbol{H}\| = \sqrt{\mathrm{tr}(\boldsymbol{H}\boldsymbol{H}^{\mathsf{T}})} \ll 1 \qquad (2.10)$$

must hold (Bertram, 2011). The corresponding skew-symmetric part of the displacement gradient is the (infinitesimal) rotation tensor $\boldsymbol{\omega} = (\boldsymbol{H} - \boldsymbol{H}^{\mathsf{T}})/2 = \mathrm{skw}(\boldsymbol{H})$.

Every second-order tensor can be unambiguously decomposed into a spherical and deviatoric part. For the strain tensor, we have

$$\boldsymbol{\varepsilon} = \boldsymbol{\varepsilon}^{\circ} + \boldsymbol{\varepsilon}', \qquad (2.11)$$

where the spherical strain $\boldsymbol{\varepsilon}^{\circ}$ describes the volumetric change of the considered body (dilatation) and the deviatoric strain $\boldsymbol{\varepsilon}'$ gives the volume preserving change of shape of the body (distortion). We can extract these strains via two isotropic fourth-order projectors $\mathbb{P}_1 = (\boldsymbol{I} \otimes \boldsymbol{I})/3$ and $\mathbb{P}_2 = \mathbb{I}^{\mathrm{S}} - \mathbb{P}_1$ as

$$\boldsymbol{\varepsilon}^{\circ} = \mathbb{P}_1\left[\boldsymbol{\varepsilon}\right] = \frac{\mathrm{tr}(\boldsymbol{\varepsilon})}{3}\boldsymbol{I}, \quad \boldsymbol{\varepsilon}' = \mathbb{P}_2\left[\boldsymbol{\varepsilon}\right] = \boldsymbol{\varepsilon} - \frac{\mathrm{tr}(\boldsymbol{\varepsilon})}{3}\boldsymbol{I}. \qquad (2.12)$$

The fourth-order identity on symmetric second-order tensors is denoted by $\mathbb{I}^{\mathrm{S}}$.

2.2 Balance equations

2.2.1 General formulation

A correct prediction of the (mechanical) behavior of a body is based on a correct application and evaluation of associated balance equations. To provide an overview of the most important equations, we introduce the general form of balance equations and subsequently derive specific applications or modifications, respectively. Balance equations associate the change of a field quantity Λ in a considered material volume v to the supply s and production p of this quantity, as well as the corresponding non-convective flux $\boldsymbol{q}$ across the boundary ∂v (Truesdell and Toupin, 1960),

$$\frac{\mathrm{d}}{\mathrm{d}t} \int_v \Lambda \, \mathrm{d}v = \int_v (p + s) \, \mathrm{d}v + \int_{\partial v} \boldsymbol{q} \cdot \mathrm{d}\boldsymbol{a}. \tag{2.13}$$

For the surface integral, the relation $\mathrm{d}\boldsymbol{a} = \boldsymbol{n} \, \mathrm{d}a$ holds, with $\mathrm{d}a$ being a surface element of the boundary ∂v and $\boldsymbol{n}$ the outer surface normal unit vector. We can transform the integral form into a local form in regular points using the divergence theorem and Reynolds transport theorem (Bertram, 2011)

$$\frac{\partial \Lambda}{\partial t} + \mathrm{div}\,(\Lambda \boldsymbol{v}) = p + s + \mathrm{div}\,(\boldsymbol{q}). \tag{2.14}$$

2.2.2 Specific formulations

Mass

We obtain the balance of mass via the density $\Lambda = \varrho$ as

$$\dot{\varrho} + \varrho \mathrm{div}\,(\boldsymbol{v}) = 0, \tag{2.15}$$

where the production p, supply s, and flux $\boldsymbol{q}$ are zero. We can calculate an alteration of mass via $\mathrm{tr}(\boldsymbol{\varepsilon}) = (\,\mathrm{d}v - \mathrm{d}v_0\,)\,/\,\mathrm{d}v_0$ or $\varrho = \varrho_0\,(1 - \mathrm{tr}(\boldsymbol{\varepsilon}))$. In the framework of small deformations, i.e., condition (2.10) or rather $\|\boldsymbol{\varepsilon}\| \ll 1$ holds, the relation $\varrho \approx \varrho_0$ is valid and all displacement fields automatically fulfill the balance of mass.

Linear momentum

The balance of linear momentum associates the rate of change of the density of linear momentum $\Lambda = \varrho\boldsymbol{v}$ to the supply via volume forces $\varrho\boldsymbol{b}$ and the flux in terms of surfaces forces $\boldsymbol{t}$, leading to an integral form

$$\frac{\mathrm{d}}{\mathrm{d}t} \int_v \varrho\boldsymbol{v}\,\mathrm{d}v = \int_v \varrho\boldsymbol{b}\,\mathrm{d}v + \int_{\partial v} \boldsymbol{t}\,\mathrm{d}a. \qquad (2.16)$$

The production is zero. Using the Lemma of Cauchy $\boldsymbol{t} = \boldsymbol{\sigma}\boldsymbol{n}$, we can write the local form as

$$\varrho\dot{\boldsymbol{v}} = \varrho\boldsymbol{b} + \mathrm{div}\,(\boldsymbol{\sigma})\,. \qquad (2.17)$$

For a quasi-static setting, the acceleration $\dot{\boldsymbol{v}}$ vanishes.

Angular momentum

Balancing the field quantity $\Lambda = \boldsymbol{x} \times \varrho\boldsymbol{v}$ yields the balance of angular momentum

$$\frac{\mathrm{d}}{\mathrm{d}t} \int_v \boldsymbol{x} \times \varrho\boldsymbol{v}\,\mathrm{d}v = \int_v \boldsymbol{x} \times \varrho\boldsymbol{b}\,\mathrm{d}v + \int_{\partial v} \boldsymbol{x} \times \boldsymbol{t}\,\mathrm{d}a, \qquad (2.18)$$

with the supply $\boldsymbol{x} \times \varrho\boldsymbol{b}$ and the flux $\boldsymbol{x} \times \boldsymbol{t}$. For a Boltzmann continuum with vanishing moment densities, the quasi-static balance of angular moment in its local form yields the symmetry of the stress tensor

(Truesdell and Toupin, 1960)

$$\boldsymbol{\sigma} = \boldsymbol{\sigma}^{\mathsf{T}}. \tag{2.19}$$

Remark: The second-order Cauchy stress tensor $\boldsymbol{\sigma}$ describes the local stress state in a material point. Similar to the strain tensor, we can decompose the stress into a spherical part $\boldsymbol{\sigma}^\circ$ and a deviatoric part $\boldsymbol{\sigma}'$

$$\boldsymbol{\sigma} = \boldsymbol{\sigma}^\circ + \boldsymbol{\sigma}', \quad \boldsymbol{\sigma}^\circ = \mathbb{P}_1\left[\boldsymbol{\sigma}\right], \quad \boldsymbol{\sigma}' = \mathbb{P}_2\left[\boldsymbol{\sigma}\right]. \tag{2.20}$$

Energy

Relating the rate of change of total energy to the power furnished by volume $\varrho \boldsymbol{b} \cdot \boldsymbol{v}$ and surface $\boldsymbol{t} \cdot \boldsymbol{v}$ forces, as well as volumetric heat supply ϱs and heat flow across the surface $\boldsymbol{q} \cdot \boldsymbol{n}$ yields the integral form for the total energy

$$\frac{\mathrm{d}}{\mathrm{d}t} \int_v \left(\varrho e + \frac{1}{2} \varrho \boldsymbol{v} \cdot \boldsymbol{v} \right) \mathrm{d}v = \int_v \left(\varrho \boldsymbol{b} \cdot \boldsymbol{v} + \varrho s \right) \mathrm{d}v + \int_{\partial v} \left(\boldsymbol{t} \cdot \boldsymbol{v} - \boldsymbol{q} \cdot \boldsymbol{n} \right) \mathrm{d}a, \tag{2.21}$$

which is the first law of thermodynamics. The associated local form of the total energy in regular points is

$$\varrho \dot{e} + \frac{1}{2} \varrho \left(\boldsymbol{v} \cdot \boldsymbol{v} \right)^{\cdot} = \varrho \boldsymbol{b} \cdot \boldsymbol{v} + \varrho s + \operatorname{div} \left(\boldsymbol{\sigma}^{\mathsf{T}} \boldsymbol{v} \right) - \operatorname{div} \left(\boldsymbol{q} \right). \tag{2.22}$$

Note that the total energy is the superposition of internal energy and kinetic energy. We can derive the local form, i. e., the balance of internal energy, by taking into account the balance of mass and balance of linear momentum

$$\varrho \dot{e} = \varrho s - \operatorname{div} \left(\boldsymbol{q} \right) + \boldsymbol{\sigma} \cdot \dot{\boldsymbol{\varepsilon}}. \tag{2.23}$$

The internal energy changes, due to the production of kinetic energy (density) $\boldsymbol{\sigma} \cdot \dot{\boldsymbol{\varepsilon}}$ due to stress power, heat flux across the surface $\operatorname{div} \left(\boldsymbol{q} \right)$

and heat supply in the volume ϱs. In a similar way, we can obtain the balance of kinetic energy in its integral form via a multiplication of the balance of linear momentum with the velocity $\boldsymbol{v}$ (Truesdell and Toupin, 1960) and finally end up with the local form

$$\frac{1}{2}\varrho\left(\boldsymbol{v}\cdot\boldsymbol{v}\right)^{\cdot} = \varrho\boldsymbol{b}\cdot\boldsymbol{v} + \mathrm{div}\left(\boldsymbol{\sigma}^{\mathsf{T}}\boldsymbol{v}\right) - \boldsymbol{\sigma}\cdot\dot{\varepsilon}. \tag{2.24}$$

The flux of kinetic energy over the surface is given by the power of external forces $\mathrm{div}\left(\boldsymbol{\sigma}^{\mathsf{T}}\boldsymbol{v}\right) = \mathrm{div}\left(\boldsymbol{\sigma}\boldsymbol{v}\right)$ and the supply of kinetic energy is $\varrho\boldsymbol{b}\cdot\boldsymbol{v}$. Energy in terms of stress power $\boldsymbol{\sigma}\cdot\dot{\varepsilon}$ is exchanged between the internal energy and the kinetic energy.

Entropy

A rate of change of entropy η is evoked via entropy production ϱp_η, entropy supply ϱs_η and entropy flux $\boldsymbol{q}_\eta\cdot\boldsymbol{n}$

$$\frac{\mathrm{d}}{\mathrm{d}t}\int_v \varrho\eta\,\mathrm{d}v = \int_v \varrho\left(s_\eta + p_\eta\right)\,\mathrm{d}v - \int_{\partial v} \boldsymbol{q}_\eta\cdot\boldsymbol{n}\,\mathrm{d}a. \tag{2.25}$$

Following the second law of thermodynamics, the entropy production is non-negative $\int_v \varrho p_\eta\,\mathrm{d}v \geq 0$ for any process. The local form of the entropy balance is given as (Coleman and Noll, 1963)

$$\varrho\dot{\eta} = \varrho s_\eta + \varrho p_\eta - \mathrm{div}\left(\boldsymbol{q}_\eta\right). \tag{2.26}$$

Generally, the entropy supply and entropy flux are assumed to be $s_\eta = s/\theta$ and $\boldsymbol{q}_\eta = \boldsymbol{q}/\theta$, see Coleman and Noll (1963). In terms of the local formulation, the second law of thermodynamics is given is

$$p_\eta \geq 0. \tag{2.27}$$

Utilizing the relation of the internal energy e, the entropy η and the Helmholtz free energy density w

$$e = \theta\eta + w, \tag{2.28}$$

as well as a proper Legendre transformation (Coleman and Gurtin, 1967), the local from the balance of internal energy and the local balance of entropy, we can derive the Clausius-Duhem inequality

$$\boldsymbol{\sigma} \cdot \dot{\boldsymbol{\varepsilon}} - \varrho\dot{w} - \varrho\dot{\theta}\eta - \frac{1}{\theta}\boldsymbol{q} \cdot \operatorname{grad}(\theta) \geq 0. \tag{2.29}$$

Chapter 3

Basics of SMC composites

3.1 Manufacturing process

Typically, SMC composites are manufactured via a compression molding process as shown in Fig. 3.1. Microstructure characteristics such as orientation or volume fraction are influenced by the manufacturing process leading to variations of the structural performance of produced parts. We give a brief overview of the manufacturing process established within IRTG 2078 to grasp the key aspects that affect the local and effective behavior of our considered SMC composites.
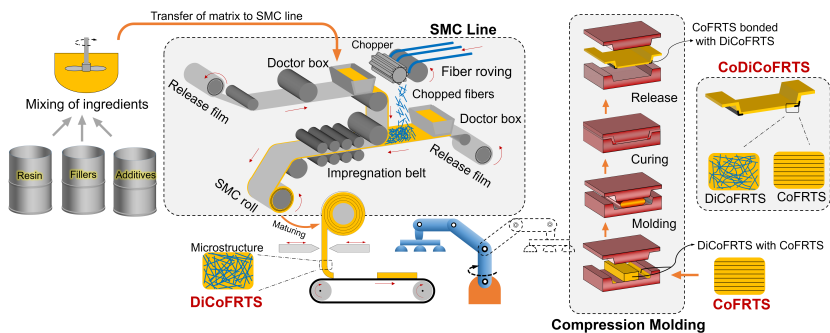
Figure 3.1: Manufacturing process of SMC composites (kindly provided by T. D. Pallicity (Karlsruhe Institute of Technology (KIT) - Institute of Engineering Mechanics))

Depending on the intended application, the resin might be mixed with additives and fillers in a preliminary step, see the left hand side in Fig. 3.1. For the material at hand, we use an unsaturated polyester polyurethane hybrid (UPPH) resin with no fillers that possesses a stable bi-stage state allowing for a co-molding of glass and carbon fibers (Bücheler et al., 2017). The so produced SMC composite is specifically designed to be used for the manufacturing of structural, load-bearing components.

Subsequently, the mixed matrix is transfered to the SMC line and filled into two doctor boxes, see the middle in Fig. 3.1. These two doctor boxed spread the matrix on two different films, one upper and one lower film. Endless fiber rovings are cut to lengths of 25.4 mm (1 inch) in the chopper and are randomly dispersed on the lower film with matrix. Thereupon, the upper film with matrix is put on top of it, so that the fibers are encased in matrix. The produced DiCo pre-preg is fed into a carrier belt that induces relative motion between fibers and matrix and hence improves impregnation. Finally, the pre-preg is rolled up for better handling and storage. Partial curing (pre-curing) of the matrix can be induced by setting specific temperature conditions during storage.

For the compression molding process of an SMC composite part, DiCo pre-pregs are cut and stacked to a specific size and thickness. This initial charge is placed on the tempered mold (typically $120°$ to $160°$) at a certain position and typically does not fully cover the complete mold. Conceivably, Co patches are added at specific positions within a co-molding process, see the right hand side in Fig. 3.1. The closing of the press induces a plug-like flow of the DiCo SMC which ultimately fills the complete mold. The flow influences the fiber positions and orientations of the DiCo material and hence yields a process-dependent inhomogeneous orientation distribution in the manufactured part. If designed correctly, the Co patches remain at their assigned positions. Usually, it takes about 2 min. to 4 min. for the matrix to cure within

the mold. After that, the mold is opened and the manufactured part is removed via ejector pins.

3.2 Fiber bundle structure[1]

Each of the utilized rovings in the manufacturing process (see Fig. 3.1) consists of about 225 aligned fibers. Despite being cut and dispersed on the film, these 225 fibers remain as bundles or tows, respectively. When encased in matrix and rolled up, these bundles remain intact, also during storage. Within the compression molding manufacturing process, the bundles are exposed to flow conditions in the mold and hence relocate and change their orientations. Nonetheless, due to various conditions, e. g., low viscosity of the matrix, plug-like flow behavior, outer (hot) lubrication layers and low shear forces, the fiber bundles mostly remain intact during the flow process. Therefore, typical SMC composite parts, manufactured via the discussed compression molding process, show a characteristic three-scale structure as presented in Fig. 1.6.

(a) Volumetric μCT image (Schöttl et al., 2021b) **(b)** Identified fiber bundles (Schöttl et al., 2021b) **(c)** Generated microstructure (Görthofer et al., 2020)
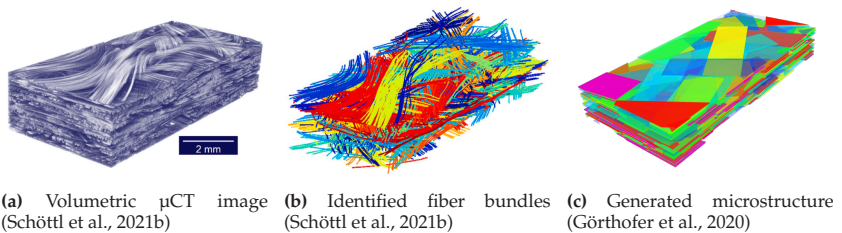
Figure 3.2: Real fiber bundle microstructure of an SMC composite (Schöttl et al., 2020; Schöttl et al., 2021b) and generated microstructure (Görthofer et al., 2020)

---

[1] This section is based on excerpts of the publication "A computational multiscale model for anisotropic failure of SMC composites" (Görthofer et al., 2022a)

Dedicated algorithms (Pinter et al., 2018; Schöttl et al., 2020; Schöttl et al., 2021b) reveal the fiber bundle structure of a manufactured component on μCT images using tracking and clustering techniques, see Fig. 3.2. Similar microstructure characteristics are observed for mesostructure analysis via optical microscopy on polished SMC composite sample surfaces (Chen et al., 2018b; Li et al., 2018a) and accounted for in hierarchical approaches (Anagnostou et al., 2018; Fitoussi et al., 2005).

3.3 Orientation tensors[1]

To take the orientation state of our considered SMC composite parts into account within the material modeling approaches, we need to depict the orientation via mathematical descriptions. For a volume containing identically shaped cylindrical fibers, following Kanatani (1984) and Advani and Tucker (1987), we describe the fiber orientation state by an orientation distribution function (ODF) $\psi : S^{n-1} \to \mathbb{R}$, defined on the unit sphere S^{n-1} in $\mathbb{R}^n$ ($n = 2, 3$). The fraction of fibers pointing in a set of directions $D \subseteq S^{n-1}$ is determined by

$$\frac{1}{|S^{n-1}|} \int_D \psi(\boldsymbol{p}) \, \mathrm{d}s, \qquad (3.1)$$

where $\mathrm{d}s$ denotes the surface element of the $(n-1)$-sphere, and $|S^{n-1}|$ denotes the surface measure of S^{n-1}. Considering $n = 3$ dimensions, we have a surface element of the unit sphere $\mathrm{d}s = \sin\theta \, \mathrm{d}\theta \, \mathrm{d}\varphi$ in terms of spherical coordinates $\{r, \theta, \varphi\}$. For physical reasons, the ODF is assumed non-negative, normalized (i. e. integrates to unity) and symmetric, i. e., $\psi(-\boldsymbol{p}) = \psi(\boldsymbol{p})$ holds for any $\boldsymbol{p} \in S^{n-1}$.

---

[1] This section is based on excerpts of the publication "Computational homogenization of SMC composites based on high fidelity representative unit cells" (Görthofer et al., 2020)

The particular forms of Eq. (3.1) for the two- and three-dimensional case $(n = 2, 3)$ are given by

$$\frac{1}{2\pi r} \int_{\varphi=0}^{2\pi} \psi(\boldsymbol{p}) \, \mathrm{d}\varphi, \quad \boldsymbol{p} \mathrel{\hat{=}} (\cos\varphi, \sin\varphi, 0)^{\mathsf{T}}, \quad \text{and} \quad (3.2)$$

$$\frac{1}{4\pi r^2} \int_{\varphi=0}^{2\pi} \int_{\theta=0}^{\pi} \psi(\boldsymbol{p}) \sin\theta \, \mathrm{d}\theta \, \mathrm{d}\varphi, \quad \boldsymbol{p} \mathrel{\hat{=}} (\sin\theta \cos\varphi, \sin\theta \sin\varphi, \cos\theta)^{\mathsf{T}}.$$
$$(3.3)$$

Hereby, the planar and spatial unit spheres and their surface measures are defined via the radius r. The corresponding ODFs $\psi(\boldsymbol{p})$ need to be planar or spatial distribution functions, respectively.

Based on the ODF, orientation tensors (OTs) may be defined by forming dyadic products of the directions $\boldsymbol{p}$ and a subsequent integration over all directions in the $(n-1)$-sphere. Due to symmetry of the ODF, the OTs of odd-order vanish. The even-order integrals yield totally symmetric and positive definite tensors with trace 1. The most commonly used OTs are the second- and fourth-order OTs $\boldsymbol{A} \in \mathbb{R}^{n \times n}$ and $\mathbb{A} \in \mathbb{R}^{n \times n \times n \times n}$

$$\boldsymbol{A} = \int_{S^{n-1}} \psi(\boldsymbol{p}) \, \boldsymbol{p} \otimes \boldsymbol{p} \, \mathrm{d}s, \quad (3.4)$$

$$\mathbb{A} = \int_{S^{n-1}} \psi(\boldsymbol{p}) \, \boldsymbol{p} \otimes \boldsymbol{p} \otimes \boldsymbol{p} \otimes \boldsymbol{p} \, \mathrm{d}s, \quad (3.5)$$

where we suppress the dependence on n for notational clarity. A general second-order OT in three spatial dimensions (defined by an orthonormal basis $\{\boldsymbol{e}_1, \boldsymbol{e}_2, \boldsymbol{e}_3\}$ may be represented as

$$\boldsymbol{A} \mathrel{\hat{=}} \begin{bmatrix} A_{11} & A_{12} & A_{13} \\ A_{12} & A_{22} & A_{23} \\ A_{13} & A_{23} & A_{33} \end{bmatrix} \quad (3.6)$$

where the constraint

$$\mathrm{tr}(\boldsymbol{A}) = A_{11} + A_{22} + A_{33} = 1 \tag{3.7}$$

is a consequence of $\int_{S^{n-1}} \psi(\boldsymbol{p}) \, \mathrm{d}s = 1$.

Due to the compression molding manufacturing process, the fiber orientation distribution turns out to be almost perfectly planar for SMC composites, i.e., the components pointing in the normal direction of the produced part vanish. Thus, we may describe such an orientation distribution by second-order OTs on the unit circle S^2. Furthermore, we can diagonalize the second-order OT $\boldsymbol{A}$ by a proper rotation matrix $\boldsymbol{R}$

$$\boldsymbol{A} \triangleq \begin{bmatrix} A_{11} & A_{12} \\ A_{12} & A_{22} \end{bmatrix} = \boldsymbol{R} \begin{bmatrix} A_1 & 0 \\ 0 & A_2 \end{bmatrix} \boldsymbol{R}^{\mathsf{T}} \tag{3.8}$$

with eigenvalues A_1 and A_2 of the planar second-order OT $\boldsymbol{A}$.

3.4 The exact closure approximation in two spatial dimensions[1]

The principal advantage of fiber orientation tensors compared to working with the full ODF is the reduced complexity (and, thus, the reduced number of degrees of freedom) necessary for numerical process simulations. Unfortunately, the second-order fiber orientation tensor does not determine the effective elastic properties of a fiber reinforced composite, in general. On the other hand, the phase space of fourth-order fiber orientation tensors is extremely complex, cf. Linn (2005). As a work-around, Tucker and co-workers (Advani and Tucker, 1987; Cintra and Tucker, 1995) pioneered working with closure approximations, i.e.,

---

[1] This section is based on excerpts of the publication "Computational homogenization of SMC composites based on high fidelity representative unit cells" (Görthofer et al., 2020)

functions g mapping second-order OTs to (reasonable) fourth-order OTs, $\mathbb{A} = g(\boldsymbol{A})$. The first closure approximations, like the linear, quadratic and hybrid closure approximations (Advani and Tucker, 1987) violated physical principles, which comes from the fact that these closure approximations could generate fourth-order OTs that do not derive from an ODF, i. e., there was no $\psi : S^{n-1} \to \mathbb{R}$, s. t. Eq. (3.5) holds. This problem could be resolved by factoring closure approximations, i. e., to seek mappings h associating an ODF ψ to a second-order OT $\boldsymbol{A}$. The resulting closure approximation subsequently computes as

$$\mathbb{A} = \int_{S^{n-1}} \psi(\boldsymbol{p})\, \boldsymbol{p} \otimes \boldsymbol{p} \otimes \boldsymbol{p} \otimes \boldsymbol{p} \ \mathrm{d}s, \quad \text{where} \quad \psi(\boldsymbol{p}) = h(\boldsymbol{A}). \qquad (3.9)$$

Thus, finding closure approximations for OTs reduces to seeking a suitable class of ODFs parameterized by second-order OTs.

As shown by Verleye and Dupret (1993), the family of angular central Gaussian distribution functions (Tyler, 1987)

$$\psi_B(\boldsymbol{p}) = \frac{1}{|S^{n-1}|}(\boldsymbol{B} \cdot \boldsymbol{p} \otimes \boldsymbol{p})^{-\frac{n}{2}}, \quad \boldsymbol{p} \in S^{n-1}, \qquad (3.10)$$

parametrized by a positive definite symmetric matrix $\boldsymbol{B} \in \mathbb{R}^{n \times n}$ with determinant 1, constitute exact solutions for the ensemble Jeffery's equation (Jeffery, 1923), and thus, to the Folgar-Tucker equation (Folgar and Tucker, 1984) with vanishing Folgar-Tucker diffusivity, which model the fiber orientation dynamics during injection and compression molding.

For $n = 3$, Montgomery-Smith et al. (2011), extending earlier work of Verleye and Dupret (1993), noticed that there is a one to one correspondence of admissible $\boldsymbol{B}$'s to second-order OTs $\boldsymbol{A}$, via the association derived from Eq. (3.4) with a distribution function $\psi = \psi_B$

$$\boldsymbol{A} = \int_{S^{n-1}} \psi_B(\boldsymbol{p})\, \boldsymbol{p} \otimes \boldsymbol{p} \ \mathrm{d}s. \qquad (3.11)$$

Unfortunately, determining $\boldsymbol{B}$ for given $\boldsymbol{A}$ involves solving a system of elliptic integrals which becomes ill-conditioned for $\det(\boldsymbol{A}) \ll 1$.

In this work, we are concerned with the two-dimensional case, i.e., $n = 2$, and show that there are simple explicit formulae for $\boldsymbol{B}$ in terms of $\boldsymbol{A}$ (and vice versa). Also, the fourth-order OT as defined in Eq. (3.5)

$$\mathbb{A} = \int_{S^{n-1}} \psi_B(\boldsymbol{p}) \, \boldsymbol{p} \otimes \boldsymbol{p} \otimes \boldsymbol{p} \otimes \boldsymbol{p} \, \mathrm{d}s \tag{3.12}$$

can be computed explicitly. To be more precise, the following holds: Let $\boldsymbol{B}$ be a diagonal matrix $\boldsymbol{B} \mathrel{\hat{=}} \mathrm{diag}(B_1, B_2)$ with $B_1 > 0$ and $B_2 = 1/B_1$. Then, $\boldsymbol{A}$ computed from (3.11) is a diagonal matrix $\boldsymbol{A} \mathrel{\hat{=}} \mathrm{diag}(A_1, A_2)$ with entries

$$A_1 = \frac{1}{1 + B_1} \quad \text{and} \quad A_2 = \frac{1}{1 + B_2}. \tag{3.13}$$

Furthermore, the (independent) components of the fourth-order OT ($\mathbb{A} = A_{ijkl} \, \boldsymbol{e}_i \otimes \boldsymbol{e}_j \otimes \boldsymbol{e}_k \otimes \boldsymbol{e}_l$) as defined in Eq. (3.12) read

$$
\begin{aligned}
A_{1111} &= \frac{1}{2} A_1 (1 + A_1), & A_{2222} &= A_2^2, \\
A_{1122} &= \frac{1}{2} A_1 A_2, & A_{1112} &= 0, & A_{1222} &= 0.
\end{aligned}
\tag{3.14}
$$

Hereby, the components are invariant under permutations of the indices. A derivation is contained in Appendix A.

Using a proper rotation, these formulae for the exact closure can also be used for non-diagonal OTs. Another consequence is the identity

$$\frac{1}{\mathrm{tr}(\boldsymbol{B}^{-\frac{1}{2}})} \, \boldsymbol{B}^{-\frac{1}{2}} = \boldsymbol{A}, \tag{3.15}$$

which only holds for $n \leq 2$. To establish this identity, consider the diagonal case. Then, the latter identity is equivalent to

$$\frac{\frac{1}{\sqrt{B_1}}}{\frac{1}{\sqrt{B_1}} + \frac{1}{\sqrt{B_2}}} = A_1 \quad \text{and} \quad \frac{\frac{1}{\sqrt{B_2}}}{\frac{1}{\sqrt{B_1}} + \frac{1}{\sqrt{B_2}}} = A_2. \tag{3.16}$$

However, using $B_1 B_2 = 1$, we deduce

$$\frac{\frac{1}{\sqrt{B_1}}}{\frac{1}{\sqrt{B_1}} + \frac{1}{\sqrt{B_2}}} = \frac{\sqrt{B_2}}{\sqrt{B_1} + \sqrt{B_2}} = \frac{\sqrt{B_1 B_2}}{B_1 + \sqrt{B_1 B_2}} = \frac{1}{B_1 + 1}, \tag{3.17}$$

which equals A_1 by the first equation in (3.13). The second identity is shown analogously.

A most widely used closure approximation is the quadratic approximation (Doi, 1981; Advani and Tucker, 1990). Hereby, the fourth-order orientation tensor $\mathbb{A}$ is approximated via the dyadic product of the second-order orientation tensor $\boldsymbol{A}$ with itself ($\mathbb{A} = \boldsymbol{A} \otimes \boldsymbol{A}$). With $\boldsymbol{A} \triangleq \mathrm{diag}(A_1, A_2)$, the entries of $\mathbb{A}$ are

$$\begin{aligned} A_{1111} &= A_1^2, & A_{2222} &= A_2^2, \\ A_{1122} &= A_1 A_2, & A_{1112} &= 0, & A_{1222} &= 0. \end{aligned} \tag{3.18}$$

When we compare the two closure approximations, we see the superiority of the exact closure Eq. (3.14) over the quadratic closure Eq. (3.18). The component A_{1122}, e.g., is off by a factor of 2 and therefore not predicted appropriately via the quadratic closure.

Chapter 4

Computational homogenization of SMC composites based on high fidelity representative unit cells[1]

4.1 Introduction

4.1.1 Research contributions

Sheet molding compound (SMC) composites combine high lightweight potential with excellent formability and are frequently used in industrial applications. To reduce safety factors in dimensioning SMC parts, the influence of processing parameters and stochastic variation of microstructural and physical properties needs to be quantified accurately.

Taking into account the inherent three-scale structure of SMC, we improve the microstructure generator of Chen et al. (2018b) in various respects. Firstly, we consistently rely upon state-of-the-art closure approximations for the fourth-order fiber orientation tensor. More precisely, we show that for planar fiber orientation state, there is an explicit formula for the fast exact closure approximation of Montgomery-Smith et al. (2011). Secondly, we exploit the use of quasi-random numbers in sampling the fiber orientation distribution, leading to

---

[1] This chapter is based on the publication "Computational homogenization of SMC composites based on high fidelity representative unit cells" (Görthofer et al., 2020)

dramatic improvements in accuracy compared to pseudo-random Monte Carlo sampling. Last but not least, we rely upon fast Fourier transform based methods for rapid computational homogenization.

With these methodological improvements at hand, we thoroughly investigate the influence of the mechanical and microstructural parameters on the effective elastic properties of SMC composites, and compare the results to direct numerical simulations on large scale digital volume images and mean-field estimates.

4.1.2 Chapter structure

In this chapter, we are concerned with E-glass fiber reinforced SMC based on an unsaturated polyester polyurethane hybrid (UPPH) resin without fillers. This material class has been investigated in terms of its molding capabilities (Hohberg et al., 2017) and the resulting mechanical properties, in particular the viscoelastic characteristics (Kehrer et al., 2018), puncture properties (Trauth et al., 2019), damaging behavior (Trauth et al., 2018; Schemmann et al., 2018b), tension-compression asymmetry and bi-axial characterization (Schemmann et al., 2018c).

Due to the high bundle aspect ratio and the strong manufacturing process dependence of the fiber orientation, the stochastic bundle orientation selection strategy of Chen et al. (2018b) proved insufficient for our purposes. More precisely, we improve the bundle deposition algorithm in various regards.

First, we consistently rely upon the powerful exact closure approximation of Montgomery-Smith et al. (2011). We derive a closed-form expression for the exact closure of planar fiber (bundle) orientations. This result, described in Sec. 3.4 and Appendix A, is surprising, because for general three dimensional fiber orientation states, a system of equations involving non-standard elliptic integrals needs to be solved numerically.

Our second improvement concerns the strategy for choosing the fiber bundle directions. In contrast to the typical pseudo-random selection strategy, for instance relied upon by Chen et al. (2018b), we advocate using quasi-random sampling in the form of Sobol's sequence (Sobol', 1967). The improvements in accuracy are dramatic, cf. Sec. 4.2.3, enabling us to use only a few bundles to gain high fidelity in targeted fiber (bundle) orientation tensors.

Last, but not least, we consistently rely upon modern FFT-based computational techniques (Moulinec and Suquet, 1994; 1998; Schneider, 2021), permitting us to quickly and thoroughly investigate the sensitivity of the effective elastic properties w. r. t. the multitude of both mechanical and geometrical parameters entering the SMC unit cell generator based computational multiscale strategy, cf. Sec. 4.4. Of course, we pay close attention to working with representative results, both in terms of spatial resolution and representativity of the underlying volume elements. Furthermore, we compare our findings to mean-field predictions and full-field simulation results on μCT image data of an SMC microstructure.

4.2   Generating SMC unit cells

4.2.1   SMC materials and processing

SMC composites are manufactured via compression molding process, cf. Bücheler et al. (2017) and Bücheler (2018). Initially, fiber tows consisting of approximately 225 individual, aligned continuous fibers with a diameter of approximately $13.5\,\mu m$ are cut to a length of $1\,\text{inch} = 25.4\,\text{mm}$. These fiber bundles are randomly dispensed onto a matrix resin foil, enveloped by another matrix resin foil, rolled up onto sheets and pre-cured. From these pre-cured sheets initial charges can be cut to be used within the compression molding process. The measured fiber

volume fraction c_F we consider for this work is $25\,\%$, cf. Görthofer et al. (2019b).
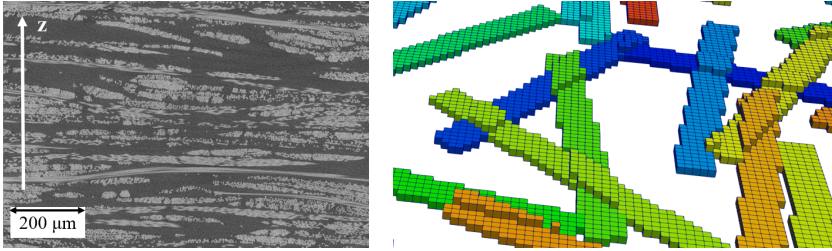
(a) Cross-section of SMC composite unit cell showing the layerwise structure in z-direction

(b) Bundle placement in a voxelized unit cell

Figure 4.1: Layerwise structure of SMC composite and algorithmic bundle placement to capture the layerwise structure

During the compression molding manufacturing process, the matrix resin is heated, flows and fills the mold, and is compressed (Hohberg et al., 2016; 2017). Hereby, the individual tows of 225 fibers are carried by the flowing resin and are flattened but remain otherwise intact. The resulting SMC microstructure, cf. Fig. 4.1a, is composed of closely packed fiber "bundles". These bundles remain almost unbent, hence we model them as planar. The fibers within a bundle are almost perfectly aligned. Thus, instead of describing the fiber orientation state by fiber OTs, we may also rely upon a description in terms of "bundle OTs" instead.

4.2.2 The successive bundle deposition method

As the point of departure for generating representative SMC unit cells serves the successive bundle deposition method described in Chen et al. (2018b), originally developed for carbon fiber SMC. Our method differs in the way the orientations are sampled, cf. Sec. 4.2.3.

In the algorithm, cuboids serve as the basic geometric primitives for modeling the fiber bundles, described by a bundle length l_B, bundle width w_B and bundle height h_B (which we assume identical for the complete microstructure). These bundles are deposited by a random sequential addition (RSA) technique (Feder, 1980) into a square unit cell with dimension $L_x = L_y = L$ and periodic boundary conditions. For physical reasons, the bundles are prohibited to overlap. To reach the fiber volume content typically encountered in industrial applications (up to $60\,\%$ bundle volume fraction), bundles are allowed to be displaced into the next layer (but not more than a single layer). This is shown in Fig. 4.1b, which represents an actual result of the bundle deposition algorithm. For efficient collision handling, a background voxel grid with voxel spacing v is superimposed.
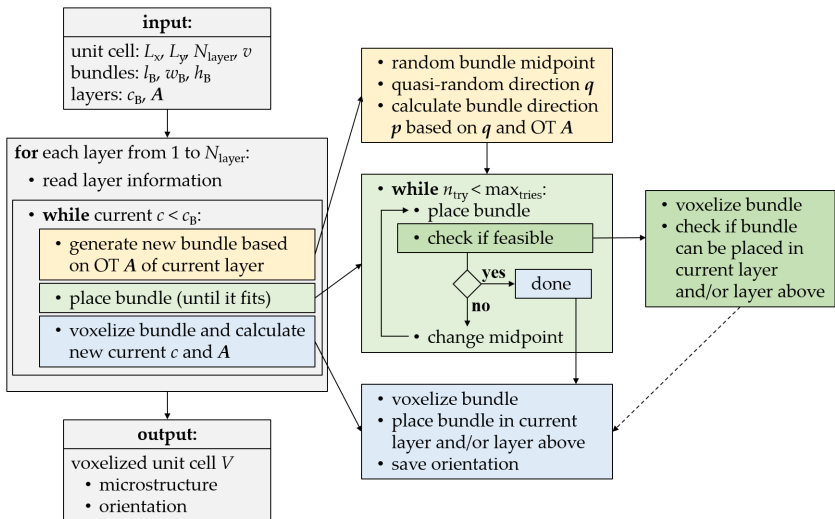
Figure 4.2: Schematic flowchart of the key steps of the algorithm

Furthermore, the number of layers and a bundle volume fraction c_B plus a bundle OT of second-order $\mathbf{A}$ can be defined for each layer. The result of the algorithm is a binary description of the microstructure on a voxel grid, together with bundle directions for the voxels containing bundles. The key steps of the algorithm are the generation of the bundles as abstract objects, determination of the directions according to the prescribed OTs, placement of the bundles in the corresponding layers and the voxelization of the bundles in the unit cell. The algorithm proceeds layer by layer, generating bundles sequentially, each of which samples random midpoints until the bundle does not overlap with the already existing bundles. Here, overlapping is defined taking into account a possible displacement into the next layer. Figure 4.2 presents a flow chart of the algorithm.

(a) $A_1 = 1.0$ (b) $A_1 = 0.5$ (c) $A_1 = 0.2$ (d) $A_1 = 0.0$
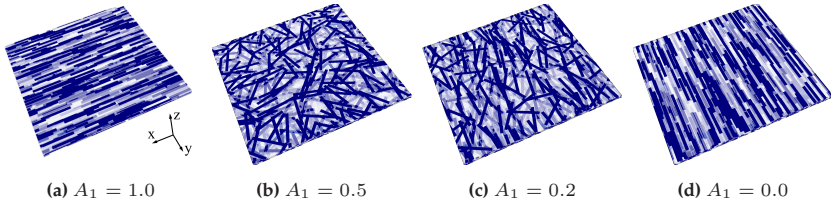
Figure 4.3: Generated unit cells with different orientations

Examples of generated unit cells based on the presented algorithm are shown in Fig. 4.3. For better illustration of the placed bundles, the number of shown layers is limited. Blue bundles are placed into a white matrix, and the shadings of blue indicate the different layers. A bundle volume fraction of $c_B = 50\%$ was chosen for all layers. The desired volume fraction is matched with a relative error of $e \leq 0.5\%$. As error measurement we normalize the difference of the desired and the actual volume fraction w. r. t. the desired volume fraction. The presented microstructures vary in the desired orientation distribution going from

unidirectional in x-direction (Fig. 4.3a) via planar isotropic in the z-plane (Fig. 4.3b) to unidirectional in y-direction (Fig. 4.3d) for all layers. Using a similar error measurement as for the volume fraction, the orientations are matched with a relative error of $e \leq 1.5\,\%$.

4.2.3 Quasi-random orientation sampling

The key addition to the microstructure generation method of Chen et al. (2018b) is the way in which orientations are sampled. There are two requirements. On the one hand, for a given planar OT $\boldsymbol{A}$, the drawn directions $\boldsymbol{p}_1, \dots, \boldsymbol{p}_K$ should match the fourth-order OT $\mathbb{A}$ determined by the exact closure to high precision, i.e., the difference

$$\left\| \mathbb{A} - \frac{1}{K} \sum_{i=1}^{K} \boldsymbol{p}_i \otimes \boldsymbol{p}_i \otimes \boldsymbol{p}_i \otimes \boldsymbol{p}_i \right\| \quad \rightarrow \quad \min. \tag{4.1}$$

should be as small as possible. Hereby, we measure the difference via the Frobenian norm. Secondly, the first property should hold even though the number of drawn directions K is not known a priori. The latter results from the bundle deposition method described in Sec. 4.2.2 - as parts of each bundle may be displaced to the next layer, the number of bundles to be drawn to match the desired fiber bundle content has to be determined dynamically during the algorithm's performance.

Notice that if we knew K beforehand we could draw the directions $\boldsymbol{p}_1, \dots, \boldsymbol{p}_K$ randomly and perform an optimization scheme to make (4.1) as small as desired.

Goldberg et al. (2017) noticed that the ODF determined by the exact closure approximation arises as a transformation of a uniformly distributed random variable on the unit sphere S^{n-1}. More precisely, suppose a second-order OT $\boldsymbol{A}$ with $\det(\boldsymbol{A}) > 0$ is given. Suppose that $\boldsymbol{B}$ is the unimodular matrix realizing the angular central Gaussian distribution ψ_B with second-order OT $\boldsymbol{A}$. Then, if $\boldsymbol{q}$ is a multivariate random variable

of vectors uniformly distributed on the unit sphere S^{n-1}, the random variable $\boldsymbol{p} = \boldsymbol{B}^{-\frac{1}{2}}\boldsymbol{q}/\|\boldsymbol{B}^{-\frac{1}{2}}\boldsymbol{q}\|$ is ψ_B distributed. Here, $\boldsymbol{B}^{-\frac{1}{2}}$ is the inverse of the square root of the matrix $\boldsymbol{B}$ which may be computed, for instance, by a spectral decomposition.

For the situation at hand, $n = 2$ holds, and the previous formula simplifies. Suppose $\boldsymbol{p}$ is a random variable uniformly distributed on the unit circle S^1. Then, by the scaling identity, the random variable (3.15),

$$\boldsymbol{p} = \frac{\boldsymbol{Aq}}{\|\boldsymbol{Aq}\|} \tag{4.2}$$

is ψ_B-distributed. Thus, surprisingly, for the planar exact closure approximation we do not need to determine the matrix $\boldsymbol{B}$ to transform a uniform distribution to the ACG distribution.
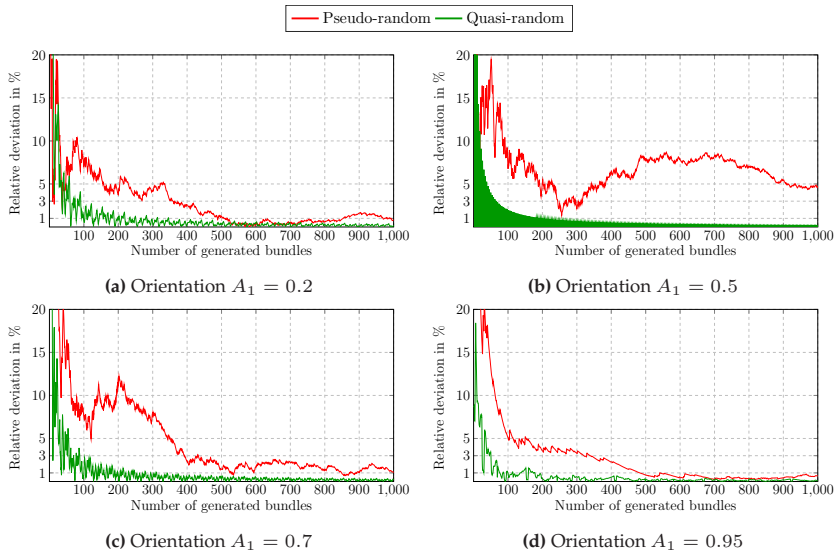
Figure 4.4: Accuracy of generated orientation

With this insight at hand we would be able to generate bundle directions by sampling from a uniform distribution on the unit circle, or, equivalently, on the interval $[0, 1]$. Such a method would be similar to the method Chen et al. (2018b) use, with the additional benefit of using the exact closure of Montgomery-Smith et al. (2011). To improve the convergence rate of this Monte-Carlo-type sampling, we use the low-discrepancy sequence introduced by Sobol' (1967) for drawing points in $[0, 1]$.

To illustrate the increase in accuracy, relative deviations based on the Frobenian norm between the desired second-order OT and the realized OT of a generated unit cell are shown in Fig. 4.4. In the diagrams, several desired orientations, represented by the largest eigenvalue A_1 of the second-order OT A, are investigated, together with a single stochastic realization.

Quasi-random sampling leads to a more-or-less monotonic decrease of the error for increased number of bundles. In contrast, for pseudo-random sampling, the error may be strongly non-monotonic. Furthermore, the reached accuracy for quasi-random sampling is much higher than for pseudo-random sampling, in accordance to theory.

4.3 Computational setup

4.3.1 Implementation, soft- and hardware

The SMC unit cell generator (Sec. 4.2) was implemented in Python 2.7 with Cython extensions. For the full-field simulations, we rely upon a fast Fourier-transform based computational micromechanics code, as described by Schneider (2018), using the staggered grid discretization (Schneider et al., 2016b) and the conjugate gradient method of Zeman et al. (2010). The computations ran on 6 threads on a desktop computer

with 32 GB RAM and an Intel i7-8700K CPU with 6 cores and a clock rate of 3.7 GHz.

The maximum runtime for a voxel mesh size of $1500 \times 1500 \times 42$ voxels ($\approx 95 \cdot 10^6$ voxels) was about $6 \cdot 5 \min = 30 \min$ for computing all components of the effective stiffness. The average run time on a voxel mesh with $750 \times 750 \times 21$ voxels ($\approx 12 \cdot 10^6$ voxels) was about $6 \cdot 30 \mathrm{\,s} = 3 \min$. The mean runtime in order to generate a unit cell with a bundle volume fraction of $c_B = 50\%$ was about $3 \mathrm{\,s}$ to $10 \mathrm{\,s}$.

Our approach is exemplified in Fig. 4.5, where both a generated SMC microstructure and the local von Mises equivalent strain and stress fields are shown for a uniaxial in-plane extensional experiment. Apparently, the fiber bundles pointing in loading direction carry the load, whereas the stress is much lower in the other bundles. Strain concentrations arise at the fiber bundle tips, but appear not to be very pronounced.

(a) Generated microstructure   (b) Local von Mises strain field   (c) Local von Mises stress field
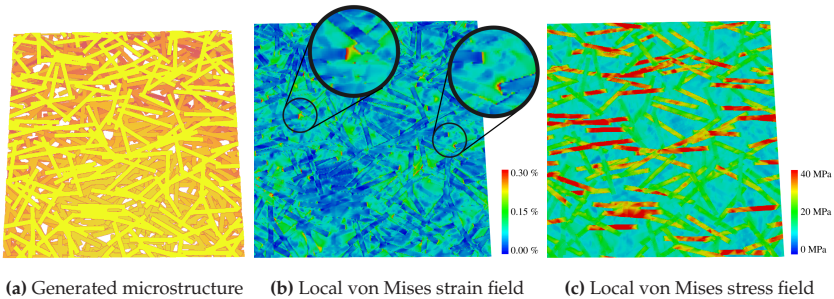
Figure 4.5: Generated SMC microstructure and computed local strain/stress fields for 0.1% applied tensile strain in horizontal direction

4.3.2 Elastic properties of the constituent phases and the bundles

The isotropic phase properties of the considered UPPH matrix resin system (Bücheler, 2018) and E-glass fibers are listed in Tab. 4.1. We computed the transversely isotropic fiber bundle properties via two different complementary methods. On the one hand we used numerical full-field homogenization of a representative bundle containing 225 unidirectionally aligned fibers with a fiber volume content within a bundle of $c_{FB} = 50\%$, see Sec. 4.2.1. A bundle volume fraction of $c_B = 50\%$ in combination with $c_{FB} = 50\%$ yields the corresponding fiber volume fraction of $c_F = 25\%$ as presented in Sec. 4.2.1. On the other hand, we used an orientation averaged mean-field estimate of Mori-Tanaka type (Mori and Tanaka, 1973; Duschlbauer et al., 2003), as described in Sec. 2.1.4 of Brylka (2017). Both methods lead to approximately the same transversely isotropic properties of the fiber bundles. These computed elastic engineering constants, with "L" standing for longitudinal and "T" for transverse, are listed in Tab. 4.1.

Table 4.1: Elastic material parameters for the considered SMC composite

E-glass fibers (Kehrer et al., 2018)	UPPH matrix (Kehrer et al., 2018)	Fiber bundles
$E_{F,iso} = 72$ GPa	$E_{M,iso} = 3.4$ GPa	$E_{B,L} = 37.73$ GPa
		$E_{B,T} = 10.33$ GPa
$\nu_{F,iso} = 0.22$	$\nu_{M,iso} = 0.385$	$\nu_{B,TT} = 0.477$
		$\nu_{B,LT} = 0.292$
$G_{F,iso} = 29.51$ GPa	$G_{M,iso} = 1.23$ GPa	$G_{B,TT} = 3.58$ GPa
		$G_{B,LT} = 3.64$ GPa

4.3.3 On isotropic, transversely isotropic and orthotropic approximations of the effective elastic properties of the SMC composite

Using fast Fourier transform based computational micromechanics enables computing the effective stiffness tensor for a generated SMC unit cell. Interpreting the 21 resulting constants may be cumbersome, in general. As we always align the axes of the unit cell with the principal axes of the OT, it may be tempting to rely upon an orthotropic approximation of the computed effective elastic tensor, and to interpret the associated engineering constants instead (see, e. g., Cowin (1985) or Böhlke (2001)). In this paragraph, we investigate numerically whether this is plausible, also including the isotropic and transversely isotropic approximation errors.

As presented in Sec. 4.3.2, we use a fiber volume fraction of $c_F = 25\,\%$ and a corresponding bundle volume fraction of $c_B = 50\,\%$, as well as the phase and bundle properties listed in Tab. 4.1 for the considered SMC composite. The underlying unit cell parameters are listed in Tab. 4.2. A detailed and structured derivation of these parameters is presented in Sec. 4.3.4.

For this study, we varied the A_1 component of the planar second-order OT $\boldsymbol{A}$, as presented in Eq. (3.8). We implemented approximations for several classes of anisotropy, cf. Browaeys and Chevrot (2004). The resulting relative approximation errors of the stiffness matrices in Voigt-Mandel notation using the Frobenian norm depending on the orientation of the unit cell is shown in Fig. 4.6. Furthemore, representative plots of the Young's modulus of the effective stiffness following Böhlke and Brüggemann (2001) are included.

Not surprisingly, an isotropic approximation of the elastic properties of an SMC composite is very inaccurate, leading to a minimum error of $17\,\%$. Instead, an orthotropic approximation of the SMC composite
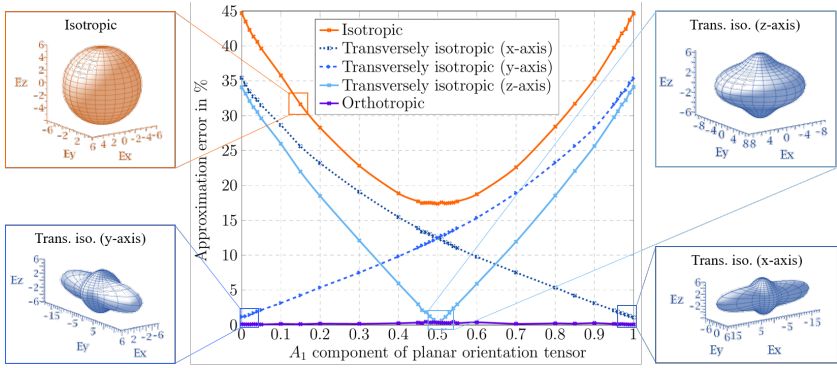
Figure 4.6: Comparison of different approximations for the effective stiffness of SMC composites, including some exemplary Young's modulus plots

stiffness tensor leads to an approximation error of less than 1%, regardless of the orientation. For particular orientations, namely unidirectional orientation of all bundles in x-direction, in y-direction and a planar isotropic orientation in the z-plane, the effective stiffness of the unit cell is transversely isotropic. Depending on the orientation, the transversely isotropic axis switches from the y-axis to the z-axis to the x-axis.

Throughout the following sections, we will analyze the transversely isotropic parameters E_{L}, E_{T}, G_{TT}, G_{LT}, ν_{TT} and ν_{LT} (Boehler, 1987), if possible. Hereby, "L" indicates the longitudinal and "T" the transverse direction. Otherwise, we will consider the orthotropic elastic parameters. We adapt the commonly used engineering notation E_{x}, E_{y}, E_{z}, G_{yz}, G_{xz}, G_{xy}, ν_{yz}, ν_{xz}, ν_{xy}, ν_{zy}, ν_{zx} and ν_{yx} (Boehler, 1987). Accordingly, we have $1 \mathrel{\hat{=}} x$, $2 \mathrel{\hat{=}} y$ and $3 \mathrel{\hat{=}} z$ w. r. t. the introduced notation. For the sake of completeness, we use 6 transversely isotropic parameters and 12 orthotropic parameters.

4.3.4 Determining the proper resolution, bundle aspect ratio as well as unit cell size and thickness
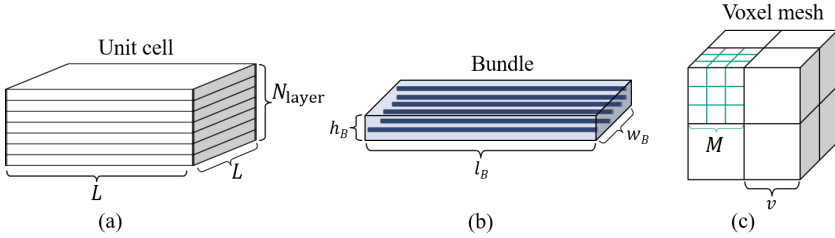
Figure 4.7: Geometric parameters needed to ensure representativity of the unit cell, (a) unit cell dimensions, (b) bundle dimensions, (c) voxel mesh size

To ensure reproducibility of the computational results, several sources of errors need to be taken care of, cf. Fig. 4.7.

1. For fixed geometry, the resolution needs to be sufficiently fine to approximate the "continuous" results to sufficient precision. The geometry produced by the bundle deposition method of Sec. 4.2 is naturally given on a voxel grid. To study the influence of the resolution, we introduce a positive integer M which we call amplification factor. For given $M \geq 1$, each original voxel is subdivided into M^3 congruent voxels for the numerical investigations.

2. For fixed microstructural parameters and sufficient resolution, the unit cell needs to be large enough to capture the statistical variation and the length correlation of the inclusions. Such unit cells are called representative volume elements (RVEs), cf. Gusev (1997). For the problem at hand, we need to investigate the dependence of effective elastic properties on the in-plane length $L_x = L_y = L$ and the number of layers N_{layer} (encoding the out-of-plane size).

3. For short fiber reinforced composites, it is known that the effective elastic properties saturate (Sun and Vaidya, 1996) for increasing aspect ratio, i. e., the quotient of fiber length and diameter. Thus, for computational purposes it is often sufficient to work with fibers that are much shorter than in reality. A natural strategy to determine this length is by successively increasing the fibers' aspect ratio until the effective elastic properties do not change significantly any more.

   For the SMC microstructures at hand, we follow a similar strategy. From µCT images of SMC (Le et al., 2008), such as Fig. 4.1a (see also Fig. 4.16a), we get a good estimate for the dimensions of a bundle's cross section, i. e., the bundle width w_B and height h_B. However, the aspect ratio l_B/w_B, where l_B denotes the bundle length, appears rather large. In general, the bundle aspect ratio of length to width varies approximately between $l_B/w_B \approx 15 - 45$, normalized w. r. t. the height h_B. Thus, we investigate whether a smaller effective bundle aspect ratio is sufficient.

Notice that effective elastic properties computed on a unit cell are independent of the unit cell length scale, i. e., there is no internal length scale present in the effective properties. Thus, the absolute length scale of the microstructure does not matter. Instead, relative length scales are of importance, i. e., the unit cell dimensions relative to the bundle dimensions, or the voxel size compared to the bundle size. For the investigation at hand, we choose the voxel size v initially produced by the bundle deposition method, cf. Fig. 4.2, as our basic length unit.

Determining the various parameters satisfying all three stated requirements involves an iterative process based, to some extent, on trial and error. For the purpose of presentation, we chose a set of "typical" parameters resulting from such an iterative process and show, by means of sensitivity studies, that their values ensure representative mechanical results (within engineering accuracy).

We consider a bundle volume fraction of $c_B = 50\%$ as well as a planar isotropic orientation with $A_1 = 0.5$, representing an SMC microstructure frequently encountered in our application. To study the influence of the in-plane length L, the effective transversely isotropic engineering constants of an SMC composite are shown in Fig. 4.8, measured in the edge length of the original voxels, as discussed above. For the investigation, all remaining parameters were kept constant at $N_{\text{layer}} = 7$, $l_B = 50$ voxels, $w_B = 5$ voxels and $h_B = 1$ voxel with a mesh resolution amplification factor of $M = 3$, using the phase properties given in Tab. 4.1. Fig. 4.8 contains both absolute values and relative errors, computed relative to the result computed at highest in-plane length considered.

(a) Absolute values $\qquad$ (b) Relative errors
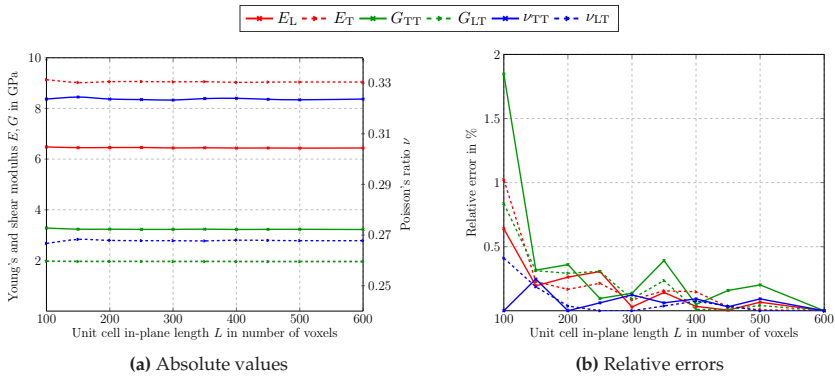
Figure 4.8: Effective transversely isotropic engineering constants computed on unit cells with increasing in-plane length L for a planar isotropic orientation distribution

Even for the lowest in-plane-length of 100 voxels, the engineering constants deviate less than 2% from their "converged" counterparts. We see that an in-plane length of $L = 150$ voxels is sufficient for ensuring a relative error less than 0.5% for all engineering constants and the chosen

geometric parameter set. Put differently, it suffices to work with a unit cell length which is three times the bundle length to obtain representative results. To ensure a degree of flexibility, we chose the unit cell in-plane length as $L = 250$ voxels.

Similar studies were conducted to determine the necessary resolution and the magnitude of the remaining geometric parameters, the layer count N_{layer} and the bundle aspect ratio $l_{\text{B}}/w_{\text{B}}$, which ensure representativity of the unit cells and the ensuing computational results. Fig. 4.9 contains the corresponding graphs for increasing amplification factor, layer count and bundle aspect ratio. The determined parameter values ensuring representative effective elastic properties are listed in Tab. 4.2.

| (a) Resolution study | (b) Layer count | (c) Bundle aspect ratio |
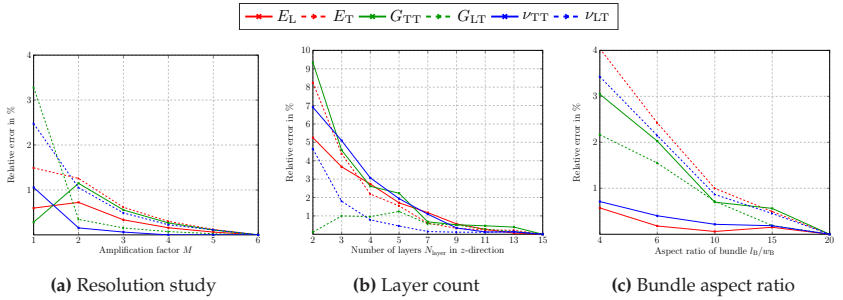
Figure 4.9: Relative error diagrams for increasing resolution, layer count and bundle aspect ratio

In accordance with Tab. 4.2, for bundle dimensions to $50 \times 5 \times 1$ voxels, a planar orientation state $A_1 = 0.5$ and a bundle volume fraction of $c_{\text{B}} = 50\,\%$, a relative error less than $1\,\%$ is ensured by choosing $M \geq 3$, cf. Fig. 4.9a.

To minimize the influence of the unit cell dimensions on the computed effective stiffness, for studying the necessary bundle aspect ratio we choose the dimensions as $L \times L \times N_{\text{layer}} = 500 \times 500 \times 7$ voxels with

an amplification factor of $M = 3$. The orientation remains planar isotropic $A_1 = 0.5$ and the bundle volume fraction is $c_B = 50\%$. For an aspect ratio of 10 and higher, the relative error is less than 1% and the effective elastic parameters do not change significantly, as we can observe in Fig. 4.9c. Therefore we choose said aspect ratio of $l_B/w_B = 10$. Thus, bundles with smaller aspect ratio than for real SMC microstructures suffice. As discussed in Sec. 4.3.4, in SMC composites, the typical bundle aspect ratio range from approximately 15 to 45.

Depending on the manufacturing process, the amount of processed material and the geometrical specifications of the component, the number of layers N_{layer} of a SMC composite varies. The μCT scan in Fig. 4.1a shows a number of layers N_{layer} of about 15 to 25. The question arises whether we need to take into account all layers in order to correctly predict the effective stiffness. For this last study, we use a unit cell in-plane length of $L = 250$ voxels, bundle dimensions of $l_B \times w_B \times h_B = 50 \times 5 \times 1$ voxels and an amplification factor of $M = 3$. The orientation distribution is planar isotropic $A_1 = 0.5$ in each layer and the bundle volume fraction is set to $c_B = 50\%$. For $N_{\text{layer}} = 7$ layers or more, the effective elastic parameters barely change, cf. Fig. 4.9b, i. e., we ensure a relative error not exceeding 1%.

Table 4.2: Geometric parameters chosen to ensure representativity of the generated unit cells and the typical parameters of the considered unit cells

Unit cell dimensions	$L \times L \times N_{\text{layer}}$	$250 \times 250 \times 7$ voxels
Bundle dimensions	$l_B \times w_B \times h_B$	$50 \times 5 \times 1$ voxels
Amplification factor	M	3
Fiber volume fraction	c_F	25%
Bundle volume fraction	c_B	50%
Fiber fraction in bundle	c_{FB}	50%
Orientation	$\boldsymbol{A} \mathrel{\hat{=}} \text{diag}(A_1, A_2)$	$A_1 = A_2 = 0.5$

4.4 Multiscale simulation-based studies of effective elastic properties

4.4.1 Influence of volume fraction

In this section we rely upon the material and geometric parameters fixed in Tab. 4.1 and Tab. 4.2. For the sensitivity analysis, we modify material parameters such as the orientation (by varying the A_1 component of the second-order OT A), the volume fraction c_B, as well as the elastic properties of matrix E_M, ν_M and fibers E_F, ν_F. Comparing the resulting effective elastic parameters helps distinguishing important properties from unimportant factors. Due to the multitude of parameters entering, the latter is crucial for improving corresponding experimental setups, for instance.

(a) Effective engineering constants

(b) Relative deviation to $c_B = 50\,\%$
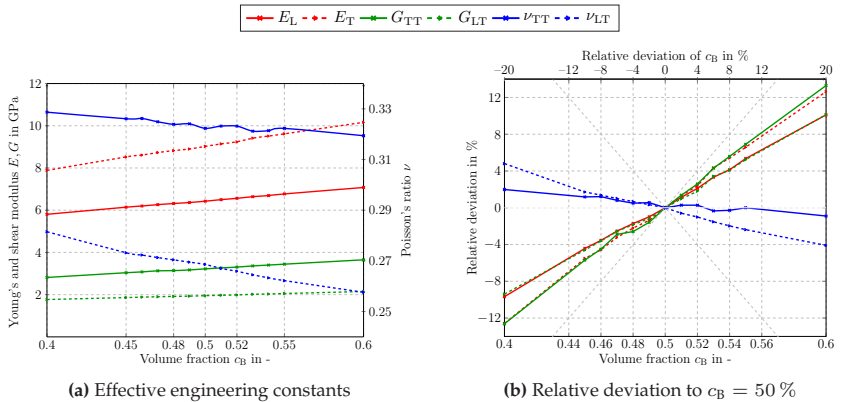
Figure 4.10: Computed effective engineering constants depending on the volume fraction for $c_B \in [40\,\%, 60\,\%]$

First, we computed the effective elastic parameters with varying volume fraction c_B. We chose a planar isotropic orientation, i.e., $A_1 = 0.5$.

Thus, the effective stiffness tensor is transversely isotropic w. r. t. the z-direction. For volume fractions ranging from $c_B = 40\,\%$ to $c_B = 60\,\%$, the corresponding effective engineering constants are plotted in Fig. 4.10. These computed stiffnesses parameters are shown in Fig. 4.10a. We see that all considered effective engineering constants depend linearly on the volume fraction. Clearly, ν_{TT} exhibits small oscillations in the considered volume fraction range. This is caused by the definition of the Poisson's ratio in terms of a quotient of fitted parameters.

To quantify the influence of changing the volume fraction, we consider volume fraction $c_B = 50\,\%$ as our reference and compare the relative deviations of the effective elastic parameters with respect to the results computed for the reference volume fraction. The computed deviations are shown in Fig. 4.10b, where the top horizontal axis shows the relative deviation of the actual volume fraction c_B from the reference volume fraction. On the vertical axis we see the corresponding relative deviations of the effective transversely isotropic engineering constants from the ones we get for $c_B = 50\,\%$. The identity lines are shown in dashed gray. The effective Young's and shear moduli are rather sensitive to a change of volume fraction. For a deviation of $\pm2\,\%$, the shear moduli differ by slightly less than $\pm2\,\%$, and for a variation of volume fraction by $\pm5\,\%$, the Young's and shear moduli are changed by about $\pm4\,\%$. In contrast, the Poisson's ratios are less sensitive to a deviation in volume fraction. Indeed, for $\pm5\,\%$ change in volume fraction, Poisson's ratio is only changed by $\pm2.5\,\%$ at most.

The volume fraction is typically considered to be the microstructural parameter with the highest influence on the effective elastic properties of fiber reinforced composites. We can confirm that by our computational experiments.

4.4.2 Influence of orientation state

In analogy to the previous section, we study the dependence of the effective elastic constants on the orientation. For this investigation, we consider all planar orientation states that may be described by the second-order OT A, parameterized by the diagonal component A_1. As already discussed in Sec. 4.3.3, these orientations vary from unidirectional in x-direction via planar isotropic in the z-plane to unidirectional in y-direction.

We plot the effective orthotropic engineering parameters in dependence of A_1 in Fig. 4.11a. In accordance with our observations from Sec. 4.3.3, some of the orthotropic parameters coincide for the mentioned special orientation states $A_1 = 0.0$, $A_1 = 0.5$ and $A_1 = 1.0$, leading to a transversely isotropic behavior.

(a) Orthotropic effective engineering constants   **(b)** Zoom on the shear moduli G_{xz} and G_{yz}
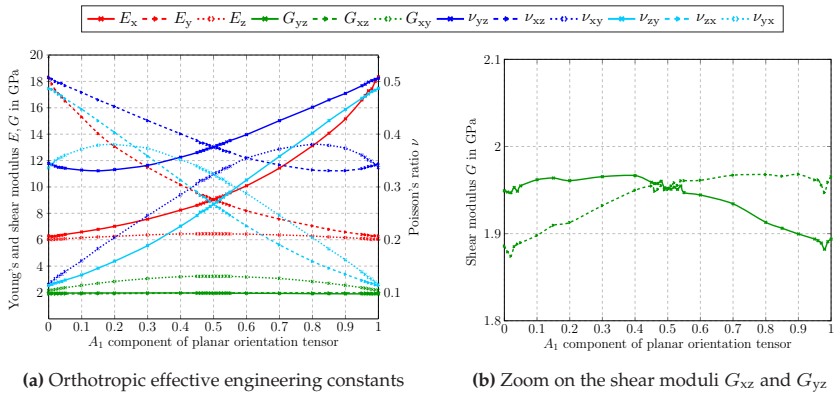
Figure 4.11: Computed effective engineering constants depending on the orientation

A few effective engineering constants are largely independent of the orientation, e. g., E_z, G_{yz}, G_{xz}, whereas others change significantly, e. g., E_x, E_y, ν_{yz}, ν_{xy}. The functional dependence of the elastic parameters

on A_1 is approximately quadratic. A first glance at Fig. 4.11a suggests that G_{xz} and G_{yz} coincide for any orientation. However, at second glance, cf. Fig. 4.11b, we see that both parameters actually differ, by almost 5% at $A_1 = 0$. However, due to the smallness of G_{xz} and G_{yz} relative to the other engineering constants, Fig. 4.11a conveys the wrong visual impression.

To investigate the orientation influence in greater detail, we limit the orientation states to a range of $A_1 \in [0.3, 0.7]$, cf. Fig. 4.12. We are concerned with the sensitivity of the effective elastic properties w. r. t. small deviations of $A_1 = 0.5$.

The effective elastic parameters for the given range are shown in Fig. 4.12a. The signed relative deviations are shown in Fig. 4.12b. On the bottom horizontal axis we see the A_1 component of the second-order OT $\boldsymbol{A}$. We consider a planar isotropic orientation with $A_1 = 0.5$ to be correct. On the top horizontal axis the relative deviation of the actual orientation component A_1 from the planar isotropic value $A_1 = 0.5$ is shown. On the vertical axis we see the corresponding relative deviations of the orthotropic effective engineering constants from the ones we have in the planar isotropic case $A_1 = 0.5$. The identity lines are shown in dashed gray.

In the vicinity of the reference orientation, the engineering constants are approximately linear functions of the orientation tensor component A_1. In accordance to our observations in Fig. 4.11, an absolute deviation of the orientation of about ± 0.01, which corresponds to a relative deviation of $\pm 2\%$, has almost no influence on certain engineering constants, such as the shear moduli or E_z. For the remaining engineering constants we observe a change of up to $\pm 2.0\%$. Absolute deviations of ± 0.02 and ± 0.05 lead to changes in the engineering constants of up to $\pm 3.5\%$ and $\pm 8.5\%$, respectively.

Thus, we see that the influence of the fiber orientation on the effective elastic tensor is of the same order of magnitude as the influence of

(a) Orthotropic effective engineering constants   **(b)** Relative deviation to $A_1 = 0.5$
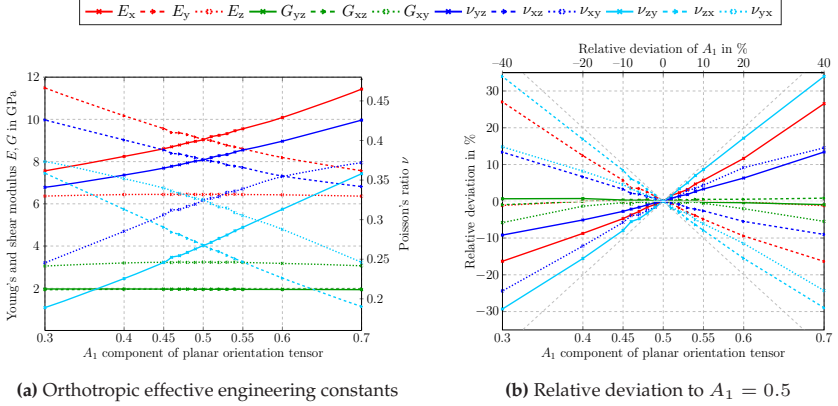
Figure 4.12: Computed effective engineering constants depending on the orientation for $A_1 \in [0.3, 0.7]$

the volume fraction. This contrasts with observations for short fiber reinforced composites (Schneider, 2017), where the influence of the fiber orientation is less pronounced.

4.4.3 Influence of matrix properties

In this section we investigate the influence of the (isotropic) elastic properties E_M and ν_M of the matrix resin on the effective elastic properties of the SMC composites. For this purpose, the transversely isotropic elastic constants of the bundles need to be recomputed, as discussed in Sec. 4.3.2, for each new set of matrix properties. Subsequently, the corresponding effective stiffness of the SMC composite unit cell is computed using the resin moduli and the corresponding updated bundle properties.

The effective elastic parameters resulting from a variation of the matrix' Young's modulus are shown in Fig. 4.13a. For a parameter range of $E_M \in [2.4\,\text{GPa}, 4.4\,\text{GPa}]$, the dependence of the effective Young's and shear moduli on the matrix' Young's modulus is approximately linear,

cf. Fig. 4.13a, whereas the effective Poisson's ratios depends on the matrix' Young's modulus in a nonlinear fashion. However, the relative deviations of the effective Poisson's ratios are comparatively small.

Quantitatively, an absolute change of the matrix' Young's modulus by ± 0.1 GPa, which corresponds to $\pm 3\%$, leads to a variation of the elastic parameters of 0.2% - 2.7%. For a change by ± 0.2 GPa, a deviation of the elastic parameters of 0.4% - 5.5% is induced. For an alteration of ± 0.3 GPa in E_{M}, which is $\pm 9\%$, a deviation of the elastic parameters of 0.6% - 8.5% follows.

(a) Variation of Young's modulus E_{M} (b) Variation of Poisson's ratio ν_{M}
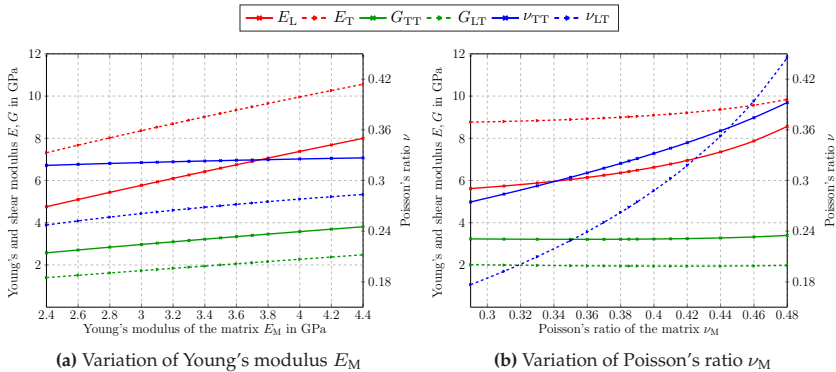
Figure 4.13: Computed effective engineering constants depending on the matrix' isotropic elastic parameters

The connection between the effective elastic parameters and the matrix' Poisson's ratio are plotted in Fig. 4.13b. Apparently, the effective shear moduli are almost independent of the matrix' Poisson's ratio, cf. Fig. 4.13b. In contrast, the longitudinal Young's modulus E_{L} and the Poisson's ratios are very sensitive to a change of the matrix Poisson's ratio ν_{M}, in particular close to incompressible matrix behavior at $\nu_{\mathrm{M}} = 0.5$.

We see that the in-plane Young's modulus E_T varies by about 0.5 GPa by changing ν_M from 0.3 to 0.4. In contrast, the out-of-plane Young's modulus E_L changes by 1 GPa. Thus, we see that if the in-plane Young's modulus is of primary concern, ν_M does not need to be determined to high precision.

4.4.4 Influence of fiber properties

In this section, we study the dependence of the effective elastic parameters on the isotropic elastic moduli of the fiber. Similarly to Sec. 4.4.3, we recompute the bundle properties when changing fiber properties. The sensitivity of the effective parameters w. r. t. Young's modulus E_F is shown in Fig. 4.14a. The effective elastic parameters depend approximately linearly on E_F. Both the effective Young's moduli and shear moduli increase for increasing fiber Young's modulus E_F, whereas the effective Poisson's ratios exhibit a decreasing behavior, similar to Sec. 4.4.1. Compared to the previous sections, the effective elastic parameters are comparatively insensitive to variations of the fiber Young's modulus E_F, in general. For instance, a deviation of the fibers' Young's modulus by ± 1 GPa leads to a deviation of the elastic parameters of $0.1\,\%$ - $0.7\,\%$.

Furthermore, we investigate the dependence of the effective elastic parameters on the Poisson's ratio of the fibers ν_F in Fig. 4.14b. The Young's and shear moduli remain almost constant within the entire considered range of ν_F. The effective Poisson's ratios increase linearly with increasing fiber Poisson's ratio ν_F. To quantify the latter observation, deviating from the reference Poisson's ratio $\nu_F = 0.22$ by ± 0.04, i. e. $\pm 18.2\,\%$, leads to a deviation of the elastic parameters of $0.2\,\%$ - $1.5\,\%$.

(a) Variation of Young's modulus E_F

(b) Variation of Poisson's ratio ν_F
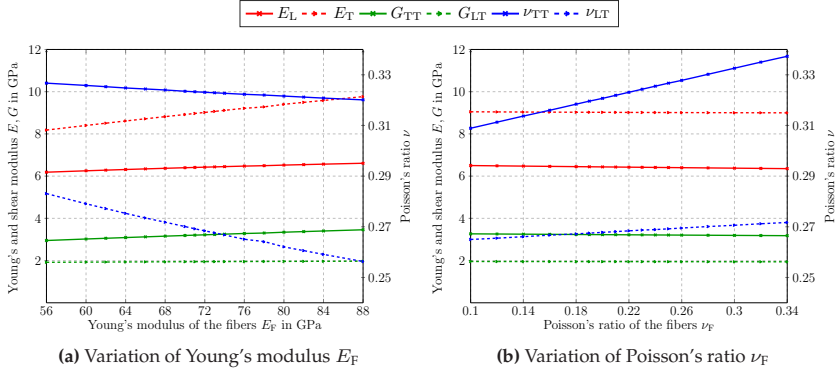
Figure 4.14: Computed effective engineering constants depending on the fibers' isotropic elastic parameters

4.4.5 Comparison to mean-field estimates and full-field computations on a µCT image

In the first part of this section, we compare our computational multiscale approach to a simple mean-field estimate, as used for instance in Schemmann et al. (2018b) for the modeling of SMC composites. More precisely, we compute the effective elastic parameters based on the Mori-Tanaka mean-field method (Mori and Tanaka, 1973). Following the approach of Benveniste (1987) as presented in Brylka (2017) we use the expression

$$
\mathbb{C} = \mathbb{C}_\mathrm{M} + c_\mathrm{F} \left(c_\mathrm{M} \left\langle \left(\mathbb{P}_0 + (\mathbb{C}_\mathrm{F} - \mathbb{C}_\mathrm{M})^{-1} \right)^{-1} \right\rangle_\mathrm{F}^{-1} + c_\mathrm{F} \left(\mathbb{C}_\mathrm{F} - \mathbb{C}_\mathrm{M} \right)^{-1} \right)^{-1}
\tag{4.3}
$$

for the effective Mori-Tanaka stiffness tensor $\mathbb{C}$. Here, $\mathbb{P}_0 = \mathbb{E}_0 \mathbb{C}_\mathrm{M}^{-1}$ denotes the the polarization tensor (Ponte Castañeda and Suquet, 1998), where $\mathbb{E}_0$ is Eshelby's tensor (Eshelby, 1957; 1959). The orientation averaging $\langle \cdot \rangle_\mathrm{F}$ can be expressed solely in terms of OTs of second- and

fourth-order, cf. Advani and Tucker (1987). For given second-order OTs, the exact closure approximation, as presented in Sec. 3.4, and the material properties in Tab. 4.1, we compute the Mori-Tanaka estimates for a variation of the orientation state in analogy to Sec. 4.4.2.

Taking a look at the effective orthotropic elastic parameters, cf. Fig. 4.15a, reveals a good qualitative agreement of the Mori-Tanaka predictions with the full-field results of Fig. 4.12a.

(a) Effective engineering constants predicted by Mori-Tanaka approach

(b) Relative deviation between Mori-Tanaka and full-field results
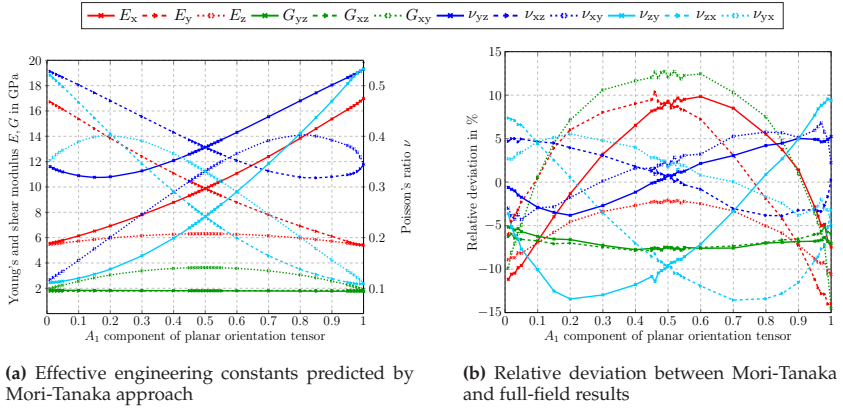
Figure 4.15: Computed effective orthotropic engineering constants based on Mori-Tanaka mean-field approximation for varying orientation

Relative errors of the effective Mori-Tanaka moduli, normalized with the full-field homogenization results are shown in Fig. 4.15b. For the majority of orientations and moduli, the relative deviations do not exceed $\pm 7\%$. However, the in-plane shear modulus and two of the six Poisson's ratios lead to higher errors up to $\pm 14\%$. In particular close to the planar isotropic fiber orientation state the in-plane shear modulus differs strongly.

We wish to highlight the differences in the approaches used. For the full-field computation, transversely isotropic bundles are embedded into an isotropic matrix, whereas the Mori-Tanaka approximation accounts for the E-glass fiber reinforcement on the single fiber level, and is insensitive to the formation of bundles.

Similar to the full-field studies concerning variations of volume fraction as well as the matrix and the fiber properties, a comparison of the Mori-Tanaka mean-field results to corresponding full-field results were conducted. However, the results are similar in trend and magnitude to the study presented. For the sake of brevity, we chose not to include those here.

To validate whether the bundle deposition methods described in Sec. 4.2 captures the essential geometric features of SMC composites, we wish to compare the SMC unit cells generated for this work to micro-computed tomography (μCT) scans of SMC composites in terms of the effective computed properties. However, the microstructure of SMC is very challenging in that regard. On the one hand it is necessary to consider a sufficiently large volume to encompass the very long fibers. On the other hand, for the computational procedures to work, it is not only necessary to separate individual fibers but to leave enough space between the fibers to accurately predict the mechanical deformation of the resin in between. Unfortunately, satisfying these two prerequisites simultaneously is extremely challenging.

For the work at hand, a $1004 \times 1024 \times 1016$ X-ray microscopy scan of a specimen of E-glass fiber reinforced UPPH, as detailed in Sec. 4.2.1, serves as the basis of our discussion. The original grey-value image was cropped and binarized, resulting in a $900 \times 700 \times 500$ voxel image. Unfortunately, computing directly on such a binarized image is not possible. Indeed, a closer look at Fig. 4.1a shows that within the fiber bundles, distinguishing individual fibers is not possible. As a work-around, we approximate the bundle structure by thickening the fibers

of the original µCT image by mathematical morphological operations (Haralick et al., 1987), which leads to a clustering of the fibers to bundles. The resulting unit cell is shown in Fig. 4.16a. The fiber thickening has the positive side-effect that it is possible to coarsen the resolution by a factor of 2, and still get almost identical effective elastic properties. Thus, for the succeeding, we work with a resolution of $450 \times 350 \times 250$ voxels.

(a) Geometry used based on a µCT scan of a SMC composite unit cell

(b) Frobenian norm of stress (in MPa) distribution for 0.5 % uniaxial extension in x-direction
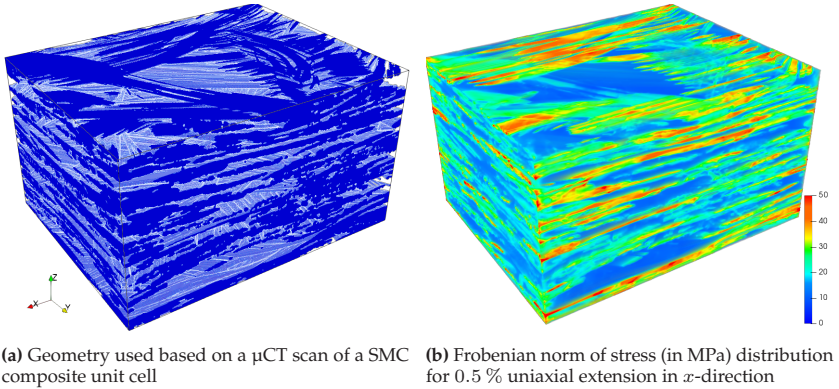
Figure 4.16: Computation of the effective stiffness based on a µCT scan of a SMC composite unit cell of $450 \times 350 \times 250$ voxels

We analyzed the fiber orientation in the volume using the star length algorithm (Smit et al., 1998) applicable to binarized voxel images to arrive at a second-order OT of

$$\boldsymbol{A} \mathrel{\hat{=}} \begin{bmatrix} 0.533 & -0.074 & -0.001 \\ -0.074 & 0.427 & 0.008 \\ -0.001 & 0.008 & 0.040 \end{bmatrix}. \tag{4.4}$$

We notice that the OT is strongly diagonally dominant, indicating that the cell axes are well-aligned with the principal axes of the OT. Furthermore, the orientation is close to planar in the x-y-plane, as the zz-component

of A is only $4\,\%$, in agreement with visual impression. Last but not least, we notice that about $25\,\%$ more fibers are directed into the machine direction x as compared to the cross direction y.

The thickening of the fibers leads to an artificial increase of the fiber volume fraction c_F, which we consider as a bundle volume fraction $c_B = 64.61\,\%$, which is larger than the $c_B = 50\,\%$ we use for the generated cells. To maintain an overall fiber volume fraction of $c_F = 25\,\%$, we adjusted the fraction of fibers within a bundle to $c_{FB} = 38.69\,\%$, leading to the transversely isotropic elastic parameters for the bundles in Tab. 4.3.

Table 4.3: Mesoscopic elastic parameters used for the μCT computation

$E_{B,L}$	$E_{B,T}$	$\nu_{B,TT}$	$\nu_{B,LT}$	$G_{B,TT}$	$G_{B,LT}$
27.3 GPa	7.32 GPa	0.51	0.31	2.42 GPa	2.58 GPa

Furthermore, we use the structure tensor of Krause et al. (2010) for determining the direction of the bundles. The elastic parameters for the bundles in Tab. 4.3 and the resin properties in Tab. 4.1 serve as the basis for computing the effective elastic parameters of the SMC composite unit cell shown in Fig. 4.16a. The stress field for uniaxial loading in x-direction is shown in Fig. 4.16b. Bundles which are aligned in loading direction bear the highest stresses, whereas bundles perpendicular to the loading direction bear the lowest stresses. The resulting effective orthotropic engineering constants are collected in Tab. 4.4.

We see that an orthotropic approximation of the effective elastic tensor is quite accurate. Furthermore, the diagonal components of the OT (4.4) translate into the relative magnitudes of the directional Young's moduli. The Young's modulus E_x in machining direction x slightly exceeds the transverse Young's modulus E_y. The Young's modulus in out-of-plane direction E_z takes a value that is only about $2/3$ of E_x. The out-of-plane

shear moduli are almost equal, with a value about $2/3$ of the in-plane shear modulus G_{xy}. The values of the Poisson's ratios lie within a range of 0.24 and 0.4, showing quite strong variation.

For comparison, we generated an SMC composite unit cell and computed the effective elastic tensor with the multiscale approach proposed in this article. As we can only prescribe two-dimensional orientation states in the bundle deposition algorithm, we chose a diagonal two-dimensional orientation tensor $\mathrm{diag}(A_1, A_2)$, s. t. the quotient A_1/A_2 equals the quotient $A_{\mathrm{xx}}/A_{\mathrm{yy}}$ of the first two diagonal elements of the OT (4.4), i. e., $A_1 = 0.552$ and $A_2 = 0.448$. For the computations, we chose a bundle volume fraction of $50\,\%$ and the bundle elastic moduli of Tab. 4.1, s. t. we arrive at a fiber volume fraction of $25\,\%$ in the end. The generated unit cell and an exemplary stress field according to the μCT scan presented in Fig. 4.16 are shown in Fig. 4.17.
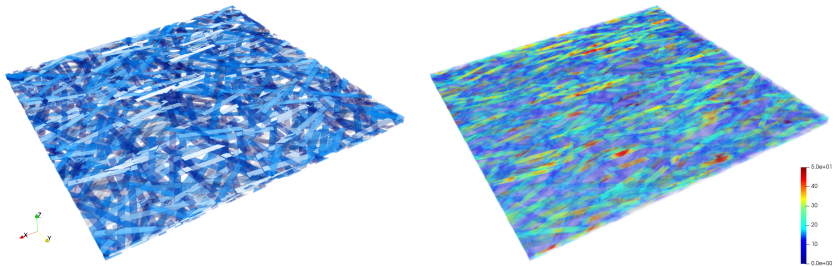
(a) Generated SMC composite unit cell based on the relevant parameters of the discussed μCT scan Fig. 4.17a

(b) Frobenian norm of stress (in MPa) distribution for $0.5\,\%$ uniaxial extension in x-direction

Figure 4.17: Computation of the effective stiffness based on a generated unit cell of $750 \times 750 \times 21$ voxels according to the given μCT scan Fig. 4.17a

The resulting orthotropic moduli are listed in Tab. 4.4. All six Poisson's ratios and the shear moduli match almost perfectly with the full-field simulation results run on the μCT image. The Young's moduli in all directions are slightly overestimated.

Furthermore, we also included the Mori-Tanaka estimates using $25\,\%$ fiber volume fraction and the original orientation tensor (4.4). The mean-field results also overestimate E_x, but recover E_z quite accurately. However, the transverse Young's modulus E_y is strongly overestimated. Similarly, all shear moduli are overestimated compared to the µCT results. However, the predictions of the Poisson's ratios are quite good.

For comparison, we included measurements of the in-plane Young's moduli, obtained by two different groups. Trauth et al. (2017a) investigated E-glass fiber renforced UPPH resin SMC specimens, with a mold coverage of the produced SMC plaques of $100\,\%$. Trauth et al. (2017a) varied the fiber volume fraction c_F between $17\,\% - 31\,\%$. They observed an increase of the resulting tensile Young's modulus E_x from $7.3\,\mathrm{GPa}$ to $12.5\,\mathrm{GPa}$. This observation agrees with our investigations, cf. Sec. 4.4.1. For the comparison at hand, Trauth et al. (2017a) investigated specimens with a fiber volume fractions of $c_\mathrm{F} = 25\,\% \pm 2\,\%$.

Furthermore, we have included the experimental investigations of Kehrer et al. (2018) in Tab. 4.4. They used dynamical mechanical analysis to determine the Young's modulus of E-glass fiber reinforced SMC composite specimen. The fiber volume fraction was roughly $c_\mathrm{F} \approx 25\,\%$ with an unknown uncertainty.

Some care has to be taken when comparing the experimental data to the computational results, because the experiments are conducted on an entire specimen. In particular, some effects concerning the variation of volume fraction and the orientation are averaged out.

The Young's moduli E_x in x-direction measured by the two groups almost coincide, whereas the the Young's moduli E_y in y-direction differ significantly (roughly $1\,\mathrm{GPa}$). However, the variances for E_y are quite large, so that the confidence intervals of both measurements have non-trivial intersection.

All three computational approaches, full-field simulation on a µCT scan, the use of a generated unit cell and the Mori-Tanaka mean-field approach,

Table 4.4: Computed effective elastic parameters for orthortopic stiffness approximation and experimentally measured parameters

	µCT scan	gener. unit cell	Mori-Tanaka	Trauth (2017a)	Kehrer (2018)
E_x in GPa	9.42	9.55	10.02	10.96 ± 0.3	10.92 ± 0.6
E_y in GPa	8.21	8.54	8.82	9.25 ± 1.0	8.28 ± 0.5
E_z in GPa	6.19	6.43	6.18		
G_{yz} in GPa	1.95	1.95	2.03		
G_{xz} in GPa	1.96	1.96	2.06		
G_{xy} in GPa	3.11	3.21	3.5		
ν_{yz}	0.398	0.388	0.407		
ν_{xz}	0.368	0.365	0.379		
ν_{xy}	0.342	0.341	0.341		
ν_{zy}	0.301	0.292	0.289		
ν_{zx}	0.242	0.245	0.234		
ν_{yx}	0.298	0.305	0.300		
e_{approx}^{ortho} in %	3.27	0.32	3.52		
c_F in %	25	25	25	25 ± 2	≈ 25

underestimate the measured E_x. Young's modulus E_y measured by Trauth et al. (2017a) is higher than our computed results, whereas E_y measured by Kehrer et al. (2018) matches quite well.

Due to the high variation in the measured tensile Young's moduli, the significance of the sensitivity studies conducted in this work is highlighted. At present, it is not possible to µCT scan and compute on an entire specimen that is used for experiments. Thus, we are comparing experiments to simulation results with different microstructural parameters, like fiber orientation, and different length scales. Still, we see that for all three computational approaches, the agreement with experiments is reasonable.

4.5   Conclusions

This chapter was devoted to extending the sequential bundle deposition method of Chen et al. (2018b) to be fast, accurate as well as predictive, and to apply the developed methods to a state-of-the art glass fiber reinforced UPPH based SMC composite. Understanding the effective behavior of SMC composites, as well as the underlying influences and corresponding sensitivities, is of central importance for using SMC composites as structural components.

One of our key innovations concerns the use of modern orientation tensor closure approximations, more precisely the exact closure approximation of Montgomery-Smith et al. (2011), and the reliance upon quasi-random numbers for sampling the orientation distribution. We found a simple formula for generating correct two-dimensional angular central Gaussian distribution, based on an explicit expression for the exact closure approximation in two dimensions. For the general, three-dimensional case, no such formula is known (and not expected to exist). The quasi-random sampling strategy enables generating high fidelity unit cells, where prescribed orientation data is matched closely. Defining the orientation tensor layer by layer permits studying the effects of manufacturing and placing the unidirectional bundle tapes, individually.

In our opinion, the principal disadvantage of the sequential bundle deposition method is the disconnection of fiber bundles upon displacing these bundles to the next layer in case of overlap. For the elastic computations, this procedure did not have any negative effect. For inelastic computations, including fiber failure, that may no longer be the case. However, such an investigation is beyond the scope of this work. Furthermore, the curvature of the bundles (Pinter et al., 2016; Schöttl et al., 2021b) is not taken into account, which might have an effect.

In order to perform detailed sensitivity analyses on parameter influences, thousands of accurate microstructures with unambiguous and known parameter values are crucial. Therefore, these analyses cannot be performed on µCT scans of real specimen or unit cells generated based on a slow or inaccurate algorithm. Based upon our improved SMC composite unit cell generator, we were able to conduct detailed sensitivity analyses quantifying the influence of all involved mechanical and microstructural parameters on the effective elastic properties of structural SMC composites. Tab. 4.5 summarizes these influences.

Table 4.5: Sensitivity of effective elastic parameters w. r. t. input parameters. The degree of darkness is proportional to the sensitivity. Numbers indicate the linear correlation in %.

	c_B	E_M	ν_M	E_F	ν_F	A_1
E_L	40	83	75	15	2	4
E_T	48	62	17	37	1	60
G_{TT}	54	65	3	33	3	6
G_{LT}	42	90	8	7	1	6
ν_{TT}	12	5	75	7	8	70
ν_{LT}	16	22	183	22	3	90

As an overview, a table containing the degree of sensitivity of the effective elastic properties on the input parameters is included, cf. Tab. 4.5. For an observable quantity q, the sensitivity s w. r. t. an input parameter p is defined via

$$q(p + \Delta p) \approx q(p)[1 + s\Delta p], \quad \text{i. e.,} \quad \frac{q(p + \Delta p) - q(p)}{q(p)} \approx s\Delta p. \quad (4.5)$$

The numbers shown in Tab. 4.5 are computed from the figures in this chapter at $\Delta p/p = 5\%$, e. g., Fig. 4.10b. The coloring of the cell is directly linked to the correlation. The darker the cell, the higher the sensitivity of

the corresponding effective stiffness parameter to a change in the input parameter.

We see that the elastic moduli of the matrix have a very strong influence on all considered elastic parameters. Also, as expected the fiber volume fraction is of principal importance. Similarly, the fiber orientation plays a major role for some selected elastic properties. Interestingly, for instance, the degree of fiber orientation has little influence on E_L, but a strong influence on E_T. This might explain the differences between the two experimental results of Tab. 4.4.

Depending on the structural application and the subjected load, different elastic parameters are of principal interest. With the conducted sensitivity analyses and the overview Tab. 4.5 at hand, we have a matrix weighting influences of the microstructural and geometrical parameters at our disposal. Thus, we may focus on determining important parameters precisely, relying upon rough estimate for the less important ones. Detailed knowledge of these sensitivities summarized in Tab. 4.5 enables accounting for uncertainty in material parameters and measurement errors. Material science research focus, underlying experimental setups and measurements can be adjusted. If, e. g., an SMC composite part needs to elastically sustain out-of-plane loads, a reliable estimation of the longitudinal Young's modulus E_L is crucial. Then, we need to determine the bundle volume fraction as well as the matrix properties accurately. The fiber properties and orientation state are less important in this case.

This work serves as the starting point for studying the inelastic behavior of SMC using more sophisticated material models, accounting for the thermomechanical material behavior involving stiffness degradation due to damage processes on the microscale.

Chapter 5

A convex anisotropic damage model based on the compliance tensor[1]

5.1 Introduction

5.1.1 Research contributions

This chapter is devoted to anisotropic continuum-damage mechanics in the quasi-static, isothermal, small-strain setting. We propose a framework for anisotropic damage evolution based on the compliance tensor as primary damage variable, in the context of generalized standard models for dissipative solids.

Based on the observation that the Hookean strain energy density of linear elasticity is jointly convex in the strain and the compliance tensor, we design thermodynamically consistent anisotropic damage models that satisfy Wulfinghoff's damage-growth criterion and feature a convex free energy. The latter property permits obtaining mesh-independent results on component scale without the necessity of introducing gradients of the damage field. We introduce the concepts of stress-extraction tensors and damage-hardening functions, implicitly describing a rigorous damage-

---

[1] This chapter is based on the publication "A convex anisotropic damage model based on the compliance tensor" (Görthofer et al., 2022b)

analogue of yield surfaces in elastoplasticity. These damage surfaces may be combined in a modular fashion and give rise to complex damage-degradation behavior.

We discuss how to efficiently integrate Biot's equation implicitly, and show how to design specific stress-extraction tensors and damage-hardening functions based on Puck's anisotropic failure criteria.

Last but not least we demonstrate the versatility of our proposed model and the efficiency of the integration procedure for a variety of examples of interest.

5.1.2 Chapter structure

We contribute to phenomenological continuum damage-mechanics with a tensorial damage variable. We advocate using the full compliance tensor as a rather natural and observable damage variable, liberating the engineer of the burden of selecting the appropriate damage variable in advance, permitting her to focus the attention on appropriate kinetic laws. Thus, when it comes to continuum damage-mechanics of phenomenological type, the proposed framework is as ab-initio as possible, since only the evolution of the damage surface in stress space needs to be identified.

The compliance tensor has been used as the primary damage variable before (Ladevèze, 1983; 2002; Ladevèze et al., 2014; Baranger, 2018). Yet, this approach has not yet entered the main stream of damage-modeling frameworks. Our theoretical contributions to compliance-based damage models are actually twofold. For a start, we point out that the standard Hookean strain energy density, regarded as a function of the strain tensor and the full compliance tensor, is de facto jointly convex in both arguments. This result is surprising, and we are not aware of an account in the literature (although we sincerely believe that others

have presumably noticed this fact before without stating it explicitly, see Thomas and Mielke (2010) for a special case).

Based on the compliance tensor, we develop a simple, modular framework for anisotropic damage mechanics. The framework provides the working engineer with a number of options which we believe to be of advantage. Indeed, due to the convexity property of the Hookean elastic energy, it is possible to develop a purely hardening damage-mechanics modeling-framework, where localization does not become an issue. Very much, there are materials which show a purely damage-hardening material response prior to sudden and brutal failure, e. g., sheet molding compound (SMC) composites (Fitoussi et al., 1996; 1998; Anagnostou et al., 2018) comprising an unsaturated polyester-polyurethane hybrid (UPPH) resin (Trauth et al., 2017a; Kehrer et al., 2018; Bücheler et al., 2017) reinforced by glass fibers (Meraghni and Benzeggagh, 1995; Schemmann et al., 2018a; Görthofer et al., 2019b).

Of course, the modeling framework is not restricted to damage-hardening, but may be adapted to softening in a straightforward manner. However, the latter scenario is rather classical in continuum damage-mechanics, and we decided to work out the details of a hardening framework in the chapter at hand, essentially due to our desire to model SMC materials.

To highlight the simplicity of our proposed compliance-type damage modeling framework, we present a first-principles development in the context of generalized standard models (GSMs) for dissipative solids (Halphen and Nguyen, 1975) and discuss the efficient resolution of the evolution equations in a predictor-corrector framework, see Sec. 5.2.

Our second contribution concerns a design methodology for the damage surfaces which draws upon similar approaches in (associative) elastoplasticity (Chaboche, 2008; McDowell, 2008; Bertram, 2011), but takes failure criteria and multiple damage surfaces (Jin and Arson, 2018; Bakhshan et al., 2018; Khayyam Rayeni et al., 2020) into account. More

precisely, building upon Puck's anisotropic failure criteria developed for continuously reinforced polymers (Puck and Schürmann, 2002; Knops, 2008), we design specific extraction tensors and damage-activation functions which present a flexible arsenal of tools that, taking the individual damaging mechanisms into consideration, permit building up an accurate and fully anisotropic continuum damage model. The details comprise Sec. 5.3.

For anisotropic damage models not to be judged as *purely academic*, it is of utmost importance to establish links to experimental data and to compare it to (dis)similar modeling approaches. In Sec. 5.4, after conducting computational investigations which clarify the influence of the different model parameters on the damage evolution and expose the developing elastic anisotropy upon loading, we study a plain-weave mesostructure of a woven carbon-fiber reinforced thermoset investigated by Simon et al. (2017). We show that the convex modeling framework permits reproducing the effective mechanical behavior of the individual tows and the composite quantitatively within the loading range of interest, see Sec. 5.4.5.

5.2 A compliance-based anisotropic damage model

5.2.1 A convex standard model for anisotropic damage

We will describe the damage model, in a small-strain and isothermal setting, as a generalized standard model (GSM) (Halphen and Nguyen, 1975), whose framework we briefly recall. In addition to the symmetric $d \times d$ infinitesimal strain tensor $\varepsilon \in \mathrm{Sym}(d)$, where $d = 2, 3$ denotes the dimension of the ambient space, a (Banach) space $\mathcal{Z}$ of internal variables

is postulated. Furthermore, a free energy (density)

$$w : \mathrm{Sym}(d) \times \mathcal{Z} \to \mathbb{R}, \quad (\varepsilon, z) \mapsto w(\varepsilon, z), \tag{5.1}$$

a continuously differentiable function of the strain tensor ε and the internal variables $z \in \mathcal{Z}$, and a force potential $\Phi^* : \mathcal{Z}' \to [0, \infty]$, a lower semicontinuous, non-negative and convex function on the continuous dual space $\mathcal{Z}'$ satisfying $\Phi^*(0) = 0$, are introduced. To ensure thermodynamic consistency, the Clausius-Duhem inequality (CDI), see Chapter 13 in Haupt (2002),

$$0 \overset{!}{\leq} \boldsymbol{\sigma} \cdot \dot{\varepsilon} - \frac{\mathrm{d}}{\mathrm{d}t}\left[w(\varepsilon, z)\right] \equiv \left[\boldsymbol{\sigma} - \frac{\partial w}{\partial \varepsilon}(\varepsilon, z)\right] \cdot \dot{\varepsilon} - \frac{\partial w}{\partial z}(\varepsilon, z) \cdot \dot{z}, \tag{5.2}$$

where $\dot{z} \equiv \mathrm{d}z/\mathrm{d}t$ denotes the material time derivative of the internal variables, needs to be satisfied. Associated to a current equilibrium state (ε, z) of a hyperelastic material, the Cauchy stress tensor $\boldsymbol{\sigma} \in \mathrm{Sym}(d)$ is defined (Halphen and Nguyen, 1975; Miehe, 2002) by

$$\boldsymbol{\sigma} = \frac{\partial w}{\partial \varepsilon}(\varepsilon, z). \tag{5.3}$$

For a prescribed loading path $\varepsilon : [0, T] \to \mathrm{Sym}(d)$ on a given interval of time and the initial condition $z(0) = z_0$ for some $z_0 \in \mathcal{Z}$, the evolution of the internal variables is governed by Biot's (dual) equation

$$\dot{z} \in \partial \Phi^* \left(-\frac{\partial w}{\partial z}(\varepsilon, z)\right), \tag{5.4}$$

where $\partial \Phi^*$ denotes the subdifferential of the convex function Φ^*

$$\partial \Phi^*(\xi) = \left\{z \in \mathcal{Z} \,\middle|\, \Phi^*\left(\tilde{\xi}\right) - \Phi^*(\xi) \geq \left(\tilde{\xi} - \xi\right) \cdot z \quad \text{for all} \quad \tilde{\xi} \in \mathcal{Z}'\right\}, \tag{5.5}$$

a subset of $\mathcal{Z}'$, see Borwein and Lewis (2006) for details. Due to these definitions, see Halphen and Nguyen (1975), generalized standard

materials are automatically thermodynamically consistent. Indeed, by Biot's (dual) equation (5.4),

$$\Phi^*(0) - \Phi^*(\xi) \geq (0 - \xi) \cdot \dot{z} \quad \text{for} \quad \xi = -\frac{\partial w}{\partial z}(\varepsilon, z) \tag{5.6}$$

holds. Using $\Phi^*(0) = 0$, rearranging the latter inequality yields

$$-\frac{\partial w}{\partial z}(\varepsilon, z) \cdot \dot{z} \equiv \xi \cdot \dot{z} \geq \Phi^*(\xi) \geq 0, \tag{5.7}$$

i. e., the Clausius-Duhem inequality (5.2) holds in view of the definition of stress (5.3). As it drives the evolution of the internal variables, the quantity $\xi \equiv -\frac{\partial w}{\partial z}(\varepsilon, z)$ is called driving force.

As internal variables z of our proposed continuum damage-mechanics model, we consider an elastic compliance tensor

$$\mathbb{S} \in \mathcal{S}_d = \{\mathbb{S} \in \mathrm{Sym}(\mathrm{Sym}(d)) \,|\, \tau \cdot \mathbb{S}[\tau] > 0 \quad \text{for all} \quad \tau \in \mathrm{Sym}(d)\backslash\{0\}\}, \tag{5.8}$$

and a general, variable $q \in \mathcal{Q}$ which describes the shape and size of the damage surface, s. t.

$$z = (\mathbb{S}, q) \in \mathcal{S}_d \times \mathcal{Q}. \tag{5.9}$$

Notice that the set $\mathcal{S}_d$ of (positive definite) compliance tensors is *not* a linear space. Instead, it is an open, convex subset of the linear space of fourth-order tensors $\mathrm{Sym}(\mathrm{Sym}(d))$ with minor and major symmetries.

For a GSM, the CDI (5.2) will always be satisfied. However, we need to ensure that the (dual) Biot's equation (5.4) guarantees that $\mathbb{S}$ remains an element of $\mathcal{S}_d$, i. e., that the compliance tensor $\mathbb{S}$ remains positive definite. In contrast, the damage-surface variables we consider live in a linear space $\mathcal{Q}$ (which we deliberately keep abstract). For the specific models presented in Sec. 5.3, q is just a finite collection of scalar values. However, our arguments cover the more general case, accounting for vector- or tensor-valued damage-surface variables in a natural way.

The free energy (density) we consider is defined by

$$w : \operatorname{Sym}(d) \times \mathcal{S}_d \times \mathcal{Q} \to \mathbb{R}, \quad (\boldsymbol{\varepsilon}, \mathbb{S}, q) \mapsto w_e(\boldsymbol{\varepsilon}, \mathbb{S}) + h(q), \qquad (5.10)$$

involving the Hookean elastic energy (density)

$$w_e : \operatorname{Sym}(d) \times \mathcal{S}_d \to [0, \infty), \quad (\boldsymbol{\varepsilon}, \mathbb{S}) \mapsto \frac{1}{2} \boldsymbol{\varepsilon} \cdot \mathbb{S}^{-1}[\boldsymbol{\varepsilon}], \qquad (5.11)$$

and an energy (density) related to the progressive degradation of the material,

$$h : \mathcal{Q} \to \mathbb{R}, \quad q \mapsto h(q), \qquad (5.12)$$

which we assume to be convex and continuously differentiable.

Notice that the Hookean elastic energy w_e (5.11) is jointly convex in both variables and infinitely often differentiable. The latter property is immediate[1], as w_e depends on $\boldsymbol{\varepsilon}$ quadratically and the Neumann-series representation

$$(\mathbb{S} + \mathbb{L})^{-1} = \sum_{k=0}^{\infty} \left(-\mathbb{S}^{-1}\mathbb{L}\right)^k \mathbb{S}^{-1}, \quad \mathbb{S} \in \mathcal{S}_d, \quad \mathbb{L} \in \operatorname{Sym}(\operatorname{Sym}(d)), \quad (5.13)$$

valid for sufficiently small $\mathbb{L}$, shows that w_e is even analytic. For the convexity, recall that a twice differentiable function defined on an open convex set is convex if and only if its Hessian is positive semidefinite everwhere, see Theorem 3.1.11 in Borwein and Lewis (2006). A direct computation shows that the Hessian admits the representation

$$D^2 w_e(\boldsymbol{\varepsilon}, \mathbb{S})[\boldsymbol{\xi}, \mathbb{L}] = \frac{1}{2} \left(\boldsymbol{\xi} - \mathbb{L}\mathbb{S}^{-1}[\boldsymbol{\varepsilon}]\right) \cdot \mathbb{S}^{-1} \left[\boldsymbol{\xi} - \mathbb{L}\mathbb{S}^{-1}[\boldsymbol{\varepsilon}]\right], \qquad (5.14)$$

for $(\boldsymbol{\varepsilon}, \mathbb{S}) \in \operatorname{Sym}(d) \times \mathcal{S}_d$ and $(\boldsymbol{\xi}, \mathbb{L}) \in \operatorname{Sym}(d) \times \operatorname{Sym}(\operatorname{Sym}(d))$, see Appendix C. Any $\mathbb{S} \in \mathcal{S}_d$ is positive definite, and thus, the Hessian in

---

[1] Alternatively, representing $\mathbb{S}$ in matrix form, the inverse may also be represented as the adjugate matrix divided by the determinant, i. e., $\mathbb{S} \mapsto \mathbb{S}^{-1}$ is a rational function of the matrix entries.

equation (5.14) is non-negative. Consequently, the elastic energy is convex (but *not* strictly convex). As we assumed the energy h (5.12) to be continuously differentiable and convex, the smoothness and convexity properties of w_e imply that the free energy w (5.10) is continuously differentiable and convex, as well. Furthermore, the formula for the Cauchy stress (5.3) becomes

$$\boldsymbol{\sigma} = \frac{\partial w}{\partial \varepsilon}(\varepsilon, \mathbb{S}, q) \equiv \mathbb{S}^{-1}[\varepsilon], \qquad (5.15)$$

i. e., for a fixed compliance tensor $\mathbb{S}$, the stress-strain relationship reduces to Hooke's law.

To conclude this paragraph, several remarks are in order.

1. Using the framework of generalized standard materials for phenomenological modeling of damage is classical. For instance, Hansen and Schreyer (1994) study a general tensor-valued damage variable coupled to plasticity in such a framework, apparently unaware of the connection.

2. In phenomenological continuum damage-mechanics, choosing the damage variable typically comes first, and the damage kinetics needs to be set up based on the resulting driving forces. Our approach frees the reader of an a priori selection of damage variable, and permits her to focus on the kinetics in terms of the quite natural stress-based driving force.

3. The compliance tensor has the attractive characteristic that it is a physical quantity which can be determined experimentally. Of course, determining all 21 independent parameters of a stiffness tensor in three spatial dimensions is a daunting task from an experimental perspective. Still, observability of the damage variable is not ensured for purely phenomenological damage vectors and tensors.

4. The compliance tensor has been used as a damage variable before (Ladevèze, 1983; 2002). However, its use seemed restricted to specific

situations, e. g., damage modeling in ceramic-matrix composites (Ladevèze et al., 2014; Baranger, 2018). In this work, we advocate using the compliance tensor as the damage variable of choice in greater generality.

5. It is more than well-known that the Hookean energy (5.11) is convex in the strain tensor. It appears much less known that the Hookean energy is *jointly* convex in the strain *and* the compliance tensor. When coupled to an energy h which makes the condensed incremental potential strictly convex, the resulting framework produces an anisotropic damage model which does not permit localization. In particular, associated finite-element computations are not affected by mesh sensitivity induced by softening behavior. We do not want to argue against damage localization. Rather, we wish to add a powerful weapon to the arsenal of continuum damage-mechanics when it comes to modeling stable anisotropic damage phenomena.

6. In classical small-strain elasto(visco)plasticity the (visco)plastic strain $\varepsilon_p \in \mathrm{Sym}(d)$ serves as an internal variable. The corresponding stored energy (density)

$$(\varepsilon, \varepsilon_p) \mapsto \frac{1}{2} \, (\varepsilon - \varepsilon_p) \cdot \mathbb{C} \, [\varepsilon - \varepsilon_p] \tag{5.16}$$

with a fixed stiffness tensor $\mathbb{C} = \mathbb{S}^{-1}$ is smooth and jointly convex in both arguments, but not strictly convex. The Hookean elastic stored energy function w_e (5.11) may be considered as a damage-analog of the elastic stored energy in classical elasto(visco)plasticity (5.16). The combined energy taking into account damage (5.11) and elasto(visco)plasticity (5.16) is jointly convex in all variables. If plasticity is neglected ($\varepsilon_p \equiv 0$) we recover the damage case and for a constant stiffness ($\mathbb{C} = \mathbb{S}^{-1} \equiv \mathrm{const.}$) we recover classical elasto(visco)plasticity. Such a model differs from the classical

presentation, which is typically based on either strain or energy equivalence (Hansen and Schreyer, 1994, Sec. 3.2.1 & 3.2.2).

7. If we regard the Hookean elastic stored energy function $(\varepsilon, \mathbb{C}) \mapsto \frac{1}{2}\varepsilon \cdot \mathbb{C}\,[\varepsilon]$ as a function of the stiffness tensor $\mathbb{C}$, it will *not* be convex. Indeed, its Hessian at $(\varepsilon, \mathbb{C})$ computes as

$$(\boldsymbol{\xi}, \mathbb{L}) \mapsto 2\boldsymbol{\xi} \cdot \mathbb{L}\,[\varepsilon] + \boldsymbol{\xi} \cdot \mathbb{C}\,[\boldsymbol{\xi}]\,, \tag{5.17}$$

which may become negative (take, for instance $\boldsymbol{\xi} = \varepsilon$ and $\mathbb{L} = -\mathbb{C}$). This lack of convexity is the reason why it is so difficult to design convex damage models for stable damage processes. Using the compliance tensor eradicates these issues with the help of a nonlinear transformation.

8. For the thermodynamics considerations at the beginning of this section to be valid, the "interfacial" energy (5.12) need not be convex, see, for example, Govindjee et al. (1995). In particular, softening behavior can be modeled in the compliance-tensor framework, as well. In that case, for obtaining a well-defined boundary-value problem, damage localization has to be overcome, for instance by adding gradient terms of the variable q to the energy (5.12).

9. The presented model cannot distinguish tensile and compressive loading. Indeed, the driving force $\mathbb{T}$ (5.18) for the compliance evolution computes as

$$\mathbb{T} = -\frac{\partial w(\varepsilon, \mathbb{S}, q)}{\partial \mathbb{S}} = -\frac{\partial w_e(\varepsilon, \mathbb{S})}{\partial \mathbb{S}} = \frac{1}{2}\boldsymbol{\sigma} \otimes \boldsymbol{\sigma} \in \mathrm{Sym}(\mathrm{Sym}(d)), \tag{5.18}$$

which is insensitive to the involution $\boldsymbol{\sigma} \mapsto -\boldsymbol{\sigma}$. Thus, in order to extend our model to account for tension-compression asymmetry, the free energy w requires a modification, see Ladevèze (1983; 2002) and Ladevèze et al. (2014).
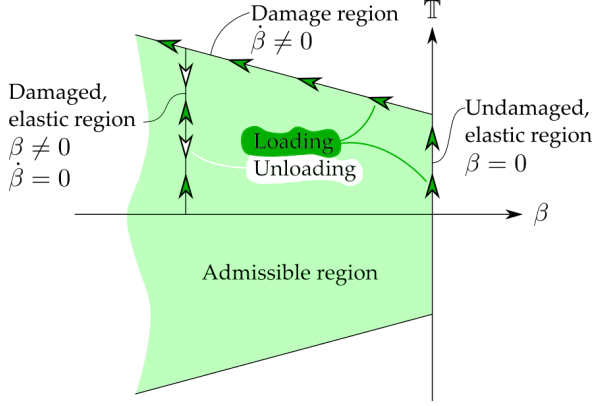
Figure 5.1: Schematic of the admissible elastic region in ($\mathbb{T}$,β)-space

To finish presenting the two-potential model, a suitable force potential Φ^* needs to be provided, entering the evolution equation of the internal variables, see Eq. (5.4),

$$(\dot{\mathbb{S}}, \dot{q}) \in \partial \Phi^* (\mathbb{T}, \beta).$$ (5.19)

In the quasi-static setting targeting a rate-independent damage model, we describe the force potential Φ^* in terms of M continuously differentiable and convex damage functions $\phi_i : \mathrm{Sym}(\mathrm{Sym}(d)) \times \mathcal{Q}' \to \mathbb{R}$, i. e.,

$$\Phi^*(\mathbb{T}, \beta) = \begin{cases} 0, & \phi_i(\mathbb{T}, \beta) \leq 0 \quad \text{for all} \quad i = 1, \dots, M, \\ +\infty, & \text{otherwise.} \end{cases}$$ (5.20)

Such a force potential gives rise to a quasi-static damage evolution in terms of an elastic domain defined by the functions ϕ_i, in strict analogy to associated elastoplasticity at small strains, see Chapter 5 in Simo and Hughes (1998). A schematic of the admissible region based on the force

potential (5.20) with corresponding driving forces $\mathbb{T}$ and β is shown in Fig. 5.1.

However, some care has to be exercised, as the elastic domain is defined in terms of the compliance driving-force $\mathbb{T}$, which takes the form $\mathbb{T} = \frac{1}{2}\boldsymbol{\sigma} \otimes \boldsymbol{\sigma}$ for the free energy w (5.10), in contrast to elastoplasticity, where the stress tensor $\boldsymbol{\sigma}$ (or a shifted version thereof) serves as the driving force.

For the specific force potential Φ^* (5.20), Biot's (dual) equation (5.4) becomes

$$\dot{\mathbb{S}} = \sum_{i=1}^{M} \dot{\mu}_i \frac{\partial \phi_i(\mathbb{T}, \beta)}{\partial \mathbb{T}} \quad \text{and} \quad \dot{q} = \sum_{i=1}^{M} \dot{\mu}_i \frac{\partial \phi_i(\mathbb{T}, \beta)}{\partial \beta}, \qquad (5.21)$$

involving the driving forces

$$\beta = -\frac{\partial w(\boldsymbol{\varepsilon}, \mathbb{S}, q)}{\partial q} \equiv -\frac{\partial h(q)}{\partial q} \in \mathcal{Q}' \qquad (5.22)$$

for the evolution of the damage-surface variables q and consistency parameters $\mu_1, \ldots, \mu_M$ which obey the Karush-Kuhn-Tucker (KKT) conditions

$$\dot{\mu}_i \geq 0, \quad \phi_i(\mathbb{T}, \beta) \leq 0, \quad \dot{\mu}_i \, \phi_i(\mathbb{T}, \beta) = 0, \quad i = 1, \ldots, M. \qquad (5.23)$$

To ensure that $\mathbb{S}$ remains in the set $\mathcal{S}_d$ of positive definite compliance tensors, a condition of the form

$$\frac{\partial \phi_i(\mathbb{T}, \beta)}{\partial \mathbb{T}} \geq 0 \quad \text{for all} \quad i = 1, \ldots, M, \qquad (5.24)$$

on the damage functions ϕ_i is sufficient. The latter condition was established by Wulfinghoff et al. (2017) as a criterion any physically meaningful vectorial or tensorial continuum-damage model should satisfy. In our context, the compliance tensor $\mathbb{S}$ serves as the damage

variable, and Wulfinghoff's criterion becomes "$\dot{\mathbb{S}} \geq 0$", i. e., $\dot{\mathbb{S}}$ is positive semidefinite.

To complete describing our model, we restrict the space of damage variables to $\mathcal{Q} = \mathbb{R}^M$, i. e., one scalar damage variable per damage-activation function ϕ_i. We define the damage-activation functions for $i = 1, \ldots, M$, to be

$$\phi_i : \mathrm{Sym}(\mathrm{Sym}(d)) \times \mathbb{R} \to \mathbb{R}, \quad (\mathbb{T}, \beta_i) \mapsto 2\mathbb{T} \cdot \mathbb{B}_i^2 - \sigma_{0,i}^2 + H_i \beta_i, \quad (5.25)$$

involving a (fourth-order, dimension-free) extraction tensor $\mathbb{B}_i \in L(\mathrm{Sym}(d))$ with minor and major symmetries, a damage-activation threshold $\sigma_{0,i}$ (analogous to the yield stress in elastoplasticity), and a positive parameter H_i with the dimensions of stress.

In principle, the extraction tensor $\mathbb{B}_i$ need not have the major symmetry for Eq. (5.29) to make sense. In this non-symmetric case, the term $\mathbb{B}_i^2$ in Eq. (5.25) needs to be replaced by $\mathbb{B}_i^{\mathsf{T_M}}\mathbb{B}_i$ in terms of the transpose $\mathbb{B}_i^{\mathsf{T_M}}$ of the extraction tensor $\mathbb{B}_i$. However, the framework (5.25) may be recovered by defining $\tilde{\mathbb{B}}_i = \sqrt{\mathbb{B}_i^{\mathsf{T_M}}\mathbb{B}_i}$. Thus, by restricting the extraction tensor to have major symmetries we do not lose generality. Furthermore, as we consider the variable q_i to be dimensionless, the associated driving force β_i has dimensions of stress and the parameter H_i is necessary for dimensional reasons.

In any case, for the damage function (5.25) the condition (5.24) to fulfill Wulfinghoff's damage growth criterion, is automatically satisfied. Indeed, for any $i = 1, \ldots, M$, we obtain,

$$\begin{aligned} \boldsymbol{\tau} \cdot \frac{\partial \phi_i(\mathbb{T}, \beta_i)}{\partial \mathbb{T}} [\boldsymbol{\tau}] &= \boldsymbol{\tau} \cdot \mathbb{B}_i^2 [\boldsymbol{\tau}] = \mathbb{B}_i [\boldsymbol{\tau}] \cdot \mathbb{B}_i [\boldsymbol{\tau}] \\ &= \|\mathbb{B}_i [\boldsymbol{\tau}]\|^2 \geq 0 \quad \text{for all} \quad \boldsymbol{\tau} \in \mathrm{Sym}(d). \end{aligned} \quad (5.26)$$

In addition to the damage functions, we assume a hardening-type damage-surface potential of power-law type

$$h(q) = \sum_{i=1}^{M} \frac{G_i}{m_i + 1} q_i^{m_i+1}, \quad m_i > 0, \tag{5.27}$$

involving a positive, dimension-free power-law exponent m_i and a positive hardening parameter G_i with dimensions of stress. Thus, according to (5.22), the damage-driving forces compute as

$$\beta_i = -G_i q_i^{m_i}, \quad i = 1, \ldots, M. \tag{5.28}$$

In view of the force potential Φ^* (5.20) and the driving forces $\mathbb{T}$ (5.18) and β (5.28), there is an *elastic domain* in the (extended) stress space, described by the conditions

$$\| \mathbb{B}_i [\boldsymbol{\sigma}] \|^2 \leq \sigma_{0,i}^2 + G_i H_i \, q_i^{m_i}, \quad i = 1, \ldots, M, \tag{5.29}$$

where no damage occurs. As defined in equations (5.21), the evolutions of the compliance and the damage-surface variables are governed by

$$\dot{\mathbb{S}} = 2 \sum_{i=1}^{M} \dot{\mu}_i \, \mathbb{B}_i^2 \quad \text{and} \quad \dot{q}_i = \dot{\mu}_i H_i, \quad i = 1, \ldots, M, \tag{5.30}$$

in case of an active damage system at index i – otherwise, $\dot{\mu}_i = 0$ holds. Several simplifications are in order. First, notice that the parameters G_i and H_i only enter (5.29) as the product $G_i H_i$. As we may redefine $\tilde{G}_i = \tilde{H}_i = \sqrt{G_i H_i}$ without changing the elastic domain (5.29), we assume $G_i = H_i$. Secondly, we may eliminate the consistency parameter from the evolution of the compliance (5.30) and integrate to get

$$\mathbb{S}(t) = \mathbb{S}_0 + 2 \sum_{i=1}^{M} \frac{q_i(t)}{H_i} \mathbb{B}_i^2, \tag{5.31}$$

where $\mathbb{S}_0 = \mathbb{S}(0)$ is the initial compliance. Thirdly, in three spatial dimensions $d = 3$, the compliance tensor $\mathbb{S}$ is described by 21 independent parameters. The latter formula (5.31) permits us to express the current compliance tensor $\mathbb{S}$ in terms of the internal variables q. Thus, with an eye towards an efficient implementation, we may a posteriori *eliminate* the compliance tensor $\mathbb{S}$ from the model.

Summary of compliance-based convex damage model (primal formulation)

Input. Initial compliance tensor $\mathbb{S}_0$, extraction tensors $\mathbb{B}_i$, hardening moduli $H_i > 0$, damage thresholds $\sigma_{0,i} > 0$, power-law exponents $m_i > 0$ ($i = 1, \ldots, M$).

Evolution equations. For given strain path $\boldsymbol{\varepsilon} : [0, T] \to \mathrm{Sym}(d)$, find damage-hardening variables $q : [0, T] \to \mathbb{R}^M$ and a stress path $\boldsymbol{\sigma} : [0, T] \to \mathrm{Sym}(d)$, s. t.

$$f_i(\boldsymbol{\sigma}, q_i) \leq 0, \quad \dot{q}_i \geq 0, \quad \dot{q}_i\, f_i(\boldsymbol{\sigma}, q_i) = 0, \quad i = 1, \ldots, M, \quad (5.32)$$

holds, with initial conditions $q(0) = 0$, and where

$$f_i(\boldsymbol{\sigma}, q_i) = \|\mathbb{B}_i\,[\boldsymbol{\sigma}]\,\|^2 - \sigma_{0,i}^2 - H_i^2 q_i^{m_i} \quad \text{and}$$

$$\boldsymbol{\varepsilon} = \left(\mathbb{S}_0 + 2 \sum_{i=1}^{M} \frac{q_i}{H_i}\, \mathbb{B}_i^2 \right) [\boldsymbol{\sigma}]. \tag{5.33}$$

Furthermore, as stated above, notice that the equations (5.30) permit us to eliminate the parameters $\dot{\mu}$ completely. Last but not least, in view of the elastic domain (5.29), we may work with the damage-activation functions f_i for $i = 1, \ldots, M$,

$$f_i : \mathrm{Sym}(d) \times \mathbb{R} \to \mathbb{R}, \quad (\boldsymbol{\sigma}, q_i) \mapsto \|\mathbb{B}_i\,[\boldsymbol{\sigma}]\,\|^2 - \sigma_{0,i}^2 - H_i^2 q_i^{m_i}, \tag{5.34}$$

instead of the original functions ϕ_i (5.25). For convenience, we epitomize the key aspects of the model in the summary box above.

5.2.2 Computational predictor-corrector framework

In this section, upon an implicit Euler discretization in time, we discuss a predictor-corrector solution strategy for the model introduced in the previous section in strict analogy to associative elastoplasticity, see Chapter 2 in Simo and Hughes (1998). Suppose that a number of discrete time steps $0 = t_0 < t_1 < \ldots < t_{N-1} < t_N = T$ is given, together with prescribed strain tensors $\varepsilon_0, \varepsilon_1, \ldots \varepsilon_N$, an initial compliance tensor $\mathbb{S}_0$ and the initial damage-hardening variable $q_0 \equiv 0 \in \mathbb{R}^M$. For any $n = 0, \ldots, N - 1$, dropping the subscript $n + 1$ for simplicity of notation, we seek $(\boldsymbol{\sigma}, q) \in \mathrm{Sym}(d) \times \mathbb{R}^M$ solving the system of equations

$$\varepsilon = \left(\mathbb{S}_0 + 2 \sum_{i=1}^{M} \frac{q_i}{H_i} \mathbb{B}_i^2 \right) [\boldsymbol{\sigma}]$$

$$f_i(\boldsymbol{\sigma}, q_i) \leq 0, \quad q_i - q_{i,n} \geq 0, \quad (q_i - q_{i,n}) f_i(\boldsymbol{\sigma}, q_i) = 0, \quad i = 1, \ldots, M,$$
$$(5.35)$$

with the damage functions f_i (5.33)$_1$. With a computational resolution in mind, we rewrite the system (5.35) in terms of active sets. For any $(\boldsymbol{\sigma}, q) \in \mathrm{Sym}(d) \times \mathbb{R}^M$, the *active set* $\mathcal{A}(\boldsymbol{\sigma}, q)$ is defined as

$$\mathcal{A}(\boldsymbol{\sigma}, q) = \{ i \in \{1, 2, \ldots, M\} \mid f_i(\boldsymbol{\sigma}, q_i) \geq 0 \}, \tag{5.36}$$

collecting all indices of inequality constraints that are either violated or satisfied exactly. Then, as a consequence of the complementarity condition in the system (5.35), $(\boldsymbol{\sigma}, q) \in \mathrm{Sym}(d) \times \mathbb{R}^M$ solves the system (5.35)

precisely if it is satisfies $q_i \geq q_{i,n}$ $(i = 1, \ldots, M)$ and solves

$$\left(\mathbb{S}_0 + 2 \sum_{i=1}^{M} \frac{q_i}{H_i} \, \mathbb{B}_i^2 \right) [\boldsymbol{\sigma}] = \boldsymbol{\varepsilon} \tag{5.37}$$

$$f_i(\boldsymbol{\sigma}, q_i) = 0 \quad \text{for all} \quad i \in \mathcal{A}(\boldsymbol{\sigma}, q).$$

We solve the latter problem by an active set strategy (Bergounioux et al., 1999; 2000), i.e., by solving the system (5.37) with a Newton method, updating the currently active set at each Newton iteration and accounting for the constraints $q_i \geq q_{i,n}$ $(i = 1, \ldots, M)$ via backtracking. The details comprise Alg. 1, where $\gamma \in (0, 1)$ is a backtracking factor. We use a backtracking factor of $\gamma = 0.9$ in our presented examples, see Sec. 5.4.
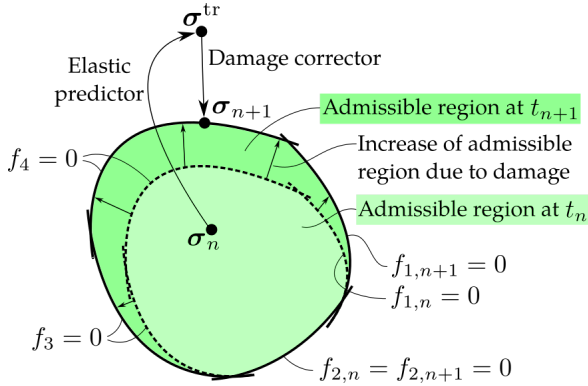
Figure 5.2: Evolution of the elastic region upon loading within a predictor-corrector framework

As long as the damage constraints are linearly independent, due to the established connections of active set strategies to semi-smooth Newton methods, see Hintermüller et al. (2002), a locally superlinear convergence

behavior can be expected. A schematic of the predictor-corrector strategy is shown in Fig. 5.2 with

$$\text{residual}(\boldsymbol{\sigma}, q) = \frac{\sqrt{\|R_1\|^2 + R_2}}{\|\boldsymbol{\sigma}\|}, \quad \text{where}$$

$$R_1 = \boldsymbol{\sigma} - \left(\mathbb{S}_0 + 2 \sum_{i=1}^{M} \frac{q_i}{H_i} \, \mathbb{B}_i^2 \right)^{-1} [\varepsilon], \quad \text{and} \qquad (5.38)$$

$$R_2 = \sum_{i=1}^{M} \max\{0, f_i(\boldsymbol{\sigma}, q_i)\}$$

for measuring convergence. Whenever the trial stress fails to be contained in the elastic region, an iterative process is initiated which ensures that the final stress state again lies on the boundary of the elastic domain. For the latter, both the elastic region may grow – as a result of the damage-hardening – and the stress may decrease – owing to increasing compliance.

For solving problem (5.37), we assemble the Newton system for the active set $\mathcal{A}(\boldsymbol{\sigma}, q)$

$$
\left(\mathbb{S}_0 + 2 \sum_{i=1}^{M} \frac{q_i}{H_i} \, \mathbb{B}_i^2 \right) [\triangle \boldsymbol{\sigma}] \quad + \quad \sum_{i=1}^{M} \frac{2}{H_i} \, \mathbb{B}_i^2 \, [\boldsymbol{\sigma}] \, \triangle q_i
$$

$$
= \quad \boldsymbol{\varepsilon} - \left(\mathbb{S}_0 + 2 \sum_{i=1}^{M} \frac{q_i}{H_i} \, \mathbb{B}_i^2 \right) [\boldsymbol{\sigma}]
$$

$$
\left(\frac{2}{H_i} \, \mathbb{B}_i^2 \, [\boldsymbol{\sigma}] \right) \cdot \triangle \boldsymbol{\sigma} \quad - \quad m_i H_i q_i^{m_i - 1} \, \triangle q_i
$$

$$
= \quad -\frac{1}{H_i} \left(\|\mathbb{B}_i \, [\boldsymbol{\sigma}]\|^2 - \sigma_{0,i}^2 - H_i^2 q_i^{m_i} \right)
$$

$$(5.39)$$

for all $i \in \mathcal{A}(\boldsymbol{\sigma}, q)$, where we divided the second line by H_i to ensure a symmetric Newton system.

Algorithm 1 Predictor-corrector strategy $(\varepsilon, q_{i,n})$ with model parameters $(\mathbb{S}_0, \mathbb{B}_i, H_i, \sigma_{0,i}, m_i)$ and algorithm parameters (maxit, tol, γ)

1: **Elastic predictor**
2: $q \leftarrow q_n$
3: $\boldsymbol{\sigma} \leftarrow \left(\mathbb{S}_0 + 2 \sum_{i=1}^{M} q_i \, \mathbb{B}_i^2 / H_i \right) [\boldsymbol{\varepsilon}]$
4: **if** all $f_i \leq 0$ **then**
5:       no damage evolution, elastic predictor step correct ✓
6: **else**
7:       **Damage corrector**
8:       $k \leftarrow 1$ ▷ Iteration counter
9:       Update residual (5.38)
10:       **while** $k <$ maxit **and** residual $>$ tol **do**
11:           $\mathcal{A} \leftarrow \mathcal{A}(\boldsymbol{\sigma}, q)$
12:           assemble Newton system (5.39)
13:           solve for $(\triangle \boldsymbol{\sigma}, \triangle q)$ ▷ $\triangle q_i := 0$ for $i \neq \mathcal{A}$
14:           $s \leftarrow 1$ ▷ Full step size
15:           $(\boldsymbol{\sigma}, q) \leftarrow (\boldsymbol{\sigma} + s \triangle \boldsymbol{\sigma}, q + s \triangle q)$
16:           $j \leftarrow 0$ ▷ Counts backtracking steps
17:           residual$_{\text{old}} \leftarrow$ residual
18:           Update residual (5.38)
19:           **while** residual $>$ residual$_{\text{old}}$ **or** $q_i < q_{i,n}$ for some i **do**
20:               (Backtracking, typically $\gamma = 0.9$)
21:               $(\boldsymbol{\sigma}, q) \leftarrow (\boldsymbol{\sigma} + (\gamma s - s) \triangle \boldsymbol{\sigma}, q + (\gamma s - s) \triangle q)$
22:               $s \leftarrow \gamma s$ ▷ Reduce current step size
23:               Update residual (5.38)
24:               $j \leftarrow j + 1$
25:           **end while**
26:           $k \leftarrow k + 1$
27:       **end while**
28: **end if**
29: compute $\mathbb{C}_{\text{algo}}$
30: **Output**
31: **return** $\boldsymbol{\sigma}$, q, $\mathbb{C}_{\text{algo}}$

5.3 Damage models with Puck-type extraction tensors accounting for average stresses

5.3.1 Basic idea

Puck introduced strength-estimation models for composites reinforced by continuous fibers (Puck and Schürmann, 2002; Knops, 2008) based on specific failure scenarios that are commonly observed in post-critical investigations of failed specimens. For the current chapter at hand, we will use these so-called Puck cases as primary drivers of the anisotropic damage evolution presented in Sec. 5.2. More precisely, we will investigate the Puck cases individually, and determine proper extraction tensors ($\mathbb{B}_\mathrm{I}$ - $\mathbb{B}_\mathrm{IV}$) in sections 5.3.2 - 5.3.5. These Puck-type extraction tensors are motivated by the stress and corresponding damage states present in the fiber bundle mesostructure of sheet molding compound (SMC) composites (Dumont et al., 2007; Görthofer et al., 2019b) in an averaged setting.

We introduce a local Cartesian coordinate system $\{e_1, e_2, e_3\}$, s. t. the fibers are aligned to the e_1-direction, see Fig. 5.3a. Then, the stress state $\boldsymbol{\sigma}$ may be decomposed into blocks

$$\boldsymbol{\sigma} = \left(\begin{array}{c|cc} \sigma_{11} & \sigma_{12} & \sigma_{13} \\ \hline \sigma_{12} & \sigma_{22} & \sigma_{23} \\ \sigma_{13} & \sigma_{23} & \sigma_{33} \end{array} \right), \tag{5.40}$$

where σ_{11} is the stress in fiber direction, the lower right block describes the stresses in the plane orthogonal to the fiber direction, and $(\sigma_{12}, \sigma_{13})$ collects the remaining shear stresses. Adopting ideas of Puck (Knops, 2008; Puck and Schürmann, 2002), we distinguish four basic cases which drive the damage evolution in a fiber bundle, for instance.

(I) Normal loading in fiber direction: σ_{11}
   ▷ Figs. 5.3a and 5.3b

(II) Normal loading perpendicular to fiber direction: σ_{22}, σ_{33}
   ▷ Figs. 5.3c and 5.3d

(III) Shear loading perpendicular to fiber direction: σ_{23}
   ▷ Fig. 5.3e

(IV) Shear loading in fiber direction: σ_{12}, σ_{13}
   ▷ Fig. 5.3f

(a) Extension in fiber direction   **(b)** Compression in fiber direction   **(c)** Extension ⊥ to fiber direction

(d) Compression ⊥ to fiber direction   **(e)** Shearing ⊥ to fiber direction   **(f)** Shearing in fiber direction
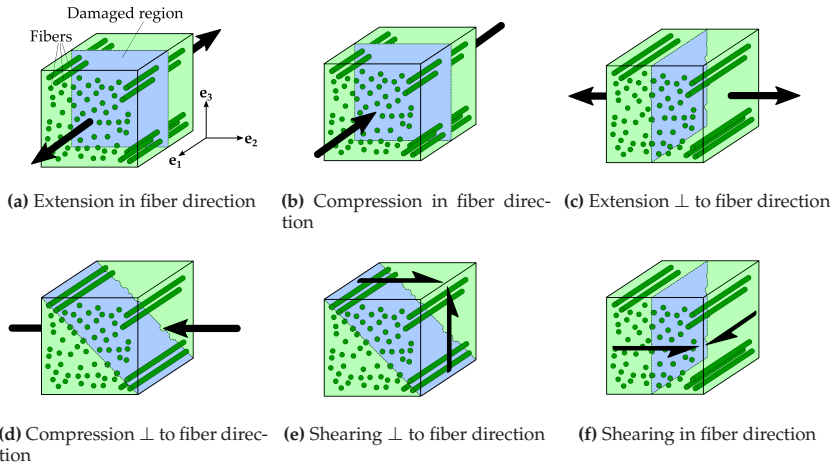
Figure 5.3: Regions of major damage (blue) resulting from different loading scenarios in a cell with aligned fibers (dark green)

The loading scenarios shown in Fig. 5.3 are only examples, e.g., loadings perpendicular to the fiber direction need not necessarily follow direction e_2. Instead, any other direction in the e_2-e_3-plane could be used, as well. Nevertheless, we may regard a general loading scenario as a superposition of the four introduced cases. In the following sections, we will derive appropriate extraction tensors ($\mathbb{B}_{I}$ - $\mathbb{B}_{IV}$) corresponding to

each of the four presented cases based on averaged stress conditions. The presented model cannot distinguish between tensile and compressive loading, as the driving force $\mathbb{T}$ (5.18) is quadratic in the stress $\boldsymbol{\sigma}$. Consequently, the six sketched loading scenarios in Fig. 5.3 reduce to the mentioned four cases, as the scenarios Fig. 5.3a and Fig. 5.3b, as well as Fig. 5.3c and Fig. 5.3d coincide for our model.

5.3.2 Normal loading in fiber direction

The first damage case is governed by loading in fiber or bundle direction, respectively, and thus solely concerns the stress σ_{11}. For fiber direction $\boldsymbol{e}_1$, the fourth-order extraction tensor $\mathbb{B}_{\mathrm{I}}$ extracting the stress in bundle direction σ_{11} from an arbitrary stress state $\boldsymbol{\sigma}$ is given by

$$\mathbb{B}_{\mathrm{I}} = \boldsymbol{e}_1^{\otimes 4}. \tag{5.41}$$

The associated damage function $(5.33)_1$ with case I extraction tensor $\mathbb{B}_{\mathrm{I}}$ (5.41) reads

$$f_{\mathrm{I}}(\boldsymbol{\sigma}, q) = \sigma_{11}^2 - H^2 q^m - \sigma_0^2, \tag{5.42}$$

and will solely induce a decrease in the Young's modulus in $\boldsymbol{e}_1$-direction. As a general note, although the damage parameters like σ_0, H, m may differ for the considered cases I to IV, we do not include additional subscripts for the sake of readability.

5.3.3 Normal loading perpendicular to fiber direction

To quantify damaging due to normal loading in any direction $S^2 \ni \boldsymbol{n} \perp \boldsymbol{e}_1$ perpendicular to the fiber direction (a unit vector with $S^2 = \{\boldsymbol{x} \in \mathbb{R}^3 \mid \|\boldsymbol{x}\| = 1\}$), for a general stress state $\boldsymbol{\sigma}$, we measure

the average normal stress perpendicular to the fiber direction

$$\frac{1}{2\pi} \int_0^{2\pi} \boldsymbol{n}(\theta)^{\otimes 4} \left[\boldsymbol{\sigma}\right] \, \mathrm{d}\theta \qquad (5.43)$$

with $\boldsymbol{n}(\theta) \stackrel{\wedge}{=} (0, \cos\theta, \sin\theta)$. The latter average may be represented in the form

$$\frac{1}{2\pi} \int_0^{2\pi} \boldsymbol{n}(\theta)^{\otimes 4} \left[\boldsymbol{\sigma}\right] \, \mathrm{d}\theta \stackrel{!}{=} \mathbb{B}_{\mathrm{II}} \left[\boldsymbol{\sigma}\right] \qquad (5.44)$$

in terms of the extraction tensor $\mathbb{B}_{\mathrm{II}}$

$$\mathbb{B}_{\mathrm{II}} = \frac{1}{2\pi} \int_0^{2\pi} \boldsymbol{n}(\theta)^{\otimes 4} \, \mathrm{d}\theta \qquad (5.45)$$

with $\boldsymbol{n}(\theta) \stackrel{\wedge}{=} (0, \cos\theta, \sin\theta)$.

We evaluate the integration for each component of the extraction tensor separately. As $\boldsymbol{n} \perp \boldsymbol{e}_1$, all components of $\mathbb{B}_{\mathrm{II}}$ with at least one index "1" are zero. The remaining components are

$$B^{\mathrm{II}}_{2222} = \frac{1}{2\pi} \int_0^{2\pi} \cos^4\theta \, \mathrm{d}\theta = \frac{3}{8}, \qquad (5.46)$$

$$B^{\mathrm{II}}_{2233} = \frac{1}{2\pi} \int_0^{2\pi} \cos^2\theta \sin^2\theta \, \mathrm{d}\theta$$

$$= B^{\mathrm{II}}_{3322} = B^{\mathrm{II}}_{2323} = B^{\mathrm{II}}_{2332} = B^{\mathrm{II}}_{3232} = B^{\mathrm{II}}_{3223} = \frac{1}{8}, \qquad (5.47)$$

$$B^{\mathrm{II}}_{3333} = \frac{1}{2\pi} \int_0^{2\pi} \sin^4\theta \, \mathrm{d}\theta = \frac{3}{8}, \qquad (5.48)$$

$$B^{\mathrm{II}}_{2223} = \frac{1}{2\pi} \int_0^{2\pi} \cos^3\theta \sin\theta \, \mathrm{d}\theta$$

$$= B^{\mathrm{II}}_{2232} = B^{\mathrm{II}}_{2322} = B^{\mathrm{II}}_{3222} = 0, \qquad (5.49)$$

$$B^{\mathrm{II}}_{3332} = \frac{1}{2\pi} \int_0^{2\pi} \cos\theta \sin^3\theta \, \mathrm{d}\theta$$

$$= B^{\mathrm{II}}_{3323} = B^{\mathrm{II}}_{3233} = B^{\mathrm{II}}_{2333} = 0. \qquad (5.50)$$

Hence, the extraction tensor is

$$\mathbb{B}_{\text{II}} = \frac{1}{4}(e_2^{\otimes 2} + e_3^{\otimes 2})^{\otimes 2} + \frac{1}{8}(e_2^{\otimes 2} - e_3^{\otimes 2})^{\otimes 2} + \frac{1}{2}(e_2 \otimes_{\text{S}} e_3)^{\otimes 2}. \quad (5.51)$$

This extraction tensor $\mathbb{B}_{\text{II}}$ is identical to the fourth-order fiber-orientation tensor for a planar isotropic orientation, see Advani and Tucker (1987). The composition of the extraction tensor with itself is

$$\mathbb{B}_{\text{II}}^2 = \frac{1}{8}(e_2^{\otimes 2} + e_3^{\otimes 2})^{\otimes 2} + \frac{1}{32}(e_2^{\otimes 2} - e_3^{\otimes 2})^{\otimes 2} + \frac{1}{8}(e_2 \otimes_{\text{S}} e_3)^{\otimes 2}. \quad (5.52)$$

The damage function $(5.33)_1$ involving the case II extraction tensor $\mathbb{B}_{\text{II}}$ (5.51) reads

$$f_{\text{II}}(\boldsymbol{\sigma}, q) = \frac{1}{32}\left(5\sigma_{22}^2 + 5\sigma_{33}^2 + 6\sigma_{22}\sigma_{33} + 4\sigma_{23}^2\right) - H^2 q^m - \sigma_0^2. \quad (5.53)$$

5.3.4 Shear loading perpendicular to fiber direction

In addition to damage caused by normal loading, we also want to account for shear-loading induced damage. For a general stress state $\boldsymbol{\sigma}$, the average shear stress transverse to the fiber direction is given by

$$\frac{1}{2\pi} \int_0^{2\pi} (n(\theta) \otimes_{\text{S}} m(\theta))^{\otimes 2} [\boldsymbol{\sigma}] \, d\theta \quad (5.54)$$

with $n(\theta) \stackrel{\wedge}{=} (0, \cos\theta, \sin\theta)$ and $m(\theta) \stackrel{\wedge}{=} (0, -\sin\theta, \cos\theta)$. We may rewrite this expression

$$\frac{1}{2\pi} \int_0^{2\pi} (n(\theta) \otimes_{\text{S}} m(\theta))^{\otimes 2} [\boldsymbol{\sigma}] \, d\theta \stackrel{!}{=} \mathbb{B}_{\text{III}} [\boldsymbol{\sigma}] \quad (5.55)$$

in terms of the extraction tensor $\mathbb{B}_{\text{III}}$ as

$$\mathbb{B}_{\text{III}} = \frac{1}{2\pi} \int_0^{2\pi} (n(\theta) \otimes_{\text{S}} m(\theta))^{\otimes 2} \, d\theta \quad (5.56)$$

with $\boldsymbol{n}(\theta) \,\hat{=}\, (0, \cos\theta, \sin\theta)$ and $\boldsymbol{m}(\theta) \,\hat{=}\, (0, -\sin\theta, \cos\theta)$.

We evaluate the integration for each component of the extraction tensor separately. As $\boldsymbol{n} \perp \boldsymbol{m} \perp \boldsymbol{e}_1$ and $n_1 = m_1 = 0$, all components with at least one index "1" are zero. For the remaining components we get

$$B_{2222}^{\mathrm{III}} = \frac{1}{2\pi} \int_0^{2\pi} \cos^2\theta \sin^2\theta \, \mathrm{d}\theta = \frac{1}{8}, \tag{5.57}$$

$$B_{2233}^{\mathrm{III}} = -\frac{1}{2\pi} \int_0^{2\pi} \sin^2\theta \cos^2\theta \, \mathrm{d}\theta$$
$$= B_{3322}^{\mathrm{III}} = -\frac{1}{8}, \tag{5.58}$$

$$B_{2323}^{\mathrm{III}} = \frac{1}{2\pi} \int_0^{2\pi} \frac{1}{4} \left(\sin^4\theta + \cos^4\theta - 2\sin^2\theta \cos^2\theta \right) \, \mathrm{d}\theta$$
$$= B_{2332}^{\mathrm{III}} = B_{3232}^{\mathrm{III}} = B_{3223}^{\mathrm{III}} = \frac{1}{8}, \tag{5.59}$$

$$B_{3333}^{\mathrm{III}} = \frac{1}{2\pi} \int_0^{2\pi} \sin^2\theta \cos^2\theta \, \mathrm{d}\theta = \frac{1}{8}, \tag{5.60}$$

$$B_{2223}^{\mathrm{III}} = \frac{1}{4\pi} \int_0^{2\pi} \left(\sin^3\theta \cos\theta - \sin\theta \cos^3\theta \right) \, \mathrm{d}\theta$$
$$= B_{2232}^{\mathrm{III}} = B_{2322}^{\mathrm{III}} = B_{3222}^{\mathrm{III}} = 0, \tag{5.61}$$

$$B_{3332}^{\mathrm{III}} = \frac{1}{4\pi} \int_0^{2\pi} \left(\sin\theta \cos^3\theta - \sin^3\theta \cos\theta \right) \, \mathrm{d}\theta$$
$$= B_{3323}^{\mathrm{III}} = B_{3233}^{\mathrm{III}} = B_{2333}^{\mathrm{III}} = 0. \tag{5.62}$$

The extraction tensor for case III therefore has the form

$$\mathbb{B}_{\mathrm{III}} = \frac{1}{8} \left(\boldsymbol{e}_2^{\otimes 2} - \boldsymbol{e}_3^{\otimes 2} \right)^{\otimes 2} + \frac{1}{2} (\boldsymbol{e}_2 \otimes_{\mathsf{S}} \boldsymbol{e}_3)^{\otimes 2}. \tag{5.63}$$

The composition of the extraction tensor with itself is

$$\mathbb{B}_{\mathrm{III}}^2 = \frac{1}{4} \mathbb{B}_{\mathrm{III}}. \tag{5.64}$$

The damage function $(5.33)_1$ for the case III extraction tensor $\mathbb{B}_{\mathrm{III}}$ (5.63) reads

$$f_{\mathrm{III}}(\boldsymbol{\sigma}, q) = \frac{1}{32}\left(\sigma_{22}^2 + \sigma_{33}^2 - 2\sigma_{22}\sigma_{33} + 4\sigma_{23}^2\right) - H^2 q^m - \sigma_0^2. \quad (5.65)$$

Comparing the extraction tensors $\mathbb{B}_{\mathrm{II}}$ (5.51) and $\mathbb{B}_{\mathrm{III}}$ (5.63), some similarities between these tensors become apparent. In fact, these similarities reflect the relationship between normal loadings (especially compression) and shear loadings perpendicular to the fiber direction, that are familiar from undergraduate engineering mechanics (Hibbeler, 2001), i. e., Mohr's circle (Mohr, 1900).

5.3.5 Shear loading in fiber direction

To evaluate damage induced by shearing in fiber direction $\boldsymbol{e}_1$, we evaluate

$$\frac{1}{2\pi}\int_0^{2\pi}(\boldsymbol{n}(\theta) \otimes_{\mathsf{S}} \boldsymbol{e}_1)^{\otimes 2}\,[\boldsymbol{\sigma}]\,\mathrm{d}\theta \quad (5.66)$$

with $\boldsymbol{n}(\theta) \mathrel{\hat{=}} (0, \cos\theta, \sin\theta)$, which we represent in the form

$$\frac{1}{2\pi}\int_0^{2\pi}(\boldsymbol{n}(\theta) \otimes_{\mathsf{S}} \boldsymbol{e}_1)^{\otimes 2}\,[\boldsymbol{\sigma}]\,\mathrm{d}\theta \stackrel{!}{=} \mathbb{B}_{\mathrm{IV}}\,[\boldsymbol{\sigma}] \quad (5.67)$$

with extraction tensor $\mathbb{B}_{\mathrm{IV}}$

$$\mathbb{B}_{\mathrm{IV}} = \frac{1}{2\pi}\int_0^{2\pi}(\boldsymbol{n}(\theta) \otimes_{\mathsf{S}} \boldsymbol{e}_1)^{\otimes 2}\,\mathrm{d}\theta \quad (5.68)$$

and $\boldsymbol{n}(\theta) \mathrel{\hat{=}} (0, \cos\theta, \sin\theta)$.

Again, we evaluate the integration for each component of the extraction tensor separately. The only non-zero components are B_{2121}, B_{2112}, B_{1221}, B_{1212}, B_{3131}, B_{3113}, B_{1331} and B_{1313}. These components are computed

as

$$B_{2121}^{\mathrm{IV}} = \frac{1}{8\pi} \int_0^{2\pi} \cos^2 \theta \, \mathrm{d}\theta$$
$$= B_{2112}^{\mathrm{IV}} = B_{1221}^{\mathrm{IV}} = B_{1212}^{\mathrm{IV}} = \frac{1}{8}, \tag{5.69}$$

$$B_{3131}^{\mathrm{IV}} = \frac{1}{8\pi} \int_0^{2\pi} \sin^2 \theta \, \mathrm{d}\theta$$
$$= B_{3113}^{\mathrm{IV}} = B_{1331}^{\mathrm{IV}} = B_{1313}^{\mathrm{IV}} = \frac{1}{8}. \tag{5.70}$$

The resulting extraction tensor for case IV may be expressed via

$$\mathbb{B}_{\mathrm{IV}} = \frac{1}{2}(\boldsymbol{e}_1 \otimes_{\mathsf{S}} \boldsymbol{e}_2)^{\otimes 2} + \frac{1}{2}(\boldsymbol{e}_1 \otimes_{\mathsf{S}} \boldsymbol{e}_3)^{\otimes 2}. \tag{5.71}$$

The composition of the extraction tensor with itself is

$$\mathbb{B}_{\mathrm{IV}}^2 = \frac{1}{4}\mathbb{B}_{\mathrm{IV}}. \tag{5.72}$$

Inserting case IV extraction tensor $\mathbb{B}_{\mathrm{IV}}$ (5.71) into damage function (5.33)$_1$ yields

$$f_{\mathrm{IV}}(\boldsymbol{\sigma}, q) = \frac{1}{8}\left(\sigma_{12}^2 + \sigma_{13}^2\right) - H^2 q^m - \sigma_0^2. \tag{5.73}$$

5.4 Computational investigations

5.4.1 Setup

We integrated the proposed damage model as a user-defined subroutine into an in-house OpenMP-parallel FFT-based computational homogenization code written in Python 3.7 with Cython extensions (Behnel et al., 2011) and FFTW (Frigo and Johnson, 2005) bindings, as described, e. g., by Schneider (2018). The balance of linear momentum was discretized

on a staggered grid (Schneider et al., 2016b) and the ensuing nonlinear systems of equations were solved by a Newton-CG scheme (Gélébart and Mondon-Cancel, 2013; Kabel et al., 2014; Wicht et al., 2020). Furthermore, we implemented Alg. 1 as a `C++` subroutine (Stroustrup, 1999) in the commercial Finite Element (FE) software ABAQUS/Standard by Dassault Systèmes Simulia (Dassault Systèmes, 2014). The computations ran on 6 - 12 threads on a desktop computer with $32\,$GB RAM and an Intel i7-8700K CPU with 6 cores and a clock rate of $3.7\,$GHz. The plain-weave presented in Sec. 5.4.5 was computed on a workstation with two AMD EPYC 7642 and 48 physical cores each, enabled SMT, and $1024\,$GB of DRAM.

For the following studies, we use the isotropic elastic parameters of unsaturated polyester polyurethane hybrid (UPPH) resin and E-glass fibers, see Kehrer et al. (2018), respectively, if not specified otherwise. Furthermore, we use the damage parameters σ_0, H and m listed in Tab. 5.1 as a point of departure for parameter variation and the different introduced damage cases. Due to the small-strain setting, we limit the strain axes to $5\,\%$ in magnitude.

Table 5.1: Standard material parameters (Kehrer et al., 2018) and reference damage parameters, serving as point of departure depending on the corresponding damage case

UPPH matrix	E-glass fibers	Damage parameters
$E_{\mathrm{M}} = 3.4\,$GPa	$E_{\mathrm{F}} = 72\,$GPa	$\sigma_0 \in [5, 30]\,$MPa
$\nu_{\mathrm{M}} = 0.385$	$\nu_{\mathrm{F}} = 0.22$	$H \in [30, 80]\,$MPa
		$m = 1$

5.4.2 Numerical studies on integration-point level

Parameter study for Puck-type extraction tensor I

The first study concerns the effects of the damage parameters σ_0, H and m on the stress and damage evolution. For this purpose, we investigate the model behavior for one active damage function and the Puck-type extraction tensor I (see Sec. 5.3.2) only. We vary the parameters and evaluate the stress-strain curves, as well as the normalized Young's modulus E_{11}/E_{11}^0 for uniaxial extension in e_1-direction and a prescribed strain ε_{11}.

For the case at hand, we extract the current Young's modulus in e_1-direction from Eq. (5.31) by

$$E_{11} = \frac{H E_{11}^0}{H + 2\,q\,E_{11}^0},\qquad (5.74)$$

where E_{11}^0 stands for the initial Young's modulus in e_1-direction. Please note that E_{11}^{-1} may be regarded as a component of a (fourth-order) tensor, as it is the 1111 component of the corresponding compliance $\mathbb{S}$. For the sake of simplicity, we will use such shorthand index notation for certain Young's moduli throughout the remainder of this work.

The influence of the damage-activation threshold σ_0 on the stress and normalized stiffness in e_1-direction is shown in Fig. 5.4. The higher the damage-activation threshold σ_0, the later the damage evolution initiates w. r. t. the applied strain ε_{11}. In Fig. 5.4a, we observe damage to initiate as soon as the stress σ_{11} equals the damage-activation threshold σ_0, which is expected. The convex hardening nature of our model gives rise to a decreasing slope of the stress-strain curve. This slope tends to zero at infinity, but remains non-negative.

With increasing damage-activation thresholds σ_0, the stress-strain behavior approaches a plateau beyond the elastic region, in which
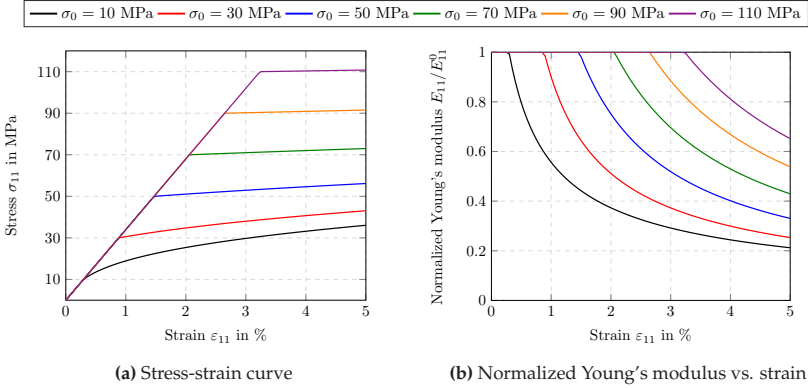
Figure 5.4: Varying the initial stress σ_0 for the proposed model

an increase of strain does not induce a further increase of stress. The reduced stiffness E_{11} in e_1-direction equals the slope of the stress-strain curve during unloading (which returns to the origin in our pure elastic-damage framework, see Sec. 5.4.2). Whereas the plateaus are more pronounced for higher damage-activation thresholds σ_0, the increase in damage and the (normalized) stiffness reduction are less pronounced, see Fig. 5.4b.

Due to the thermodynamically consistent GSM framework of our proposed model, an upper bound for the damage variables is ensured, governing the asymptotic behavior of the (normalized) stiffness reduction, see Fig. 5.4b. Evaluating the CDI (5.2) for the considered case at hand, we find the upper bound for the damage variable w. r. t. Puck case I to be $q_{\mathrm{I}} \leq \sqrt[m]{\sigma_{11}^2/H^2}$.

The effect of changing the hardening parameter H on the stress and damage evolution is shown in Fig. 5.5. As the damage-activation threshold σ_0 remains unchanged for this study, the elastic regions (σ_{11} below $30\,\mathrm{MPa}$) coincide for all stress-strain curves, see Fig. 5.5a.

(a) Stress-strain curve

(b) Normalized Young's modulus vs. strain
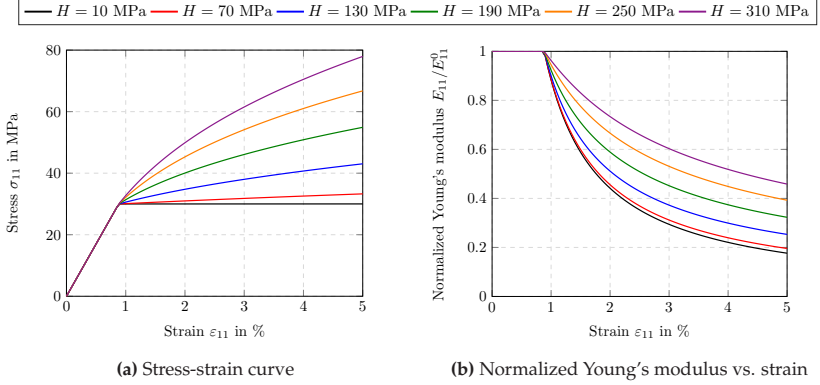
Figure 5.5: Varying the hardening parameter H for the proposed model

In the damage region, the slope of the stress-strain curve increases with the hardening parameter H. Indeed, the hardening parameter H describes the hardening capacity of the model. For $H \to 0$, the slope tends to zero and approaches the plateau already observed in Fig. 5.4a. For $H \to \infty$, an active damage function f $(5.33)_1$ will become inactive for small values of the damage variable $q \to 0$, resulting in a damage region that can hardly be distinguished from a purely elastic material behavior.

Independent of the hardening parameter, damage evolution initiates at the same strain level (and therefore the same stress level), see Fig. 5.5b. The stiffness reduction is inversely proportional to the hardening parameter H.

In Fig. 5.6, we fix the damage-activation threshold σ_0 as well as the hardening parameter H and vary the power-law exponent m. In contrast to the influence of the hardening parameter H (see Fig. 5.5), the slope of the stress-strain curve is inversely proportional to the exponent m in the damage region, see Fig. 5.6a.

(a) Stress-strain curve

(b) Normalized Young's modulus vs. strain
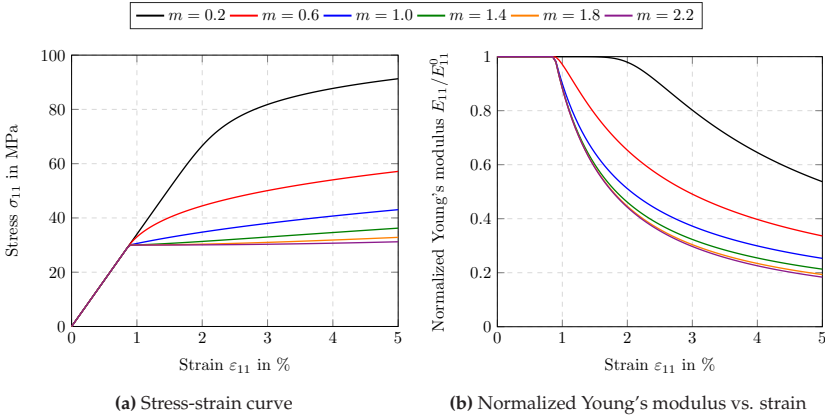
Figure 5.6: Varying the power-law exponent m for the proposed model

For increasing exponents m, the stress-strain curves approach the plateau-like behavior. For small values of m, after exceeding the damage-activation threshold σ_0, the stress-strain curves remain approximately linear and only develop a significant amount of damage for higher loading levels.

Fig. 5.6b shows the damage evolution to be inversely proportional to the exponent m, leading to a lower remaining (normalized) stiffness component E_{11} for higher exponents m.

For representing the stiffness tensor $\mathbb{C} = \mathbb{S}^{-1}$ graphically, we use the Young's modulus surface (YMS) plots introduced by Böhlke and Brüggemann (2001), i. e., for fixed compliance tensor $\mathbb{S} \in \mathcal{S}_d$, the image of the nonlinear mapping

$$S^2 \to \mathbb{R}^3, \quad \boldsymbol{n} \mapsto E(\mathbb{S}, \boldsymbol{n}) \, \boldsymbol{n}, \tag{5.75}$$

where the Young's modulus $E(\mathbb{S}, \boldsymbol{n})$ in direction $\boldsymbol{n}$ is determined by

$$E(\mathbb{S}, \boldsymbol{n}) = \frac{1}{(\boldsymbol{n} \otimes \boldsymbol{n}) \cdot \mathbb{S}\left[\boldsymbol{n} \otimes \boldsymbol{n}\right]}. \tag{5.76}$$

Asymmetry properties of the stiffness tensor $\mathbb{C}$ become apparent in the corresponding YMS plot. Examples of such YMS plots are shown in Fig. 5.7.

(a) Initial isotropic state   (b) Final anisotropic state
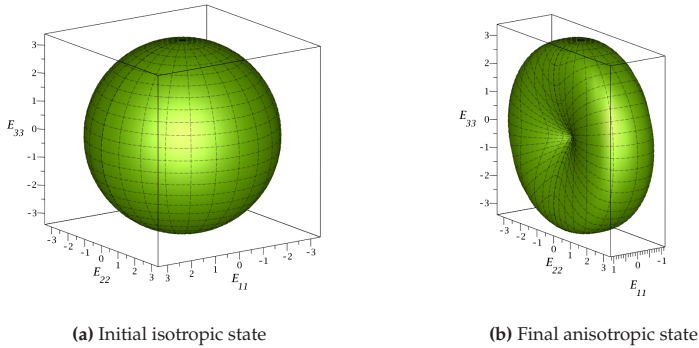
Figure 5.7: YMS plots (see Böhlke and Brüggemann (2001)) showing the reduction of the stiffness tensor based on Puck case I

The initially isotropic stiffness tensor with UPPH material parameters (see Tab. 5.1) has a spherical shape, as shown in Fig. 5.7a. As discussed above, the induced damage model based on Puck case I leads to a reduction of the stiffness E_{11} in the $\boldsymbol{e}_1$-direction. The YMS plot is contracted in the direction of loading, whereas the directional Young's moduli in the orthogonal plane remain unaffected, see Fig. 5.7b.

Stiffness reduction for different Puck-type extraction tensors

In the following, we will discuss possible damage evolutions and corresponding stiffness reductions based on Puck-type extraction tensors II, III and IV (see Sec. 5.3). For these cases, the influence of the damage-hardening parameters σ_0, H and m is similar to case I, which we discussed in Sec. 5.4.2. We consider an initially isotropic stiffness tensor with UPPH material parameters. The corresponding YMS plot is shown in Fig. 5.7a. Specific loadings will evoke a damage evolution due to the Puck cases II, III and IV. We apply a normal strain ε_{22} for case II, a shear strain ε_{23} for case III and a shear strain ε_{13} for case IV, forcing the respective complementary stress components to zero. The resulting YMS plots are shown in Fig. 5.8.

(a) Case II (b) Case III (c) Case IV
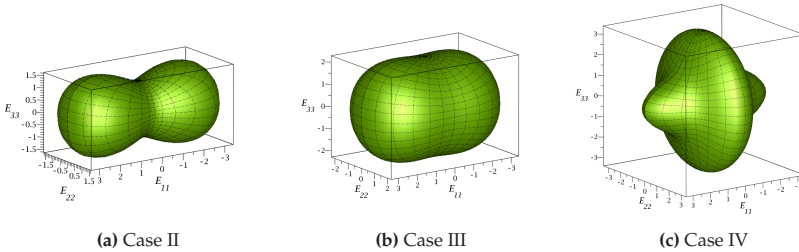
Figure 5.8: YMS plots (see Böhlke and Brüggemann (2001)) illustrating the reduction of the stiffness tensor based on the Puck cases II, III and IV

For all three cases the Young's modulus in e_1-direction remains unchanged. As shortly discussed in Sec. 5.3.4, Puck cases II and III are interlinked due to similar effects of averaged normal loadings and shear loadings perpendicular to the fiber direction. Inspecting Figs. 5.8a and 5.8b, corresponding to Puck cases II and III, we observe a reduction of the Young's moduli within the e_2-e_3-plane for both cases, but with different characteristics. For the loading scenarios considered here, the

stiffness reduction in directions e_2 and e_3 is more pronounced for Puck case II compared to Puck case III. Fig. 5.8c shows that damage based on Puck case IV does not affect the Young's moduli in the e_2-e_3-plane. Young's moduli in the e_1-e_3-plane and e_1-e_2-plane are reduced equally, leading to a transversely isotropic stiffness with the fiber direction e_1 as the axis of symmetry.

Non-monotonic loading

To show the capabilities of our model in general, we perform loading-unloading experiments for different loading directions in a successive fashion. To mimic uniaxial normal loadings and corresponding shear loadings, we subsequently apply normal and shear strains ε_{11}, ε_{22}, ε_{33}, ε_{23}, ε_{13} and ε_{12}, each with mixed boundary conditions permitting solely the corresponding stresses σ_{11}, σ_{22}, σ_{33}, σ_{23}, σ_{13} and σ_{12}, to be non-zero, see Fig. 5.9a and Fig. 5.9b. Lateral contraction is permitted. Between each of these six loading steps we unload to zero strain and stress.

(a) Strain vs. time   (b) Stress vs. time   (c) Damage evolution vs. time
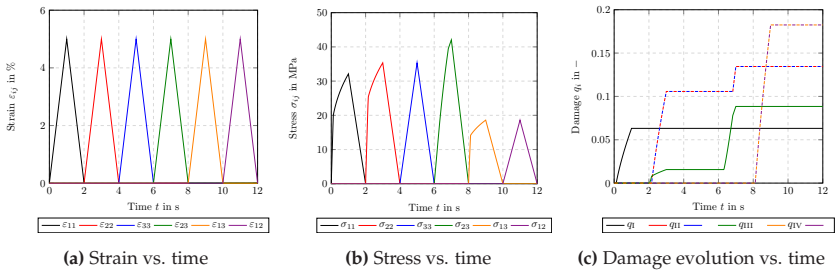
Figure 5.9: Complex loading history addressing each stress-tensor component separately

The resulting evolution of the stress components is plotted in Fig. 5.9b. We see a linear elastic region for each individual loading step and a damage region for all but the σ_{33} and σ_{12} cases. On these occasions, the

threshold for damage initiation is not triggered. As all normal loadings in the e_2-e_3-plane evoke damage due to case II, σ_{33} cannot induce damage beyond the level previously induced. The stress-strain curves for the shear stresses σ_{13} and σ_{12} exhibit a similar behavior. These observations are also reflected in the damage evolution, see Fig. 5.9c. Due to the applied stress σ_{22}, the damage variable representing case II increases. For increasing stress σ_{33}, the damage variables remain unaffected up to the level $\sigma_{33} = \sigma_{22}$. The same line of argument applies to σ_{13} and σ_{12}. Again, we observe the connection between Puck cases II and III, i.e., each of the damage variables increases whenever a loading scenario is applied which progresses the other case.
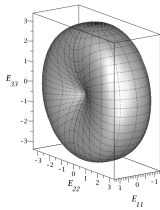
(a) Loading step 1 (ε_{11})
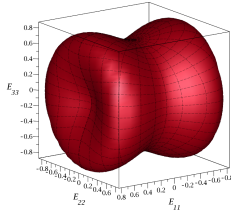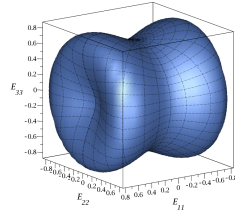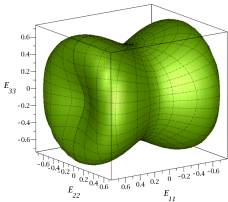
(b) Loading step 2 (ε_{11} and ε_{22})

(c) Loading step 3 (ε_{11}, ε_{22} and ε_{33})

(d) Loading step 4 (ε_{11}, ε_{22}, ε_{33} and ε_{23})

(e) Loading step 5 (ε_{11}, ε_{22}, ε_{33}, ε_{23} and ε_{13})
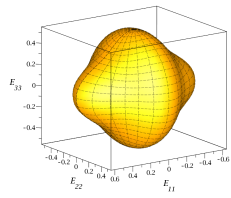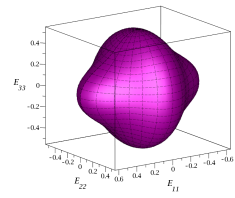
(f) Loading step 6 (ε_{11}, ε_{22}, ε_{33}, ε_{23}, ε_{13} and ε_{12})

Figure 5.10: Evolution of an initially isotropic stiffness upon complex loading, see Fig. 5.9a, visualized via YMS plots

The damaged stiffness tensors corresponding to each loading step are visualized via their YMS plots in Fig. 5.10. The different colors of the plots represent the different loading steps shown in Fig. 5.9. Note that the ranges of the axes are adjusted accordingly and therefore vary from plot to plot as the damage increases from step to step.

Comparing Fig. 5.10b and Fig. 5.10c, as well as Fig. 5.10e and Fig. 5.10f, we see that, in accordance with Fig. 5.9c, no further damage is induced between these loading steps. The presented YMS plots demonstrate the capability of our model to evolve the stiffness tensor in a complex and anisotropic way. The model is capable of handling *any* initial stiffness, not restricted by a specific symmetry class, i. e., transversely isotropic or orthotropic. Furthermore, the stiffness tensor may also develop anisotropy – within the permissible set $\mathcal{S}_d$ (5.8) – as a result of a damaging process, owing to the introduced damage functions.

Multiaxial loading with increasing loading level

In a study combining the six loading steps from the previous section 5.4.2 to one superposed loading case, we apply a three-dimensional strain state s. t. all strains are active simultaneously. To investigate the model behavior, the predicted stiffness degradation, as well as the evolution of the damage variables more closely, we gradually increase the strain levels in five steps from 0 % to 5 % via 1 % increments with intermediate unloading, see Fig. 5.11a.

As in Sec. 5.4.2, we analyze the stress and the damage evolution, as well as the stiffness reduction. Fig. 5.11b shows the evolution of the individual stress components during the combined loading. We see that after each loading-unloading step the level of damage increases. This is also reflected in the evolution of the damage variables, see Fig. 5.11c. After each loading-unloading step, the damage variables continue to increase whenever the maximum stresses of the previous step are exceeded.

(a) Strain vs. time   **(b)** Stress vs. time   **(c)** Damage evolution vs. time
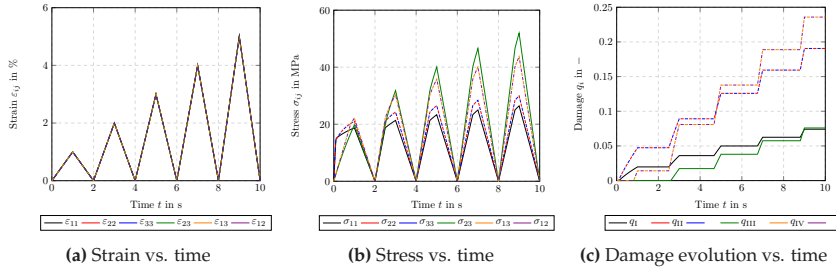
Figure 5.11: Step wise increase of multiaxial loading to evoke all stresses and damage functions simultaneously

(a) Strain 0 %   **(b)** Strain 2 %   **(c)** Strain 5 %
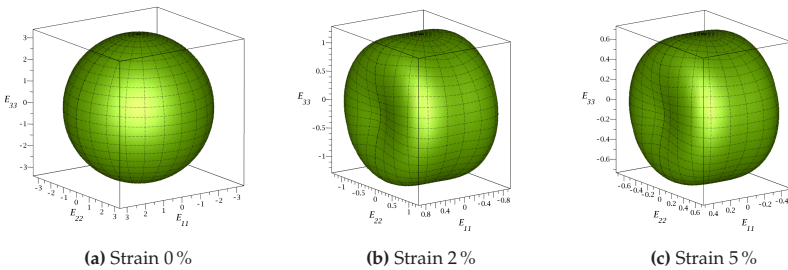
Figure 5.12: Evolution of an initially isotropic stiffness during multiaxial loading steps, visualized via YMS plots

The YMS plots corresponding to $2\,\%$ and $5\,\%$ loading, as well as the initially isotropic YMS plot, are shown in Fig. 5.12. The stiffness tensor gradually reduces based on all four introduced Puck cases (see Sec. 5.3) simultaneously. Apparently, the multiaxial loading evokes a stiffness reduction in all directions, as we observe a superposition of the individual loading scenarios investigated in Sec. 5.4.2 and Sec. 5.4.2. Please note, that, similar to the previous section, the ranges of the axes are adjusted accordingly and therefore vary from plot to plot.

Cyclic tensile loading with increasing loading level

We conduct an analysis of the model response upon cyclic loading via uniaxial extension. We successively apply a normal strain ε_{11} to induce cyclic uniaxial loading in the $\boldsymbol{e}_1$-direction. We apply the strain ε_{11} in five cycles from $0\,\%$ to $5\,\%$ with an increasing magnitude of $1\,\%$ per cycle. For this analysis, we restrict to Puck case I. The resulting stress-strain curves and damage-strain curves are shown in Fig. 5.13.

(a) Stress-strain curve **(b)** Damage-strain curve
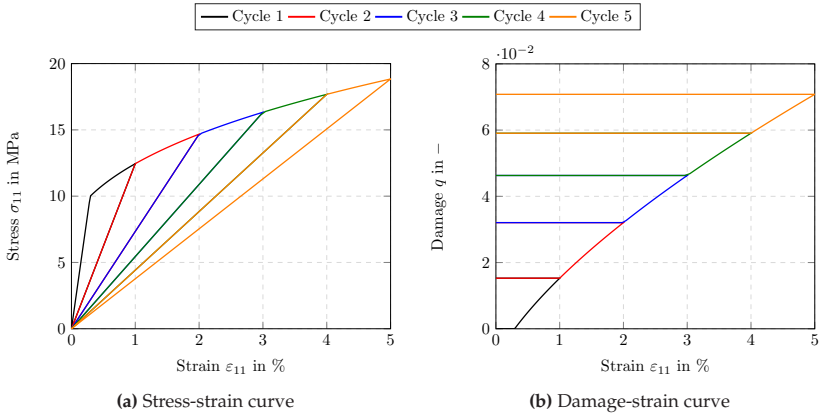
Figure 5.13: Cyclic tensile loading with increasing loading level for Puck case I

Upon loading, the material behaves linear elastically until a specific critical stress threshold or the maximum stress of the previous cycle is reached, see Fig. 5.13a. During the in-between unloading to $\varepsilon_{11} = 0\,\%$ and reloading, the damage variables do not evolve further. Besides, the pure damaging character of the model is highlighted, as no remaining residual strains occur. The step wise evolution of the damage variable q is shown in Fig. 5.13b.

Note that the presented model is capable to predict damage onset upon both, tensile and compressive loading. Due to the definition of the damage functions the quadratic nature of the driving force $\mathbb{T}$ (5.18), the damage evolution is driven in similar fashions by both, tensile and compressive stresses. Considering a single damage variable q for, both, the tensile and the compressive regime, would lead to a combined damage evolution. Accounting for tension-compression asymmetry requires an extension of the model at hand, see the conclusion.

5.4.3 Response for a continuous fiber microstructure

Application of separate loading cases

After discussing the model response for homogeneous stress states, we account for heterogeneous stress states in two ways to show the basic feasibilities of our damage model. First, we shall investigate a microstructure with a continuous fiber reinforcement. In the next sections, we will turn our attention to mesoscale simulations.

To account for damage evolution in the matrix, we introduce two extraction tensor corresponding to the spherical and deviatoric projectors of fourth-order

$$\mathbb{B}_{\mathrm{sph}} = \mathbb{P}_1 = \frac{1}{3} \boldsymbol{I} \otimes \boldsymbol{I}, \quad \mathbb{B}_{\mathrm{dev}} = \mathbb{P}_2 = \mathbb{I}^{\mathrm{S}} - \mathbb{P}_1, \qquad (5.77)$$

that allow describing a damage evolution in response to dilatation and distortion. We use damage-activation functions based on these two extraction tensors (5.77) and corresponding damage parameters $\sigma_0 = 30$ MPa, $H = 130$ MPa and $m = 1$ for both cases. Furthermore, the matrix of the fiber reinforced microstructure is endowed with the elastic properties of UPPH, as defined in Tab. 5.1. The fibers are modeled in a purely elastic fashion using the elastic moduli of E-glass, see Tab. 5.1. The continuous-fiber reinforced microstructure

is geometrically modeled by 50 inclusions with a diameter of $13\,\mu m$ and a total volume fraction of about $40\,\%$. We generated the microstructure by the adaptive shrinking-cell algorithm of Torquato and Jiao (2010). The setup represents aligned fibers in a UPPH matrix as present in SMC composite bundles (Meyer et al., 2020; Kim et al., 2011b), where the fiber direction e_1 coincides with the primary direction of the Puck cases.

In three different loading scenarios, we apply three different macroscopic strains via mixed boundary conditions, see Kabel et al. (2016) for details. For each scenario, we analyze the induced damage fields of the associated variables q_{sph} and q_{dev}. In scenario 1, we apply the macroscopic normal strain $\bar{\varepsilon}_{22}$ perpendicular to the fiber direction (in horizontal direction). In scenarios 2 and 3, we apply macroscopic shear strains $\bar{\varepsilon}_{12}$ and $\bar{\varepsilon}_{23}$, in fiber direction and transverse to the fiber direction.

(a) Loading $\bar{\varepsilon}_{22}$, q_{sph} **(b)** Loading $\bar{\varepsilon}_{12}$, q_{sph} **(c)** Loading $\bar{\varepsilon}_{23}$, q_{sph}

(d) Loading $\bar{\varepsilon}_{22}$, q_{dev} **(e)** Loading $\bar{\varepsilon}_{12}$, q_{dev} **(f)** Loading $\bar{\varepsilon}_{23}$, q_{dev}
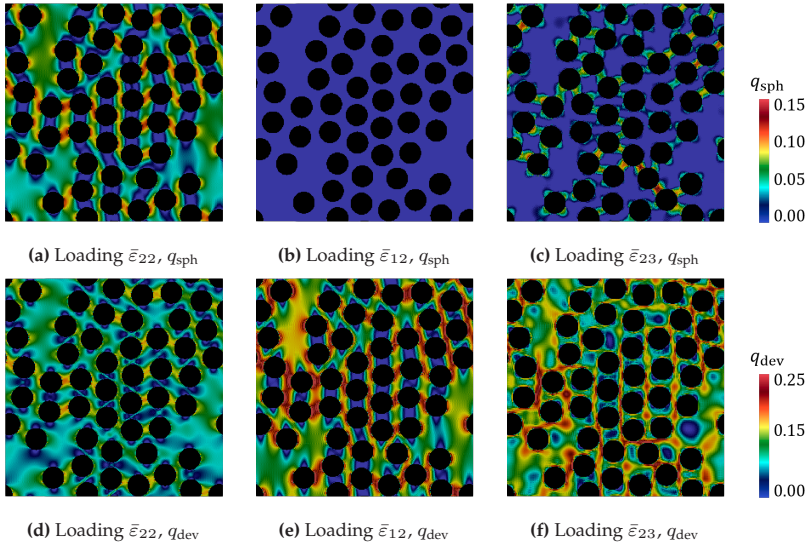
Figure 5.14: Model response for a continuous-fiber reinforced microstructure based on spherical and deviatoric damage and three different loading cases

The average runtime for a resolution of 256×256 pixels and 50 time steps was about 100 s on 12 threads. An accompanying resolution study is discussed in Sec. 5.4.3. Fig. 5.14 shows the damage fields for q_{sph} and q_{dev} for the introduced cases and corresponding to the different loading scenarios.

Fig. 5.14a shows that normal loading perpendicular to the fiber direction leads to a dilatation-triggered damage evolution in the respective direction, as a result of stress concentrations at the inclusion boundaries. As a consequence of the complexity of the induced stress state, damage due to distortion is initiated, as well, see Fig. 5.14a. In general, the stress level is higher for regions with more closely packed inclusions, inducing a significantly higher level of damage in those regions. Damage initiates at the inclusion boundaries and evolves in the loading direction, deflected by other inclusions. Shear loading in fiber direction leads to an associated damage evolution due to distortion, as shown in Fig. 5.14e. As the applied shear is oriented in fiber direction, the deformation is not hindered by these fibers and spherical stresses do not occur. Hence, damage due to dilatation does not evolve, see Fig. 5.14b. Applying a macroscopic shear perpendicular to fiber direction evokes both, the evolution of damage due to spherical stresses, see Fig. 5.14c, as well as deviatoric stresses, see Fig. 5.14f.

Resolution study

The presented resolution study demonstrates that the proposed damage model leads to mesh-independent results even without gradient enhancement. This does not come by surprise, as we specifically designed such a hardening-type damage model. Still, even in the case of hardening, a resolution study is imperative to ensure mesh-independent results. In particular, we will justify the resolution employed in Sec. 5.4.3. Fig. 5.15 shows a continuous-fiber reinforced microstructure with the same properties as for Fig. 5.14. We vary the resolution from 64×64

to 1024×1024 pixels. Similar to scenario 1, see Fig. 5.14a, we apply a macroscopic strain $\bar{\varepsilon}_{22}$ for all resolutions, so that both damage cases, i. e., dilatation and distortion, are being activated. The strain is successively increased from $0\,\%$ to $5\,\%$ within 50 equidistant loading steps.

The resulting distribution of the predominant damage variable q_{sph} for damage due to dilatation is shown in Fig. 5.15. We observe that areas of low and high damage level are captured also for low resolution, but there are slight differences in the achieved damage level. Also, as expected, localization behavior is not evident.

(a) 64^2 (b) 128^2 (c) 256^2

(d) 512^2 (e) 1024^2

q_{sph}
0.15
0.10
0.05
0.00
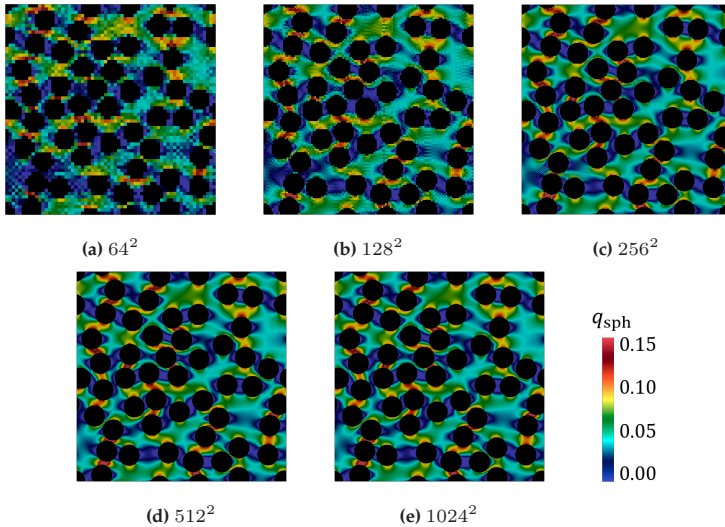
Figure 5.15: Model response for a continuous-fiber reinforced microstructure evaluated at five different resolutions

To get a more qualitative insight, the macroscopic stress-strain curves are shown in Fig. 5.16a. For a resolution of 64×64 pixels, the computed stresses are overestimated. For higher resolutions with 128×128

to 1024×1024 pixels, the differences are small. Investigating the relative deviations $\left(\bar{\sigma}_{22}^{\mathrm{reso}} - \bar{\sigma}_{22}^{1024}\right)/\bar{\sigma}_{22}^{1024}$ of the computed effective stress $\bar{\sigma}_{22}$ relative to the stress at a resolution of 1024×1024, see Fig. 5.16b, we observe that, for resolutions with 256×256 pixels and higher, the deviations are below $1\,\%$.

(a) Stress-strain curve

(b) Relative stress deviation w.r.t. $\bar{\sigma}_{22}$ for 1024^2 pixels
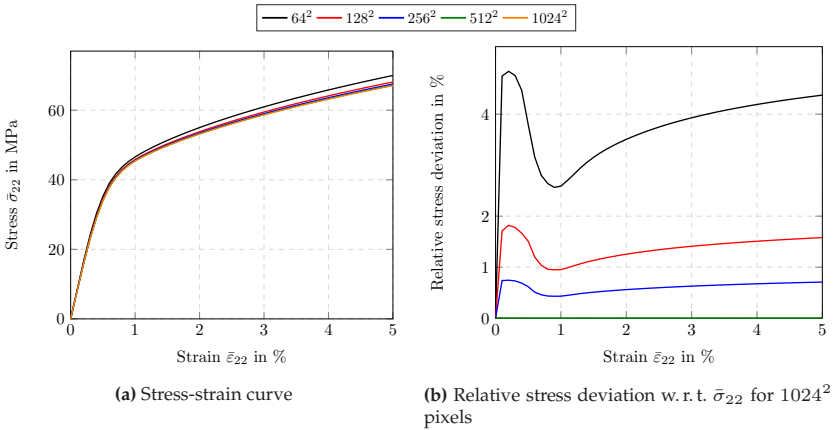
Figure 5.16: Resolution study for the continuous-fiber reinforced microstructure

The iteration counts and timings are collected in Tab. 5.2. The total outer iterations (including Newton and CG iterations) for all loading steps vary in a narrow window around approximately $2\,950$ for all resolutions considered. To give a comparable standard for the inner (material) iterations, we compute the average number of inner iterations over all voxels and subsequently take the maximum value over all loading steps. A value of about 2.8 inner iterations per voxel, irrespective of the resolution, indicates quadratic convergence of the Newton method. Both, the overall timing for computing all inner iterations, as well as the total timing, increase roughly with the degrees of freedom.

Based on this resolution study, a resolution of 256×256 pixels represents a compromise between an accurate prediction and a short runtime, see Sec. 5.4.3.

Table 5.2: Iterations and timings for the conducted resolution study

resolution	iterations		timings	
	total outer	max. average inner	t_{inner}	t_{total}
64^2	2953	2.774	2 s	9 s
128^2	2897	2.814	6 s	26 s
256^2	3012	2.843	22 s	108 s
512^2	3023	2.853	88 s	524 s
1024^2	2987	2.858	352 s	1793 s

5.4.4 Tensile tests of bone specimens with different fiber bundle orientations

As a first macroscopic example, we compute the predicted damage evolution for a tensile bone specimen (see Fig. 5.17) with aligned E-glass fibers in a surrounding UPPH matrix. We assume the fibers to be arranged as fiber bundles with a volume fraction of $50\,\%$, as discussed in Görthofer et al. (2020), see also Sec. 4.3.2. The resulting (effective) transversely isotropic stiffness parameters are listed in Tab. 5.3.

Table 5.3: Material parameters for the transversely isotropic SMC composite fiber bundles

E_{L}	E_{T}	G_{LT}	ν_{LT}	ν_{TT}
37.73 GPa	10.33 GPa	3.64 GPa	0.292	0.477

We model the tensile bone specimen in the commercial FE software ABAQUS/Standard (Dassault Systèmes, 2014) by a C++ user material subroutine, as stated in Sec. 5.4.1. The specimen is subjected to a displacement-controlled loading in e_1-direction up to a strain of $5\,\%$, as shown in Fig. 5.17a. We vary the orientation of the fiber bundles from $0°$ to $90°$ in the e_1-e_2-plane (see Fig. 5.17b) and evaluate the stiffness evolution due to damage. We consider all four Puck cases with damage-hardening parameters as listed in Tab. 5.1. The hardening parameter for case I is set to $230\,\mathrm{MPa}$ to delay the respective damage evolution. We exploit the symmetry of the tensile bone specimen and model only one eighth of the part, as shown in Fig. 5.17a. The average runtime for 11375 fully integrated continuum eight-node brick elements (C3D8) and 100 steps is about $120\,\mathrm{s}$ to $180\,\mathrm{s}$ on 6 threads.

(a) Loading and dimensions in mm

(b) Considered orientations in discussed analysis (see Fig. 5.18 - Fig. 5.21, cases (a) - (d) each)
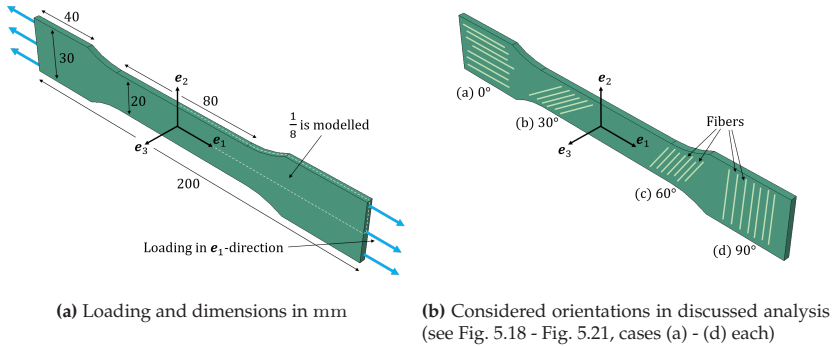
Figure 5.17: Tensile bone specimen with different material orientations

We compute the direction-dependent Young's moduli via equation (5.76) and normalized each w.r.t. the initial Young's modulus in the corresponding direction, similar to Sec. 5.4.2. This provides a scalar value E/E_0 between 1 and 0 for each evaluated direction, with $E/E_0 = 1$ if the material (point) is sound and $E/E_0 = 0$ for a totally damaged

material (point). We plot the resulting distributions of the normalized Young's moduli for the global coordinate system directions (e_1, e_2 and e_3) in Fig. 5.18 - Fig. 5.20, respectively.

In Fig. 5.18 we see the reduction of the normalized Young's modulus in loading direction e_1. The damage in bundle direction is proportional to the amount of fiber bundles that are aligned to the loading direction. As shown in Fig. 5.7 (see Sec. 5.4.2) damage in bundle direction results from stress in the respective direction based on Puck case I. If all bundles are aligned perpendicular to the loading direction (see Fig. 5.18d) the material is damaged due to Puck cases II and III. Based on the considered material parameters, the reduction of the normalized Young's modulus is less pronounced for these cases compared to case I. Fig. 5.18b and Fig. 5.18c, with bundles being rotated $30°$ and $60°$ about the e_3-axis, exhibit a combined damage evolution due to cases I, II and III. The resulting normalized Young's modulus in e_1-direction decreases with a decreasing influence of case I and subsequently increases again with increasing influence of cases II and III.

(a) $0°$ rotation   **(b)** $30°$ rotation   **(c)** $60°$ rotation   **(d)** $90°$ rotation
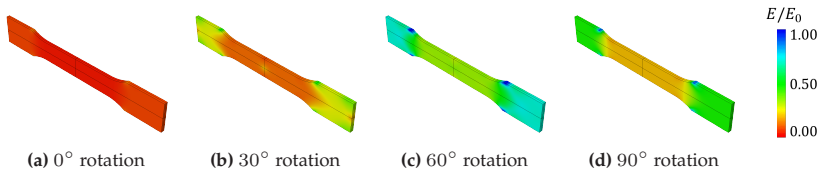
Figure 5.18: Normalized Young's modulus in e_1-direction for different fiber bundle orientations

The normalized Young's modulus in e_2-direction is shown in Fig. 5.19. We see a normalized Young's modulus of value 1 for fiber bundles which are aligned to the e_1-direction (see Fig. 5.19a) and for a rotation of $90°$ (see Fig. 5.19d). Either Puck case I or cases II and III are active in loading direction e_1 (but no combination!) and, therefore, the normalized

Young's modulus in e_2-direction for these two bundle orientations remains unaffected. If the bundles are aligned in $30°$ or $60°$ about the e_1-axis, a combination of cases I - III will be active, leading to a reduction of the normalized Young's modulus in e_2-direction (see Fig. 5.19b and Fig. 5.19c).

(a) $0°$ rotation   **(b)** $30°$ rotation   **(c)** $60°$ rotation   **(d)** $90°$ rotation
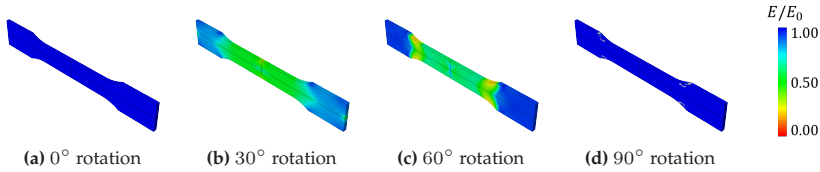
Figure 5.19: Normalized Young's modulus in e_2-direction for different fiber bundle orientations

The normalized Young's modulus evaluated in e_3-direction is shown in Fig. 5.20. Similar to the e_2-direction, we observe no damaging in the considered direction, provided the bundles are aligned in loading direction e_1, as only Puck case I is active. The corresponding normalized stiffness has the value 1 in Fig. 5.20a. Due to the definition of the Puck cases, involving an averaging procedure, stiffness degradation perpendicular to the fiber directions (cases II and III) is interlinked, as discussed in Sec. 5.3.4 and Sec. 5.4.2. Consequently, damage in e_3-direction is proportional to the rotation angle of the bundle orientation, see Fig. 5.20b - Fig. 5.20d. This is a direct consequence of the increasing influence of Puck cases II and III. As the bundle orientation varies based on a rotation around the e_3-axis, this direction always remains perpendicular to the fiber direction. Hence, the normalized Young's moduli evaluated in directions e_3 and e_2 differ, especially for a bundle orientation of $90°$, compare Fig. 5.20d and Fig. 5.19d.

In addition to evaluating the damaged stiffness w. r. t. the global axes (e_1, e_2 and e_3), we would like to analyze the stiffness degradation

(a) $0°$ rotation   **(b)** $30°$ rotation   **(c)** $60°$ rotation   **(d)** $90°$ rotation
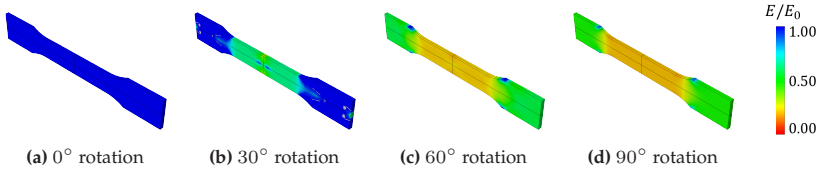
Figure 5.20: Normalized Young's modulus in e_3-direction for different fiber bundle orientations

w. r. t. the local axes, namely in bundle direction ($0°$, $30°$, $60°$ and $90°$) and perpendicular to the bundle direction. Fig. 5.21 shows the distribution of the normalized Young's modulus evaluated in the bundle direction. Provided the bundles are aligned to the loading direction e_1, the local bundle axis and the global e_1-axis coincide, as do the resulting normalized Young's moduli, see Fig. 5.21a and Fig. 5.18a.

The further we rotate the bundle direction away from the loading direction, the higher is the remaining normalized Young's modulus in bundle direction. As damage in bundle direction is solely caused by Puck case I (see Sec. 5.4.2 and Sec. 5.4.2), the respective damage variables do not evolve if all fibers are aligned perpendicular to the loading direction, see Fig. 5.21d.

(a) $0°$ rotation   **(b)** $30°$ rotation   **(c)** $60°$ rotation   **(d)** $90°$ rotation
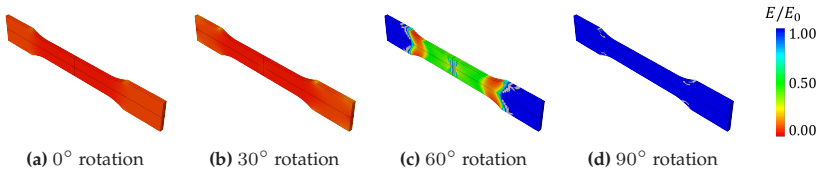
Figure 5.21: Normalized Young's modulus in fiber direction for different fiber bundle orientations

For the setup considered, the normalized Young's modulus perpendicular to the bundle direction is the normalized Young's modulus in e_3-direction, as already discussed above. Hence, the distributions of the normalized stiffness perpendicular to the fiber direction are shown in Fig. 5.20. If all bundles are aligned to the loading direction (see Fig. 5.20a), no damage perpendicular to the bundles will evolve, in contrast to Fig. 5.21. The normalized Young's modulus perpendicular to the bundle direction increases with increasing orientation angle. If all bundles are aligned perpendicular to the loading direction (see Fig. 5.20d), the corresponding damage perpendicular to the bundle direction is highest, which is a direct consequence of Puck cases II and III.

5.4.5 A plain-weave composite under shear loading

(a) Voxelized weave microstructure with four tows

(b) Relative reduction (5.81) of shear modulus G_{12}
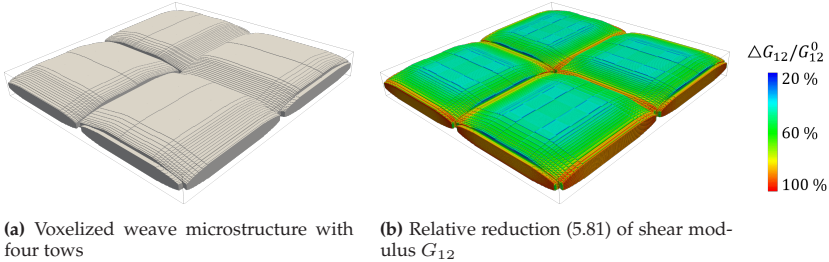
Figure 5.22: Microstructure and predicted relative reduction of the shear modulus G_{12} in a plaine weave composite

Last but not least, we demonstrate the utility of our model framework for modeling anisotropic damage evolution in a woven fiber reinforced composite. Simon et al. (2017) investigated the mechanical behavior of a plain-weave composite manufactured from continuous carbon fibers reinforcing an epoxy matrix resin, see Fig. 5.22a. The carbon fibers are

aligned unidirectionally in fiber tows that are regularly interwoven. As each of these tows consists of thousands of carbon fibers, it is customary to work with a multiscale scheme that considers three different scales: the macroscopic scale is large compared to the woven unit cell, see Fig. 5.22a, which constitutes the mesoscale. Within the latter, the tows are considered homogeneous and anisotropic. On the microscale, the tows get resolved in terms of continuous carbon fibers in an epoxy resin. The linear elastic moduli of the considered materials are listed in Tab. 5.4.

Table 5.4: Elastic moduli of matrix, fibers and tows (Simon et al., 2017, Tab. 1 & 2)

	Young's modulus in GPa			shear modulus in GPa			Poisson's ratio		
epoxy	E	$=$	3	G	$=$	1.09	ν	$=$	0.38
fibers	E_L	$=$	290	G_{LT}	$=$	20	ν_{LT}	$=$	0.2
	E_T	$=$	20	G_{TT}	$=$	9	ν_{TT}	$=$	0.11
tows	E_L	$=$	144	G_{LT}	$=$	2.58	ν_{LT}	$=$	0.29
	E_T	$=$	7.84	G_{TT}	$=$	1.91	ν_{TT}	$=$	0.39

These comprise the isotropic epoxy matrix and the transversely isotropic carbon fibers. The transversely isotropic engineering constants for the tows were obtained by linear elastic homogenization. Please note that the subscripts "L" and "T" refer to longitudinal and transverse, respectively.

Based on earlier work (Stier et al., 2015; Bednarcyk et al., 2015; 2014), Simon et al. (2017) presented a regularized orthotropic continuum damage-model based on the framework developed by Barbero and co-workers (Barbero and Lonetti, 2002; Lonetti et al., 2003; 2004)) and concisely summarized in his book (Barbero, 2013). More precisely, their strategy takes the orthotropic engineering constants as the point of departure, and models their degradation on an individual basis in terms

of associated scalar damage variables. Based on the associated driving forces, damage surfaces are defined, together with appropriate kinetic laws.

Expressing the dependence of the stiffness tensor on the orthotropic engineering constants is most easily realized in terms of the compliance tensor, the approach of Simon et al. (2017) appears superficially similar to our approach. However, we do not fix the damage variables a priori. Rather, they emerge naturally in our framework based on the chosen extraction tensors and damage-activation functions.

In this paragraph, we demonstrate that our model is capable of reproducing the damage behavior upon quasi-static loading of the weave composite. The protocol we present is straightforward and proceeds step by step. As a first step, we introduce a number of extraction tensors which capture elementary damage cases evoked by pure normal- and shear-loading scenarios. The tensors extract the associated normal and shear stress components from the applied stress state $\boldsymbol{\sigma}$. These extraction tensors are uncoupled. Hence, damage in a certain direction is solely driven by the associated loading case, e. g., normal damage in $\boldsymbol{e}_1$-direction due to normal loading in $\boldsymbol{e}_1$-direction,

$$\mathbb{B}_{11} = \boldsymbol{e}_1^{\otimes 4}, \qquad \mathbb{B}_{22} = \boldsymbol{e}_2^{\otimes 4}, \qquad \mathbb{B}_{33} = \boldsymbol{e}_3^{\otimes 4}, \qquad (5.78)$$

$$\mathbb{B}_{23} = (\boldsymbol{e}_2 \otimes_S \boldsymbol{e}_3)^{\otimes 2}, \quad \mathbb{B}_{13} = (\boldsymbol{e}_1 \otimes_S \boldsymbol{e}_3)^{\otimes 2}, \quad \mathbb{B}_{12} = (\boldsymbol{e}_1 \otimes_S \boldsymbol{e}_2)^{\otimes 2}. \qquad (5.79)$$

Combining suitable damage-activation functions based on these extraction tensors permit modeling a wide range of damage-evolution predictions. In particular, they enable us to describe the stiffness reduction for the scenario considered by Simon et al. (2017).

We first capture the damage evolution in a neat epoxy sample under non-monotonic uniaxial loading and choose an extraction tensor of type (5.78)$_1$. Subsequently, we account for the damage onset due to shear

loading by using a second damage-activation function in combination with an extraction tensor of type $(5.79)_3$. The identified parameters for the epoxy damage-model are summarized in Tab. 5.5, which were chosen to reproduce the results of Simon et al. (2017) best.

Furthermore, we employ a number of damage-activation functions and suitable extraction tensors to capture the damage evolution in the fiber tows. We fix the the longitudinal tow direction to correspond to the local e_1-direction. The response to shear loading in longitudinal and transverse directions is best described with extraction tensors of the forms $(5.79)_1$ and $(5.79)_3$. As the reduction of the two orthotropic Young's moduli in the transverse plane (and hence the associated damage evolutions) is not identical, we introduce an additional extraction tensor

$$\mathbb{B} = 4\,e_2^{\otimes 4} + e_3^{\otimes 4}, \tag{5.80}$$

which is supplemented by a fourth damage-activation function with an extraction tensor that drives damage in e_2-direction $(5.78)_2$ only. Tab. 5.5 comprises a complete list of the identified damage parameters.

Table 5.5: Extraction tensors and identified damage parameters to capture the mechanical behavior of epoxy and tow

	extraction tensor	σ_0 in MPa	H in MPa	m
epoxy	$(5.78)_1$	0.5	180	0.47
	$(5.79)_3$	101	41	0.97
tow	$(5.79)_1$	8	275	0.3
	$(5.79)_3$	10	245	0.3
	$(5.78)_2$	79	30	0.9
	(5.80)	200	630	0.4

The listed extraction tensors and damage parameters at hand allow us to reproduce the structural behavior of, both, the neat epoxy and the

tows, the latter in terms of stress-strain curves and the reduction of the orthotropic engineering constants. The corresponding results are shown in Fig. 5.23.
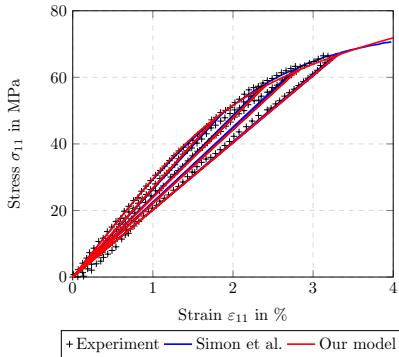
(a) Neat epoxy behavior under normal loading
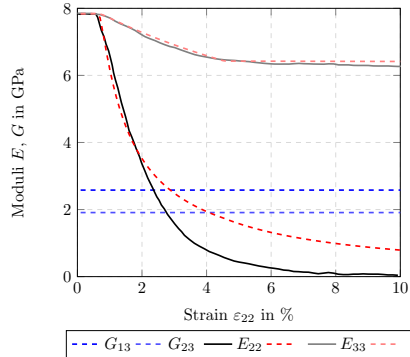
(b) Tow behavior under transverse normal loading
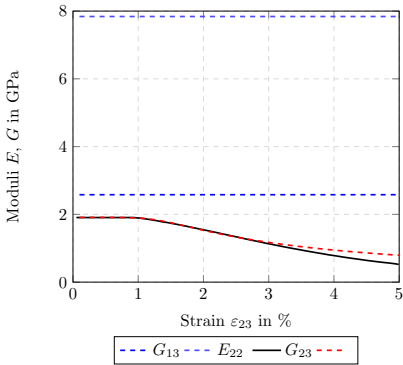
(c) Tow behavior under transverse shear loading
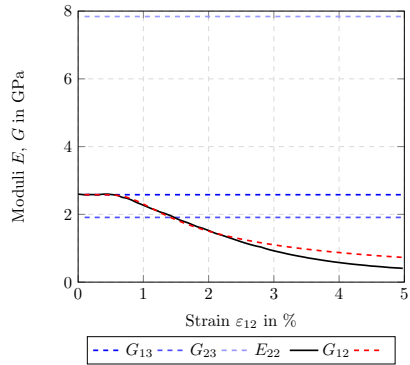
(d) Tow behavior under longitudinal shear loading

Figure 5.23: Comparison of predicted stress-strain curve and reductions of the orthotropic engineering constants based on introduced extraction tensors (see Tab. 5.5). Our model predictions are dashed in (b)-(d)

With the introduced extraction tensors and damage parameters at hand, we are able to reproduce the experimental results obtained for the neat epoxy resin, as well as the predictions computed by Simon et al. (2017) quite accurately, see Fig. 5.23a. The decrease in the individual orthotropic engineering-constants are shown in Fig. 5.23b to Fig. 5.23d, where dashed lines correspond to our model and solid lines refer to the references (Simon et al., 2017; Bednarcyk et al., 2015).

For all considered loading cases, our proposed framework makes it simple to account for those engineering constants which remain unaffected during the loading. Fig. 5.23b shows that the reduction of Young's modulus E_{33} is predicted correctly up to an applied strain of 10%. The shear moduli are predicted quite well up to a strain level of 5%, see Fig. 5.23c and Fig. 5.23d. Only the evolution of Young's modulus E_{22} shows some deviations beyond a strain level of 3%, as our model is unable to capture the slope of reduction accurately enough for this case. To sum up, the proposed framework permits reproducing the reduction of all affected engineering constants accurately for small deformations of up to 3%.

For the identified parameter set listed in Tab. 5.5, we investigate the plain-weave composite that was also studied by Simon et al. (2017), see Fig. 5.22a. The mesostructure, with a required tow-volume fraction of approximately 75%, was generated by a level-set approach developed by Sonon and co-workers (Sonon et al., 2012; Sonon and Massart, 2013; Wintiba et al., 2017)) and discretized on a regular grid with $512 \times 512 \times 56$ voxels.
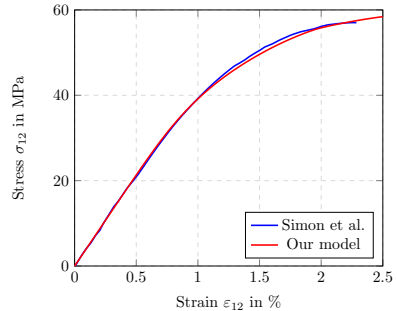
Figure 5.24: Comparison of effective stress-strain curves for plain weave under shear loading

Just as Simon et al. (2017), we investigate the longitudinal shear response of the plain-weave cell. For this purpose, we analyze the effective stress-strain curve, as well as the reduction of the shear modulus G_{12} measured in terms of the relative error

$$\triangle G_{12} = G_{12}^0 - G_{12} \tag{5.81}$$

w. r. t. the initial, undamaged shear modulus G_{12}^0. The predicted full-field distribution of this relative reduction is shown in Fig. 5.22b, and coincides well with the results presented by Simon et al. (2017), Fig. 9. Moreover, the effective stress-strain curves of the plain-weave composite subjected to longitudinal shear match well for the entire loading regime, see Fig. 5.24.

5.5   Conclusions

In this article, a generalized standard material (GSM) model for anisotropic damage evolution based on the compliance tensor as the primary damage variable was developed. Based on the insight that the Hookean elastic energy density, considered as a function of the elastic strain and the compliance tensor, is a convex function of both arguments, a convex framework for quasi-static damage evolution was established, preventing damage localization intrinsically. Indeed, by choosing the energy (density) related to the progressive degradation of the material appropriately, the condensed incremental potential (Miehe, 2002) is strictly convex and of superlinear growth, which prevents localization for such a model. Of course, working with a softening-type energy for the damage-surface variables is also possible, and should be studied more closely in subsequent work.

Section 5.2 is organized to emphasize the modular fashion that the compliance-based damage model is built up. The model might be

extended in subsequent work, for instance accounting for strain-rate sensitivity within the model. For an overview of the assumptions leading to specific specializations of the evolution of internal variables, we refer to the overview in Appendix B. The modeling framework is general enough to incorporate coupling to other inelastic models, such as plasticity or viscoplasticity (Rousselier, 1979; McDowell, 2008), entirely within the proposed framework. Also, due to its inherent stability, an extension to fatigue damage, as observed for certain fiber reinforced polymers (Sauer and Richardson, 1980; Bartkowiak et al., 2019; 2020), appears promising (Magino et al., 2022).

The modular character of the model was exemplified by specific extraction tensors motivated by Puck's anisotropic failure criteria (Puck and Schürmann, 2002; Knops, 2008), see Sec. 5.3. With these ingredients at hand, we demonstrated the model's capabilities of developing complex anisotropic stiffness states, see Sec. 5.4, not restricted a priori by a specific degree of (an)isotropy of the stiffness tensor, emphasizing that the model is capable of handling *any* initial stiffness. We also showed the model's capabilities on meso and volume-element scale, based upon a straightforward numerical treatment. With these achievements at hand, accounting for additional failure criteria (Kaddour et al., 2004; Fritzsche et al., 2008; Bouhala et al., 2013) or coupling the model to phase-field fracture models (Miehe et al., 2010; Schneider et al., 2016a; Gerasimov and De Lorenzis, 2019) appears possible.

Returning to our original motivation, i. e., modeling anisotropic damage of SMC composite materials, requires incorporating the presented modeling framework into a three-scale homogenization scheme (Anagnostou et al., 2018). The underlying fiber bundle mesostructure (Schöttl et al., 2021b; Meyer et al., 2020; Dumont et al., 2007) has to be accounted for, and the model parameters have to be fitted to experimental data. For the latter purpose, a convenient experimental program is necessary (Schemmann et al., 2018c).

From a mathematical perspective, a thorough mathematical analysis of our model is desirable, whereas an extension to tension-compression asymmetry appears imperative in order to model load reversals.

Chapter 6

A computational multiscale model for anisotropic failure of SMC composites[1]

6.1 Introduction

6.1.1 Research contributions

We present a holistic multiscale approach for constructing anisotropic criteria describing the macroscopic failure of SMC composites. The approach is based on full-field anisotropic damage evolution on the microscale, and the failure criteria emerge naturally by accounting for the evolving microscopic damage.

Based on findings of scientific studies, we evaluate experimental investigations regarding distributions of ultimate strength and stiffness reduction of sheet molding compound composite specimens. We summarize the characteristic microstructure, recapture micro-computed tomography analysis and the identification of linear elastic properties.

We use our anisotropic damage model introduced in Chapter 5 on the microscale. The model directly operates on the compliance tensor, captures matrix and bundle damage via dedicated stress-based damage

---

[1] This chapter is based on the publication "A computational multiscale model for anisotropic failure of SMC composites" (Görthofer et al., 2022a)

criteria and allows for a comparison of simulation and experimental results. To identify the damage material-parameters used in the non-linear and time-consuming full-field simulations, we utilize Bayesian optimization with Gaussian processes.

We validate the full-field predictions on the microscale and subsequently identify macroscopic failure criteria based on distributions taken from experimental findings. We propose failure surfaces in stress space and stiffness-reduction triggered failure surfaces to cover both a structural analysis and a design process perspectives.

6.1.2 Chapter structure

In this chapter, we introduce a methodology for identifying anisotropic failure surfaces to be used in component-scale simulations based on computational micromechanics. The presented multiscale approach allows for a scale-transition of full-field damage evolution within matrix and fiber bundles to an experimentally supported identification of application-based failure criteria for the SMC composite on the macroscale.

With the desire to apply SMC composites as load-bearing structural components in mind, we start this chapter by analyzing experimental investigations as well as simulation-based studies published by different research groups, cf., Fitoussi et al. (1996; 1998); Anagnostou et al. (2018), Chen et al. (2018b); Li et al. (2018a) and the International Research Training Group "Integrated engineering of continuous-discontinuous long fiber reinforced polymer structures" (GRK 2078) (Kehrer et al., 2018; Trauth, 2020; Schemmann et al., 2018a; Schöttl et al., 2021a). We give a brief overview of the considered SMC composite and a set of representative experimental investigations on neat UPPH and SMC composite specimens in Sec. 6.2. An analysis of µCT-based in-situ

experiments offers further insight into the behavior of SMC composites during loading.

To represent the anisotropic elasto-damageable behavior of SMC composites (Fitoussi et al., 2005; Ogihara and Koyanagi, 2010; Trauth et al., 2017a), we choose a modular anisotropic damage model which is formulated in the setting of generalized standard materials (Görthofer et al., 2022b) and utilizes a convex dissipation potential (Halphen and Nguyen, 1975; Hansen and Schreyer, 1994), see Chapter 5. This framework relies upon modular damage-activation functions and stress extraction tensors, fulfills Wulfinghoff's damage growth criterion (Wulfinghoff et al., 2017) and ensures a well-posed model precluding localization. We provide an overview of the model and the associated set of parameters in Sec. 6.3. To capture the anisotropic damage in the SMC composite fiber bundles, we develop a set of extraction tensors motivated by Puck's theory (Puck and Schürmann, 2002; Knops, 2008) accounting for maximum stress states. To model the UPPH matrix behavior, we introduce an extraction tensor accounting for damage due to dilatation.

We identify all associated damage parameters via a Bayesian optimization approach with Gaussian regression, as presented in Sec. 6.4. Using an anisotropic kernel function and parallel executions of FFT-based full-field computational homogenization (Schneider, 2021) simulations, we are able to unambiguously identify damage parameter sets for the SMC composite in Sec. 6.5.

In Sec. 6.6, we analyze our full-field damage predictions and compare the results with μCT scans provided by Schöttl et al. (2020); Schöttl et al. (2021a). Furthermore, we compute three-dimensional, effective failure surfaces for the SMC composite, using failure criteria based on failure distributions evaluated in the experimental investigations, see Sec. 6.2. Hence, we provide both full-field damage evolution in SMC composites on the microscale as well as macroscopic failure surfaces for different

failure criteria taking the anisotropic and heterogeneous microstructure of SMC composites into account. These micromechanics-based failure surfaces are formulated in stress space to be used in a structural analysis (Görthofer et al., 2019b), as well as via residual stiffnesses to be used in a design (optimization) process (Revfi et al., 2021). Our presented multiscale approach helps paving the way for an application-based anisotropic damage and failure evaluation of SMC composites on component scale level.

6.2   Experimental investigations

6.2.1   Neat UPPH

Within the IRTG 2078 neat UPPH specimens could be manufactured by M. Bartkowiak (Institute for Applied Materials – Materials Science and Engineering), based on preliminary research by Kehrer, Trauth and co-workers (Kehrer et al., 2018; Kehrer, 2019; Trauth, 2020). The formation of bubbles within the neat UPPH, which lead to local stress concentrations and hence foster premature failure, could be minimized, allowing for a meaningful investigation of said material not only in the elastic, but now also in the non-linear regime.

Figure 6.1: Neat UPPH bone specimens loaded in different directions (with courtesy of M. Bartkowiak and A. Trauth, Institute for Applied Materials – Materials Science and Engineering) in analogy to investigations by Kehrer et al. (2018)

Specimens oriented in different directions were cut from manufactured neat UPPH sheets and tested uniaxially. The resulting stress-strain

curves, as well as the shape of the specimens, are shown in Fig. 6.1. The measured Young's moduli, according to DIN EN ISO 527-4 (Technisches Komitee CEN/TC 249, 1997), coincide with the Young's moduli measured by Kehrer et al. (2018), as shown in the histogram Fig. 6.2a.

The computed mean value for the considered experiments is $3.38\,\mathrm{GPa}$ with a standard deviation of $0.06\,\mathrm{GPa}$. Furthermore, the non-linear regime up to failure is visible. As the structural behavior of the different specimens cannot be distinguished, it is reasonable to use an isotropic model for UPPH.

(a) Young's modulus

(b) Ultimate strength

(c) Young's modulus at failure

(d) Stiffness reduction at failure
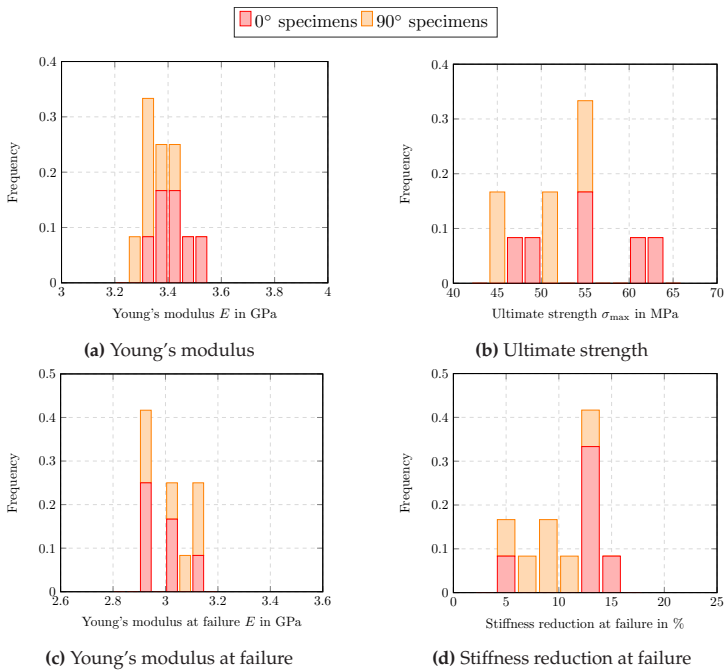
Figure 6.2: Analysis of the neat UPPH bone specimens shown in Fig. 6.1

The ultimate strength, i. e., the stress at failure, has an average value of 52.6 MPa with a standard deviation of 5.5 MPa, see Fig. 6.2b. The bandwidth of values for the ultimate strength, also accounting for the different orientations, are highlighted as horizontal coloring in Fig. 6.1. Assuming a pure elasto-damageable behavior, we determined the Young's moduli at failure as a measure of stiffness reduction (or damage evolution) via $\triangle\sigma/\triangle\varepsilon$, see Fig. 6.2c. The mean of all Young's moduli at failure is 3.01 GPa with a standard deviation of 0.08 GPa. Relating the Young's moduli at failure to the corresponding initial Young's moduli we get the stiffness reduction shown in Fig. 6.2d. On average, this reduction is $10.67\,\%$ with a standard deviation of $3.19\,\%$.

6.2.2 SMC composite

For our SMC composite, we follow a similar procedure to the investigations on neat UPPH specimens. Based on previously conducted experimental investigations in terms of dynamic mechanical analysis (Kehrer et al., 2018; 2020), as well as loading and unloading scenarios, conceivably coupled to acoustic emission analysis (Trauth et al., 2017a; 2021; Trauth, 2020), we know damage to be the predominant mechanism in the considered high performance SMC composite. Hence, we neglect viscous and plastic effects and focus on the analysis of uniaxial tensile tests to evaluate the onset of damage. Therefore, specimens with different orientations were cut from manufactured SMC composite sheets with a fiber volume fraction of $25\,\%$. These sheets were produced in a two-dimensional compression molding flow-process where the bi-staged sheets are placed in the middle of the tool. Four different specimen geometries were used, see Fig. 6.3 – two rectangular specimens (types A and B) and two bone specimens (types C and D) with widths of 15 mm and 30 mm, respectively.
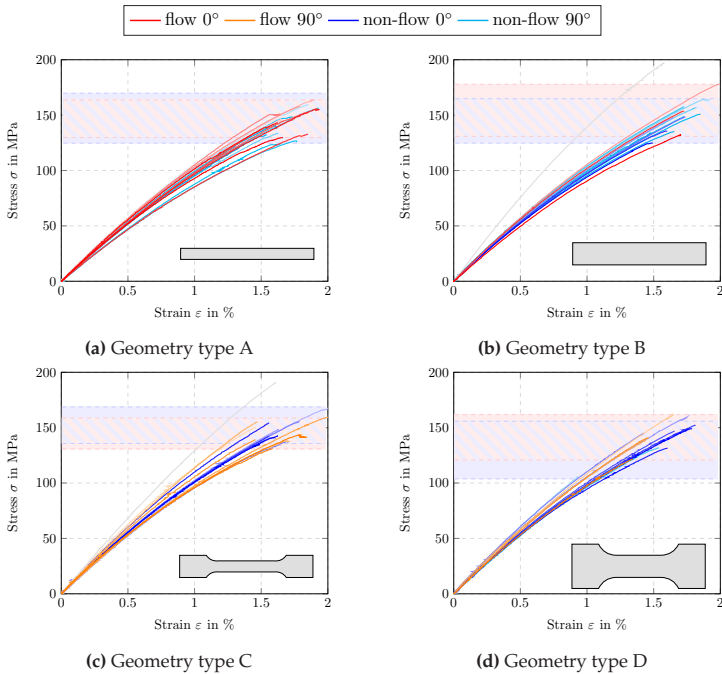
Figure 6.3: SMC composite specimens of different geometry types, loaded in different directions, investigated by Trauth, Bartkowiak and co-workers (Trauth et al., 2017a; Trauth, 2020)

Fig. 6.4a shows the measured Young's moduli corresponding to the stress-strain curves in Fig. 6.3. These Young's moduli have a mean of $11.85\,\mathrm{GPa}$ with a standard deviation of $1.92\,\mathrm{GPa}$, and confirm the moduli measured by Trauth et al. (2017a) and Kehrer et al. (2018). The measured ultimate strength has a mean of $144.78\,\mathrm{MPa}$ and a standard deviation of $15.15\,\mathrm{MPa}$, as shown in Fig. 6.4b. The total bandwidth of the ultimate strength is highlighted in Fig. 6.3. The histogram and normal distribution of the damaged (reduced) Young's moduli at failure are shown in Fig. 6.4c. On average, the damaged Young's moduli

145

take a value of $8.85\,\mathrm{GPa}$ with a standard deviation of $0.94\,\mathrm{GPa}$. The average stiffness reduction at failure is $23.67\,\%$ with a standard deviation of $12.79\,\%$, as shown in Fig. 6.4d.

(a) Young's modulus

(b) Ultimate strength

(c) Young's modulus at failure

(d) Stiffness reduction at failure
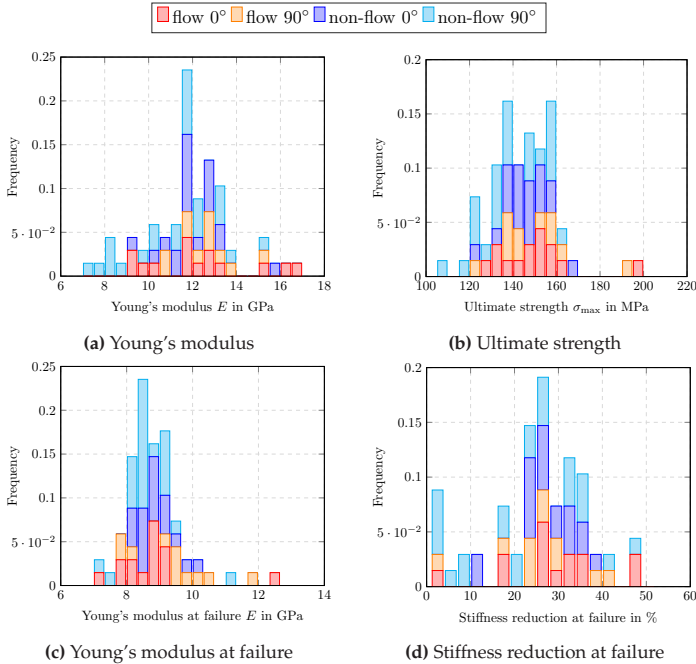
Figure 6.4: Analysis of the SMC composite specimens shown in Fig. 6.3

6.2.3 In-situ µCT scan analysis

In addition to pre-processing µCT scans on unscathed specimens, also in-situ µCT scans were performed by Schöttl et al. (2020); Schöttl et al. (2021a). Snapshots of a specimen loaded vertically in such an in-situ experiment, aiming mainly at damage evolution and microcrack

segmentation, are shown in Fig. 6.5. The characteristic fiber bundle microstructure is clearly visible in the μCT scan shown in Fig. 6.5a.

(a) Initial (b) Loading step 1 (c) Loading step 3 (d) Loading step 4
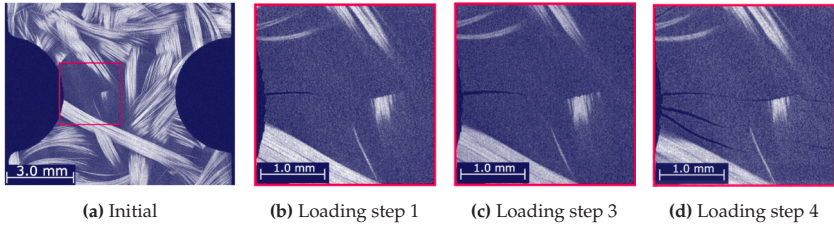
Figure 6.5: Snapshots of an in-situ SMC composite specimen for different loading steps in vertical direction showing the evolution of microcracks, as investigated by Schöttl et al. (2020) and Schöttl et al. (2021a). All shown snapshots are published under CC BY 4.0 license in Schöttl et al. (2021a).

Cyclic loading with increased loading steps and in-between holding times for μCT scan analysis evoke a relatively stable damage evolution within the material due to microcrack propagation and hence allow for damage detection via scanning (Schöttl et al., 2020). The investigations show matrix damage perpendicular to the loading direction to be the primary damage mechanism (Schöttl et al., 2020; Trauth et al., 2017a). Microcracks initiate at rims of matrix-rich areas – mainly at the edge or at fiber bundle interfaces – and progress through the material, diverted by bundles (Schöttl et al., 2021a). Depending on the orientation of individual bundles and hence the associated local stress state, microcracks either follow the principal bundle direction or run through it. Increasing the loading level leads to a higher microcrack density and a wider spread, until eventually total macroscopic failure is inevitable, see Fig. 6.5c and Fig. 6.5d. Fiber or bundle breakage is hardly observed and partially occurs at the point of macroscopic failure (Meraghni and Benzeggagh, 1995; Trauth et al., 2017b).

6.3 A modular framework to describe anisotropic damage based on extraction tensors

6.3.1 A compliance-based anisotropic damage model

To describe damage evolution within the SMC composite, we implement a corresponding model (Görthofer et al., 2022b) formulated in the framework of generalized standard materials (GSM) (Halphen and Nguyen, 1975). The modular nature of the model allows for an effortless employment to describe both damage within the matrix and the fiber bundles, based on associated extraction tensors. In the following, we briefly recall the most important aspects of the damage model (Görthofer et al., 2022b) as presented in Chapter 5.

The first potential in the GSM framework is the free energy in terms of a Hookean elastic energy and an energy related to the progressive damage

$$w : \mathrm{Sym}(d) \times \mathcal{S}_d \times \mathbb{R}^M \to \mathbb{R},$$

$$(\boldsymbol{\varepsilon}, \mathbb{S}, q) \mapsto \frac{1}{2} \boldsymbol{\varepsilon} \cdot \mathbb{S}^{-1} [\boldsymbol{\varepsilon}] + \sum_{i=1}^{M} \frac{H_i}{m_i + 1} q_i^{m_i+1}, \quad m_i > 0. \tag{6.1}$$

The former is jointly convex in the strain $\boldsymbol{\varepsilon}$ and the compliance $\mathbb{S}$ and infinitely often differentiable. The latter is introduced as a power-law hardening type in terms of M different damage variables q_i, hardening parameters H_i and exponents m_i and hence is convex and continuously differentiable. The space of symmetric $d \times d$ infinitesimal strain tensors $\boldsymbol{\varepsilon}$ is $\mathrm{Sym}(d)$ (with d being the dimension, i. e., $d \in [2, 3]$), the compliance tensors are $\mathbb{S} \in \mathcal{S}_d = \{\mathbb{S} \in \mathrm{Sym}(\mathrm{Sym}(d)) \mid \boldsymbol{\tau} \cdot \mathbb{S}[\boldsymbol{\tau}] > 0 \text{ for all } \boldsymbol{\tau} \in \mathrm{Sym}(d) \backslash \{0\}\}$,

and the damage variables $q \in \mathbb{R}^M$ are M scalars in real space. A more detailed discussion can be found in (Görthofer et al., 2022b).

The second potential in the GSM framework is the force potential

$$
\Phi^*(\mathbb{T}, \beta) = \begin{cases} 0, & \phi_i(\mathbb{T}, \beta) \leq 0 \quad \text{for all} \quad i = 1, \dots, M, \\ +\infty, & \text{otherwise}, \end{cases} \tag{6.2}
$$

which we introduce via M convex and continuously differentiable damage-activation functions

$$
\begin{aligned} \phi_i : \operatorname{Sym}(\operatorname{Sym}(d)) \times \mathbb{R} &\to \mathbb{R}, \\ (\mathbb{T}, \beta_i) &\mapsto 2\mathbb{T} \cdot \mathbb{B}_i^2 - \sigma_{0,i}^2 + H_i \beta_i, \quad i = 1, \dots, M. \end{aligned} \tag{6.3}
$$

Each damage-activation function is formulated in terms of the conjugate driving forces $\mathbb{T} \in \operatorname{Sym}(\operatorname{Sym}(d))$ for the compliance and $\beta_i \in \mathbb{R}$ for the damage variables, respectively. Furthermore, a fourth-order extraction tensor $\mathbb{B}_i \in L(\operatorname{Sym}(d))$ and a damage-activation threshold $\sigma_{0,i}$ are introduced per damage-activation function ϕ_i. As the driving forces are given by their potential-based relations $\mathbb{T} = \frac{1}{2}\boldsymbol{\sigma} \otimes \boldsymbol{\sigma}$ and $\beta_i = -H_i q_i^{m_i}$, we simplify the damage-activation functions ϕ_i in terms of the stress $\boldsymbol{\sigma}$ and the damage variables q_i as

$$
\begin{aligned} f_i : \operatorname{Sym}(d) \times \mathbb{R} &\to \mathbb{R}, \\ (\boldsymbol{\sigma}, q_i) &\mapsto \|\mathbb{B}_i[\boldsymbol{\sigma}]\|^2 - \sigma_{0,i}^2 - H_i^2 q_i^{m_i}, \quad i = 1, \dots, M. \end{aligned} \tag{6.4}
$$

Biot's dual equation (Borwein and Lewis, 2006) in the context of the introduced potentials (6.1) and (6.2) yields the evolution equations for the internal variables $\mathbb{S}$ and q, where the consistency parameters need to obey the classical Karush-Kuhn-Tucker (KKT) conditions (Karush, 1939; Kuhn and Tucker, 1951). With a little work, we eliminate the consistency parameters and reformulate the equations, s. t. we compute

the compliance at time t as

$$\mathbb{S}(t) = \mathbb{S}_0 + 2\sum_{i=1}^{M} \frac{q_i(t)}{H_i}\mathbb{B}_i^2,$$ (6.5)

where $\mathbb{S}_0 = \mathbb{S}(0)$ is the initial compliance. The associated KKT conditions referring to the simplified damage-activation functions f_i and damage variables q_i read

$$f_i(\boldsymbol{\sigma}, q_i) \leq 0, \quad \dot{q}_i \geq 0, \quad \dot{q}_i\, f_i(\boldsymbol{\sigma}, q_i) = 0, \quad i = 1, \ldots, M.$$ (6.6)

6.3.2 Influence of the model parameters

The model is able to describe progressive, fully anisotropic damage of any (anisotropic) initial stiffness $\mathbb{C}_0 = \mathbb{S}_0^{-1}$ via any number of damage-activation functions (6.4). Each damage-activation function f_i involves three parameters, a damage-activation threshold $\sigma_{0,i}$, a hardening parameter H_i and a power-law exponent m_i. As the squared norm of the extracted stress $\|\mathbb{B}_i\,[\boldsymbol{\sigma}]\,\|^2$ reaches $\sigma_{0,i}^2$, damage evolution is triggered, and the damage variable q_i increases. The damage evolution and hence the non-linear hardening-type stress-strain relation are governed by H_i and m_i. The influence of the parameters on the predicted stress-strain relations is shown in Fig. 6.6 as an example. Here, a single damage-activation function f to describe damage in loading direction, in analogy to Govindjee et al. (1995), is used. We choose the set of damage parameters as $\sigma_0 = 30\,\mathrm{MPa}$, $H = 130\,\mathrm{MPa}$ and $m = 1$ for reference. For each study shown in Fig. 6.6, we vary one of these parameters and keep the others constant.

Increasing the damage-activation threshold σ_0 retards the damage initiation and increases the elastic region, see Fig. 6.6a. The hardening parameter H and the power-law exponent m have an opposing influence on the damage region, as we observe when comparing Fig. 6.6b and

Fig. 6.6c. Whereas an increase of H increases the hardening-type behavior, an increase of m decreases the hardening.

(a) Activation threshold σ_0 **(b)** Hardening parameter H **(c)** Power-law exponent m
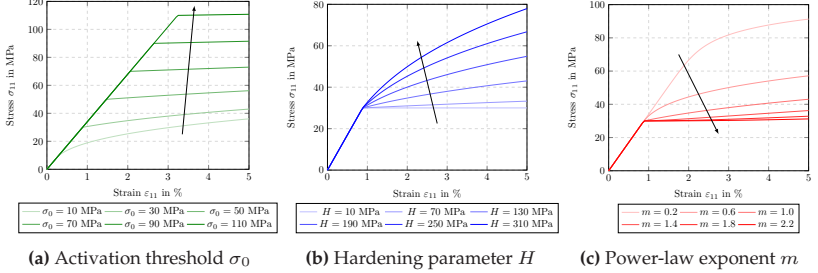
Figure 6.6: Influence of the model parameters σ_0, H and m on the predicted stress-strain relation

6.3.3 Extraction tensors accounting for dilatation and distortion

Spherical stress state

To model damage induced by dilatation, i. e., due to spherical stress states, the corresponding extraction tensor $\mathbb{B}$ is the spherical projector $\mathbb{P}_1$, well-known from linear elasticity

$$\mathbb{B} = \mathbb{P}_1 = \frac{1}{3} \boldsymbol{I} \otimes \boldsymbol{I}. \tag{6.7}$$

Due to its characteristic $\mathbb{P}_1 [\boldsymbol{\sigma}] = \boldsymbol{\sigma}^\circ$, the extracted stresses of the defined damage-activation functions (6.4) read

$$\|\mathbb{B} [\boldsymbol{\sigma}] \|^2 = \|\boldsymbol{\sigma}^\circ\|^2. \tag{6.8}$$

151

Deviatoric stress state

In analogy to spherical stress states, we model damage induced by distortion, i. e., by deviatoric stress states, via an extraction tensor $\mathbb{B}$ of the form

$$\mathbb{B} = \mathbb{P}_2 = \mathbb{I}^S - \mathbb{P}_1. \tag{6.9}$$

Due to the characteristic of the deviatoric projector $\mathbb{P}_2\left[\boldsymbol{\sigma}\right] = \boldsymbol{\sigma}'$, the corresponding extracted stresses are

$$\left\| \mathbb{B}\left[\boldsymbol{\sigma}\right] \right\|^2 = \left\| \boldsymbol{\sigma}' \right\|^2. \tag{6.10}$$

6.3.4 Puck-type extraction tensors accounting for maximum stresses

Basic idea

Motivated by the basic stress states present in laminates, as investigated by Puck and co-workers (Puck and Schürmann, 2002; Knops, 2008), we define extraction tensors to account for damage due to normal as well as shear loading, both in fiber bundle direction and perpendicular to it. Let $\{e_1, e_2, e_3\}$ be a Cartesian coordinate system, where e_1 corresponds to the alignment direction of the fibers, see Fig. 6.7. Then the stress tensor $\boldsymbol{\sigma}$ admits the block decomposition

$$\boldsymbol{\sigma} = \left(\begin{array}{c|cc} \sigma_{11} & \sigma_{12} & \sigma_{13} \\ \hline \sigma_{12} & \sigma_{22} & \sigma_{23} \\ \sigma_{13} & \sigma_{23} & \sigma_{33} \end{array} \right). \tag{6.11}$$

The stress in fiber direction is given by σ_{11}, the lower right block describes the transverse stresses in the plane orthogonal to the fiber direction, and $(\sigma_{12}, \sigma_{13})$ are the remaining shear stresses in longitudinal fiber bundle direction. Given the basic stress state in a fiber

bundle (see Eq. (6.11)), the traction vector t in an arbitrary direction n is $t = \sigma n$. To account for the maximum stresses in terms of a Puck-type setting, we need to maximize specific (extracted) stresses over certain directions using the pencil glide approach (Krawietz, 1981; 2001). We distinguish four different loading scenarios that yield four associated extraction tensors.
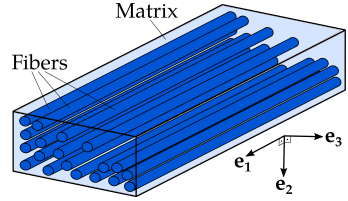
Figure 6.7: Schematic of a fiber bundle with local coordinate system $\{e_1, e_2, e_3\}$

Normal loading in fiber direction

The traction vector pointing in fiber direction e_1 is

$$t_1 = (e_1 \cdot \sigma e_1) \, e_1, \tag{6.12}$$

with the scalar stress

$$t_1 = e_1 \cdot \sigma e_1 = \sigma_{11}. \tag{6.13}$$

This stress is unambiguously defined by the given bundle direction e_1. The extraction tensor capturing normal loading in fiber direction is

$$\mathbb{B} = e_1^{\otimes 4}. \tag{6.14}$$

Accordingly, the extracted stress reads

$$\|\mathbb{B}[\sigma]\|^2 = \sigma_{11}^2. \tag{6.15}$$

In the context of Puck's theory on laminates we apply this extraction tensor to capture damage evolution in fiber bundle direction. Nontheless, it is not limited to fiber bundles and can be generally applied to describe

damage due to normal loading, similarly to the introduced tensor by Govindjee et al. (1995).

Normal loading perpendicular to fiber direction

An arbitrary traction vector perpendicular to the fiber direction is given via the direction $S^2 \ni \boldsymbol{k} \perp \boldsymbol{e}_1$, where $S^2 = \{\boldsymbol{x} \in \mathbb{R}^3 \mid \|\boldsymbol{x}\| = 1\}$, as

$$\boldsymbol{t}_\sigma = (\boldsymbol{k} \cdot \boldsymbol{\sigma}\boldsymbol{k})\,\boldsymbol{k}. \tag{6.16}$$

We need to maximize the normal stress pointing into direction $\boldsymbol{k}$

$$t_\sigma = \boldsymbol{k} \cdot \boldsymbol{\sigma}\boldsymbol{k}, \tag{6.17}$$

over all admissible directions

$$t_\sigma^{\mathrm{max}} = \max_{\boldsymbol{k} \perp \boldsymbol{e}_1} \boldsymbol{k} \cdot \boldsymbol{\sigma}\boldsymbol{k}. \tag{6.18}$$

Hence, t_σ^{max} is the maximum principal stress of the stress state on the $\boldsymbol{e}_1$-plane. This stress state is described by

$$\boldsymbol{\sigma}_\sigma = \sigma_{ij}\boldsymbol{e}_i \otimes \boldsymbol{e}_j, \quad i,j = 2,3, \tag{6.19}$$

with the corresponding principal stresses

$$\lambda_{2,3} = \frac{\sigma_{22} + \sigma_{33}}{2} \pm \sqrt{\left(\frac{\sigma_{22} - \sigma_{33}}{2}\right)^2 + \sigma_{23}^2}. \tag{6.20}$$

Following the classical convention for principal stresses $\lambda_2 > \lambda_3$, we get

$$t_\sigma^{\mathrm{max}} = \lambda_2. \tag{6.21}$$

We derive the associated extraction tensor and the damage-activation function via the condition

$$\|\mathbb{B}\left[\boldsymbol{\sigma}\right]\|^2 \stackrel{!}{=} (t_\sigma^{\max})^2 .$$ (6.22)

While this condition (6.22) does not allow for an explicit closed-form description of the associated extraction tensor, the extracted stresses are given via

$$\|\mathbb{B}\left[\boldsymbol{\sigma}\right]\|^2 = \left(\frac{\sigma_{22} + \sigma_{33}}{2} + \sqrt{\left(\frac{\sigma_{22} - \sigma_{33}}{2} \right)^2 + \sigma_{23}^2} \right)^2 .$$ (6.23)

Based on the procedures and results for the alternate loading scenarios (see Sec. 6.3.4), as well as extraction tensors formulated in an average stress manner Görthofer et al. (2022b), we postulate a damage extraction tensor for normal loading perpendicular to the fiber direction of the form

$$\mathbb{B} = \frac{\sqrt{2}}{2} \left(\boldsymbol{e}_2^{\otimes 2} + \boldsymbol{e}_3^{\otimes 2} \right)^{\otimes 2} + \frac{\sqrt{2}}{4} \left(\boldsymbol{e}_2^{\otimes 2} - \boldsymbol{e}_3^{\otimes 2} \right)^{\otimes 2} + (\boldsymbol{e}_2 \otimes_\mathsf{S} \boldsymbol{e}_3)^{\otimes 2} .$$ (6.24)

The associated extracted stress therefore reads

$$\|\mathbb{B}\left[\boldsymbol{\sigma}\right]\|^2 = \frac{1}{4} \left(5\sigma_{22}^2 + 5\sigma_{33}^2 + 6\sigma_{22}\sigma_{33} + 4\sigma_{23}^2 \right) .$$ (6.25)

Shear loading perpendicular to fiber direction

In order to evaluate the stress state due to shear loading perpendicular to the fiber direction, we need to consider the shear part of the traction vector, namely

$$\boldsymbol{t}_\tau = \boldsymbol{\sigma} \boldsymbol{k} - (\boldsymbol{k} \cdot \boldsymbol{\sigma} \boldsymbol{k}) \, \boldsymbol{k}.$$ (6.26)

We decompose the shear traction vector into shear stresses perpendicular and parallel to the fiber direction

$$t_\tau = t_{\tau\perp} + t_{\tau\|}. \tag{6.27}$$

The shear traction vector parallel to the fiber direction is

$$t_{\tau\|} = (e_1 \cdot t_\tau) e_1 = (e_1 \cdot \sigma k) e_1, \tag{6.28}$$

and, analogously, the shear traction vector perpendicular to the fiber direction is

$$t_{\tau\perp} = \sigma k - \underbrace{(k \cdot \sigma k) k}_{t_\sigma} - \underbrace{(e_1 \cdot \sigma k) e_1}_{t_{\tau\|}}$$

$$= (I - k \otimes k - e_1 \otimes e_1) \sigma k$$

$$= (m \cdot \sigma k) m, \tag{6.29}$$

where $S^2 \ni m \perp k \perp e_1$ and $m \perp e_1$. The sought scalar shear stress is given as

$$t_{\tau\perp} = m \cdot \sigma k, \tag{6.30}$$

which we need to maximize over all admissible directions $m \perp k \perp e_1$

$$t_{\tau\perp}^{\max} = \max_{m\perp k\perp e_1} m \cdot \sigma k. \tag{6.31}$$

Note that the directions m and k are not independent. For a given bundle direction e_1, we express m as a function of k via the condition $I = m \otimes m + k \otimes k + e_1 \otimes e_1$. Using this relation we get the expression

$$t_{\tau\perp}^{\max} = \max_{k\perp e_1} \sqrt{\|\sigma k\|^2 - (k \cdot \sigma k)^2 - (e_1 \cdot \sigma k)^2}, \tag{6.32}$$

involving only a single unknown unit vector k.

Analogously to normal loading perpendicular to the fiber direction, $t_{\tau\perp}^{\max}$ is the maximum shear stress on the plane defined by the bundle direction e_1. In accordance with principal stresses computed for the case above, the maximum shear stress is

$$t_{\tau\perp}^{\max} = \frac{|\lambda_2 - \lambda_3|}{2} = \sqrt{\left(\frac{\sigma_{22} - \sigma_{33}}{2}\right)^2 + \sigma_{23}^2}. \tag{6.33}$$

The associated extraction tensor and the damage-activation function are computed via the condition

$$\|\mathbb{B}\left[\boldsymbol{\sigma}\right]\|^2 \overset{!}{=} \left(t_{\tau\perp}^{\max}\right)^2, \tag{6.34}$$

which is ensured, provided

$$\mathbb{B}^2\left[\boldsymbol{\sigma}\right] \overset{!}{=} \frac{\sigma_{22} - \sigma_{33}}{4}\left(e_2^{\otimes 2} - e_3^{\otimes 2}\right) + \sigma_{23}\left(e_2 \otimes_{\mathsf{S}} e_3\right) \tag{6.35}$$

holds. Evaluating this condition yields an explicit form of the extraction tensor

$$\mathbb{B} = \frac{\sqrt{2}}{4}\left(e_2^{\otimes 2} - e_3^{\otimes 2}\right)^{\otimes 2} + \left(e_2 \otimes_{\mathsf{S}} e_3\right)^{\otimes 2}, \tag{6.36}$$

and the corresponding extracted stress

$$\|\mathbb{B}\left[\boldsymbol{\sigma}\right]\|^2 = \frac{1}{4}\left(\sigma_{22}^2 + \sigma_{33}^2 - 2\sigma_{22}\sigma_{33} + 4\sigma_{23}^2\right). \tag{6.37}$$

Shear loading in fiber direction

We account for the maximum stress due to shear loading in fiber direction via the corresponding shear traction vector (6.28)

$$\boldsymbol{t}_{\tau\|} = \left(e_1 \cdot \boldsymbol{\sigma k}\right) e_1 = t_{\tau\|} e_1. \tag{6.38}$$

We maximize the associated shear stress over all admissible directions $\boldsymbol{k} \perp \boldsymbol{e}_1$

$$t_{\tau\|}^{\max} = \max_{\boldsymbol{k} \perp \boldsymbol{e}_1} \boldsymbol{e}_1 \cdot \boldsymbol{\sigma} \boldsymbol{k}, \tag{6.39}$$

i. e. we search the normal direction $\boldsymbol{k}$ that points into direction of the maximum stress (Krawietz, 1981; 2001). As the stress is symmetric $\boldsymbol{\sigma}^{\mathsf{T}} = \boldsymbol{\sigma}$, the relation

$$t_{\tau\|} = \boldsymbol{e}_1 \cdot \boldsymbol{\sigma} \boldsymbol{k} = \boldsymbol{k} \cdot \boldsymbol{\sigma} \boldsymbol{e}_1 \tag{6.40}$$

holds. We define a corresponding projector $\boldsymbol{P}_k$ with the characteristics $\boldsymbol{P}_k \boldsymbol{k} = \boldsymbol{k}$ and $\boldsymbol{P}_k^{\mathsf{T}} = \boldsymbol{P}_k$ as

$$\boldsymbol{P}_k = \boldsymbol{I} - \boldsymbol{e}_1 \otimes \boldsymbol{e}_1. \tag{6.41}$$

Application of this projector to the stress state yields

$$t_{\tau\|} = \boldsymbol{k} \cdot \boldsymbol{\sigma} \boldsymbol{e}_1 = \boldsymbol{P}_k \boldsymbol{k} \cdot \boldsymbol{\sigma} \boldsymbol{e}_1 = \boldsymbol{k} \cdot \boldsymbol{P}_k \boldsymbol{\sigma} \boldsymbol{e}_1 = \sigma_{12} \boldsymbol{e}_2 + \sigma_{13} \boldsymbol{e}_3. \tag{6.42}$$

The shear stress is maximized whenever

$$\boldsymbol{k} \overset{!}{=} \frac{\boldsymbol{P}_k \boldsymbol{\sigma} \boldsymbol{e}_1}{\|\boldsymbol{P}_k \boldsymbol{\sigma} \boldsymbol{e}_1\|} \tag{6.43}$$

holds, yielding

$$t_{\tau\|}^{\max} = \frac{\boldsymbol{P}_k \boldsymbol{\sigma} \boldsymbol{e}_1}{\|\boldsymbol{P}_k \boldsymbol{\sigma} \boldsymbol{e}_1\|} \cdot \boldsymbol{P}_k \boldsymbol{\sigma} \boldsymbol{e}_1 = \|\boldsymbol{P}_k \boldsymbol{\sigma} \boldsymbol{e}_1\| = \sqrt{\sigma_{12}^2 + \sigma_{13}^2}. \tag{6.44}$$

The essential relation

$$\|\mathbb{B}\left[\boldsymbol{\sigma}\right]\|^2 \overset{!}{=} \left(t_{\tau\|}^{\max}\right)^2, \tag{6.45}$$

holds, if

$$\mathbb{B}^2\left[\boldsymbol{\sigma}\right] \overset{!}{=} \sigma_{12}\left(\boldsymbol{e}_1 \otimes_{\mathsf{S}} \boldsymbol{e}_2\right) + \sigma_{13}\left(\boldsymbol{e}_1 \otimes_{\mathsf{S}} \boldsymbol{e}_3\right). \tag{6.46}$$

Evaluating this relation gives an explicit form for the associated extraction tensor

$$\mathbb{B} = (e_1 \otimes_{\mathsf{S}} e_2)^{\otimes 2} + (e_1 \otimes_{\mathsf{S}} e_3)^{\otimes 2}, \tag{6.47}$$

and the corresponding extracted stress

$$\|\mathbb{B}\,[\boldsymbol{\sigma}]\,\|^2 = \sigma_{12}^2 + \sigma_{13}^2. \tag{6.48}$$

6.4 Bayesian optimization process

The presented framework takes damage parameters into account (see Sec. 6.3.1 and Sec. 6.3.2), which need to be identified to describe the elasto-damageable behavior of our SMC composite properly. The model and its parameters serve as input for the FFT-based full-field homogenization computed with our in-house code homKIT (see Fig. 6.8 and Sec. 6.5.1 for further information). The stress-strain response computed by homKIT is compared to the experimental results discussed in Sec. 6.2 via a corresponding error measure, yielding an optimization problem for the identification of proper damage parameters.
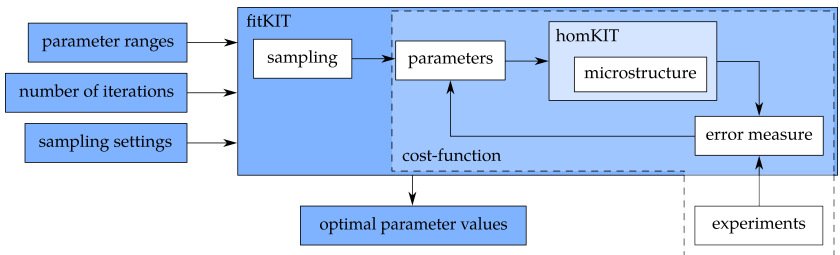
Figure 6.8: Simplified schematic workflow of parameter identification routine

We choose a Bayesian optimization approach (Mockus, 1989; 1994), as our problem at hand involves an objective function that is expensive to evaluate (each call involves a full-field homogenization on a three-dimensional voxel image) and derivatives that are not easily. Similar conditions hold for, e.g., ductile phase-field fracture (Noii et al., 2021). Bayesian optimization uses a surrogate model of the actual problem accounting for probabilities and uncertainties based on Bayesian statistics (Bolstad and Curran, 2016).

We describe the problem in terms of an abstract cost function

$$c : \mathcal{R} \to \mathbb{R}, \quad p \mapsto c(p), \tag{6.49}$$

combining the full-field homogenization based on a parameter set $p \in \mathcal{R} \subset \mathbb{R}^b$, and the error measure. The feasible domain $\mathcal{R}$ for the parameter set p represents the parameter ranges and is frequently chosen as hyper-rectangle with $p \in \mathcal{R} \subset \mathbb{R}^b : l_i \leq p_i \leq u_i, \ i = 1, \ldots, b$, for scalar lower and upper bounds l_i and u_i. We seek a minimizer p of the cost function

$$c(p) \to \min_{p \in \mathcal{R} \subset \mathbb{R}^b} . \tag{6.50}$$

In general, we do not know the (continuous) cost function, but only a certain amount of discrete values for parameter sets $p_{1:r} = (p_1, \ldots, p_r) \in \mathcal{R}^r$, which we assemble in a vector $c_{1:r} = [c(p_1), \ldots, c(p_r)]^\mathsf{T} \in \mathbb{R}^r$. The cost function values for the remainder of parameter sets are uncertain, yielding an infinite number of possible cost functions. Hence, we use a surrogate cost function model based on Gaussian process regression (Williams and Rasmussen, 2006) to account for the uncertainty within the Bayesian optimization procedure. We assume all possible cost function values to be distributed normally

$$c(p) \sim \mathcal{N}(m(p), K(p, p')) \quad \text{for all} \quad p \in \mathcal{R}, \tag{6.51}$$

with a mean $m : \mathcal{R} \to \mathbb{R}$ and a kernel (covariance) $k : \mathcal{R} \times \mathcal{R} \to \mathbb{R}$. The kernel k defines the correlations of two parameter sets p and p'.

Condition (6.51) has to hold for all parameter sets $p \in \mathcal{R}$ yielding a normal distribution of all cost functions. Therefore, given the already known parameter sets $p_{1:r}$ with associated cost function values $c_{1:r}$, all possible (surrogate) cost functions have to be drawn according to the multivariate normal distribution (6.51) with the mean vector $m_{1:r} = [m(p_1), \ldots, m(p_r)]^\mathsf{T} \in \mathbb{R}^r$ and the covariance matrix

$$K_{1:r,1:r} = \begin{bmatrix} k(p_1, p_1) & \ldots & k(p_1, p_r) \\ \vdots & \ddots & \vdots \\ k(p_r, p_1) & \ldots & k(p_r, p_r) \end{bmatrix} \in \mathbb{R}^{r \times r}. \qquad (6.52)$$

The multivariate normal distribution (6.51) has to hold for any new parameter set p_{r+1}, as well. Hence, the joint distribution based on all parameter sets – known and new – $(p_{1:r}, p_{r+1})$ follows a multivariate normal distribution that reads

$$\begin{bmatrix} c_{1:r} \\ c(p_{r+1}) \end{bmatrix} \sim \mathcal{N} \left(0, \begin{bmatrix} K_{1:r,1:r} & K_{1:r,r+1} \\ K_{1:r,r+1}^\mathsf{T} & k(p_{r+1}, p_{r+1}) \end{bmatrix} \right), \qquad (6.53)$$

with the kernel evaluations $K_{1:r,r+1} = [k(p_1, p_{r+1}), \ldots, k(p_r, p_{r+1})]^\mathsf{T}$ and $k(p_{r+1}, p_{r+1})$. For convenience we assume the mean to be zero $m_{1:r} \equiv 0$ Frazier (2018).

Consequently, the (conditional) posterior probability distribution of the cost function $c(p_{r+1})$ for the new parameter set p_{r+1}, given the already known $c_{1:r}$, is computed as

$$c(p_{r+1}) \mid c_{1:r} = \mathcal{N} \left(\widetilde{m}(p_{r+1}), \widetilde{v}^2(p_{r+1}) \right) \qquad (6.54)$$

with a posterior mean $\widetilde{m}(p_{r+1})$ and a posterior variance $\widetilde{v}^2(p_{r+1})$. Here, the Sherman-Morrison-Woodbury formula (Hager, 1989) can be utilized

(Williams and Rasmussen, 2006) and yields

$$\widetilde{m}(p_{r+1}) = K_{1:r,r+1}^{\mathsf{T}} K_{1:r,1:r}^{-1} c_{1:r}, \tag{6.55}$$

$$\widetilde{v}^2(p_{r+1}) = k(p_{r+1}, p_{r+1}) - K_{1:r,r+1}^{\mathsf{T}} K_{1:r,1:r}^{-1} K_{1:r,r+1}^{\mathsf{T}}. \tag{6.56}$$

The posterior mean $\widetilde{m}(p_{r+1})$ is estimated on the given, known data $c_{1:r}$ weighted by the kernel. The posterior variance $\widetilde{v}^2(p_{r+1})$ is given by the prior covariance which is corrected by a term that takes the known correlations into account. The posterior mean approximates the actual cost function and is updated and improved with each evaluated parameter set p_{r+1}. For an infinity number of evaluations $r \to \infty$, we recapture the actual (deterministic) cost function.

As we know the different parameters of the different damage-activation functions to have different levels of relevance on the anisotropic behavior of our SMC composite, we use the Màtern 5/2 kernel (Matérn, 2013)

$$k(p, p') = \gamma_p^2 \left(1 + \sqrt{5}\, \delta\,(p, p') + \frac{5}{3} \delta\,(p, p')^2 \right) \exp\left(-\sqrt{5}\, \delta\,(p, p')\right) \tag{6.57}$$

with an anisotropic distance function $\delta\,(p, p')$ between parameter sets p and p'

$$\delta\,(p, p') = \sqrt{\sum_{i=1}^{b} \frac{(p_i - p_i')^2}{\alpha_i^2}}. \tag{6.58}$$

The Màtern 5/2 kernel (6.57) is not restricted to smooth cost functions. Each of the hyperparameters $(\alpha_1, \ldots, \alpha_b)$ is determined to represent the relevance of its associated damage parameter. The hyperparameter γ_p^2 controls the width of the kernel, i.e., the general level of correlation between two parameter sets. For a more detailed discussion on kernel functions, the reader is referred to the book of Williams and Rasmussen (2006).

For each evaluation, we want to choose a new parameter set p_{r+1} that is closer to the sought minimum of the cost function. Hence, a promising parameter set p_{r+1} has a large improvement $\langle c(p_*) - c(p_{r+1})\rangle$ w. r. t. the currently best parameter set $p_* = \mathrm{argmin}_{i \leq r} c(p_i)$. As we do not know $c(p_{r+1})$ beforehand, we take the expected value $\mathcal{E}$ of the improvement given all already known evaluations $c_{1:r}$ and maximize it, yielding

$$p_{r+1} = \mathrm{argmax}\,\mathrm{EI}(p), \qquad (6.59)$$

with the "expected improvement" (EI) acquisition function (Mockus et al., 1978; Brochu et al., 2010)

$$\mathrm{EI}(p) = \mathcal{E}\left(\langle c(p_*) - c(p)\rangle \mid c_{1:r}\right) \qquad (6.60)$$

and Macaulay brackets $\langle \cdot \rangle = \max(0, \cdot)$. We evaluate (6.60) in closed form (Brochu et al., 2010) and arrive at

$$\mathrm{EI}(p) = \langle \triangle c(p)\rangle + \widetilde{v}(p)\,\mathrm{PDF}\left(\frac{\triangle c(p)}{\widetilde{v}(p)}\right) - |\triangle c(p)|\,\mathrm{CDF}\left(\frac{\triangle c(p)}{\widetilde{v}(p)}\right) \quad (6.61)$$

with the probability and cumulative density functions PDF and CDF. The expected difference is defined as $\triangle c(p) = c(p_*) - \widetilde{m}(p) - \xi$, including a shift-parameter ξ that helps controlling the exploration and exploitation trade-off (Brochu et al., 2010). This trade-off between choosing (new) parameter sets with a high uncertainty (high $\widetilde{v}(p)$) or a high expected quality (high $\triangle c(p)$) is the elementary part of all acquisition functions.

To initialize a certain number of cost function values for the optimization process, we use a Latin-Hypercube sampling approach (McKay et al., 1979) for the parameter sets within our hyper-rectangular domain $\mathcal{R}$. The Bayesian optimization process is stopped after a given amount of iterations and the parameter set p_* yielding the smallest cost function value $c(p_*)$ is considered as the optimal choice.

6.5 Identification of damage parameters in SMC composites

6.5.1 Computational setup

We integrated the proposed damage model as a user-defined subroutine in our in-house OpenMP-parallel FFT-based computational homogenization code written in Python 3.7 with Cython extensions (Behnel et al., 2011) and FFTW (Frigo and Johnson, 2005) bindings, as described by Schneider (2018) (homKIT, see Fig. 6.8). We use the discretization by Moulinec and Suquet (1998) and a Newton-CG scheme to solve the ensuing nonlinear systems of equations (Gélébart and Mondon-Cancel, 2013; Wicht et al., 2020). We implemented the Bayesian optimization procedure in combination with the kernel evaluations and the error measure in terms of a Python 3.7 code, incorporating GPyOpt (Paleyes et al., 2016) (fitKIT, see Fig. 6.8). We executed the optimization iterations in parallel, using a batch sampling as introduced by Thompson (1933).

For the computations we used either 6 - 12 threads on a desktop computer with 32 GB RAM and an Intel i7-8700K CPU with 6 cores and a clock rate of 3.7 GHz, or a workstation with two AMD EPYC 7642 with 48 physical cores each, enabled SMT and 1024 GB of DRAM.

6.5.2 Definition of the parameter set to be identified

The linear elastic properties of the UPPH matrix and fibers are listed in Tab. 6.1. To derive the properties of a fiber bundle, we implemented two different approaches, numerical full-field homogenization of a representative bundle (Moulinec and Suquet, 1998), as well as mean-field Mori-Tanaka homogenization (Mori and Tanaka, 1973; Duschlbauer et al., 2003), see also Sec. 4.3.2. Both approaches lead to approximately the

same transversely isotropic stiffness properties that are listed in Tab. 6.1, where "L" and "T" refer to longitudinal and transverse, respectively. Measurements and comparisons of the effective elastic properties of SMC composites were performed by Trauth (2020).

Table 6.1: Elastic material parameters for the considered SMC composite

E-glass fibers (Kehrer et al., 2018)	UPPH matrix (Kehrer et al., 2018)	Fiber bundles
$E_{F,iso} = 72$ GPa	$E_{M,iso} = 3.4$ GPa	$E_{B,L} = 37.73$ GPa
		$E_{B,T} = 10.33$ GPa
$\nu_{F,iso} = 0.22$	$\nu_{M,iso} = 0.385$	$\nu_{B,TT} = 0.477$
		$\nu_{B,LT} = 0.292$
$G_{F,iso} = 29.51$ GPa	$G_{M,iso} = 1.23$ GPa	$G_{B,TT} = 3.58$ GPa
		$G_{B,LT} = 3.64$ GPa

To capture matrix and bundle damage, the dominant mechanisms in SMC composites (Fitoussi et al., 2005; Ogihara and Koyanagi, 2010; Trauth et al., 2017a), we we utilize the following three damage-activation functions (6.4). Matrix damage evolution due to normal loading in terms of dilatation is captured via a damage-activation function in combination with an extraction tensor of type (6.7). Bundle damage in transverse and longitudinal direction, accounting for normal and shear stresses, is described via damage-activation functions in combination with extraction tensors of types (6.24) and (6.47), respectively.

Each damage-activation function comes with three parameters (σ_0, H, m), as discussed in Sec. 6.3.2. We know the power-law exponent m to have a contrary influence on the non-linear regime compared to the hardening parameter H. To describe the behavior of SMC composites, we assume a linear damage hardening evolution and hence set the power-law exponent to $m = 1$ for each damage-activation function. This

leaves us with six parameters to be identified adequately in order to fit the predicted behavior of our model to the experimental observations. A summary of the applied extraction tensors, the associated parameters and their allowed ranges for the optimization process is given in Tab. 6.2.

Table 6.2: Extraction tensors and damage parameters used for modeling the behavior of the SMC composite

	Type	$\mathbb{B}$	σ_0 in MPa	H in MPa
UPPH	Sec. 6.3.3	(6.7)	$[5, 50]$	$[\ 50, 400]$
Bundle	Sec. 6.3.4	(6.24)	$[5, 40]$	$[100, 700]$
	Sec. 6.3.4	(6.47)	$[5, 40]$	$[\ 50, 400]$

6.5.3 Preliminary study on neat UPPH

In a preliminary study, we fit the material model with solely a single damage-activation function to the experimental results on neat UPPH specimens as presented in Sec. 6.2.1. We use a representative experiment showing the mean behavior of all conducted experiments on UPPH, see Fig. 6.1.

As known from previous investigations (Kehrer et al., 2018; Kehrer, 2019; Trauth, 2020), neat matrix specimens behave slightly different to the matrix within the composite. Hence, we apply an extraction tensor of type (6.14). Furthermore, the preliminary study does not replace the UPPH parameter identification in a coupled approach of matrix and bundles within the SMC composite. Nonetheless, a preliminary study helps to understand the general material behavior of UPPH and can also be considered a stand-alone damage parameter identification for the neat UPPH.

Utilizing the Bayesian optimization process discussed in Sec. 6.4, we run an optimization with 100 initial hypercube samplings and subsequent 3000 evaluations, using 150 batches of 20 parallel executions each. We update the surrogate model and hence the acquisition function after the computation of each batch. The computations are performed on a single voxel with isotropic material parameters for UPPH as presented in Tab. 6.1. Based on knowledge gathered in trail computations, we set the parameter ranges for the optimization to $\sigma_0 \in [0, 30]$ MPa and $H \in [500, 600]$ MPa.

We use a least square ansatz for the cost function value regarding a parameter set p

$$c(p) = \sqrt{\frac{1}{N} \sum_{i=1}^{N} \left(\sigma_i^{\exp} - \sigma_i^{\sim}\right)^2} \tag{6.62}$$

comparing the difference of the experimentally measured and the predicted stress-strain curves. We evaluate the measured stress $\sigma_i^{\exp}$ and the computed stress $\sigma_i^{\sim}$ for N given strain values.

The cost function values $c(p)$ of a representative optimization run with its total 3100 iterations are shown in Fig. 6.9. The associated parameter sets $p = \{\sigma_0, H\}$ are plotted in Fig. 6.10. The lighter lines show the computed results of all 3100 iterations, whereas the darker lines represent the best results per batch, i. e., the parameter set that leads to the minimum cost function value per batch.

Within the first 100 iterations, the hypercube sampling is evident as possible parameter sets of the hyper-rectangle $\mathcal{R}$ are scanned in a regular fashion (see Fig. 6.10) and hence the cost function values vary strongly (see Fig. 6.9). For the next batch of 20 more iterations, the cost function varies around a value of approximately 0.06 MPa with an 95 % confidence interval of about ±0.01 MPa. After the next update of the optimization surrogate model, the cost function values converge to approximately 0.058 MPa for the remainder of the optimization run with
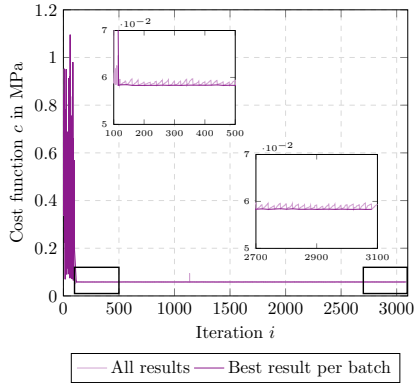
Figure 6.9: Values of the cost function $c(p)$ over iterations

an associated parameter set as shown in Fig. 6.10. Solely after about 1100 iterations an alternative parameter set (way off the other sets promising to be an optimal choice) was tested and then discarded, yielding a short increase of the cost function. The choice of said parameter set is evoked by the batch sampling discussed below. In all following iterations, the 95 % confidence interval of the computed cost function value is of the order of 10^{-5} MPa, i.e., we are very confident that our result is correct. The associated values of the parameter set converge to values of about $\sigma_0 = 12.07$ MPa and $H = 555.95$ MPa, see Fig. 6.10a and Fig. 6.10b.

The remaining variation of the parameter values and the associated gradual behavior of the cost function considering all iterations (see lighter lines in Fig. 6.9 and Fig. 6.10) is caused by the batch sampling (Thompson, 1933). Here, for each batch, the most likely best parameter set is chosen together with 19 other parameter sets sampled via a beta distribution, to ensure an appropriate balance of the exploration and exploitation trade-off (see Sec. 6.4). Hence, the immediate quality is to

(a) Damage-activation threshold σ_0

(b) Hardening parameter H
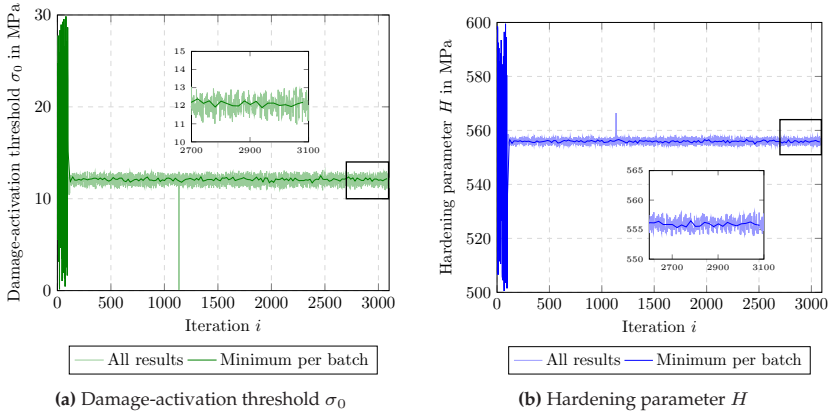
Figure 6.10: Values of damage-activation threshold σ_0 and hardening parameter H over iterations

be improved together with the aim to gather new information possibly improving a currently high uncertainty.

If we only consider the best result per batch (see darker lines in Fig. 6.9 and Fig. 6.10), we find the mentioned variations to reduce significantly after the initial hypercube sampling and a few following iterations. Hence, we basically found the optimal parameter set with the corresponding minimal cost function value.

To check convergence of our algorithm, we repeated the discussed optimization process in 100 runs with different initial samplings. All computed optimal cost function values and associated parameters coincide up to computational accuracy. Hence, we can reliably repeat the computation of the best parameter set and assume the values of $\sigma_0 = 12.07$ MPa and $H = 555.95$ MPa (with a cost function value of 0.058 MPa, which is $0.11\,\%$ of the mean ultimate strength) to be correct.

A comparison of the experimental stress-strain curves as presented in Sec. 6.2.1, cf. Fig. 6.1, and the computed stress-strain curve is shown in Fig. 6.11. The applied damage-activation function based on the extraction tensor (6.14) in terms of our anisotropic damage evolution framework, in combination with the identified parameter set, allows for an accurate prediction of the macroscopic stress-strain relation of neat UPPH.
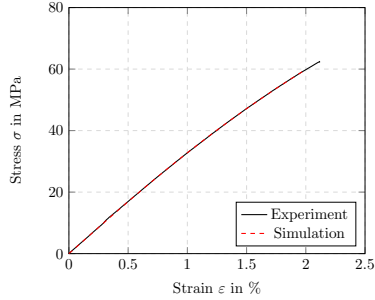
Figure 6.11: Comparison of effective stress-strain curves

6.5.4 Study on SMC composite microstructures

Similarly to the pre-study conducted on neat UPPH in the previous section 6.5.3, we optimize the parameter set needed to describe proper damage evolution in the SMC composite (see Sec. 6.5.2). The allowed ranges for this parameter set during the optimization process are shown in Tab. 6.2. We chose these ranges based on trail studies to provide an optimization hyper-rectangular space that is as large as necessary but as small as possible.

We ran our optimization with 300 initial hypercube samplings and subsequent 3000 iterations, computed in 250 batches with 12 parallel executions on 8 threads each. We update the surrogate model and hence the acquisition function after the computation of each batch.

The underlying microstructure is a generated unit cell (Görthofer et al., 2020), as shown in Fig. 6.12a, with a fiber volume fraction of $25\,\%$ and a planar isotropic orientation, matching the conditions of the specimens discussed in Sec. 6.2.2.

(a) $\mathrm{diag}(0.5, 0.5, 0)$ – Planar isotropic orientation **(b)** $\mathrm{diag}(0.7, 0.3, 0)$ – Higher alignment in $\boldsymbol{e}_x$-direction **(c)** $\mathrm{diag}(1, 0, 0)$ – Unidirectional orientation in $\boldsymbol{e}_x$-direction
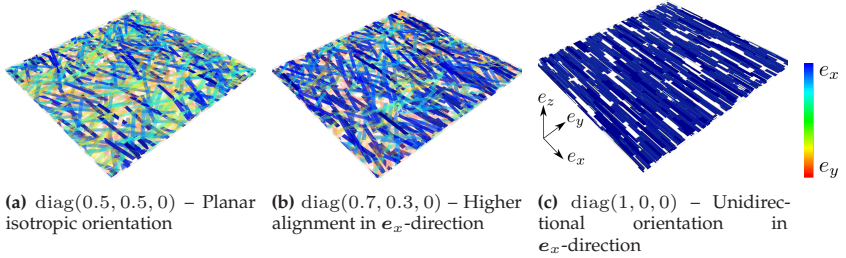
Figure 6.12: Example of generated unit cells. Coloring indicates bundle orientation. Matrix is hidden.

Using the introduced microstructure generation approach (Görthofer et al., 2020), we transfer our results to SMC composite unit cells with different orientations, see Fig. 6.12 and Sec. 6.6. Therefore, we generated additional unit cells with fiber bundles oriented in $\boldsymbol{e}_x$-direction to a higher extent and unit cells with a pure unidirectional bundle alignment in $\boldsymbol{e}_x$-direction, see Fig. 6.12b and Fig. 6.12c. The associated fiber orientation tensors of second-order (Advani and Tucker, 1987) are given in the captions.

The cost function values $c(p)$ of the 300 initial samples and the best result per batch for the subsequent iterations are shown in Fig. 6.13. The lighter areas mark the 95 % confidence interval for each result. We observe a high variation in the cost function values for the 300 initial sampling iterations, as we raster the complete hyper-rectangular parameter space. In a sense, we maximize the exploitation and minimize the expectation in our discussed trade-off (see Sec. 6.4), to gain as much knowledge about the cost function behavior as possible during initialization.

In the following 1400 iterations the variation of the cost function decreases, but nonetheless remains relatively high, see Fig. 6.13a and Fig. 6.13b. As the behavior of the cost function is governed by six parameters, the individual influences need to be explored, which is

(a) All iterations　　　**(b)** Iterations 1500 - 1900　　　**(c)** Last 400 iterations
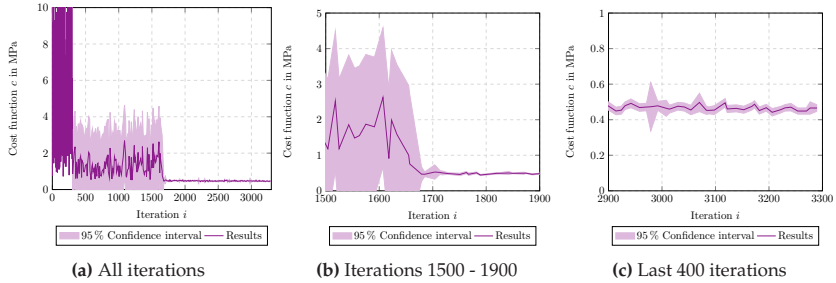
Figure 6.13: Best value per batch of the cost function $c(p)$ over iterations

responsible for this prolonged variation with its quite large confidence interval. After about a total of 1700 iterations, a possible optimum is found with a cost function value of approximately 0.45 MPa and a small confidence interval of the order of ± 0.01 MPa, see Fig. 6.13b. For the remainder of the optimization process, the variation of the best cost function value per batch is negligibly small with an associated small confidence interval, see Fig. 6.13c.

Table 6.3: Extraction tensors and identified SMC composite damage parameters

	$\mathbb{B}$	σ_0 in MPa	s in %	H in MPa	s in %
UPPH	(6.7)	43.99	24	177.84	3
Bundle	(6.24)	29.36	11	381.64	4
	(6.47)	28.60	51	123.81	7

Hence, we can assume the best overall cost function value of about 0.44 MPa (which is $0.33\,\%$ of the mean ultimate strength) to be reasonably close to the actual optimum. The corresponding values of the best parameter set to describe damage evolution in our SMC composite are listed in Tab. 6.3. Furthermore, the sensitivity s of each parameter in

terms of its associated hyperparameter related to all hyperparameters is added. In general, the identified optimum of the cost function shows a higher sensitivity w. r. t. the damage-activation threshold σ_0 compared to the hardening parameter H.

A comparison of the experimentally measured stress-strain curve (see Sec. 6.2.2, cf. Fig. 6.3) and the computed stress-strain curve is given in Fig. 6.14. These curves, representing the macroscopic structural behavior of our SMC composite, are in good agreement. With our defined damage cases, the corresponding damage-activation functions, extraction tensors and identified parameters at hand, we can predict the macroscopic behavior of the SMC composite unit cell accurately.
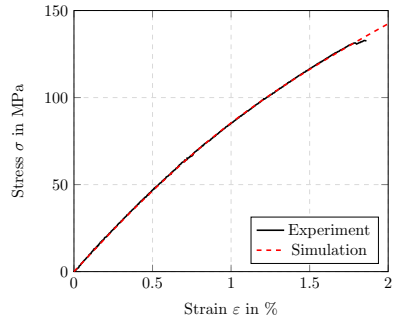
Figure 6.14: Comparison of effective stress-strain curves

6.6 Identification of macroscopic failure surfaces for SMC composites

6.6.1 Full-field damage evolution

The introduced damage cases and identified parameters do not only allow for the prediction of the macroscopic stress-strain behavior, but also help us to evaluate the evolution and full-field distribution of damage on the microscale. With damage in terms of microcrack evolution (Schöttl et al., 2020; Schöttl et al., 2021a) in mind, we analyze the predicted damage in the UPPH matrix. The evolution of damage over different loading steps is shown in Fig. 6.15. In analogy to the discussed

experiments, we consider a slice of a planar isotropic microstructure that is loaded in vertical direction. Damage in the matrix mainly initiates at the rims of matrix rich regions at bundle edges and corners, see Fig. 6.15a and Fig. 6.15b. With increasing loading level, on the one hand the damage level of existing damaged regions increases and expands, and on the other hand additional damaged areas arise, see Fig. 6.15c and Fig. 6.15d. At a certain loading level, a large share of the matrix is damaged, i.e., the density of microcracks is relatively high, compare Fig. 6.5d. Correspondingly, bundle damage evolves as the matrix damage increases. The sum of all these types of damage, matrix damage followed by bundle damage, eventually accumulates to macroscopic failure of the SMC composite. The full-field distribution of bundle damage is discussed in Appendix D.

(a) Strain 1 %   **(b)** Strain 1.5 %   **(c)** Strain 2 %   **(d)** Strain 2.5 %
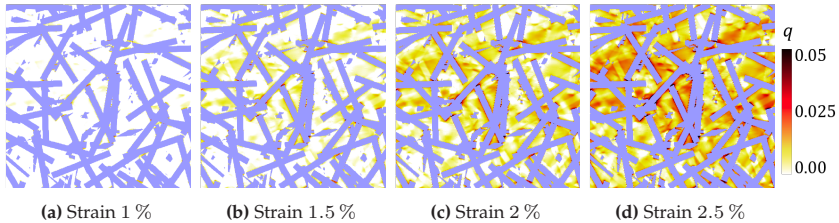
Figure 6.15: Evolution of matrix damage during increased loading in vertical direction, in analogy to experimental observations as presented in Fig. 6.5

Our presented framework allows for the generation and computation of microstructures with orientations deviating from the planar isotropic state. The distribution of the predicted damage in the UPPH matrix due to a loading of 2.5 % strain in e_x-direction is shown in Fig. 6.16. Basically, we observe a larger distribution of matrix damage for the planar isotropic orientation in comparison to orientations with a preferred alignment in loading direction. The less bundles are oriented in loading direction,

the less these bundles can bear the applied loading. Consequently, the loading level in the matrix is higher and so is the general damage level. Occurring damage is distributed in the transition areas between bundles at the bundle tips, and localizes especially at rims of matrix rich areas, see Fig. 6.16b and Fig. 6.16c. Corresponding analyzes regarding the distributions of bundle damage w. r. t. the orientation are given in Appendix D.

(a) Planar isotropic orientation **(b)** Higher alignment in e_x-direction **(c)** Unidirectional orientation in e_x-direction
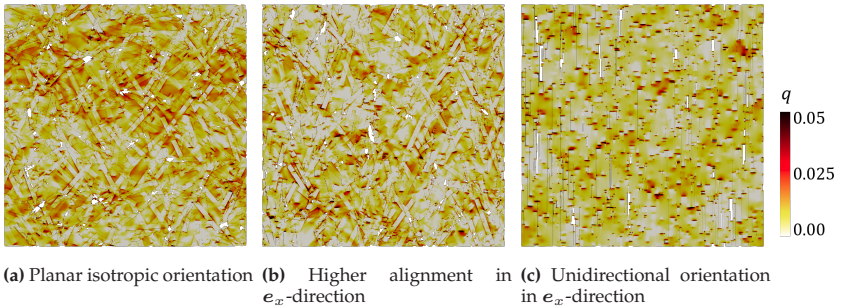
Figure 6.16: Predicted UPPH matrix damage according to Sec. 6.3.3 for different orientations and loading of 2.5 % strain in e_x-direction (see Fig. 6.12 for corresponding microstructures). Bundles are hidden.

6.6.2 Structural analysis perspective

Utilizing the experimental observations discussed in Sec. 6.2, we derive different macroscopic failure criteria based on corresponding full-field damage distributions. To investigate the influence of the interaction between fiber bundle orientation and loading direction on the damage evolution and the consequent point of failure, we load generated microstructures with different orientation states (see Fig. 6.12) in different, non-uniform distributed directions $n \in S^2 = \{x \in \mathbb{R}^3 \mid \|x\| = 1\}$.

175

Therefore, we sample 1000 directions on a unit half sphere with positive e_z-direction, see Fig. 6.17. In analogy to the conducted experiments, we apply an effective uniaxial strain boundary condition in all sampled directions.

For each direction, we compute the damage evolution and the stress response, and evaluate the macroscopic stiffness reduction. For the latter, we compare the current effective stiffness with the initial stiffness in terms of the directional Young's modulus $E(\boldsymbol{n})$ computed via the stress-strain relation $\triangle\sigma(\boldsymbol{n})/\triangle\varepsilon(\boldsymbol{n})$. Given a direction $\boldsymbol{n}$, the associated directional stress $\sigma(\boldsymbol{n})$ can be extracted via

Figure 6.17: Sampled directions on unit half sphere

$$\sigma(\boldsymbol{n}) = \boldsymbol{\sigma} \cdot (\boldsymbol{n} \otimes \boldsymbol{n}) \,, \tag{6.63}$$

and similarly for the directional strain.

Fig. 6.18 shows the resulting failure surfaces of a planar isotropic microstructure for different stiffness reductions, derived from the range of reductions known from the experimental observations, see Fig. 6.4d. These plots define the maximum allowable stresses for a given level of admissible damage before total failure. Hence, these failure surfaces serve as criterion on a macroscopic integration point level whether a part will sustain a certain stress level or not.

For comparability, we depict the failure surfaces in terms of a constrained plot in the $\{\boldsymbol{e}_x, \boldsymbol{e}_y, \boldsymbol{e}_z\}$-space. Note that the negative axes for the stresses in the $\boldsymbol{e}_x$-$\boldsymbol{e}_y$-plane are caused by the corresponding loading directions that point into negative $\boldsymbol{e}_x$- and/or $\boldsymbol{e}_y$-direction, see Fig. 6.17. The associated directional stress levels themselves are always positive.

(a) 10 % reduction   **(b)** 20 % reduction   **(c)** 30 % reduction   **(d)** 40 % reduction

Figure 6.18: Failure surface plots for a microstructure with planar isotropic orientation

Evaluating Fig. 6.18, the planar isotropic nature of the microstructure is apparent, as the failure surface is rotationally symmetric about the e_z-axis, i. e., the directional stress evoking a certain stiffness reduction remains the same irrespective of the loading direction within the e_x-e_y-plane. Choosing an admissible stiffness reduction of 20 % would allow for a directional stress of about 120 MPa in the e_x-e_y-plane, see Fig. 6.18b. An increasing e_z-component of the loading direction leads to lower allowed stress levels before failure, as the supporting influence of the fiber bundles decreases for an increasing deviation of the loading direction away from the isotropic e_x-e_y-plane.

Considering a microstructure with bundles being preferably aligned in e_x-direction, see Fig. 6.12b, we obtain the failure surfaces shown in Fig. 6.19. The influence of the non-isotropic bundle orientation is noticeable through the elongated shape of the failure surface in e_x-direction. As more bundles are aligned in e_x-direction, the corresponding stress level is highest and decreases for loadings with increasing components in e_y-direction and/or e_z-direction.

For an allowed stiffness reduction of 20 %, an SMC composite part with said orientation could bear stresses of up to 250 MPa in e_x-direction and about 75 MPa in e_y-direction, see Fig. 6.19b. If we also add a component in e_z-direction with an angle of about 45°, the structure withstands stresses between 75 MPa and 105 MPa before total failure.

(a) 10 % reduction   **(b)** 20 % reduction   **(c)** 30 % reduction   **(d)** 40 % reduction
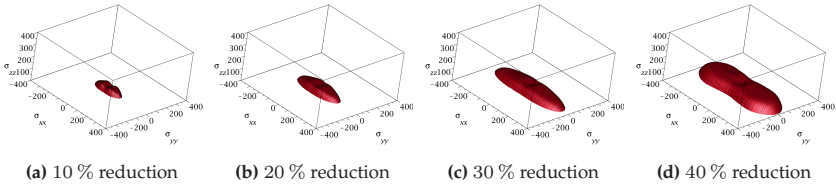
Figure 6.19: Failure surface plots for a microstructure with higher alignment in e_x-direction

For a microstructure with (fully) aligned bundles in e_x-direction, see Fig. 6.12c, the resulting failure surfaces follow a similar pattern as for the slight orientation in e_x-direction shown in Fig. 6.19, but are more pronounced in their extremes, see Fig. 6.20. Furthermore, the failure surfaces are rotationally symmetric about the e_x-axis, i. e., the admissible stress level remains unchanged for any loading direction in a e_y-e_z-plane. For all loading directions with no component in e_x-direction, the allowed stress level is lowest.

(a) 10 % reduction   **(b)** 20 % reduction   **(c)** 30 % reduction   **(d)** 40 % reduction
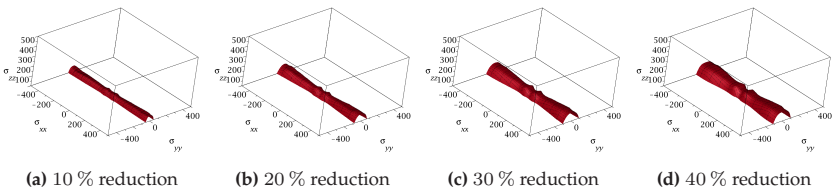
Figure 6.20: Failure surface plots for a microstructure with unidirectional orientation in e_x-direction

The bulges, that become more pronounced for higher stiffness reductions, are caused by the reinforcing character of the fiber bundles for any loading direction with at least a small component in e_x-direction. The bearable stress significantly increases for any loading direction with a

non-zero component in e_x-direction, see Fig. 6.20d. A further increase of the e_x-component further increases the bearable stress level, but its effect decreases.

6.6.3 Design perspective

In addition to the structural analysis of our SMC composite, we use our approach to analyze the SMC composite loading conditions from a design perspective. For that case, we consider loadings that evoke specific stress levels, e. g., motivated by given component specifications or boundary conditions, and evaluate the resulting stiffness reduction. The gained knowledge on stiffness reduction due to given stress levels helps identifying and revisiting critical component areas during the design process to counter failure from the start.

To scrutinize the relation between applied stress level and resulting stiffness reduction, we compute the directional-dependent relative residual Young's modulus (RRYM) as

$$\delta(\boldsymbol{n}) = \frac{E(\boldsymbol{n})}{E_0(\boldsymbol{n})} \tag{6.64}$$

via the current (damaged) Young's modulus $E(\boldsymbol{n})$ and the initial Young's modulus $E_0(\boldsymbol{n})$ in a direction $\boldsymbol{n}$. Hence, a value of $\delta(\boldsymbol{n}) = 100\,\%$ represents a sound Young's modulus in that direction $\boldsymbol{n}$.

Similar to the analysis conducted in Sec. 6.6.2, we depict the RRYM via iso-surface plots in the $\{\boldsymbol{e}_x, \boldsymbol{e}_y, \boldsymbol{e}_z\}$-space. Note that the negative axes for the RRYM in the $\boldsymbol{e}_x$-$\boldsymbol{e}_y$-plane are caused by the corresponding loading directions that point into negative $\boldsymbol{e}_x$- and/or $\boldsymbol{e}_y$-direction, see Fig. 6.17. The associated directional RRYM themselves are always positive.

For a microstructure with planar isotropic orientation, the RRYM plots are shown in Fig. 6.21. For an applied stress of $10\,\mathrm{MPa}$, the behavior is purely elastic and damage does not initiate yet, which yields a

value of $\delta(\boldsymbol{n}) = 100\,\%$ in all directions, see Fig. 6.21a. If the stress level is $60\,\mathrm{MPa}$, damage evolves and the stiffness is reduced, see Fig. 6.21b. The stiffness reduction is smallest in the $\boldsymbol{e}_x$-$\boldsymbol{e}_y$-plane and highest for loading in out-of-plane $\boldsymbol{e}_z$-direction, which is in line with the observations made in Fig. 6.18. The RRYM is rotationally symmetric about the $\boldsymbol{e}_z$-axis due to the planar isotropic nature of the microstructure. For higher loadings, the RRYM decreases further, as shown in Fig. 6.21c. For convenience, we highlighted the undamaged regions with values of $\delta(\boldsymbol{n}) = 100\,\%$ in the $\boldsymbol{e}_x$-$\boldsymbol{e}_y$-plane in gray. A stress level of $180\,\mathrm{MPa}$ results in a RRYM within the $\boldsymbol{e}_x$-$\boldsymbol{e}_y$-plane of about $\delta(\boldsymbol{n}) = 67\,\%$, which corresponds to the experimental observations, compare Fig. 6.21d and Fig. 6.4. If we load the microstructure with a component in $\boldsymbol{e}_z$-direction having a $45°$ angle, the RRYM would be $\delta(\boldsymbol{n}) = 53\,\%$ for the same loading level.

(a) 10 MPa stress **(b)** 60 MPa stress **(c)** 120 MPa stress **(d)** 180 MPa stress
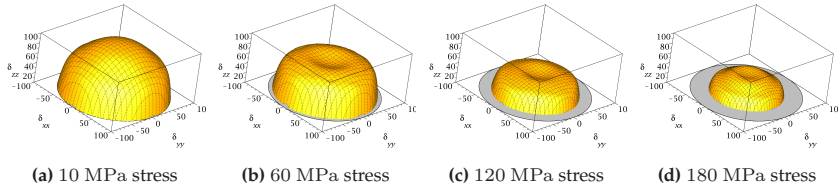
Figure 6.21: Relative residual Young's modulus plots for a microstructure with planar isotropic orientation

The RRYM plots for an SMC composite microstructure that is preferably oriented in $\boldsymbol{e}_x$-direction are shown in Fig. 6.22. For stress levels that induce damage, the RRYM is highest in $\boldsymbol{e}_x$-direction due to the reinforcing nature of the bundles and decreases towards a loading in $\boldsymbol{e}_y$-direction. The RRYM is lowest for loadings in out-of-plane $\boldsymbol{e}_z$-direction, as we lack any supportive effect of the fiber bundles, see Fig. 6.22c. For an applied stress of $120\,\mathrm{MPa}$, the RRYM is about $90\,\%$ in $\boldsymbol{e}_x$-direction and

about 60 % in e_y-direction. Similar to observations made in Fig. 6.21d, we see the formation of bulges in Fig. 6.22d. Even a small proportion of bundles oriented in loading direction have a comparatively high influence on the overall damage evolution, and the RRYM in vicinity of the e_z-direction immediately increases with a comparatively high slope.

(a) 10 MPa stress   **(b)** 60 MPa stress   **(c)** 120 MPa stress   **(d)** 180 MPa stress
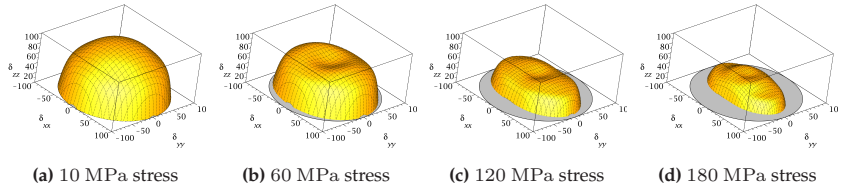
Figure 6.22: Relative residual Young's modulus plots for a microstructure with higher alignment in e_x-direction

The resulting RRYM plots for a microstructure with unidirectionally aligned bundles in e_x-direction are shown in Fig. 6.23. These plots are rotationally symmetric about the unidirectional e_x-axis. The general behavior is similar to the one observed in Fig. 6.22, but more extreme. Again, we observe a higher sensitivity of the RRYM in vicinity to loadings in the e_y-e_z-plane and a lower sensitivity for loadings oriented in bundle direction e_x.

(a) 10 MPa stress   **(b)** 60 MPa stress   **(c)** 120 MPa stress   **(d)** 180 MPa stress
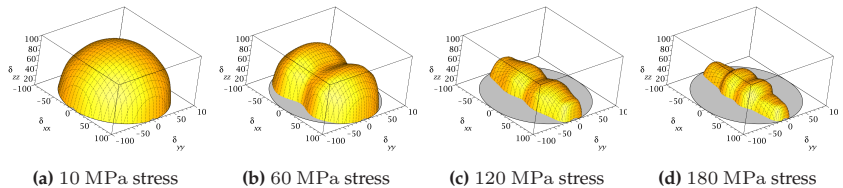
Figure 6.23: Relative residual Young's modulus plots for a microstructure with unidirectional orientation in e_x-direction

6.7   Conclusions

This chapter was devoted to identifying macroscopic and anisotropic failure criteria for SMC composites that are motivated by damage evolution on the microscale. Accumulating damage in matrix and bundles in terms of microcracking (Fitoussi et al., 2005; Ogihara and Koyanagi, 2010; Schöttl et al., 2021a) on the microscale yields a hardening regime on the macroscale and eventually ends in abrupt failure (Meraghni and Benzeggagh, 1995; Trauth, 2020).

To capture such a structural behavior, we applied an anisotropic and modular framework (Görthofer et al., 2022b). The modular concept allows for the description of fully anisotropic stiffness degradation based on extraction tensors. Inspired by Puck's theory for laminates (Puck and Schürmann, 2002; Knops, 2008), as well as dilatation and distortion, we introduced a number of extraction tensors specifically designed to model damage evolution in SMC composites.

With the help of Bayesian optimization (Frazier, 2018), integrating a Mátern $5/2$ kernel, an anisotropic distance function for the underlying Gaussian process and an "expected improvement" acquisition function, we were able to identify all necessary parameters in the highly heterogeneous solution space. An implementation combining the experimental results, an FFT-based full-field homogenization approach (Schneider, 2021), generated SMC composite microstructures (Görthofer et al., 2020) and a corresponding error measure, allowed for a successful minimization of the cost function.

We compared our predicted full-field damage results to corresponding in-situ µCT scan analyzes. Matrix damage in the form of microcracks initiates at the rims of matrix rich regions and is followed by bundle damage. Utilizing generated SMC composite microstructures (Görthofer et al., 2020), we transfered our findings onto microstructures with individually selected orientations.

To propel scale-transition, we identified appropriate micromechanics-based anisotropic failure surfaces. We proposed, on the one hand, failure surfaces in stress space considering given admissible stiffness reductions, useful for structural analysis processes. On the other hand, we introduced relative residual stiffness (failure) surfaces based on predetermined component boundary conditions, which are vital for (virtual) design processes. We analyzed the influence of the fiber bundle orientation on both approaches for specific representative microstructures.

The presented framework forms a foundation for a micromechanically and physically motivated database for anisotropic failure criteria on integration point level for SMC composites. In analogy to databases identified for plasticity and short fiber reinforced composites (Köbler et al., 2018; Gajek et al., 2021), a proper discretization and sampling of the orientation space can be established for orientation-dependent SMC composite failure criteria. Furthermore, an uncertainty quantification of the resulting damage and consequent macroscopic failure w. r. t. microscopic parameter variations (such as phase properties or volume fractions) can be investigated. The implemented damage model directly operates on the compliance tensor, which allows for a straightforward coupling of damage evolution to other phenomena such as plasticity (Simo and Ju, 1987; Ju, 1989) in future applications.

Chapter 7

Summary and outlook

In this thesis, we were concerned with full-field modeling of SMC composites. To provide an understanding of the SMC composite under consideration, we presented an overview on the manufacturing process and the resulting characteristic microstructure in **Chapter 3**.

The main focus of our research regarded damage modeling of SMC composites on the microscale and a consecutive holistic approach to transfer the results to be used within macroscopic structural material models. The research aimed at a deeper understanding of the material behavior on the microscale to propel the use of SMC composites as structural, load-bearing components. Within this thesis, we focused on three main research topics.

Having accurate SMC composite microstructures (including important properties such as orientation distribution) is a key foundation for corresponding material models to be developed, verified and validated. Hence, in **Chapter 4**, we presented a method to generate SMC composite microstructures using an adapted random sequential addition approach. As we relied upon an exact closure approximation in two dimensions and a quasi-random orientation sampling, we were able to generate high fidelity representative unit cells. Using our improved unit cell generator, we conducted a detailed sensitivity analysis via thousands of microstructures, i.e., we thoroughly investigated the influence of microstructural and mechanical parameters on the effective elastic properties of our SMC composite. These results, on the one hand

provide detailed relations between microscopic and elastic macroscopic parameters, and on the other hand serve as starting point for studying the inelastic behavior of SMC composites.

In **Chapter 5**, we presented a general convex framework to compute anisotropic damage evolution via a direct operation on the compliance tensor. The model is formulated in the setting of generalized standard materials, is thermodynamically consistent and fulfills Wulfinghoff's damage growth criterion. Using a modular ansatz based on extraction tensors, we were able to formulate the model so that it can be adapted and applied to any hardening-type material. Furthermore, we designed specific extraction tensors motivated by Puck's theory on laminates in an averaged stress setting. A multitude of different examples showed the capability of predicting *any* anisotropic damage evolution on the micro- and the macroscale. In future applications, the modular character allows for an extension of the model to also account for softening-type behavior, as well as coupling to further phenomena such as plasticity.

We applied our damage model to the considered SMC composite in **Chapter 6**. Upon analyzing the behavior of the material via different experimental investigations and in-situ μCT testing in combination with results taken from corresponding publications, we identified the main damage phenomena on the microscale and the associated macroscopic structural behavior. We introduced new sets of extraction tensors accounting for damage in the fiber bundles and the matrix. Therefore, we used Puck-type criteria in combination with a pencil glide ansatz to account for maximum stresses, as well as ansatzes taking into account distortion and dilatation. A Bayesian optimization based on Gaussian distributions and an anisotropic distance function enabled identification of all associated damage parameters via corresponding comparisons to experimental results. Computations and FFT-based full-field homogenization on different generated microstructures loaded in 1000 directions allowed for an holistic approach identifying macroscopic

failure criteria based on damage evolution on the microscale. Here, we provided both a design perspective and a structural analysis perspective in terms of different failure surfaces. A sampling of the orientation space for the presented approach can provide a database for orientation-dependent SMC composite failure criteria in future work and give a meaningful basis for macroscopic phenomenological failure modeling. Furthermore, an uncertainty quantification of microscopic anisotropic damage evolution and predicted macroscopic failure regarding variations of microscopic properties can be conducted.

Taking all results into consideration, this thesis provides tools to generate bundle microstructures, model any hardening-type damage material and a corresponding setup to identify all necessary damage parameters in the framework of FFT-based full-field computations. Furthermore, we applied our models to account for damage evolution in SMC composites on the microscale in combination with an approach to identify anisotropic failure criteria on the macroscale. Our research can be extended to describe SMC composites in more detail via an adaption of the bundle generator or the damage model via further experimental investigations (Schemmann et al., 2018c;a). Furthermore, an extension towards fatigue (Bartkowiak et al., 2020; Magino et al., 2022) would be possible. A coupling to sophisticated compression molding flow models (Meyer et al., 2020) could form the basis of an improved virtual process chain for SMC composites (Görthofer et al., 2019b). Via a combination with a proper plasticity model and a new set of extraction tensors, the damage model could be used to describe DiCoFRTP such as LFT in the third doctoral generation of IRTG 2078.

Appendix A

Proofs for the explicit exact closure approximation

First, we wish to show the first identity of (3.13). (The second identity follows by symmetry considerations.) Thus, we wish to prove the equation

$$\frac{1}{2\pi} \int_0^{2\pi} \frac{\cos^2 \phi}{B_1 \cos^2 \phi + B_2 \sin^2 \phi} \, d\phi = \frac{1}{1 + B_1}. \tag{A.1}$$

Denote the left hand side of (A.1) by A_1. By symmetry, we have

$$A_1 = \frac{2}{\pi B_1} \int_0^{\frac{\pi}{2}} \frac{1}{1 + \alpha \tan^2 \phi} \, d\phi \quad \text{with} \quad \alpha = \frac{B_2}{B_1}. \tag{A.2}$$

Substituting $x = \tan \phi$ yields

$$A_1 = \frac{2}{\pi B_1} \int_0^{\infty} \frac{1}{(1 + \alpha x^2)(1 + x^2)} \, dx. \tag{A.3}$$

Decomposing the integrand into partial fractions yields[1]

$$\frac{1}{(1 + \alpha x^2)(1 + x^2)} = \frac{\alpha}{\alpha - 1} \frac{1}{1 + \alpha x^2} - \frac{1}{\alpha - 1} \frac{1}{1 + x^2} \tag{A.4}$$

---

[1] If $\alpha = 1$, temporarily set $\alpha = 1 - \varepsilon$ for $\varepsilon > 0$ small, and let $\varepsilon \to 0$ in the end.

Thus,

$$A_1 = \frac{2}{\pi B_1} \left[\frac{\alpha}{\alpha - 1} \int_0^\infty \frac{1}{1 + \alpha x^2}\, dx - \frac{1}{\alpha - 1} \int_0^\infty \frac{1}{1 + x^2}\, dx \right]. \quad \text{(A.5)}$$

Using the identities (easily shown by substitution)

$$\int_0^\infty \frac{1}{1 + \alpha x^2}\, dx = \frac{1}{\sqrt{\alpha}} \int_0^\infty \frac{1}{1 + x^2}\, dx, \quad \text{(A.6)}$$

$$\int_0^\infty \frac{1}{1 + x^2}\, dx = \frac{\pi}{2}, \quad \text{(A.7)}$$

we arrive at the identity

$$A_1 = \frac{1}{B_1} \frac{\sqrt{\alpha} - 1}{\alpha - 1} = \frac{1}{B_1} \frac{1}{\sqrt{\alpha} + 1} = \frac{1}{\sqrt{B_1}} \frac{1}{\sqrt{B_2} + \sqrt{B_1}} = \frac{1}{1 + B_1}, \quad \text{(A.8)}$$

where we have used $B_1 B_2 = 1$ for the last equality. Thus, we have shown (A.1).

Next, we wish to show Eq. $(3.14)_1$. By definition we have

$$A_{1111} = \frac{1}{2\pi} \int_0^{2\pi} \frac{\cos^4 \phi}{B_1 \cos^2 \phi + B_2 \sin^2 \phi}\, d\phi. \quad \text{(A.9)}$$

Following identical steps as for A_1 we arrive at the identity

$$A_{1111} = \frac{2}{\pi B_1} \int_0^\infty \frac{1}{(1 + \alpha x^2)(1 + x^2)^2}\, dx. \quad \text{(A.10)}$$

Decomposing the integrand into partial fractions yields

$$\frac{1}{(1 + \alpha x^2)(1 + x^2)^2} =$$
$$\frac{\alpha^2}{(1 - \alpha)^2} \frac{1}{1 + \alpha x^2} - \frac{\alpha}{(1 - \alpha)^2} \frac{1}{1 + x^2} + \frac{1}{1 - \alpha} \frac{1}{(1 + x^2)^2} \quad \text{(A.11)}$$

Notice

$$\int_0^\infty \frac{1}{1 + \alpha x^2}\, \mathrm{d}x = \frac{1}{\sqrt{\alpha}}\frac{\pi}{2}, \tag{A.12}$$

$$\int_0^\infty \frac{1}{1 + x^2}\, \mathrm{d}x = \frac{\pi}{2}, \tag{A.13}$$

$$\int_0^\infty \frac{1}{(1 + x^2)^2}\, \mathrm{d}x = \frac{\pi}{4}. \tag{A.14}$$

The last integral can be evaluated, for instance, by differentiating $\int_0^\infty \frac{1}{z+x^2}\, \mathrm{d}x = \frac{1}{\sqrt{z}}\frac{\pi}{2}$ at $z = 1$. Consequently, we get

$$A_{1111} = \frac{1}{B_1}\left[\frac{\alpha(\sqrt{\alpha} - 1)}{(1 - \alpha)^2} + \frac{1}{2}\frac{1}{1 - \alpha}\right], \tag{A.15}$$

which we rewrite, using the second identity in (A.8),

$$\begin{aligned}
A_{1111} &= \frac{1}{2B_1(1 + \sqrt{\alpha})}\frac{1}{(1 - \sqrt{\alpha})}\left[\frac{2\alpha(\sqrt{\alpha} - 1)}{1 - \alpha} + 1\right] \\
&= \frac{A_1}{2}\left[\frac{1}{1 - \sqrt{\alpha}} - \frac{2\alpha}{1 - \alpha}\right].
\end{aligned} \tag{A.16}$$

The last factor can be further processed,

$$\begin{aligned}
\frac{1}{1 - \sqrt{\alpha}} - \frac{2\alpha}{1 - \alpha} &= \frac{1 + \sqrt{\alpha} - 2\alpha}{1 - \alpha} = 1 - \frac{\alpha - \sqrt{\alpha}}{1 - \alpha} = 1 + \frac{\sqrt{\alpha}}{1 + \sqrt{\alpha}} \\
&= 1 + \frac{\sqrt{B_2}}{\sqrt{B_1} + \sqrt{B_2}} = 1 + \frac{1}{B_1 + 1} = 1 + A_1,
\end{aligned} \tag{A.17}$$

where for the last two transformations we used $B_1 B_2 = 1$ and (A.8). Thus, we finally arrive at

$$A_{1111} = \frac{1}{2}A_1(1 + A_1), \tag{A.18}$$

which we wanted to prove.

Equation $(3.14)_2$ follows similarly to Eq. $(3.14)_1$. Equation $(3.14)_4$ and Eq. $(3.14)_5$ are trivially satisfied as the integrand is an odd function (w. r. t. π). Last but not least, Eq. $(3.14)_3$ follows from the identity

$$A_1 = A_{1111} + A_{1122} \tag{A.19}$$

which can be either proven abstractly, i. e., $A_{ij} = \sum_{k=1}^{n} A_{ijkk}$ holds, or concretely for the integrals using $\cos^2 \phi + \sin^2 \phi = 1$.

Appendix B

Evolution equations for internal variables

In this appendix, we give a short overview on the formulations regarding the evolution of the internal variables and the associated Karush-Kuhn-Tucker (KKT) conditions of our damage model as presented in Sec. 5.2.

<table>
<tr><td colspan="2" align="center">Summary of formulations for evolution equations for internal variables of the damage model presented in Sec. 5.2</td></tr>
<tr><td align="center">General formulation</td><td align="center">$z = (\mathbb{S}, q) \quad$ (5.9)</td></tr>
<tr><td align="center">$\dot{z} \in \partial \Phi^* \left(-\dfrac{\partial w}{\partial z}(\varepsilon, z) \right)$</td><td align="center">$(\dot{\mathbb{S}}, \dot{q}) \in \partial \Phi^* (\mathbb{T}, \beta)$</td></tr>
<tr><td align="center">$\Phi^* \longleftrightarrow \phi_i \quad$ (5.20)</td><td align="center">$\phi_i(\mathbb{T}, \beta) \quad$ (5.25)</td></tr>
<tr><td align="center">$\dot{\mathbb{S}} = \displaystyle\sum_{i=1}^{M} \dot{\mu}_i \dfrac{\partial \phi_i(\mathbb{T}, \beta)}{\partial \mathbb{T}}$</td><td align="center">$\dot{\mathbb{S}} = 2 \displaystyle\sum_{i=1}^{M} \dot{\mu}_i \, \mathbb{B}_i^2$</td></tr>
<tr><td align="center">$\dot{q} = \displaystyle\sum_{i=1}^{M} \dot{\mu}_i \dfrac{\partial \phi_i(\mathbb{T}, \beta)}{\partial \beta}$</td><td align="center">$\dot{q}_i = \dot{\mu}_i H_i, \quad i = 1, \ldots, M$</td></tr>
</table>

Summary of Karush-Kuhn-Tucker (KKT) conditions for internal variables of the damage model presented in Sec. 5.2

Karush-Kuhn-Tucker (KKT) conditions   (5.23)

$$\dot{\mu}_i \geq 0, \quad \phi_i(\mathbb{T}, \beta) \leq 0, \quad \dot{\mu}_i\, \phi_i(\mathbb{T}, \beta) = 0, \quad i = 1, \ldots, M$$

Express KKT conditions in terms of $\boldsymbol{\sigma}$ and q_i (5.28), (5.34)

$$\dot{q}_i \geq 0, \quad f_i(\boldsymbol{\sigma}, q_i) \leq 0, \quad \dot{q}_i\, f_i(\boldsymbol{\sigma}, q_i) = 0, \quad i = 1, \ldots, M$$

Appendix C

Convexity of the Hookean elastic energy density

In this appendix, we compute the Hessian of the Hookean elastic energy (density) w_e, see formula (5.11). We show the Hookean elastic energy (density) to be jointly convex in both the strain and the compliance. This characteristic feature in combination with a hardening-type damage potential enables us to design a damage evolution framework which is convex itself.

For a twice (Fréchet) differentiable function $f : U \subseteq X \to \mathbb{R}$ on an open subset of a (Banach) vector space, the Hessian at some point $x \in U$ may be represented as a quadratic form

$$D^2 f(x) : X \to \mathbb{R}, \tag{C.1}$$

which may be computed by the directional second derivative

$$D^2 f(x)[y] = \frac{1}{2} \frac{\mathrm{d}^2}{\mathrm{d}\lambda^2} f(x + \lambda y)\bigg|_{\lambda=0}. \tag{C.2}$$

For our problem at hand, we have $U = \mathrm{Sym}(d) \times \mathcal{S}_d$ and $X = \mathrm{Sym}(d) \times \mathrm{Sym}(\mathrm{Sym}(d))$. Then, the Hessian of the elastic energy (5.11)

$$
\begin{aligned}
w_e : \quad \mathrm{Sym}(d) \times \mathcal{S}_d \quad &\to \quad \mathbb{R} \\
w_e(\boldsymbol{\varepsilon}, \mathbb{S}) \quad &= \quad \tfrac{1}{2}\, \boldsymbol{\varepsilon} \cdot \mathbb{S}^{-1}\, [\boldsymbol{\varepsilon}]
\end{aligned}
\tag{C.3}
$$

at $(\varepsilon, \mathbb{S})$ in direction $(\boldsymbol{\xi}, \mathbb{L})$ computes as

$$
\begin{aligned}
\mathrm{D}^2 w_e(\varepsilon, \mathbb{S})[\boldsymbol{\xi}, \mathbb{L}] &= \frac{1}{2} \frac{\mathrm{d}^2}{\mathrm{d}\lambda^2} \left(\frac{1}{2} (\varepsilon + \lambda \boldsymbol{\xi}) \cdot (\mathbb{S} + \lambda \mathbb{L})^{-1} [\varepsilon + \lambda \boldsymbol{\xi}] \right) \Big|_{\lambda=0} \\
&= \frac{1}{2} \frac{\mathrm{d}}{\mathrm{d}\lambda} \left(\boldsymbol{\xi} \cdot (\mathbb{S} + \lambda \mathbb{L})^{-1} [\varepsilon + \lambda \boldsymbol{\xi}] \right. \\
&\quad \left. - \frac{1}{2} (\varepsilon + \lambda \boldsymbol{\xi}) \cdot (\mathbb{S} + \lambda \mathbb{L})^{-1} \mathbb{L} (\mathbb{S} + \lambda \mathbb{L})^{-1} [\varepsilon + \lambda \boldsymbol{\xi}] \right) \Big|_{\lambda=0} \\
&= -\frac{1}{2} \boldsymbol{\xi} \cdot \mathbb{S}^{-1} \mathbb{L} \mathbb{S}^{-1} [\varepsilon] + \frac{1}{2} \boldsymbol{\xi} \cdot \mathbb{S}^{-1} [\boldsymbol{\xi}] \\
&\quad - \frac{1}{2} \varepsilon \cdot \mathbb{S}^{-1} \mathbb{L} \mathbb{S}^{-1} [\boldsymbol{\xi}] + \frac{1}{2} \varepsilon \cdot \mathbb{S}^{-1} \mathbb{L} \mathbb{S}^{-1} \mathbb{L} \mathbb{S}^{-1} [\varepsilon] \\
&= \frac{1}{2} \boldsymbol{\xi} \cdot \mathbb{S}^{-1} [\boldsymbol{\xi}] - \boldsymbol{\xi} \cdot \mathbb{S}^{-1} \mathbb{L} \mathbb{S}^{-1} [\varepsilon] + \frac{1}{2} \varepsilon \cdot \mathbb{S}^{-1} \mathbb{L} \mathbb{S}^{-1} \mathbb{L} \mathbb{S}^{-1} [\varepsilon] \\
&= \frac{1}{2} (\boldsymbol{\xi} - \mathbb{L} \mathbb{S}^{-1} [\varepsilon]) \cdot \mathbb{S}^{-1} \left[\boldsymbol{\xi} - \mathbb{L} \mathbb{S}^{-1} [\varepsilon] \right].
\end{aligned}
$$

$$(\mathrm{C}.4)$$

We see that for any admissible strain and compliance $(\varepsilon, \mathbb{S}) \in \mathrm{Sym}(d) \times \mathcal{S}_d$ and any direction $(\boldsymbol{\xi}, \mathbb{L}) \in \mathrm{Sym}(d) \times \mathrm{Sym}(\mathrm{Sym}(d))$, the Hessian is non-negative and hence the elastic energy is convex.

Appendix D

Full-field damage evolution for different microstructures

An increase of the total loading in combination with evolving matrix damage leads to an increase of load being distributed onto specific fiber bundles. Inevitable, damage is also evoked within these bundles in the form of microcracks running through the bundles along the principal direction and interface debonding.

The evolution of bundle damage associated to normal stresses perpendicular to the bundle direction is shown in Fig. D.1 for different loading levels in vertical direction (in analogy to Fig. 6.15 and Fig. 6.5). The higher the loading, the higher the number of bundles that are damaged and the higher the damage level in certain bundles. Generally, bundles perpendicular to the loading direction encounter the highest damage, whereas bundles in loading direction are hardly damaged for the case at hand, see Fig. D.1d.

Analogously, we encounter damage in bundles due to shear in longitudinal bundle direction, which is shown in Fig. D.2. For higher loading levels, bundles that a preferably oriented in loading direction are damaged according to the Puck-type shear criterion, whereas bundles perpendicular to the loading direction are hardly damaged. Hence, our applied Puck-type cases as discussed in Sec. 6.3.4 and Sec. 6.3.4 are somewhat complementary in their effect on the overall damage

(a) Strain 1 %   (b) Strain 1.5 %   (c) Strain 2 %   (d) Strain 2.5 %
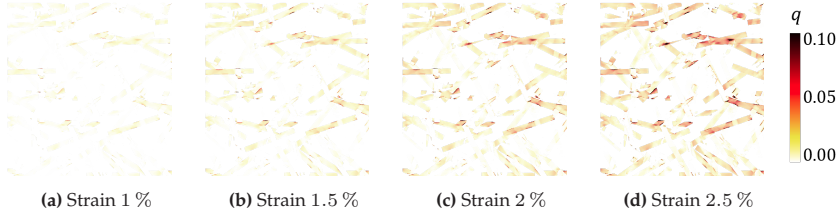
Figure D.1: Evolution of bundle damage perpendicular to bundle direction during increased loading in vertical direction, in analogy to experimental observation as presented in Fig. 6.5

evolution, offering a full coverage of possible stiffness degradations in the bundles.

(a) Strain 1 %   (b) Strain 1.5 %   (c) Strain 2 %   (d) Strain 2.5 %
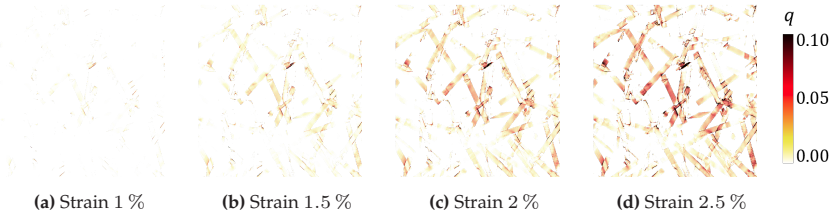
Figure D.2: Evolution of bundle damage in bundle direction during increased loading in vertical direction, in analogy to experimental observation as presented in Fig. 6.5

The evolution and distribution of matrix damage is affected by the orientation of the SMC composite microstructure, see Sec. 6.6.1. The alignment of bundles is essential, as their reinforcing character is more pronounced the more bundles point into loading direction. Correspondingly, damage in bundles due to normal stresses perpendicular to the principal directions is higher and further distributed, the less fibers are oriented in loading direction, see Fig. D.3. In the limit of

a pure unidirectional orientation, bundles do not undergo damage perpendicular to their principal direction, see Fig. D.3c.

(a) Planar isotropic orientation **(b)** Higher alignment in e_x-direction **(c)** Unidirectional orientation in e_x-direction
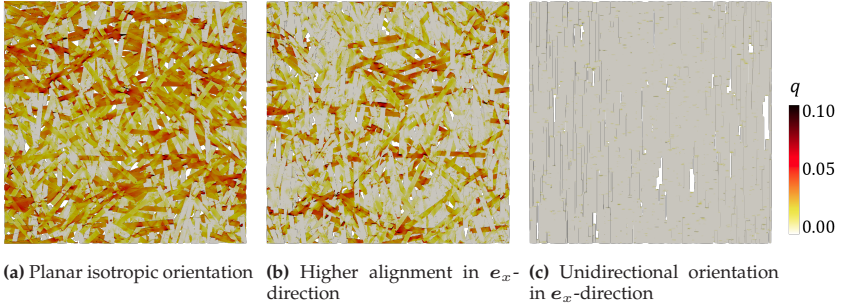
Figure D.3: Predicted bundle damage according to Sec. 6.3.4 for different orientations and loading in e_x-direction (see Fig. 6.12 for corresponding microstructures). Matrix is hidden.

Damage due to shear stresses in principal bundle direction is also affected by the orientation of the SMC composite microstructure, see Fig. D.4. In concurrence with the other damage cases (see Fig. 6.16 and Fig. D.3), the damage level of bundles for the considered case is higher, if more bundles are aligned in loading direction, see Fig. D.4b. For an orientation state in vicinity to a unidirectional alignment in loading direction, damage due to shear stresses localizes mainly at bundle tips at the rims of matrix rich areas, see Fig. D.4c. In these regions, bundles are subjected to local stress excesses due to the prior matrix damage, see Fig. 6.16c, and hence damage evolution is accelerated.
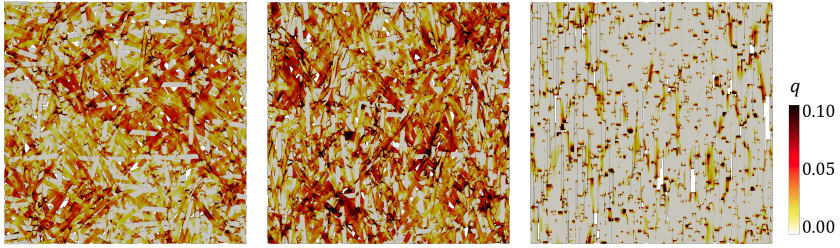
(a) Planar isotropic orientation

(b) Higher alignment in e_x-direction

(c) Unidirectional orientation in e_x-direction

Figure D.4: Predicted bundle damage according to Sec. 6.3.4 for different orientations and loading in e_x-direction (see Fig. 6.12 for corresponding microstructures). Matrix is hidden.

Bibliography

Abu Al-Rub, R. K., Voyiadjis, G. Z., 2009. Gradient-enhanced coupled plasticity-anisotropic damage model for concrete fracture: Computational aspects and applications. International Journal of Damage Mechanics 18 (2), 115–154.

Abu-Farsakh, G. A., Asfa, A. M., 2020. A unified damage model for fibrous composite laminae subject to in-plane stress-state and having multi material-nonlinearity. International Journal of Damage Mechanics 29 (9), 1329–1344.

Advani, S. G., Tucker, C. L., 1987. The Use of Tensors to Describe and Predict Fiber Orientation in Short Fiber Composites. Journal of Rheology 31 (8), 751–784.

Advani, S. G., Tucker, C. L., 1990. Closure approximations for three-dimensional structure tensors. Journal of Rheology 34 (3), 367–386.

Aifantis, E. C., 1984. On the Microstructural Origin of Certain Inelastic Models. Journal of Engineering Materials and Technology 106 (4), 326–330.

Alabdullah, M., Ghoniem, N. M., 2020. A thermodynamics-based damage model for the non-linear mechanical behavior of SiC/SiC ceramic matrix composites in irradiation and thermal environments. International Journal of Damage Mechanics 29 (10), 1569–1599.

Altendorf, H., Jeulin, D., 2011. Random walk based stochastic modeling of 3D fiber systems. Physical Review E 83 (4), 1–10.

Anagnostou, D., Chatzigeorgiou, G., Chemisky, Y., Meraghni, F., 2018. Hierarchical micromechanical modeling of the viscoelastic behavior coupled to damage in SMC and SMC-hybrid composites. Composites Part B: Engineering 151, 8–24.

Arif, M. F., Meraghni, F., Chemisky, Y., Despringre, N., Robert, G., 2014. In situ damage mechanisms investigation of PA66/GF30 composite: Effect of relative humidity. Composites Part B: Engineering 58, 487–495.

Asadi, A., Miller, M., Singh, A. V., .Moon, R. J., Kalaitzidou, K., 2017. Lightweight sheet molding compound (SMC) composites containing cellulose nanocrystals. Composite Structures 160, 211–219.

Bakhshan, H., Afrouzian, A., Ahmadi, H., Taghavimehr, M., 2018. Progressive failure analysis of fiber-reinforced laminated composites containing a hole. International Journal of Damage Mechanics 27 (7), 963–978.

Balzani, D., Ortiz, M., 2012. Relaxed incremental variational formulation for damage at large strains with application to fiber-reinforced materials and materials with truss-like microstructures. International Journal for Numerical Methods in Engineering 92 (6), 551–570.

Bandivadekar, A., Bodek, K., Cheah, L., Evans, C., Groode, T., Heywood, J., Kasseris, E., Kromer, M., Weiss, M., 2008. On the Road in 2035 - Reducing transportation's petroleum consumption and GHG emissions. Tech. rep., Massachusetts Institute of Technology (MIT).

Baptiste, D., 2003. Non linear behavior micromechanical multi-scale modelling of discontinuous reinforced composites. Materials Science Forum 426-432, 3939–3944.

Baranger, E., 2018. Extension of a fourth-order damage theory to anisotropic history: Application to ceramic matrix composites under a multi-axial non-proportional loading. International Journal of Damage Mechanics 27 (2), 238–252.

Barbero, E. J., 2013. Finite Element Analysis of Composite Materials Using Abaqus. CRC Press, Taylor and Francis Group, LLC, New York.

Barbero, E. J., Lonetti, P., 2002. An Inelastic Damage Model for Fiber Reinforced Laminates. Journal of Composite Materials 36 (8), 941–962.

Bargmann, S., Klusemann, B., Markmann, J., Schnabel, J. E., Schneider, K., Soyarslan, C., Wilmers, J., 2018. Generation of 3D representative volume elements for heterogeneous materials: A review. Progress in Materials Science 96, 322–384.

Bartkowiak, M., Liebig, W., Weidenmann, K. A., 2020. Fatigue damage behavior of continuous-discontinuous fiber reinforced sheet molding compounds. In: Proceedings of the 4th International Conference Hybrid 2020 Materials and Structures, Web-Conference, Germany. DGM - Deutsche Gesellschaft für Materialkunde e.V.

Bartkowiak, M., Weit, H., Montesano, J., Weidenmann, K. A., 2019. Characterization of discontinuous fiber reinforced sheet molding compounds under tension-tension fatigue load. In: Kalaitzidou, K. (Ed.), Proceedings of the American Society for Composites - 34th Technical Conference on Composite Materials, Atlanta, USA. Vol. 28428. DEStech Publications.

Bažant, Z. P., 1991. Why Continuum Damage is Nonlocal: Micromechanics Arguments. Journal of Engineering Mechanics 117 (5), 1070–1087.

Becker, R., Needleman, A., Richmond, O., Tvergaard, V., 1988. Void growth and failure in notched bars. Journal of the Mechanics and Physics of Solids 36 (3), 317–351.

Bednarcyk, B. A., Stier, B., Simon, J. W., Reese, S., Pineda, E. J., 2015. Meso- and micro-scale modeling of damage in plain weave composites. Composite Structures 121, 258–270.

Bednarcyk, B. A., Stier, B., Simon, J. W., Reese, S., Pineda, E. J., Arnold, S. M., 2014. Damage Analysis of Composites Using a Three-Dimensional Damage Model: Micro-Scale Architectural Effects. In: Proceedings of the American Society for Composites - 29th Technical Conference, La Jolla, USA. Vol. 513. Curran.

Behnel, S., Bradshaw, R., Citro, C., Dalcin, L., Seljebotn, D. S., Smith, K., 2011. Cython: The Best of Both Worlds. Computing in Science Engineering 13 (2), 31–39.

Belytschko, T., Bažant, Zdeněk P., Hyun, Y.-W., Chang, T.-P., 1986. Strain-Softening Materials and Finite-Element Solutions. Computers and Structures 23 (2), 163–180.

Ben Cheikh Larbi, A., Sai, K., Sidhom, H., Baptiste, D., 2006. Constitutive Model of Micromechanical Damage to Predict Reduction in Stiffness of a Fatigued SMC Composite. Journal of Materials Engineering and Performance 15 (5), 575–580.

Benveniste, Y., 1987. A new approach to the application of Mori-Tanaka's theory in composite materials. Mechanics of Materials 6 (2), 147–157.

Beremin, F. M., Pineau, A., Mudry, F., Devaux, J.-C., D'Escatha, Y., Ledermann, P., 1983. A local criterion for cleavage fracture of a nuclear pressure vessel steel. Metallurgical Transactions A 14 (11), 2277–2287.

Bergounioux, M., Haddou, M., Hintermüller, M., Kunisch, K., 2000. A Comparison of a Moreau–Yosida-Based Active Set Strategy and Interior Point Methods for Constrained Optimal Control Problems. SIAM Journal on Optimization 11 (2), 495–521.

Bergounioux, M., Ito, K., Kunisch, K., 1999. Primal-Dual Strategy for Constrained Optimal Control Problems. SIAM Journal on Control and Optimization 37 (4), 1176–1194.

Bertram, A., 2011. Elasticity and Plasticity of Large Deformations. Springer, Berlin/Heidelberg.

Bhattacharyya, M., Dureisseix, D., Faverjon, B., 2020. Numerical homogenisation based on asymptotic theory and model reduction for coupled elastic-viscoplastic damage. International Journal of Damage Mechanics 29 (9), 1416–1444.

Boehler, J. P., 1987. Applications of Tensor Functions in Solid Mechanics. CISM Courses No. 292. Springer, Wien.

Böhlke, T., 2001. Crystallographic Texture Evolution and Elastic Anisotropy: Simulation, Modeling and Applications. Shaker Verlag, Aachen.

Böhlke, T., Brüggemann, C., 2001. Graphical representation of the generalized Hooke's law. Technische Mechanik 21 (2), 145–158.

Böhlke, T., Henning, F., Hrymak, A., Kärger, L., Weidenmann, K. A., Wood, J. T. (Eds.), 2019. Continuous-Discontinuous Fiber-Reinforced Polymers. Carl Hanser Verlag GmbH & Co. KG, Munich.

Bolstad, W. M., Curran, J. M., 2016. Introduction to Bayesian Statistics. John Wiley & Sons, Inc., Hoboken, New Jersey.

Borwein, J., Lewis, A., 2006. Convex Analysis and Nonlinear Optimization: Theory and Examples. Springer, New York.

Bouhala, L., Makradi, A., Belouettar, S., Kiefer-Kamal, H., Fréres, P., 2013. Modelling of failure in long fibres reinforced composites by X-FEM and cohesive zone model. Composites Part B: Engineering 55, 352–361.

Bretz, L., Häfner, B., Lanza, G., 2021. Non-destructive measurement of fiber mass content of glass fiber sheet molding compound using Terahertz radiation. Measurement 168, 108386.

Bretz, L., Wilke, M., Häfner, B., Lanza, G., 2020. Comparison of anomaly detection capabilities of pulse phase thermography in transmission and reflection setup on Sheet Molding Compound. In: Proceedings of the 4th International Conference Hybrid 2020 Materials and Structures, Germany.

Brinson, H. F., Brinson, L. C., 2008. An Introduction to Polymer Engineering Science & Viscoelasticity. Springer, New York, NY.

Brochu, E., Cora, V. M., De Freitas, N., 2010. A Tutorial on Bayesian Optimization of Expensive Cost Functions, with Application to Active User Modeling and Hierarchical Reinforcement Learning. arXiv 1012.2599.

Browaeys, J. T., Chevrot, S., 2004. Decomposition of the elastic tensor and geophysical applications. Geophysical Journal International 159, 667–678.

Brünig, M., Ricci, S., 2005. Nonlocal continuum theory of anisotropically damaged metals. International Journal of Plasticity 21 (7), 1346–1382.

Brylka, B., 2017. Charakterisierung und Modellierung der Steifigkeit von langfaserverstärktem Polypropylen. Doctoral thesis, Schriftenreihe Kontinuumsmechanik im Maschinenbau Nr. 10, KIT Scientific Publishing, Karlsruhe Institute of Technology (KIT).

Bücheler, D., 2018. Locally continuous-fiber reinforced sheet molding compound. Doctoral thesis, Wissenschaftliche Schriftenreihe des Fraunhofer ICT Nr. 79, Karlsruhe Institute of Technology (KIT), Fraunhofer Verlag, Stuttgart.

Bücheler, D., Trauth, A., Damm, A., Böhlke, T., Henning, F., Kärger, L., Seelig, T., Weidenmann, K. A., 2017. Processing of continuous-discontinuous-fiber-reinforced thermosets. In: SAMPE Europe Conference. Stuttgart.

Chaboche, J.-L., 1981. Continuous damage mechanics - a tool to describe phenomena before crack initiation. Nuclear Engineering and Design 64 (2), 233–247.

Chaboche, J.-L., 1993. Development of Continuum Damage Mechanics for Elastic Solids Sustaining Anisotropic and Unilateral Damage. International Journal of Damage Mechanics 2 (4), 311–329.

Chaboche, J. L., 2008. A review of some plasticity and viscoplasticity constitutive theories. International Journal of Plasticity 24 (10), 1642–1693.

Chen, Q., Zhu, H., Ju, J. W., Jiang, Z., Yan, Z., Li, H., 2018a. Stochastic micromechanical predictions for the effective properties of concrete considering the interfacial transition zone effects. International Journal of Damage Mechanics 27 (8), 1252–1271.

Chen, Z., Huang, T., Shao, Y., Li, Y., Xu, H., Avery, K., Zeng, D., Chen, W., Su, X., 2018b. Multiscale finite element modeling of sheet molding compound (SMC) composite structure based on stochastic mesostructure reconstruction. Composite Structures 188, 25–38.

Cicekli, U., Voyiadjis, G. Z., Abu Al-Rub, R. K., 2007. A plasticity and anisotropic damage model for plain concrete. International Journal of Plasticity 23 (10–11), 1874–1900.

Cintra, J. S., Tucker, C. L., 1995. Orthotropic closure approximations for flow-induced fiber orientation. Journal of Rheology 39 (6), 1095–1122.

Coleman, B. D., Gurtin, M. E., 1967. Thermodynamics with internal state variables. The Journal of Chemical Physics 47 (2), 597–613.

Coleman, B. D., Noll, W., 1963. The thermodynamics of elastic materials with heat conduction and viscosity. Archive for Rational Mechanics and Analysis 13 (1), 167–178.

Cowin, S. C., 1985. The relationship between the elasticity tensor and the fabric tensor. Mechanics of Materials 4 (2), 137–147.

Dassault Systèmes, 2014. Abaqus Documentation Version 6.14. Vol. 651. Simulia Corporation, Vélizy-Villacoublay, France.

De Borst, R., 1996. Softening, damage and higher-order continua. Proceedings of the 2nd Conference on Fracture Mechanics of Concrete Structures 1, 1631–1640.

Desmorat, R., 2016. Anisotropic damage modeling of concrete materials. International Journal of Damage Mechanics 25 (6), 818–852.

Desrumaux, F., Meraghni, F., Benzeggagh, M. L., 2000. Micromechanical modelling coupled to a reliability approach for damage evolution prediction in composite materials. Applied Composite Materials 7 (4), 231–250.

Desrumaux, F., Meraghni, F., Benzeggagh, M. L., 2001. Generalised Mori-Tanaka Scheme to Model Anisotropic Damage Using Numerical Eshelby Tensor. Journal of Composite Materials 35, 603–624.

Doghri, I., Tinel, L., 2005. Micromechanical modeling and computation of elasto-plastic materials reinforced with distributed-orientation fibers. International Journal of Plasticity 21 (10), 1919–1940.

Doi, M., 1981. Molecular dynamics and rheological properties of concentrated solutions of rodlike polymers in isotropic and liquid crystalline phases. Journal of Polymer Science: Polymer Physics Edition 19 (2), 229–243.

Dougill, J. W., 1976. On stable progressively fracturing solids. Zeitschrift für angewandte Mathematik und Physik 27, 423–437.

Drugan, W. J., Willis, J. R., 1996a. A micromechanics-based nonlocal constitutive equation and estimates of representative volume element size for elastic composites. Journal of the Mechanics and Physics of Solids 44 (4), 497–524.

Drugan, W. J., Willis, J. R., 1996b. A micromechanics-based nonlocal constitutive equations and estimates of representative volume element size for elastic composites. Journal of the Mechanics and Physics of Solids 44, 497–524.

Dumont, P. J., Orgéas, L., Favier, D., Pizette, P., Venet, C., 2007. Compression moulding of SMC: in situ experiments, modelling and simulation. Composites Part A: Applied Science and Manufacturing 38, 353–368.

Duschlbauer, D., Pettermann, H., Böhm, H., 2003. Mori-Tanaka based evaluation of inclusion stresses in composites with nonaligned reinforcements. Scripta Materialia 48 (3), 223–228.

Ernst, H., Heinrich, F., Bräuning, R., Potyra, T., Matos, E., Stadtfeld, H. C., Walch, M., 2006. Herstellungsprozess des SMC-Kofferraumdeckels des neuen VW-Cabriolets EOS und neue Technologien zur Herstellung von SMC-Bauteilen im Direktverfahren. In: 9. Internationale AVK-Tagung für verstärkte Kunststoffe und technische Duroplaste: Wettbewerbsfähig durch Verbundwerkstoffe. Essen.

Eshelby, J., 1957. The determination of the elastic field of an ellipsoidal inclusion and related problems. Proceedings of the Royal Society of London. Series A, Mathematical and Physical Sciences 241 (1226), 376–396.

Eshelby, J., 1959. The elastic field outside an ellipsoidal inclusion. Proceedings of the Royal Society of London. Series A, Mathematical and Physical Sciences 252 (1271), 561–569.

Fassin, M., Eggersmann, R., Wulfinghoff, S., Reese, S., 2019. Gradient-extended anisotropic brittle damage modeling using a second order damage tensor – Theory, implementation and numerical examples. International Journal of Solids and Structures 167, 93–126.

Feder, J., 1980. Random sequential adsorption. Journal of Theoretical Biology 87 (2), 237–254.

Fengler, B., Hrymak, A., Kärger, L., 2019. Multi-objective CoFRP patch optimization with consideration of manufacturing constraints and integrated warpage simulation. Composite Structures 221, 110861.

Fette, M., Hentschel, M., Santafe, J. G., Wille, T., Büttemeyer, H., Schiebel, P., 2017. New methods for computing and developing hybrid sheet molding compound structures for aviation industry. In: Procedia CIRP. Vol. 66.

Fitoussi, J., Bocquet, M., Meraghni, F., 2013. Effect of the matrix behavior on the damage of ethylene-propylene glass fiber reinforced composite subjected to high strain rate tension. Composites Part B: Engineering 45 (1), 1181–1191.

Fitoussi, J., Bourgeois, N., Guo, G., Baptiste, D., 1996. Prediction of the anisotropic damaged behavior of composite materials: introduction of multilocal failure criteria in a micro-macro relationship. Computational Materials Science 5, 87–100.

Fitoussi, J., Guo, G., Baptiste, D., 1998. A statistical micromechanical model of anisotropic damage for S.M.C. composites. Composites Science and Technology 58 (5), 759–763.

Fitoussi, J., Meraghni, F., Jendli, Z., Hug, G., Baptiste, D., 2005. Experimental methodology for high strain-rates tensile behaviour analysis of polymer matrix composites. Composites Science and Technology 65 (14), 2174–2188.

Fliegener, S., Luke, M., Gumbsch, P., 2014. 3D microstructure modeling of long fiber reinforced thermoplastics. Composites Science and Technology 104, 136–145.

Folgar, F. P., Tucker, C. L., 1984. Orientation behavior of fibers in concentrated suspensions. Journal of Reinforced Plastics and Composites 3, 98–119.

Forest, S., Berdin, C., Besson, J., Bugat, S., Lorentz, E., 2004. Local Approach to Fracture. Les Presses de l'Ecole des Mines, Paris.

Franko, M., Sedlaček, M., Podgornik, B., Nagode, M., 2017. Validation of linear damage rules using random loading. International Journal of Damage Mechanics 26 (3), 463–469.

Frazier, P. I., 2018. A Tutorial on Bayesian Optimization. arXiv 1807.02811, 1–22.

Frigo, M., Johnson, S. G., 2005. The Design and Implementation of FFTW3. In: Proceedings of the IEEE. Vol. 93.

Fritzsche, P., Weder, M., Wyss, I., Hörmann, M., Müller, J., 2008. A procedure for the simulation of failure in thermoplastic composites. Composite Structures 85 (4), 337–349.

Gajek, S., Schneider, M., Böhlke, T., 2021. An FE-DMN method for the multiscale analysis of fiber reinforced plastic components. Computer Methods in Applied Mechanics and Engineering 384, 113952.

Ganjiani, M., 2018. A thermodynamic consistent rate-dependent elastoplastic-damage model. International Journal of Damage Mechanics 27 (3), 333–356.

Gélébart, L., Mondon-Cancel, R., 2013. Non-linear extension of FFT-based methods accelerated by conjugate gradients to evaluate the mechanical behavior of composite materials. Computational Materials Science 77, 430–439.

Gerasimov, T., De Lorenzis, L., 2019. On penalization in variational phase-field models of brittle fracture. Computer Methods in Applied Mechanics and Engineering 354, 990–1026.

Germain, N., Besson, J., Feyel, F., 2007. Composite layered materials: Anisotropic nonlocal damage models. Computer Methods in Applied Mechanics and Engineering 196 (41–44), 4272–4282.

Ghossein, E., Lévesque, M., 2013. Random generation of periodic hard ellipsoids based on molecular dynamics: A computationally-efficient algorithm. Journal of Computational Physics 253, 471–490.

Gitman, I. M., Askes, H., Sluys, L., 2007. Representative volume: Existence and size determination. Engineering Fracture Mechanics 74, 2518–2534.

Goidescu, C., Welemane, H., Pantale, O., Karama, M., Kondo, D., 2015. Anisotropic unilateral damage with initial orthotropy: A micromechanics-based approach. International Journal of Damage Mechanics 24 (3), 313–337.

Goldberg, N., Ospald, F., Schneider, M., 2017. A fiber orientation-adapted integration scheme for computing the hyperelastic Tucker average for short fiber reinforced composites. Computational Mechanics 60 (4), 595–611.

Görthofer, J., Meyer, N., Pallicity, T. D., Schöttl, L., Trauth, A., Schemmann, M., Hohberg, M., Pinter, P., Elsner, P., Henning, F., Hrymak, A., Seelig, T., Weidenmann, K., Kärger, L., Böhlke, T., 2019a. Motivating the development of a virtual process chain for sheet molding compound composites. In: Proceedings in Applied Mathematics and Mechanics (PAMM). Vol. 19.

Görthofer, J., Meyer, N., Pallicity, T. D., Schöttl, L., Trauth, A., Schemmann, M., Hohberg, M., Pinter, P., Elsner, P., Henning, F., Hrymak, A., Seelig, T., Weidenmann, K., Kärger, L., Böhlke, T., 2019b. Virtual process chain of sheet molding compound: Development, validation and perspectives. Composites Part B: Engineering 169, 133–147.

Görthofer, J., Schneider, M., Hrymak, A., Böhlke, T., 2022a. A computational multiscale model for anisotropic failure of sheet molding compound composites. Composite Structures 288, 115322.

Görthofer, J., Schneider, M., Hrymak, A., Böhlke, T., 2022b. A convex anisotropic damage model based on the compliance tensor. International Journal of Damage Mechanics 31 (1), 43–86.

Görthofer, J., Schneider, M., Ospald, F., Hrymak, A., Böhlke, T., 2020. Computational homogenization of sheet molding compound composites based on high fidelity representative volume elements. Computational Materials Science 174, 109456.

Govindjee, S., Kay, G. J., Simo, J. C., 1995. Anisotropic modelling and numerical simulation of brittle damage in concrete. International Journal for Numerical Methods in Engineering 38, 3611–3633.

Guo, G., Fitoussi, J., Baptiste, D., 1997. Modelling of damage behavior of a short-fiber reinforced composite structure by the finite element analysis using a micro-macro law. International Journal of Damage Mechanics 6, 278–299.

Gurson, A. L., 1977. Continuum Theory of Ductile Rupture by Void Nucleation and Growth: Part I – Yield Criteria and Flow Rules for Porous Ductile Media. Journal of Engineering Materials and Technology 99 (1), 2–15.

Gusev, A., 1997. Representative volume element size for elastic composites: numerical study. Journal of the Mechanics and Physics of Solids 45, 1449–1459.

Hager, W., 1989. Updating the Inverse of a Matrix. SIAM Review 31 (2), 221–239.

Halphen, N., Nguyen, Q., 1975. Sur les matériaux standards generalisés. Journal de Mécanique 14, 508–520.

Hansen, N. R., Schreyer, H. L., 1994. A thermodynamically consistent framework for theories of elastoplasticity coupled with damage. International Journal of Solids and Structures 31 (3), 359–389.

Haralick, R. M., Sternberg, S. R., Zhuang, X., 1987. Image analysis using mathematical morphology. IEEE Transactions on Pattern Analysis and Machine Intelligence 9 (4), 532–550.

Harper, L., Qian, C., Luchoo, R., Warrior, N., 2017. 3D geometric modelling of discontinuous fibre composites using a force-directed algorithm. Journal of Composite Materials 51 (17), 2389–2406.

Hashin, Z., Shtrikman, S., 1962. A variational approach to the theory of the elastic behaviour of polycrystals. Journal of the Mechanics and Physics of Solids 10 (4), 343–352.

Haupt, P., 2002. Continuum Mechanics and Theory of Materials, 2nd Edition. Springer, Berlin, Heidelberg, New York.

Hibbeler, R. C., 2001. Engineering Mechanics. Pearson Education.

Hill, R., 1963. Elastic properties of reinforced solids: Some theoretical principles. Journal of the Mechanics and Physics of Solids 11 (5), 357–372.

Hintermüller, M., Ito, K., Kunisch, K., 2002. The Primal-Dual Active Set Strategy as a Semismooth Newton Method. SIAM Journal on Optimization 13 (3), 865–888.

Hohberg, M., Kärger, L., Bücheler, D., Henning, F., 2017. Rheological In-Mold Measurements and Characterizations of Sheet-Molding-Compound (SMC) Formulations with Different Constitution Properties by Using a Compressible Shell Model. International Polymer Processing 32 (5), 659–668.

Hohberg, M., Kärger, L., Hrymak, A., Henning, F., 2016. Process Simulation of Sheet Molding Compound (SMC) as key for the integrated Simulation Chain. In: NAFEMS Seminar: "Simulation of Composites - Ready for Industry 4.0?".

Holzapfel, G. A., 2000. Nonlinear Solid Mechanics: A Continuum Approach for Enineering. John Wiley & Sons, Ltd., New York.

Huang, B., Zhao, L., 2012. Bridging and roughening of short fibers in SMC and parametric optimum. Composites Part B: Engineering 43 (8), 3146–3152.

Islam, M., Tudryn, G. J., Picu, C. R., 2016. Microstructure modeling of random composites with cylindrical inclusions having high volume fraction and broad aspect ratio distribution. Computational Materials Science 125, 309–318.

Jeffery, G. B., 1923. The motion of ellipsoidal particles immersed in a viscous fluid. Proc. Roy. Soc. London A 102, 161–179.

Jendli, Z., Fitoussi, J., Meraghni, F., Baptiste, D., 2005. Anisotropic strain rate effects on the fibre-matrix interface decohesion in sheet moulding compound composites. Composites Science and Technology 65 (3-4), 387–393.

Jendli, Z., Meraghni, F., Fitoussi, J., Baptiste, D., 2009. Multi-scales modelling of dynamic behaviour for discontinuous fibre SMC composites. Composites Science and Technology 69 (1), 97–103.

Jin, W., Arson, C., 2018. Micromechanics based discrete damage model with multiple non-smooth yield surfaces: Theoretical formulation, numerical implementation and engineering applications. International Journal of Damage Mechanics 27 (5), 611–639.

Ju, J. W., 1989. On energy-based coupled elastoplastic damage theories: Constitutive modeling and computational aspects. International Journal of Solids and Structures 25 (7), 803–833.

Ju, J. W., Wu, Y., 2016. Stochastic micromechanical damage modeling of progressive fiber breakage for longitudinal fiber-reinforced composites. International Journal of Damage Mechanics 25 (2), 203–227.

Junker, P., Riesselmann, J., Balzani, D., 2021. Efficient and robust numerical treatment of a gradient-enhanced damage model at large deformations. arXiv 2102.08819.

Junker, P., Schwarz, S., Jantos, D. R., Hackl, K., 2019. A fast and robust numerical treatment of a gradient-enhanced model for brittle damage. International Journal for Multiscale Computational Engineering 17 (2), 151–180.

Kabel, M., Böhlke, T., Schneider, M., 2014. Efficient fixed point and Newton-Krylov solvers for FFT-based homogenization of elasticity at large deformations. Computational Mechanics 54 (6), 1497–1514.

Kabel, M., Fliegener, S., Schneider, M., 2016. Mixed boundary conditions for FFT-based homogenization at finite strains. Computational Mechanics 57 (2), 193–210.

Kaddour, A. S., Hinton, M. J., Soden, P. D., 2004. A comparison of the predictive capabilities of current failure theories for composite laminates: Additional contributions. Composites Science and Technology 64 (3-4), 449–476.

Kanatani, K.-I., 1984. Distribution of directional data and fabric tensors. International Journal of Engineering Science 22 (2), 149–164.

Kanit, T., Forest, S., Galliet, I., Mounoury, V., Jeulin, D., 2003. Determination of the size of the representative volume element for random composites: statistical and numerical approach. Journal of the Mechanics and Physics of Solids 40 (13–14), 3647–3679.

Karush, W., 1939. Minima of functions of several variables with inequalities as side constraints. Master's thesis, Department of Mathematics, University of Chicago, Chicago.

Kehrer, L., Wicht, D., Wood, J. T., Böhlke, T., 2018. Dynamic mechanical analysis of pure and fiber-reinforced thermoset- and thermoplastic-based polymers and free volume-based viscoelastic modeling. GAMM-Mitteilungen 41 (1), 1–16.

Kehrer, L., Wood, J. T., Böhlke, T., 2020. Mean-field homogenization of thermoelastic material properties of a long fiber-reinforced thermoset and experimental investigation. Journal of Composite Materials 54 (25), 3777–3799.

Kehrer, M. L., 2019. Thermomechanical Mean-Field Modeling and Experimental Characterization of Long Fiber-Reinforced Sheet Molding Compound Composites. Doctoral thesis, Schriftenreihe Kontinuumsmechanik im Maschinenbau Nr. 15, KIT Scientific Publishing, Karlsruhe Institute of Technology (KIT), Karlsruhe.

Khayyam Rayeni, H., Mazaheri, A. H., Taheri-Behrooz, F., 2020. Strength prediction of woven composite rings using progressive damage modeling. International Journal of Damage Mechanics 29 (6), 851–873.

Kim, I. B., Ri, C. S., So, Y. I., 2016. A damage mechanics model of materials with voids and cracks. International Journal of Damage Mechanics 25 (6), 773–796.

Kim, M. S., Lee, W. I., Han, W. S., Vautrin, A., 2011a. Optimization of location and dimension of SMC pre-charge in compression molding process. Computers and Structures 89 (15–16), 353–368.

Kim, M. S., Lee, W. I., Han, W. S., Vautrin, A., 2011b. Optimization of location and dimension of SMC pre-charge in compression molding process. Computers and Structures 89 (15–16), 353–368.

Knops, M., 2008. Analysis of Failure in Fiber Polymer Laminates: The Theory of Alfred Puck. Springer, Berlin, Heidelberg and New York.

Köbler, J., Schneider, M., Ospald, F., Andrä, H., Müller, R., 2018. Fiber orientation interpolation for the multiscale analysis of short fiber reinforced composite parts. Computational Mechanics 61 (6), 729–750.

Krajcinovic, D., 1984. Continuum damage mechanics. Applied Mathematics Reviews 37, 1–6.

Krajcinovic, D., 1989. Damage Mechanics. Mechanics of Materials 8, 3647–3679.

Krause, M., Hausherr, J. M., Burgeth, B., Herrmann, C., Krenkel, W., 2010. Determination of the fibre orientation in composites using the structure tensor and local X-ray transform. Journal of Materials Science 45 (4), 888–896.

Krawietz, A., 1981. Passivity, convexity and normality of elastic-plastic materials. Ingenieur-Archiv 51, 257–274.

Krawietz, A., 2001. Efficient Integration in the Plasticity of Crystals with Pencil Glide and Deck Glide. Technische Mechanik 21 (4), 243–250.

Kuhn, H. W., Tucker, A. W., 1951. Nonlinear programming. In: Neyman, J. (Ed.), Proceedings of the Second Berkeley Symposium on Mathematical Statistics and Probability. University of California Press, Berkeley.

Kupzik, D., Ding, J., Coutandin, S., Fleischer, J., 2020. Digital Process Management for the Integrated Bending of Thermoplastic CFRP Tapes. Procedia CIRP 93, 514–519.

Ladevèze, P., 1983. On an anisotropic damage theory. In: Proceedings of the CNRS. Vol. 351.

Ladevèze, P., 2002. An anisotropic damage theory with unilateral effects: applications to laminates and to three-and four-dimensional composites. Continuum Damage Mechanics of Materials and Structures , 205–234.

Ladevèze, P., Baranger, E., Genet, M., Cluzel, C., 2014. Damage and lifetime modeling for structure computations. Ceramic Matrix Composites: Materials, Modeling and Technology , 465–519.

Ladevèze, P., Lemaitre, J., 1984. Damage effective stress in quasi unilateral conditions. In: Proceedings of the 16th International congress of theoretical and applied mechanics, Lyngby, Denmark.

Langer, J., Gerstenmeyer, M., Schulze, V., 2020. Investigation of automated nibbling as an alternative cutting technology for machining of fiber-reinforced polymers. In: 4th International Conference Hybrid 2020 Materials and Structures, Web-Conference, Germany.

Le, T.-H., Dumont, P., Orgéas, L., Favier, D., Salvo, L., Boller, E., 2008. X-ray phase contrast microtomography for the analysis of the fibrous microstructure of SMC composites. Composites Part A: Applied Science and Manufacturing 39 (1), 91–103.

Lee, H. K., Simunovic, S., 2001. A damage constitutive model of progressive debonding in aligned discontinuous fiber composites. International Journal of Solids and Structures 38 (5), 875–895.

Lemaitre, J., 1986. Local approach of fracture. Engineering Fracture Mechanics 25 (5), 523 – 537.

Lemaitre, J., 1996. A Course on Damage Mechanics, 2nd Edition. Springer, Berlin and London.

Lemaitre, J., Chaboche, J.-L., 1990. Mechanics of Solid Materials. Cambridge University Press.

Li, W. S., Wu, J. Y., 2018. A consistent and efficient localized damage model for concrete. International Journal of Damage Mechanics 27 (4), 541–567.

Li, X., Qu, X., Qi, C., Shao, Z., 2020. An analytical model of multi-stress drops triggered by localized microcrack damage in brittle rocks during progressive failure. International Journal of Damage Mechanics 29 (9), 1345–1360.

Li, Y., Chen, Z., Su, L., Chen, W., Jin, X., Xu, H., 2018a. Stochastic Reconstruction and Microstructure Modeling of SMC Chopped Fiber Composites. Composite Structures 200, 153–164.

Li, Y., Yu, Z., Reese, S., Simon, J.-W., 2018b. Evaluation of the out-of-plane response of fiber networks with a representative volume element model. Tappi Journal , 1–20.

Liang, S., Ren, X., Li, J., 2018. A mesh-size-objective modeling of quasi-brittle material using micro-cell informed damage law. International Journal of Damage Mechanics 27 (6), 913–936.

Linn, J., 2005. The Folgar-Tucker model as a differential algebraic system for fiber orientation calculation. Berichte des Fraunhofer ITWM 75, 1–14.

Liu, D., He, M., Cai, M., 2018. A damage model for modeling the complete stress-strain relations of brittle rocks under uniaxial compression. International Journal of Damage Mechanics 27 (7), 1000–1019.

Liu, X. Z., Zhu, H. H., Ju, J. W., Chen, Q., Jiang, Z. W., Yan, Z. G., 2020. Investigation of the unbiased probabilistic behavior of the fiber-reinforced concrete's elastic moduli using stochastic micromechanical approach. International Journal of Damage Mechanics 29 (7), 1059–1075.

Lonetti, P., Barbero, E. J., Zinno, R., Greco, F., 2004. Erratum: Interlaminar Damage Model for Polymer Matrix Composites. Journal of Composite Materials 38 (9), 799–800.

Lonetti, P., Zinno, R., Greco, F., Barbero, E. J., 2003. Interlaminar Damage Model for Polymer Matrix Composites. Journal of Composite Materials 37 (16), 1485–1504.

Luo, Q., Liu, D., Qiao, P., Zhou, Z., Zhao, Y., Sun, L., 2020. Micro-CT-based micromechanics and numerical homogenization for effective elastic property of ultra-high performance concrete. International Journal of Damage Mechanics 29 (1), 45–66.

Magino, N., Köbler, J., Andrä, H., Welschinger, F., Müller, R., Schneider, M., 2022. A multiscale high-cycle fatigue-damage model for the stiffness degradation of fiber-reinforced materials based on a mixed variational framework. Computer Methods in Applied Mechanics and Engineering 388, 114198.

Matérn, B., 2013. Spatial Variation. Vol. 36. Springer, New York.

Matouš, K., Geers, M. G. D., Kouznetsova, V. G., Gillman, A., 2017. A review of predictive nonlinear theories for multiscale modeling of heterogeneous materials. Journal of Computational Physics 330, 192–220.

McDowell, D., 2008. Viscoplasticity of heterogeneous metallic materials. Materials Science and Engineering: R: Reports 62 (3), 67–123.

McKay, M. D., Beckman, R. J., Conover, W. J., 1979. A Comparison of Three Methods for Selecting Values of Input Variables in the Analysis of Output from a Computer Code. Technometrics 21 (2), 239–245.

Meraghni, F., Benzeggagh, M. L., 1995. Micromechanical modelling of matrix degradation in randomly oriented discontinuous-fibre composites. Composites Science and Technology 55 (2), 171–186.

Meraghni, F., Blakeman, C. J., Benzeggagh, M. L., 1996. Effect of interfacial decohesion on stiffness reduction in a random discontinuous-fibre composite containing matrix microcracks. Composites Science and Technology 56 (5), 541–555.

Meraghni, F., Desrumaux, F., Benzeggagh, M. L., 2002. Implementation of a constitutive micromechanical model for damage analysis in glass mat reinforced composite structures. Composites Science and Technology 62 (16), 2087–2097.

Meyer, N., Schöttl, L., Bretz, L., Hrymak, A., Kärger, L., 2020. Direct bundle simulation approach for the compression molding process of sheet molding compound. Composites Part A: Applied Science and Manufacturing 132, 105809.

Miehe, C., 2002. Strain-driven homogenization of inelastic microstructures and composites based on an incremental variational formulation. International Journal for Numerical Methods in Engineering 55, 1285–1322.

Miehe, C., Welschinger, F., Hofacker, M., 2010. Thermodynamically consistent phase-field models of fracture: Variational principles and multi-field FE implementations. International Journal for Numerical Methods in Engineering 83 (10), 1273–1311.

Mockus, J., 1989. Bayesian Approach to Global Optimization. Springer, Dordrecht.

Mockus, J., 1994. Application of Bayesian approach to numerical methods of global and stochastic optimization. Journal of Global Optimization 4 (4), 347–365.

Mockus, J., Tiesis, V., Zilinskas, A., 1978. The application of Bayesian methods for seeking the extremum. In: L. C. W. Dixon and G. P. Szegö (Ed.), Towards Global Optimisation 2. North Holland Publishing, pp. 117–129.

Mohr, O., 1900. Welche Umstände bedingen die Elastizitätsgrenze und den Bruch eines Materials. Zeitschrift des Vereins Deutscher Ingenieure 46 (1524-1530), 1572–1577.

Montgomery-Smith, S., He, W., Jack, D. A., Smith, D. E., 2011. Exact tensor closures for the three-dimensional Jeffery's equation. Journal of Fluid Mechanics 680, 321–335.

Moradi, M., Bagherieh, A. R., Esfahani, M. R., 2020. Constitutive modeling of steel fiber-reinforced concrete. International Journal of Damage Mechanics 29 (3), 388–412.

Mori, T., Tanaka, K., 1973. Average stress in matrix and average elastic energy of materials with misfitting inclusions. Acta Metallurgica 21 (5), 571–574.

Motaghi, A., Hrymak, A. N., 2017. Microstructure characterization in direct sheet molding compound. Polymer Composites 40, 69–77.

Moulinec, H., Suquet, P., 1994. A fast numerical method for computing the linear and nonlinear mechanical properties of composites. Comptes Rendus de l'Académie des Sciences. Série II 318 (11), 1417–1423.

Moulinec, H., Suquet, P., 1998. A numerical method for computing the overall response of nonlinear composites with complex microstructure. Computer Methods in Applied Mechanics and Engineering 157, 69–94.

Murakami, S., 2012. Continuum Damage Mechanics: A Continuum Mechanics Approach to the Analysis of Damage and Fracture. Vol. 185 of Solid mechanics and its applications. Springer, Dordrecht.

Murakami, S., Ohno, N., 1981. A Continuum Theory of Creep and Creep Damage. In: Ponter, A., Hayhurst, D. (Eds.), Creep in Structures. Springer, Berlin, Heidelberg, pp. 422–444.

Nasab, A. S., Mashayekhi, M., 2019. Application of an efficient anisotropic damage model to the prediction of the failure of metal forming processes. International Journal of Damage Mechanics 28 (10), 1556–1579.

Noii, N., Khodadadian, A., Ulloa, J., Aldakheel, F., Wick, T., Francois, S., Wriggers, P., 2021. Bayesian inversion for unified ductile phase-field fracture. arXiv 2104.11114, 1–61.

Ogihara, S., Koyanagi, J., 2010. Investigation of combined stress state failure criterion for glass fiber/epoxy interface by the cruciform specimen method. Composites Science and Technology 70 (1), 143–150.

Okabe, T., Onodera, S., Kumagai, Y., Nagumo, Y., 2018. Continuum damage mechanics modeling of composite laminates including transverse cracks. International Journal of Damage Mechanics 27 (6), 877–895.

Onodera, S., Okabe, T., 2020. Analytical model for determining effective stiffness and mechanical behavior of polymer matrix composite laminates using continuum damage mechanics. International Journal of Damage Mechanics 29 (10), 1512–1542.

Ortiz, M., 1985. A constitutive theory for the inelastic behavior of concrete. Mechanics of Materials 4 (1), 67–93.

Ortiz, M., Popov, E. P., 1982. A physical model for inelasticity of concrete. Proceedings of the Royal Society A 383, 101–125.

Paleyes, A., Vehtari, A., Saul, A., Damianou, A., Winkelmolen, F., Shen, H., Hensman, J., Gonzalez, J., Massiah, J., Fass, J., Lawrence, N., Palm, R. B., Jenatton, R., Kamronn, S., Dai, Z., 2016. GPyOpt: A Bayesian Optimization framework in Python. `http://github.com/SheffieldML/GPyOpt`.

Pallicity, T. D., Böhlke, T., 2021. Effective viscoelastic behavior of polymer composites with regular periodic microstructures. International Journal of Solids and Structures 216, 167–181.

Pijaudier-Cabot, G., Bažant, Z. P., 1987. Nonlocal Damage Theory. Journal of Engineering Mechanics 113 (10), 1512–1533.

Pinter, P., Bertram, B., Weidenmann, K. A., 2016. Algorithms for the determination of curvature from 3D CT images - A comparison. In: Euro Hybrid Materials and Structures. Kaiserslautern, Germany.

Pinter, P., Dietrich, S., Bertram, B., Kehrer, L., Elsner, P., Weidenmann, K., 2018. Comparison and error estimation of 3D fibre orientation analysis of computed tomography image data for fibre reinforced composites. NDT & E International 95, 26–35.

Ponte Castañeda, P., Suquet, P., 1998. Nonlinear composites. Advances in Applied Mechanics 34 (12), 172–195.

Puck, A., Schürmann, H., 2002. Failure analysis of FRP laminates by means of physically based phenomenological models. Composite Science and Technology 62, 1633–1662.

Pupurs, A., Varna, J., 2017. Steady-state energy release rate for fiber/matrix interface debond growth in unidirectional composites. International Journal of Damage Mechanics 26 (4), 560–587.

Quey, R., Renversade, L., 2018. Optimal polyhedral description of 3D polycrystals: method and application to statistical and synchotron X-ray diffraction data. Computer Methods in Applied Mechanics and Engineering 330, 308–333.

Rahimi, A. S., Ayatollahi, M. R., Torabi, A. R., 2020. Elastic-plastic damage prediction in notched epoxy resin specimens under mixed mode I/II loading using two virtual linear elastic failure criteria. International Journal of Damage Mechanics 29 (7), 1100–1116.

Ramtani, S., Berthaud, Y., Mazars, J., 1992. Orthotropic behavior of concrete with directional aspects: modelling and experiments. Nuclear Engineering and Design 133 (1), 97–111.

Reddy, N., 2015. A review on completely biodegradable composites developed using soy-based matrices. Journal of Reinforced Plastics and Composites 34 (18), 1457–1475.

Reese, S., Brepols, T., Fassin, M., Poggenpohl, L., Wulfinghoff, S., 2021. Using structural tensors for inelastic material modeling in the finite strain regime – a novel approach to anisotropic damage. Journal of the Mechanics and Physics of Solids 146, 104174.

Revfi, S., Mikus, M., Behdinan, K., Albers, A., 2021. On the bead design in LFT structures: the influence of manufacturing-induced residual stresses. Design Science 7, e5.

Richter, T., Wong, W. H., Albers, A., 2020. LDA Models for Objective Validation in the early Phase of Product Development. In: Horvath, I., Keenaghan, G. (Eds.), Tools and Methods of Competitive Engineering. Dublin, Ireland.

Rohrmüller, B., Gumbsch, P., Hohe, J., 2020. Microstructural characterization of glass fiber reinforced SMC by nanoindentation and single-fiber push-out test. In: Proceedings of the 4th International Conference Hybrid 2020 Materials and Structures, Germany.

Roubíček, T., 2009. Rate-independent processes in viscous solids at small strains. Mathematical Methods in the Applied Sciences 32 (7), 825–862.

Rousselier, G., 1979. Contribution to the research on fracture properties of metals in the elasto-plastic field. Bulletin de la Direction des Etudes et Recherches. Serie A, Nucleaire, Hydraulique, Thermique , 1–191.

Sauer, J. A., Richardson, G. C., 1980. Fatigue of polymers. International Journal of Fracture 16, 499–532.

Schäferling, M., Berger, D., Häfner, B., Lanza, G., 2018. Data fusion for quality assurance of fibre-reinforced plastics. In: Proceedings of the International Symposium on Structural Health Monitoring and Nondestructive Testing. Saarbrücken, Germany.

Schemmann, M., Gajek, S., Böhlke, T., 2018a. Biaxial Tensile Tests and Microstructure-Based Inverse Parameter Identification of Inhomogeneous SMC Composites. In: Altenbach, H., Jablonski, F., Müller, W. H., Naumenko, K., Schneider, P. (Eds.), Advances in Mechanics of Materials and Structural Analysis: In Honor of Reinhold Kienzler. Vol. 80. Springer International Publishing, pp. 329–342.

Schemmann, M., Görthofer, J., Seelig, T., Hrymak, A., Böhlke, T., 2018b. Anisotropic meanfield modeling of debonding and matrix damage in SMC composites. Composites Science and Technology 161, 143–158.

Schemmann, M., Lang, J., Helfrich, A., Seelig, T., Böhlke, T., 2018c. Cruciform Specimen Design for Biaxial Tensile Testing of SMC. Journal of Composites Science 2 (1), 12.

Schmidt, T., Balzani, D., 2016. Relaxed incremental variational approach for the modeling of damage-induced stress hysteresis in arterial walls. Journal of the Mechanical Behavior of Biomedical Materials 58, 149–162.

Schneider, D., Schoof, E., Huang, Y., Selzer, M., Nestler, B., 2016a. Phase-field modeling of crack propagation in multiphase systems. Computer Methods in Applied Mechanics and Engineering 312, 186–195.

Schneider, M., 2017. The Sequential Addition and Migration method to generate representative volume elements for the homogenization of short fiber reinforced plastics. Computational Mechanics 59, 247–263.

Schneider, M., 2018. On the Barzilai-Borwein basic scheme in FFT-based computational homogenization. International Journal for Numerical Methods in Engineering 118 (8), 482–494.

Schneider, M., 2021. A review of nonlinear FFT-based computational homogenization methods. Acta Mechanica 232, 2051–2100.

Schneider, M., Ospald, F., Kabel, M., 2016b. Computational homogenization of elasticity on a staggered grid. International Journal for Numerical Methods in Engineering 105 (9), 693–720.

Schober, M., Hohe, J., Kuboki, T., 2017. Combined Macro- and Micro-Mechanical Analysis of Instable Crack Propagation in Interlaminar Fracture Toughness Tests. In: Proceedings of the 7th GACM Colloquium on Computational Mechanics. Stuttgart, Germany.

Schöttl, L., Dörr, D., Pinter, P., Weidenmann, K. A., Elsner, P., Kärger, L., 2020. A novel approach for segmenting and mapping of local fiber orientation of continuous fiber-reinforced composite laminates based on volumetric images. NDT & E International 110, 102194.

Schöttl, L., Kolb, P., Liebig, W. V., Weidenmann, K. A., Inal, K., Elsner, P., 2020. Crack characterization of discontinuous fiber-reinforced composites by using micro-computed tomography: Cyclic in-situ testing, crack segmentation and crack volume fraction. Composites Communications 21, 100384.

Schöttl, L., Liebig, W. V., Weidenmann, K. A., Inal, K., Elsner, P., 2021a. The use of the empirical crack orientation tensor to characterize the damage anisotropy. Composites Communications 25, 100613.

Schöttl, L., Weidenmann, K. A., Sabiston, T., Inal, K., Elsner, P., 2021b. Fiber bundle tracking method to analyze sheet molding compound microstructure based on computed tomography images. NDT & E International 117, 102370.

Schwab, F., 2019. Curing Simulations of a Fibre-reinforced Thermoset on a Micro- and Nano-Scale. Doctoral thesis, Karlsruhe Institute of Technology (KIT), Karlsruhe.

Schwarz, S., Junker, P., Hackl, K., 2021. Variational regularization of damage models based on the emulated RVE. Continuum Mechanics and Thermodynamics 33, 69–95.

Sharma, A., Daggumati, S., 2020. Computational micromechanical modeling of transverse tensile damage behavior in unidirectional glass fiber-reinforced plastic composite plies: Ductile versus brittle fracture mechanics approach. International Journal of Damage Mechanics 29 (6), 943–964.

Shirinbayan, M., Fitoussi, J., Abbasnezhad, N., Meraghni, F., Surowiec, B., 2017. Mechanical characterization of a low density sheet molding compound (LD-SMC): Multi-scale damage analysis and strain rate effect. Composites Part B: Engineering 131, 8–20.

Simo, J., Ju, J., 1987. Strain- and stress-based continuum damage models - I. Formulation. International Journal of Solids and Structures 23 (7), 821–840.

Simo, J. C., Hughes, T. J. R., 1998. Computational Inelasticity. Springer, New York.

Simon, J. W., Höwer, D., Stier, B., Reese, S., Fish, J., 2017. A regularized orthotropic continuum damage model for layered composites: intralaminar damage progression and delamination. Computational Mechanics 60 (3), 445–463.

Smit, T. H., Schneider, E., Odgaard, A., 1998. Star length distribution: a volume-based concept for the characterization of structural anisotropy. Journal of Microscopy 191 (3), 249–257.

Sobol', I. M., 1967. On the point distribution in a cube and their approximate evaluation of integrals. USSR Computational Mathematics and Mathematical Physics 7 (4), 86–112.

Sonon, B., François, B., Massart, T. J., 2012. A unified level set based methodology for fast generation of complex microstructural multi-phase RVEs. Computer Methods in Applied Mechanics and Engineering 223-224, 103–122.

Sonon, B., Massart, T. J., 2013. A level-set based representative volume element generator and XFEM simulations for textile and 3D-reinforced composites. Materials 6 (12), 5568–5592.

Stier, B., Bednarcyk, B. A., Simon, J. W., Reese, S., 2015. Investigation of Micro-Scale Architectural Effects on Damage of Composites. National Aeronautics and Space Administration: NASA/TM-2015-218740 .

Stroustrup, B., 1999. An overview of the C++ programming language. In: Zamir, S. (Ed.), The Handbook of Object Technology. CRC Press LLC, Boca Raton, pp. 15/1–15/24.

Sun, C. T., Vaidya, R. S., 1996. Prediction of composite properties from a representative volume element. Composites Science and Technology 56, 171–179.

Susu, L. M., 2017. Analysis and optimal control of a damage model with penalty. Doctoral thesis, Technische Unversität Dortmund, Fakultät für Mathematik, Dortmund, Germany.

Technisches Komitee CEN/TC 249, 1997. Determination of Tensile Properties of Plastics - Part 4: Test Conditions for Isotropic and Orthotropic Fibre-Reinforced Plastic Composites (ISO 527-4: 1997). Deutsches Institut für Normung e.V., Berlin, Germany.

Thomas, M., Mielke, A., 2010. Damage of nonlinearly elastic materials at small strain - Existence and regularity results. ZAMM Zeitschrift fur Angewandte Mathematik und Mechanik 90 (2), 88–112.

Thompson, W. R., 1933. On the likelihood that one unknown probability exceeds another in view of the evidence of two samples. Biometrika 25 (3/4), 285–294.

Torquato, S., Jiao, Y., 2010. Robust algorithm to generate a diverse class of dense disordered and ordered sphere packings via linear programming. Physical Review E: Statistical, Nonlinear, and Soft Matter Physics 82 (6), 061302.

Trauth, A., 2020. Characterisation and Modelling of Continuous-Discontinuous Sheet Moulding Compound Composites for Structural Applications. Doctoral thesis, Karlsruhe Institute of Technology (KIT), Karlsruhe, Germany.

Trauth, A., Bondy, M., Weidenmann, K. A., Altenhof, W., 2018. Mechanical properties and damage evolution of a structural sheet molding compound based on a novel two step curing resin system. Materials and Design 143, 224–237.

Trauth, A., Kehrer, L., Pinter, P., Weidenmann, K., Böhlke, T., 2021. On the effective elastic properties based on mean-field homogenization of sheet molding compound composites. Composites Part C: Open Access 4.

Trauth, A., Pinter, P., Weidenmann, K., 2017a. Investigation of Quasi-Static and Dynamic Material Properties of a Structural Sheet Molding Compound Combined with Acoustic Emission Damage Analysis. Journal of Composites Science 1 (2), 18.

Trauth, A., Pinter, P., Weidenmann, K. A., 2017b. Acoustic Emission Analysis during Bending Tests of Continuous and Discontinuous Fiber Reinforced Polymers to Be Used in Hybrid Sheet Molding Compounds. Key Engineering Materials 742, 644–651.

Trauth, A., Weidenmann, K. A., Altenhof, W., 2019. Puncture properties of a hybrid continuous-discontinuous sheet moulding compound for structural applications. Composites Part B: Engineering 158, 46–54.

Truesdell, C., Toupin, R. A., 1960. Encyclopedia of Physics: Principles of Thermodynamics and Statics. Springer, Berlin, Heidelberg.

Tvergaard, V., 1982. Material failure by void coalescence in localized shear bands. International Journal for Solids and Structrures 18 (8), 659–672.

Tyler, D. E., 1987. Statistical analysis for the angular central Gaussian distribution on the sphere. Biometrika 74 (3), 579–589.

United Nations Environment Programme, 2015. Paris Agreement. Tech. Rep. 1, United Nations Framework Convention on Climate Change.

United Nations Environment Programme, 2019. Climate Action: Why It Matters. Tech. Rep. 2, Sustainable Development Goals.

Verleye, V., Dupret, F., 1993. Prediction of fiber orientation in complex injection molded parts. In: Developments in Non-Newtonian Flows. Vol. 175.

Voyiadjis, G. Z. (Ed.), 2015. Handbook of Damage Mechanics. Springer, New York, United States.

Wang, S., Xu, W., 2020. A coupled elastoplastic anisotropic damage model for rock materials. International Journal of Damage Mechanics 29 (8), 1222–1245.

Wardeh, M. A., Toutanji, H. A., 2017. Parameter estimation of an anisotropic damage model for concrete using genetic algorithms. International Journal of Damage Mechanics 26 (6), 801–825.

Wei, Q., Gu, B., Sun, B., 2020. Ballistic penetration damages and energy absorptions of stacked cross-plied composite fabrics and laminated panels. International Journal of Damage Mechanics 29 (9), 1465–1484.

Wicht, D., Schneider, M., Böhlke, T., 2020. On Quasi-Newton methods in fast Fourier transform-based micromechanics. International Journal for Numerical Methods in Engineering 121 (8), 1665–1694.

Wilkinson, A. N., Ryan, A. J., 1998. Polymer Processing and Structure Development. Springer, Dordrecht.

Williams, C. K. I., Rasmussen, C. E., 2006. Gaussian Processes for Machine Learning. Vol. 2. The MIT press.

Willis, J. R., 1981. Variational and related methods for the overall properties of composites. Advances in Applied Mechanics 21, 1–78.

Wintiba, B., Sonon, B., Ehab Moustafa Kamel, K., Massart, T. J., 2017. An automated procedure for the generation and conformal discretization of 3D woven composites RVEs. Composite Structures 180, 955–971.

Witten, E., Sauer, M., Kühnel, M., 2017. Composites Market Report 2017 - Market Developments, Trends, Outlook and Challenges. Tech. rep., AVK Industrievereinigung verstärkte Kunststoffe.

Wu, Y., Ju, J. W., 2017. Elastoplastic damage micromechanics for continuous fiber-reinforced ductile matrix composites with progressive fiber breakage. International Journal of Damage Mechanics 26 (1), 3–27.

Wulfinghoff, S., Fassin, M., Reese, S., 2017. A damage growth criterion for anisotropic damage models motivated from micromechanics. International Journal of Solids and Structures 121, 21–32.

Xu, X., Gao, F., Zhang, Z., 2018. Thermo-mechanical coupling damage constitutive model of rock based on the Hoek-Brown strength criterion. International Journal of Damage Mechanics 27 (8), 1213–1230.

Yan, H., Jin, H., Yao, R., 2020. Prediction of the damage and fracture of cast steel containing pores. International Journal of Damage Mechanics 29 (1), 166–183.

Yang, L., Liu, J., Yu, B., Ju, J. W., 2017. Failure path-independent methodology for structural damage evolution and failure mode analysis of framed structures. International Journal of Damage Mechanics 26 (2), 274–292.

Yang, Y., Chen, J., Huang, Z., 2020. Damage evolution in fibrous composites caused by interfacial debonding. International Journal of Damage Mechanics 29 (1), 67–85.

Yazdani, S., Schreyer, H. L., 1990. Combined plasticity and damage mechanics model for plain concrete. Journal of Engineering Mechanics 116, 1435–1450.

Zeman, J., Vondřejc, J., Novak, J., Marek, I., 2010. Accelerating a FFT-based solver for numerical homogenization of periodic media by conjugate gradients. Journal of Computational Physics 229 (21), 8065–8071.

Zhang, W., Cai, Y., 2010. Continuum Damage Mechanics and Numerical Applications. Springer, Heidelberg, London, New York.

Zhang, Y., Ju, J. W., Zhu, H., Chen, Q., Guo, Q., Yan, Z., 2019. A novel damage model based on micromechanics for hybrid fiber reinforced cementitious composites under uniaxial compression. International Journal of Damage Mechanics 28 (7), 1095–1132.

Zheng, Q. S., Du, D. X., 2001. An explicit and universally applicable estimate for the effective properties of multiphase composites which accounts for inclusion distribution. Journal of the Mechanics and Physics of Solids 49, 2765–2788.

Band 1   Felix Fritzen
Microstructural modeling and computational homogeni-
zation of the physically linear and nonlinear constitutive
behavior of micro-heterogeneous materials.
ISBN 978-3-86644-699-1

Band 2   Rumena Tsotsova
Texturbasierte Modellierung anisotroper Fließpotentiale.
ISBN 978-3-86644-764-6

Band 3   Johannes Wippler
Micromechanical finite element simulations of crack
propagation in silicon nitride.
ISBN 978-3-86644-818-6

Band 4   Katja Jöchen
Homogenization of the linear and non-linear mechanical
behavior of polycrystals.
ISBN 978-3-86644-971-8

Band 5   Stephan Wulfinghoff
Numerically Efficient Gradient Crystal Plasticity
with a Grain Boundary Yield Criterion and
Dislocation-based Work-Hardening.
ISBN 978-3-7315-0245-6

Band 6   Viktor Müller
Micromechanical modeling of short-fiber
reinforced composites.
ISBN 978-3-7315-0454-2

Band 7   Florian Rieger
Work-hardening of dual-phase steel.
ISBN 978-3-7315-0513-6

Band 8   Vedran Glavas
**Micromechanical Modeling and Simulation
of Forming Processes.**
ISBN 978-3-7315-0602-7

Band 9   Eric Bayerschen
**Single-crystal gradient plasticity with an accumulated
plastic slip: Theory and applications.**
ISBN 978-3-7315-0606-5

Band 10   Bartholomäus Brylka
**Charakterisierung und Modellierung der Steifigkeit von
langfaserverstärktem Polypropylen.**
ISBN 978-3-7315-0680-5

Band 11   Rudolf Neumann
**Two-Scale Thermomechanical Simulation
of Hot Stamping.**
ISBN 978-3-7315-0714-7

Band 12   Mauricio Lobos Fernández
**Homogenization and materials design of mechanical
properties of textured materials based on zeroth-,
first- and second-order bounds of linear behavior.**
ISBN 978-3-7315-0770-3

Band 13   Malte Schemmann
**Biaxial Characterization and Mean-field Based Damage
Modeling of Sheet Molding Compound Composites.**
ISBN 978-3-7315-0818-2

Band 14   Jürgen Albiez
**Finite element simulation of dislocation
based plasticity and diffusion in multiphase
materials at high temperature.**
ISBN 978-3-7315-0918-9

Sheet molding compound (SMC) composites offer good formability and high freedom in design at comparatively low costs. To apply SMC composites within structural components, a deeper understanding of its characteristic inhomogeneous and anisotropic bundle microstructure and the associated damage evolution is of importance. In this work, we introduce an algorithm based on random sequential addition that allows for a fast generation of high fidelity SMC composite microstructures. An exact closure approximation and a quasi-random orientation sampling lead to a remarkable accuracy. Hence, we comprehensively investigate the sensitivity of the effective elastic properties w.r.t. microstructural parameters. Furthermore, we introduce a framework for anisotropic damage evolution in the context of generalized standard materials. A modular formulation using our concept of extraction tensors and damage-hardening functions, allows for the description of complex damage-degradation behavior and a wide range of applications. To capture the specific damage evolution in SMC composites, we introduce extraction tensors motivated by Puck's laminate theory accounting for different damage mechanisms. Additionally, we present a holistic multiscale approach for constructing anisotropic failure criteria based on full-field simulations of microscale damage evolution. We propose failure surfaces in stress space and stiffness-reduction triggered failure surfaces to cover both a structural analysis and a design process perspective.

ISBN 978-3-7315-1205-9

9 783731 512059